

# **Electrification of Heavy Duty Vehicles**

**DTL**  
MCI - Digital Twin Laboratory

January 12, 2024

# Contents

<b>1</b>	<b>Introduction</b>	<b>11</b>
1.1	Scope of the project . . . . .	11
1.2	Structure of the document . . . . .	12
<b>I</b>	<b>Hydrostatic Power-train</b>	<b>13</b>
<b>2</b>	<b>Hydrostatic transmission</b>	<b>14</b>
2.1	Dynamical Mathematical model . . . . .	14
2.2	Steady state equations . . . . .	16
<b>3</b>	<b>Driver gear model</b>	<b>17</b>
<b>4</b>	<b>Pump and motor volumetric displacement actuator</b>	<b>19</b>
<b>5</b>	<b>Diesel engine model</b>	<b>22</b>
<b>6</b>	<b>Vehicle Control architecture</b>	<b>24</b>
6.1	Introduction . . . . .	24
6.2	Nomenclature . . . . .	24
6.3	Introduction . . . . .	26
6.4	Control architecture . . . . .	26
6.4.1	Introduction . . . . .	26
6.4.2	Control layout . . . . .	29
6.5	Case study . . . . .	32
6.5.1	Simulation results . . . . .	32
6.5.1.1	Scenario 1 . . . . .	32
6.5.1.2	Scenario 2 . . . . .	35
6.5.1.3	Scenario 3 . . . . .	37
6.5.1.4	Scenario 4 . . . . .	39
<b>II</b>	<b>Electrification of an Hydrostatic Power-train</b>	<b>42</b>
<b>7</b>	<b>Introduction</b>	<b>43</b>
<b>8</b>	<b>Power source</b>	<b>45</b>
8.1	The PEM fuel-cell . . . . .	45
8.1.1	Introduction . . . . .	45
8.1.2	Background on electrochemical process . . . . .	46

8.1.3	The Nernst equation . . . . .	51
8.1.4	Dynamic model of PEM fuel-cell . . . . .	52
8.1.5	Material conservation . . . . .	55
8.1.6	PEMFC output voltage . . . . .	57
8.1.7	PEMFC model structure . . . . .	60
8.1.8	The whole mathematical model of the PEMFC . . . . .	62
<b>9</b>	<b>Energy storage</b>	<b>64</b>
9.1	The fly-wheel equipment . . . . .	64
9.2	The lithium-ion battery . . . . .	64
9.2.1	The dynamical model of the lithium-ion battery . . . . .	66
9.3	Battery management . . . . .	71
9.3.1	Preliminaries . . . . .	71
9.3.2	Battery state of charge estimator . . . . .	72
9.3.3	Model based SOC estimation with extended Kalman filter . . . . .	73
<b>10</b>	<b>The DC/DC converter</b>	<b>74</b>
10.1	Zero Voltage Switching Architecture . . . . .	74
10.1.1	Control for ZVS converter . . . . .	76
10.2	Resonant Zero Current Switching Architecture . . . . .	77
10.2.1	Nomenclature . . . . .	77
10.2.2	Model Description . . . . .	78
10.2.3	Modulation Strategy . . . . .	80
10.2.4	Simulation results . . . . .	81
<b>11</b>	<b>The Drivetrain</b>	<b>82</b>
11.1	The Electrical Driver - Inverter . . . . .	82
11.1.1	General description . . . . .	82
11.1.2	Space vector modulation . . . . .	83
<b>12</b>	<b>Internal design of a permanent magnet synchronous machine (PMSM)</b>	<b>86</b>
12.1	Preliminary dimensioning . . . . .	86
12.2	Basic of interior machine design . . . . .	87
12.3	16 poles 12 slots solution . . . . .	89
12.4	8 poles 12 slots solution . . . . .	93
12.5	16 poles 12 slots solution . . . . .	96
12.6	PMSM thermal model . . . . .	99
12.7	Power losses . . . . .	99
12.7.1	Resistive losses (Copper power losses) . . . . .	100
12.7.2	Losses in iron circuit . . . . .	100
12.7.3	Additional losses . . . . .	105
12.7.4	Mechanical losses . . . . .	105
12.7.5	Estimated temperature distribution . . . . .	105
<b>13</b>	<b>Control based model of a PMSM</b>	<b>107</b>
13.1	PMSM model respect to a stationary reference frame . . . . .	108
13.2	PMSM model respect to a rotating reference frame . . . . .	111
13.3	PMSM torque derivation . . . . .	115
13.4	Equivalent circuit of a PMSM . . . . .	117

<b>14 Control of a PMSM</b>	<b>118</b>
14.1 Classical Field Oriented Control of a PMSM . . . . .	118
14.2 Normalization and control implementation. . . . .	121
14.3 Model predictive control of a PMSM . . . . .	122
14.3.1 Discrete-time model . . . . .	122
14.3.2 Control scheme . . . . .	124
14.4 Predictive speed control . . . . .	125
14.4.1 Discrete-time model . . . . .	126
14.4.2 Control scheme . . . . .	126
<b>15 Direct-Torque Control (DTC)</b>	<b>128</b>
<b>16 Advanced Controls for PMSM Applications</b>	<b>129</b>
16.1 PMSM Current Loci and Over-Speed Management . . . . .	129
16.2 Robust field weakening control architecture . . . . .	132
16.3 Sensor-less (encoder-less) control structure with low rate failure synchronization at zero-speed . . . . .	132
16.4 Safety and electromagnetic compatibility . . . . .	132
16.5 Fault detection and fault tolerant control . . . . .	132
<b>III Case Study</b>	<b>133</b>
<b>17 Introduction</b>	<b>134</b>
<b>18 Liebherr diesel engine D934</b>	<b>135</b>
18.1 Technical data . . . . .	135
18.2 Equivalent model . . . . .	138
<b>19 Case study for Liebherr diesel engine D934 electrification</b>	<b>140</b>
19.0.1 Full torque ANSYS analysis . . . . .	141
<b>20 Case study for Liebherr PR736 full electrification</b>	<b>144</b>
20.0.1 Full torque ANSYS analysis . . . . .	145
<b>21 Mercedes-Benz diesel engine OM471</b>	<b>148</b>
21.1 Technical data . . . . .	148
21.2 Equivalent model . . . . .	150
<b>22 Case study for Mercedes-Benz diesel engine OM471 electrification</b>	<b>153</b>
22.0.1 Full torque ANSYS analysis . . . . .	154
<b>IV Appendix</b>	<b>157</b>
<b>23 Hydraulic Valve Piston Control</b>	<b>158</b>
23.1 Introduction . . . . .	158
23.2 Model derivation . . . . .	160
23.2.1 Permanent magnet actuator . . . . .	160
23.2.2 Four-ways valve piston actuated . . . . .	162
23.2.3 The whole model . . . . .	164

---

23.2.3.1	System parameters . . . . .	165
23.2.4	System approximation . . . . .	165
23.3	Control implementation . . . . .	166
23.3.1	Continuous-time domain . . . . .	168
23.3.2	Discrete-time domain . . . . .	170
<b>24</b>	<b>Moving Coil</b>	<b>174</b>
<b>25</b>	<b>Moving reference frames</b>	<b>180</b>
<b>V</b>	<b>ANSYS Tutorial for PMSM design</b>	<b>186</b>
<b>26</b>	<b>Nomenclature and Scope of the document</b>	<b>187</b>
<b>27</b>	<b>RMxprt Toolbox for IPMSM</b>	<b>188</b>
27.1	Introduction . . . . .	188
27.2	Setup of RMxprt design . . . . .	188
27.3	Preparation for Maxwell-Analysis of the RMxprt design . . . . .	193
<b>28</b>	<b>Maxwell Analysis</b>	<b>194</b>
28.1	Maxwell 2D Design . . . . .	194
28.1.1	Transient Analysis . . . . .	194
28.1.2	Magnetostatic Analysis . . . . .	196
28.2	Maxwell 3D Design . . . . .	197
28.2.1	Transient Analysis . . . . .	198

# List of Figures

2.1	Hydrostatic transmission - the whole transmission power-train is made two, independent lines, one for the left side ( $L$ ) and one for the right side ( $R$ ) as follows.	15
3.1	Drive-gear representation.	17
3.2	Drive-gear representation as flexible shaft model.	18
3.3	Track representation.	18
4.1	Swash-plate actuator.	20
4.2	State feedback control of the volumetric displacement actuator.	21
5.1	Engine model and control architecture.	23
5.2	Engine model and control architecture.	23
6.1	Power-train control overview.	27
6.2	Total volumetric displacement for the right drive-line.	27
6.3	Total volumetric displacement for the left drive-line.	28
6.4	Engine anti-stall implementation.	29
6.5	Drive line delta pressure limitation.	30
6.6	Steering and maximum speed limitation.	30
6.7	Global volumetric displacement construction comprehensives of the compensations.	31
6.8	Architecture of the final volumetric displacement containing the engine stall and over-pressure compensation for right track.	31
6.9	Architecture of the final volumetric displacement containing the engine stall and over-pressure compensation for left track.	32
6.10	Description of the test scenario 1.	33
6.11	Simulation results scenario 1.	34
6.12	Simulation results scenario 1.	34
6.13	Volumetric displacements.	35
6.14	Description of the test scenario 2.	36
6.15	Simulation results scenario 2.	36
6.16	Simulation results scenario 2.	37
6.17	Volumetric displacements.	37
6.18	Description of the test scenario 3.	38
6.19	Simulation results scenario 3.	38
6.20	Simulation results scenario 3.	39
6.21	Volumetric displacements.	39
6.22	Description of the test scenario 4.	40
6.23	Simulation results scenario 3.	40
6.24	Simulation results scenario 3.	41

6.25 Volumetric displacements. . . . .	41
7.1 Electrical layout overview. . . . .	43
8.1 Schematic diagram of different fuel cells . . . . .	46
8.2 Themal machines. . . . .	47
8.3 Temperature-entropy diagram for a Carnot cycle. . . . .	48
8.4 Schematic diagram and chemical reaction of PEMFC. . . . .	53
8.5 Schematic diagram of a PEM fuel cell and voltage drop across it. . . . .	56
8.6 Equivalent circuit of the double-layer charging effect inside a PEMFC. . . . .	59
8.7 Block diagram for building a dynamic model of PEMFC. . . . .	61
8.8 Block diagram for building an electrical circuit model for PEMFC. . . . .	61
8.9 $V - I$ and $P - I$ characteristic curves for a 70 kW PEMFC. . . . .	62
9.1 Schematic energy diagram of a lithium cell at open circuit. . . . .	65
9.2 Schematic energy diagram of a lithium cell at open circuit. . . . .	65
9.3 Open circuit voltage as a function of state of charge for different lithium-ion cell chemistries. . . . .	67
9.4 Equivalent circuit of the cell. . . . .	67
9.5 Behavior of the cell polarization, when a cell is subjected to a discharge pulse followed by a rest. . . . .	68
9.6 Circuit that models the diffusion voltage process. . . . .	68
9.7 Measuring parameter values from a pulse response. . . . .	69
9.8 The enhanced self-correcting cell model equivalent circuit. . . . .	71
9.9 Classification of SOC estimation methods. . . . .	72
10.1 DC/DC converter based on galvanic insulated ZVS. . . . .	74
10.2 ZVS control architecture and equivalent control model. . . . .	75
10.3 ZVS modulation strategy based on phase shift $\vartheta$ of the leg $Q_3Q_4$ respect to the leg $Q_1Q_2$ . . . . .	76
10.4 CLL-ZCS resonant converter. . . . .	79
10.5 Resonance circuit analysis as function of the load. . . . .	81
10.6 Description of the modulation law. . . . .	81
11.1 Driver description. . . . .	82
11.2 Representation of the space vector modulation and relation with inverter switches state. . . . .	83
11.3 Space vector representation of a generic voltage vector $\vec{u}_{\alpha\beta}$ . . . . .	84
11.4 Inverter state representation of the voltages $v_1$ and $v_2$ . . . . .	84
11.5 Inverter state representation of the voltages $v_3$ and $v_4$ . . . . .	85
11.6 Inverter state representation of the voltages $v_5$ and $v_6$ . . . . .	85
11.7 Inverter state representations of the voltage $v_0$ . . . . .	85
12.1 Inverter fault representation. . . . .	87
12.2 Permanent magnet operating point. . . . .	88
12.3 Magnetic circuit representation . . . . .	89
12.4 PMSM - description of the main “to be designed” geometric quantities. . . . .	91
12.5 Internal permanent magnet synchronous machine. . . . .	92
12.6 Magnetostatic analysis. . . . .	93
12.7 PMSM - description of the main “to be designed” geometric quantities. . . . .	94

12.8 Internal permanent magnet synchronous machine. . . . .	95
12.9 Magnetostatic Analysis. . . . .	95
12.10PMSM - description of the main “to be designed” geometric quantities. . . . .	97
12.11Internal permanent magnet synchronous machine. . . . .	98
12.12Magnetostatic analysis. . . . .	99
12.13Determination of hysteresis loss. . . . .	101
12.14Approximate hysteresis curves of magnetic sheets. <i>M400-65A</i> contains more silicon than <i>M800-65A</i> , which is a common material in small motors. . . . .	102
12.15Eddy currents in a sheet material. The magnetic flux density <i>B</i> is varying in the directions given by the arrow and the corresponding eddy currents circulate around the magnetic flux. The eddy currents try, according to Lenz’s law, to prohibit the flux from penetrating the lamination. The dashed line is for the magnetic sheet <i>M400-65A</i> and the solid line for the magnetic sheet <i>M800-65A</i> . . . . .	103
12.16Iron losses of two different magnetic sheets at an alternating flux of 50 Hz as a function od the maximum value of flux density. The curves include both the hysteresis loss and the eddy current loss. . . . .	104
12.17Per slot thermal model and equivalent circuit of the PMSM. . . . .	105
12.18Typical coil insulation structure. . . . .	106
13.1 Stationary and rotating reference frame . . . . .	108
13.2 Stationary $\alpha\beta$ reference frame . . . . .	109
13.3 Rotating <i>dq</i> reference frame . . . . .	111
13.4 Rotating and rotor reference frame representation of the pmsm equivalent circuit. . . . .	117
14.1 Internal current control of the classical FOC of a PMSM. . . . .	118
14.2 Vector diagram of the PMSM and effect of the $i_d$ current component on the terminal voltage $\vec{v}_g$ . . . . .	119
14.3 Another representation of the FOC of a PMSM with a state observer. . . . .	120
14.4 <b>FOC of a PMSM</b> using predictive current control. . . . .	125
14.5 Predictive speed control of a <b>PMSM</b> . . . . .	127
16.1 Current limit circle and voltage limit ellipses in $i_d - i_q$ plane. . . . .	130
16.2 Some possible current control strategies and their properties. . . . .	131
16.3 S. . . . .	132
18.1 Liebherr diesel engine D934 - maximum torque curve. . . . .	135
18.2 Liebherr diesel engine D934 - maximum power curve available at the crank-shaft. . . . .	136
18.3 Liebherr diesel engine D934 - Consumption [g/kWh]. . . . .	136
18.4 Liebherr diesel engine D934 - step response. . . . .	137
18.5 Liebherr diesel engine D934 - step response. . . . .	137
18.6 Liebherr diesel engine D934 - step response. . . . .	138
18.7 Engine model and control architecture. . . . .	139
19.1 Speed and torque behaviour. . . . .	141
19.2 Motor current and motor inductances in the DQ reference frame at full load. . . . .	142
19.3 Motor fluxes in the DQ reference frame and power losses at full load. . . . .	142
19.4 Motor terminal voltages at full load. . . . .	143
20.1 Torque speed limit curve. . . . .	144
20.2 Speed and torque behaviour. . . . .	146

20.3 Motor current and motor inductances in the DQ reference frame at full load. . . . .	146
20.4 Motor fluxes in the DQ reference frame and power losses at full load. . . . .	147
20.5 Motor terminal voltages at full load. . . . .	147
21.1 Mercedes-Benz diesel engine OM471 - maximum torque and friction curve. . . . .	148
21.2 Mercedes-Benz diesel engine OM471 - maximum available power at the crankshaft. .	149
21.3 Mercedes-Benz diesel engine OM471 - braking curve. . . . .	149
21.4 Mercedes-Benz diesel engine OM471 - Nominal consumption in [g/kWh]. . . . .	150
21.5 Mercedes-Benz diesel engine OM471 - Specific consumption in %. . . . .	150
21.6 Engine model and control architecture. . . . .	152
22.1 Speed and torque behaviour. . . . .	154
22.2 Motor current and motor inductances in the DQ reference frame at full load. . . . .	155
22.3 Motor fluxes in the DQ reference frame and power losses at full load. . . . .	155
22.4 Motor terminal voltages at full load. . . . .	156
23.1 Four-way valve actuated piston during position changing. . . . .	159
23.2 Permanent magnet spool valve actuator. . . . .	160
23.3 Description of the test signals used for system identification and linearization. . .	166
23.4 Control system layout based on state feedback and state observer for the continuous time domain. . . . .	167
23.5 Control system layout based on state feedback and state observer for the discrete time domain. . . . .	168
23.6 State feedback control. . . . .	169
23.7 Control system layout of the approximated model in continuous time domain. . .	170
23.8 State space representation of a same system: (b) continuous-time domain case; (a) discrete-time domain case. . . . .	171
23.9 (a) Region bounded by lines $\omega = \omega_1$ , $\omega = -\omega_2$ , $\sigma = -\sigma_1$ and $\sigma = -\sigma_2$ in the $s$ -plane; (b) the corresponding region in the $z$ plane. . . . .	172
23.10 Control system layout for the discrete-time domain case. . . . .	173
24.1 Moving coil actuator. . . . .	174
24.2 Evaluation of the $D\vec{B}/Dt$ . . . . .	175
24.3 Lorentz force applied to the coil charge due to effect of the speed. . . . .	177
25.1 Inertial reference frames in relative motion along one axis. . . . .	180
25.2 Inertial reference frames in relative motion. . . . .	182
28.1 Magnetostatic analysis result. . . . .	197
28.2 Simulation results: stator currents. . . . .	199
28.3 Simulation results: DQ-Stator currents and electromagnetic torque. . . . .	200
28.4 Simulation results: DQ-fluxes and DQ-inductances. . . . .	200

# List of Tables

8.1 Standard thermodynamic properties (enthalpy and entropy). . . . .	50
10.1 Components data of the ZVS dc/dc converter. . . . .	75
27.1 PMSM Data as Case Study. . . . .	188
27.2 Machine setup. . . . .	189
27.3 Machine-Stator setup. . . . .	189
27.4 Machine-Stator-Core setup. . . . .	190
27.5 Machine-Stator-Core-Slot setup. . . . .	190
27.6 Machine-Stator-Winding setup. . . . .	191
27.7 Machine-Stator-Winding (End-Insulation) setup. . . . .	191
27.8 Machine-Rotor setup. . . . .	192
27.9 Machine-Rotor-Core setup. . . . .	192
27.10Machine-Rotor-Core-Pole setup. . . . .	192
27.11Machine-Shaft setup. . . . .	193
27.12General - Solution setup. . . . .	193
27.13Generic Rotating Machine - Solution setup. . . . .	193
28.1 PhaseA Excitation setup. . . . .	195
28.2 PhaseA Excitation setup. . . . .	195
28.3 PhaseA Excitation setup. . . . .	196
28.4 Magnetostatic solution setup. . . . .	196
28.5 PhaseA Excitation setup. . . . .	198
28.6 PhaseA Excitation setup. . . . .	198
28.7 PhaseA Excitation setup. . . . .	199

# Chapter 1

## Introduction

### 1.1 Scope of the project

Scope of the project is to design an electrical power-train of a heavy duty vehicle, in particular of a bulldozer tracked vehicle. The original power-train configuration is made by a diesel engine (power source) followed by two hydrostatic transmissions (one for each track), which each one is made by a hydraulic pump and a hydraulic motor. The mechanical end of each hydrostatic transmission is connected to a driver gear which, in turn, is connected to the track of the vehicle. The electrification consists of designing all the components which are necessary in order to replace the whole functionalities of the original vehicle. In order to identify the main components necessary for the design of an electrical vehicle it is necessary to consider different case study

- Full electrification: the whole system consisting of diesel engine and hydrostatic transmission is replaced by an electrical drive train.
- Power source electrification: the only diesel engine and the source of power is electrified. The internal hydrostatic transmission is not modified.

The main components which can be preliminary identified are as follows

- A power source
  - PEM fuel cell (optional)
  - Battery accumulator like lithium-ion battery
- An electrical drives based on inverter
- An electrical motor which in general, due to torque weight ratio, is a permanent magnet synchronous machine (PMSM).

Additional components are

- A DC/DC converter, mandatory in the case of PEM fuel cell
- A bidirectional DC/DC converter with insulation (optional) for ancillary service

Concerning the power source, in this project, the use of a PEM fuel-cell is taken into account. The operative part of the project consists into the modelization, via **simscape** - Matlab/Simulink environment, of the main components and in the implementation of the whole

control strategy. In such a way, the output of the project is a set of mathematical models and a collection of the main design criteria which have been encountered during the design of the electrification.

The following document, will trace a guideline path concerning the design of the electrification.

## 1.2 Structure of the document

The document contains three parts

- **The hydrostatic power-train** – here the description of the actual heavy duty vehicle is reported. Additional information regarding the vehicle control are also reported.
- **Electrification of the hydrostatic power-train** – here a more in deep description of the main electrical equipments are reported.
- **Case study** – here some case study of electrification are reported.

# **Part I**

## **Hydrostatic Power-train**

# Chapter 2

## Hydrostatic transmission

### 2.1 Dynamical Mathematical model

The heavy duty vehicle power-train is, in general, performed by a diesel engine followed by two hydrostatic transmissions (one for each truck), where each one is composed by a variable displacement hydraulic pump followed by a variable (or fixed) displacement hydraulic motor. In the following, we will consider the case where both pump and motor are equipped with a adjustable displacements (which means variable volumetric flow).

The use of both adjustable volumetric displacement pump and motor permits to extend the operating working area, in terms of speed and torque, of the whole transmission line. Basically, this kind of transmission is often identified as a continuous variable gear-ratio. Figure 2.1 depicts a typical hydrostatic power train, where the dynamic equations can be represented as follows

#### Section R.

$$\left\{ \begin{array}{l} \Delta\dot{p}_R = \frac{1}{\beta} [D_p^R \omega_p^R - D_m^R \omega_m^R - q_d^R] \\ \dot{\omega}_m^R = \frac{1}{J_m} [\tau_m^R - \tau_\vartheta^R - b_m \omega_m^R] \quad \text{where} \quad \tau_m^R = D_m^R \Delta p_R \\ \dot{\omega}_l^R = \frac{1}{J_l} [\tau_\vartheta^R n_m / n_l - \tau_l^R - b_l \omega_l^R] \\ \dot{\tau}_\vartheta^R = k_\vartheta [\omega_m^R - \omega_l^R n_m / n_l] \end{array} \right. \quad (2.1.1)$$

where  $D_m^R = d_m^R V_m^{nom}$ ,  $D_p^R = d_p^R V_p^{nom}$  and where  $V^{nom}$  means the nominal volumetric displacement of the pump or motor.

The term  $D_p \omega_p$  represents the total flow at the output of the pump, while the term  $D_m \omega_m$  represents the total flow at the input of the motor. The equation  $\Delta\dot{p} = \frac{1}{\beta} [D_p \omega_p - D_m \omega_m - q_d]$  represents the continuity's law of the hydrostatic driveline.

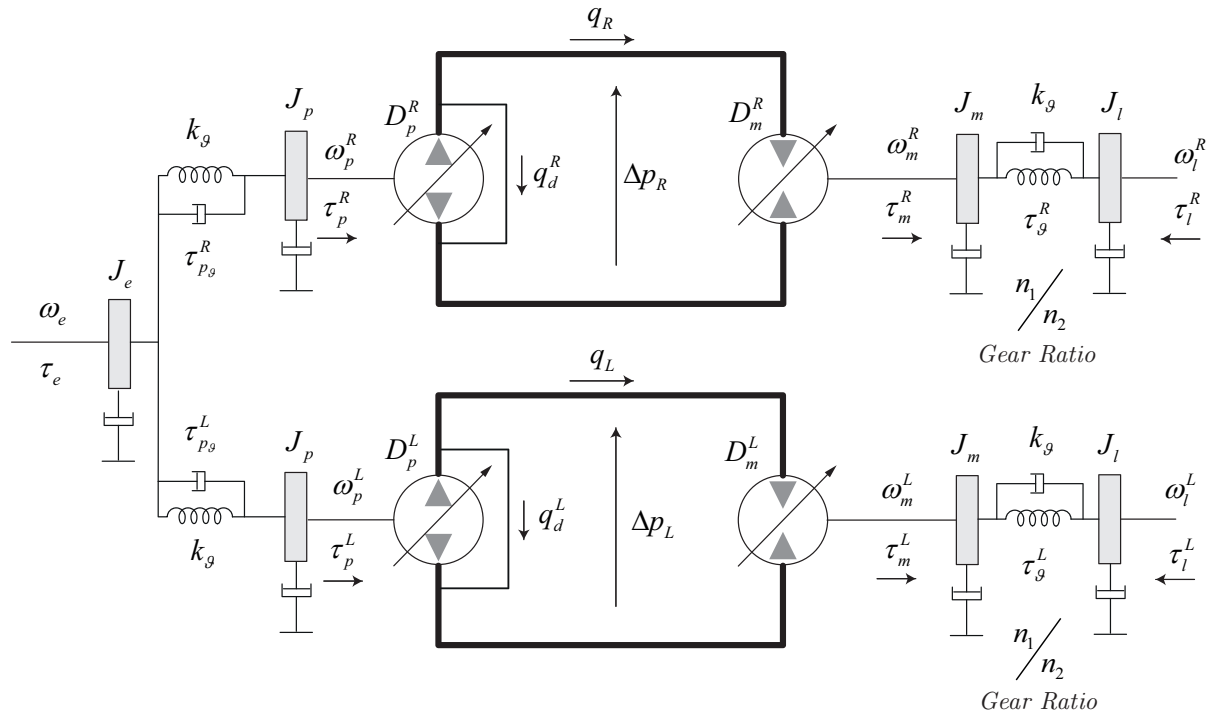


Figure 2.1: Hydrostatic transmission - the whole transmission power-train is made two, independent lines, one for the left side ( $L$ ) and one for the right side ( $R$ ) as follows.

### Section $L$ .

$$\left\{ \begin{array}{l} \Delta \dot{p}_L = \frac{1}{\beta} [D_p^L \omega_p^L - D_m^L \omega_m^L - q_d^L] \\ \dot{\omega}_m^L = \frac{1}{J_m} [\tau_m^L - \tau_\vartheta^L - b_m \omega_m^L] \quad \text{where} \quad \tau_m^L = D_m^L \Delta p_L \\ \dot{\omega}_l^L = \frac{1}{J_l} [\tau_\vartheta^L n_m / n_l - \tau_l^L - b_l \omega_l^L] \\ \dot{\tau}_\vartheta^L = k_\vartheta [\omega_m^L - \omega_l^L n_m / n_l] \end{array} \right. \quad (2.1.2)$$

where  $D_m^L = d_m^L V_m^{nom}$ ,  $D_p^L = d_p^L V_p^{nom}$  and where  $V^{nom}$  means the nominal volumetric displacement of the pump or motor.

Equations of the source side (engine) can be written as follows

$$\left\{ \begin{array}{l} \dot{\omega}_e = \frac{1}{J_e} [\tau_e - \tau_{p\vartheta}^R - \tau_{p\vartheta}^L - b_p \omega_e] \\ \dot{\omega}_p^R = \frac{1}{J_p} [\tau_{p\vartheta}^R - \tau_p^R - b_p \omega_p^R] \\ \dot{\omega}_p^L = \frac{1}{J_p} [\tau_{p\vartheta}^L - \tau_p^L - b_p \omega_p^L] \\ \dot{\tau}_{p\vartheta}^R = k_\vartheta [\omega_e - \omega_p^R] \\ \dot{\tau}_{p\vartheta}^L = k_\vartheta [\omega_e - \omega_p^L] \end{array} \right. \quad (2.1.3)$$

This final group of equations represent the Newton's law at the engine side.

## 2.2 Steady state equations

An important aspect, which has to be taken into account, is the evaluation of the hydrostatic transmission in steady state condition and the relations among torques and rotational speeds, as follows

$$\eta_p^v D_p \omega_p = \frac{D_m \omega_m}{\eta_m^v} \quad (2.2.1)$$

Eq. (2.2.1) represent the steady state flow balance between pump and motor. The terms  $\eta_p^v$  and  $\eta_m^v$  are the volumetric efficiency of the pump and motor respectively. Eq. (2.2.1) can be also represented as follows

$$\boxed{\omega_m = \left( \frac{D_p}{D_m} \right) \omega_p (\eta_p^v \eta_m^v)} \quad (2.2.2)$$

where eq. (2.2.2) shows that the hydraulic motor speed is proportional to the pump volumetric displacement and inversely proportional to the motor volumetric displacement.

The equation Eq. (2.2.3) represents a balance of power among pump and motor

$$\frac{\tau_m \omega_m}{\eta_m^m} = \eta_p^m \tau_p \omega_p \quad (2.2.3)$$

and can also be represented as shown in Eq. (2.2.4)

$$\boxed{\tau_p = \frac{1}{\eta_p^m \eta_m^m} \left( \frac{D_p}{D_m} \right) \tau_m} \quad (2.2.4)$$

where  $\eta_p^m$  and  $\eta_m^m$  are the mechanical efficiency of the pump and motor respectively,  $D_m = V_m^{nom} d_m$  where

$$d_m \in [0.36, 1] = [d_m^{min}, d_m^{max}]$$

and  $D_p = V_p^{nom} d_p$  where

$$d_p \in [-1, 1] = [-d_p^{max}, d_p^{max}].$$

The torque which the engine has to sustain (for steady-state condition) is proportional to the load and to the pump volumetric displacement and inversely proportional to the motor volumetric displacement.

# Chapter 3

## Driver gear model

The hydraulic motor is connected to the track (undercarriages) via a gear device which is also called *drive-gear*, see also Figure 3.1.

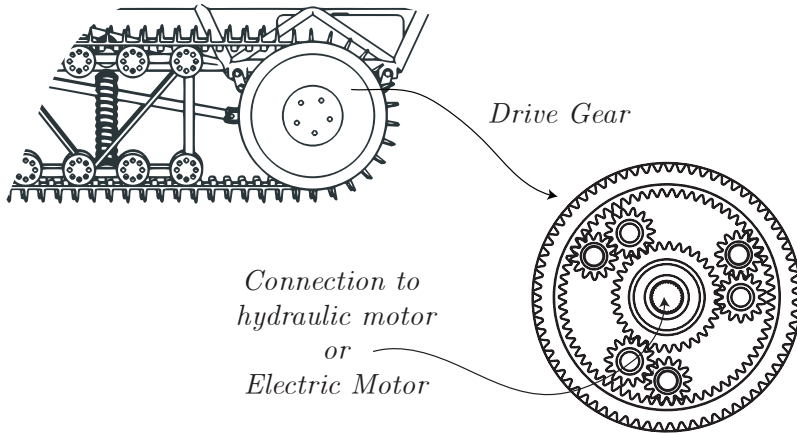


Figure 3.1: Drive-gear representation.

Along this document we suppose that the rotational low speed side has been measured for condition monitoring and control.

The mathematical model of the gear is here reported in a very simplified form:

$$\omega_l = \omega_m / n_{tg} \quad (3.0.1)$$

where  $\omega_l$  is the low speed high torque side connected to the track and  $\omega_m$  is the high speed low torque connected to the hydraulic motor. The term  $n_{tg}$  represents the ratio between high speed and low speed of the gear.

The planetary gear or *driver gear* is here modelled as a flexible shaft (as already reported),

$$\left\{ \begin{array}{l} \dot{\omega}_m = \frac{1}{J_m} [\tau_m - \tau_\vartheta^m - b_m \omega_m] \\ \dot{\omega}_l = \frac{1}{J_l} [\tau_\vartheta^l - \tau_l - b_l \omega_l] \\ \dot{\tau}_\vartheta = k_\vartheta [\omega_m - \omega_l n_{tg}] \\ n_{tg} = \frac{n_m}{n_l} \\ \tau_\vartheta = \tau_\vartheta^m = \frac{\tau_\vartheta^l}{n_{tg}} \end{array} \right. \quad (3.0.2)$$

where  $\tau_\vartheta^m$  is the torsional torque seen at high speed gear side as well as  $\tau_\vartheta^l$  is the torsional torque seen at low speed gear side, see also Figure 3.2.

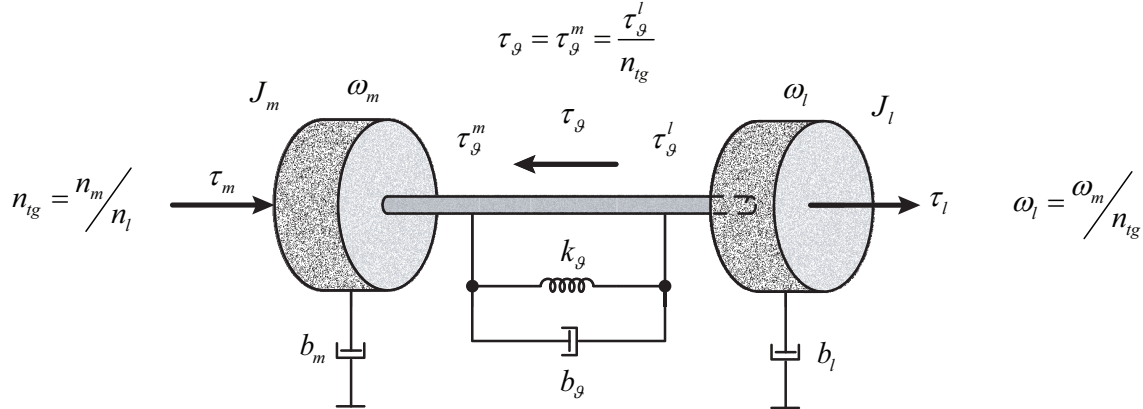


Figure 3.2: Drive-gear representation as flexible shaft model.

A practical example can be as follows.

Let  $n_{tg} = 41.4$  be the gear ratio of the *drive-gear* and let  $R = 0.44056$  m be its radius. Considering a maximum (nominal) vehicle speed of  $v_{tr} = 11$  km h<sup>-1</sup> we obtain a maximum (nominal) hydraulic motor speed of  $\omega_m^{nom} = 2742$  min<sup>-1</sup>, see also Figure 3.3.

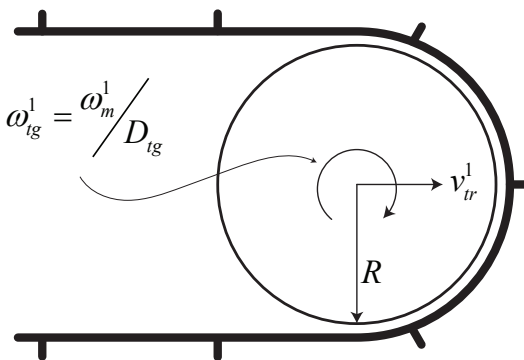


Figure 3.3: Track representation.

## Chapter 4

# Pump and motor volumetric displacement actuator

The pump or motor swash-plate is, in general, actuated by a hydrostatic servo, which is followed by a valve and an electromechanical system actuators. The overall dynamic, which means the dynamic how the swash-plate position is actuated (that means also the dynamic how a certain amount of volumetric displacement is set), plays an important role into the dynamic response of the hydrostatic power-train. Hence, as shown in Figure 4.1, the pump and motor swash-plate actuator can be summarized by a four way spool valve, which is driven by an electromechanical actuator (solenoid or permanent magnet moving coil), and by a double chamber servo actuator. The overall plant, in term of mathematical model (electromechanical and hydrostatic), can be linearized by a double integrator (see also Chapter 23), as follows

$$D(s) = k \frac{1}{s^2} U(s) \quad (4.0.1)$$

where  $D(s)$  represents the per unit volumetric displacement  $d(t)$  and  $U(s)$  is the control input. Hence, the model represented by eq. (4.0.1) is the transfer function between the voltage input (voltage which controls the electromechanical actuator) and the per unit volumetric displacement which is directly correlated to the actual volumetric flow which is also correlated to the position of the swash-plate.

The control architecture of the volumetric displacement is assumed to be implemented as a state feedback control, see also Figure 4.2.

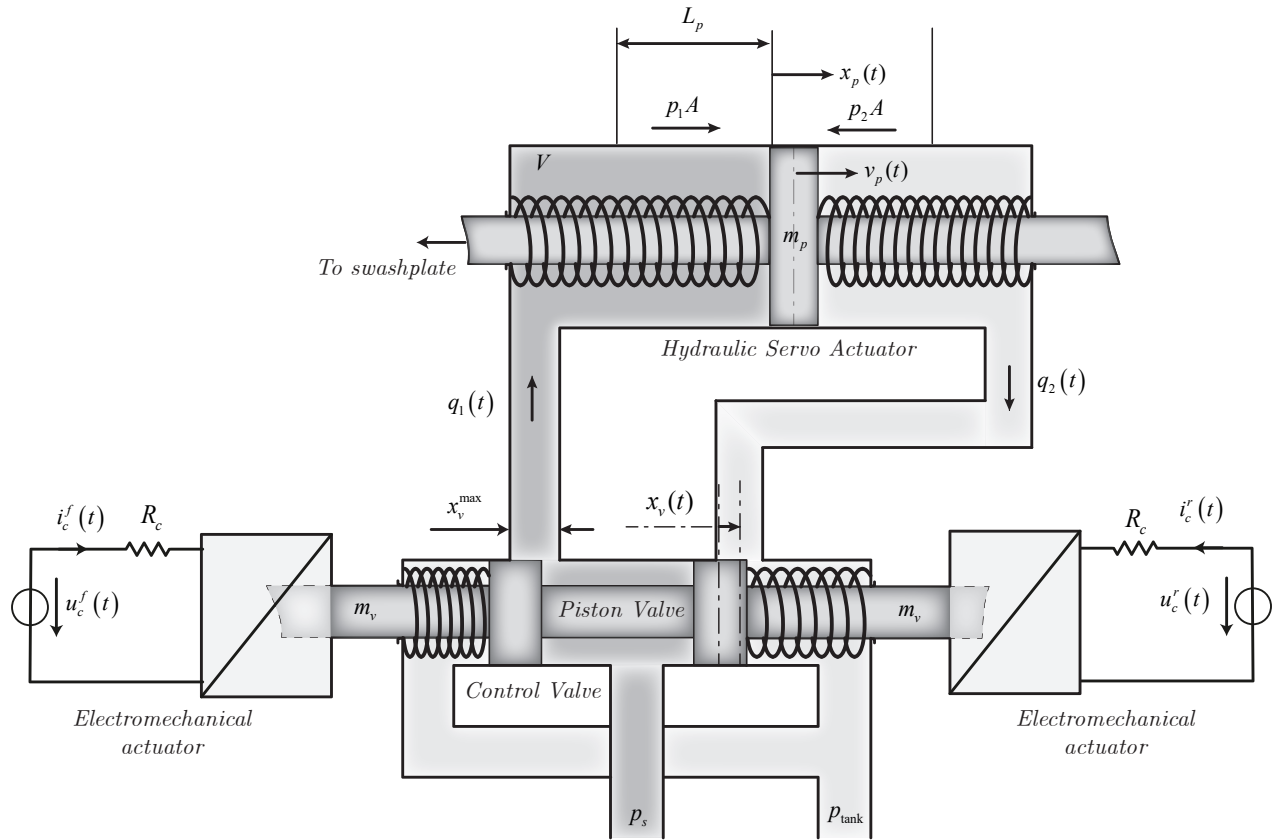


Figure 4.1: Swash-plate actuator.

The whole volumetric displacement system (model and control) of both pump and motor can be modelized in state space form as follows (see also Figure 4.2).

The transfer function

$$H(s) = k \frac{1}{s^2}$$

can be represented in state space form using the controllable canonical form as follows

$$\tilde{\mathbf{A}} = \begin{bmatrix} 0 & 1 \\ 0 & 0 \end{bmatrix} \quad \tilde{\mathbf{B}} = \begin{bmatrix} 0 \\ 1 \end{bmatrix} \quad \mathbf{C} = [k \ 0] \quad (4.0.2)$$

Resulting in the following system

$$\begin{aligned} \dot{\vec{x}}(t) &= \tilde{\mathbf{A}}\vec{x}(t) + \tilde{\mathbf{B}}u(t) \\ y(t) &= \mathbf{C}\vec{x}(t) \end{aligned} \quad (4.0.3)$$

where  $y(t) = d(t)$ . For more details see Chapter 23.

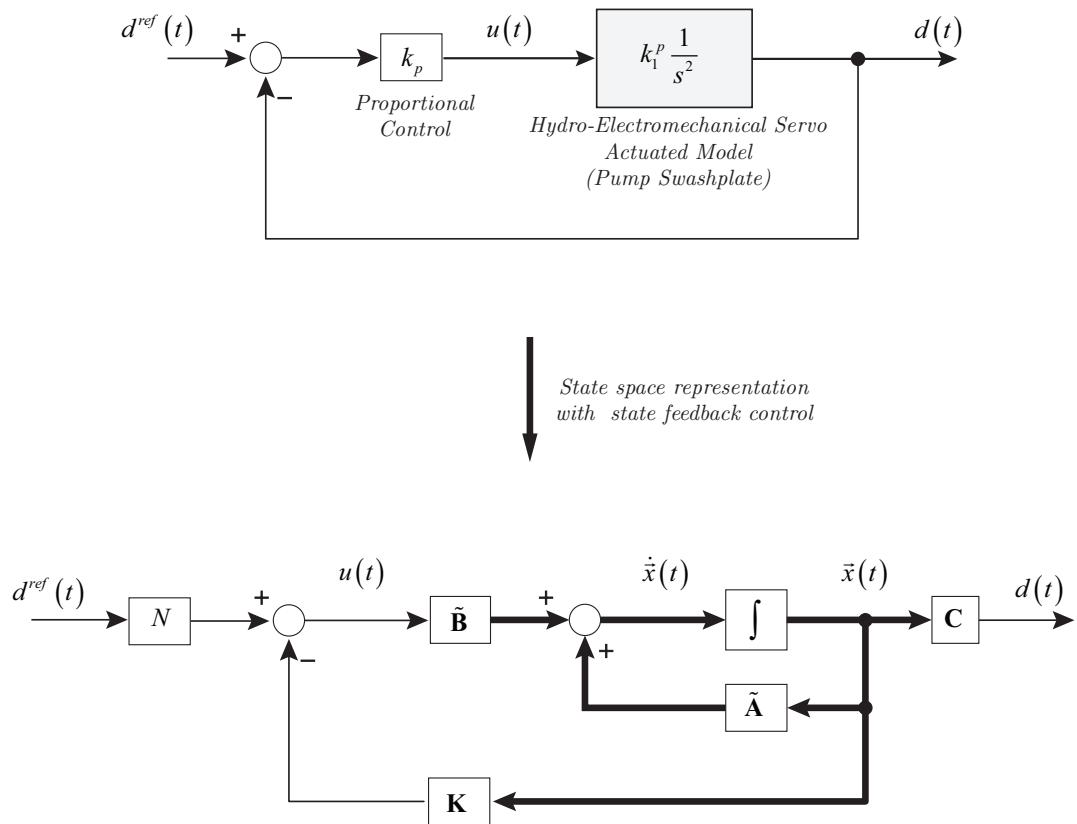


Figure 4.2: State feedback control of the volumetric displacement actuator.

# Chapter 5

## Diesel engine model

In this section the description of the IC-engine is reported. The knowledge of the torque and power curve of the engine plays an important role in the performance of the engine anti-stall control.

In the following, we describe how the IC-engine has been modelized. We start to consider two curves:

- Torque curve: maximum torque available for a given rotor speed and maximum displacement of the throttle.
- Torque friction curve: torque generated by the friction for a given rotor speed. This friction is considered always present, for any value of the throttle. See also Figure 5.1

The mechanical model of the engine can be described as follows

$$J \frac{d\omega_e}{dt} = \theta_f(t) \tau^{nom}(\omega_e) + \tau^b(\omega_e) - \tau_{load} \quad (5.0.1)$$

where  $\tau^{nom}(\omega_e)$  and  $\tau^b(\omega_e)$  are shown in Figure 5.1 while  $\theta_f(t)$  is the throttle which is generated by the external speed loop control as shown in Figure 5.2 and  $J = 7.5 \text{ kg m}^{-2}$ .

The speed control is performed by a PI-controller and it adapts the throttle displacement in order to keep the request speed tracked.

An additional second order filter is taken into account in order to modelize additional dynamics.

The controller can be described as follows

$$\begin{cases} \tilde{\omega}_e(t) = \frac{1}{\omega_e^{nom}} (\omega_e^{\text{ref}} - \omega_e(t)) \\ \theta(t) = k_p \tilde{\omega}_e(t) + \theta^i(t) \\ \frac{d\theta^i}{dt}(t) = k_i \tilde{\omega}_e(t) \end{cases} \quad (5.0.2)$$

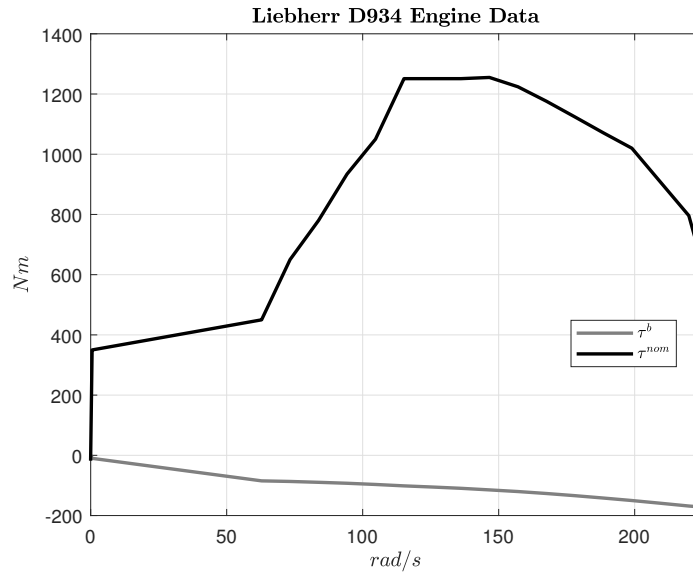


Figure 5.1: Engine model and control architecture.

The control output  $\theta$  is passed through a second order filter:

$$\theta_f(s) = \frac{\omega_0^2}{s^2 + 2\zeta\omega_0 s + \omega_0^2} \theta(s) \quad (5.0.3)$$

where  $\zeta = 1$  and  $\omega_0 = 2\pi 25 \text{ Hz}$ .

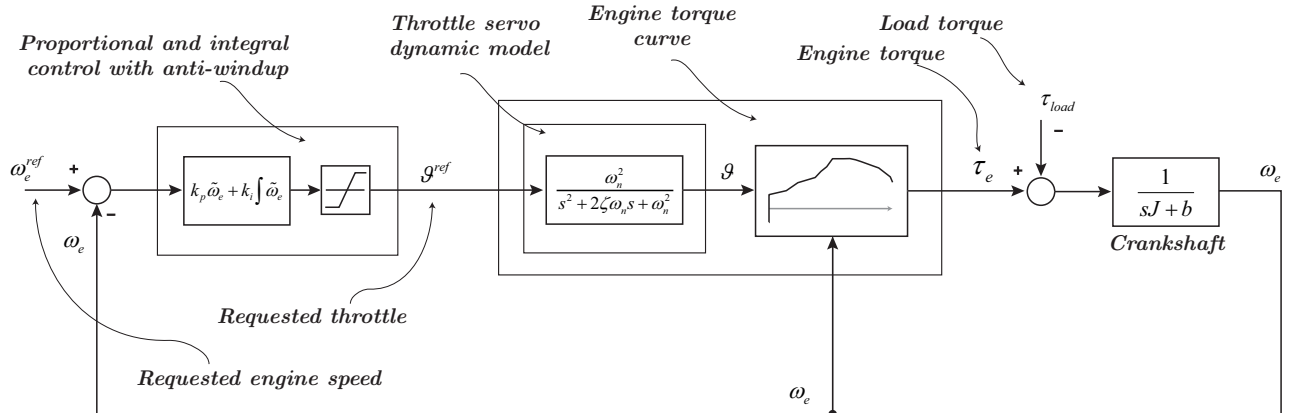


Figure 5.2: Engine model and control architecture.

# Chapter 6

## Vehicle Control architecture

### 6.1 Introduction

The following document reports the description of some control systems used in the management of an heavy duty vehicle. The set of control systems specification can be summarized as follows

- Limit load control: the electronic control system regulates the engine speed and controls the driving speed depending on the required thrust force.
- Maximum speed limiter: controls the travel drive (speed) so that the set travel speed is not exceeded (e.g. downhill)
- Tracks synchronization control: adapts both sides of the tracks so that, for example, when driving straight ahead, the machine actually drives straight ahead.
- Pressure control: automatically reduces the pump adjustment when the high pressure limits are exceeded in order to prevent unnecessary energy loss via the pressure relief valves (e.g. in plowing operations).

As first step a mathematical model of the hydrostatic power-train has been presented. The reason of the mathematical model has different scopes

- find the fundamental motion equations of the system
- find the interconnection among the different dynamic equations
- find a possible model representation for model predictive control implementation

### 6.2 Nomenclature

- $v_{track}^R$ : speed of the right track in  $\text{km h}^{-1}$ .
- $v_{track}^L$ : speed of the left track in  $\text{km h}^{-1}$ .
- $v_{track}^{sum} = v_{track}^R + v_{track}^L$ : sum of the speed of the right and left track in  $\text{km h}^{-1}$ .
- $v_{track}^{diff} = v_{track}^R - v_{track}^L$ : sum of the difference between the right and left track  $\text{km h}^{-1}$ .
- $v_{track}^{ref}|_R$ : speed set-point of the right track in  $\text{km h}^{-1}$ .

- $v_{track}^{ref}|_L$ : speed set-point of the left track in  $\text{km h}^{-1}$ .
- $v_{track}^{ref}|_R^{max}$ : maximum speed set-point of the right track in  $\text{km h}^{-1}$ .
- $v_{track}^{ref}|_L^{max}$ : maximum speed set-point of the left track in  $\text{km h}^{-1}$ .
- $\omega_l^R$ : rotational speed of the follower (side which is connected to the track) of the right driver gear in  $\text{rad s}^{-1}$ .
- $\omega_l^L$ : rotational speed of the follower (side which is connected to the track) of the left driver gear in  $\text{rad s}^{-1}$ .
- $\omega_m^R$ : rotational speed of the driver (side which is connected to the hydraulic motor) of the right driver gear in  $\text{rad s}^{-1}$ .
- $\omega_m^L$ : rotational speed of the driver (side which is connected to the hydraulic motor) of the left driver gear in  $\text{rad s}^{-1}$ .
- $\omega_m^{ref}$ : hydraulic motor rotational speed set-point.
- $n_{tg}$ : drive gear ration.
- $R_{tg}$ : radius of the sprocket wheel connected to the track.
- $V_m^{nom}$ : nominal capacity of the hydraulic motor.
- $V_p^{nom}$ : nominal capacity of the hydraulic pump.
- $\eta_m^v$ : volumetric efficiency of the hydraulic motor.
- $\eta_m^m$ : mechanical efficiency of the hydraulic motor.
- $\eta_p^v$ : volumetric efficiency of the hydraulic pump.
- $\eta_p^m$ : mechanical efficiency of the hydraulic pump.
- $d_p^R$ : right drive-line, per unit pump volumetric displacement, where  $d_p \in [-d_p^{\max}, d_p^{\max}]$ ,  $d_p^{\max}$  is in per unit.
- $d_m^R$ : right drive-line, per unit motor volumetric displacement, where  $d_m \in [d_m^{\min}, d_m^{\max}]$ ,  $d_m^{\max}$  and  $d_m^{\min}$  are in per unit.
- $d_L$ : left drive-line, per unit global volumetric displacement, where  $d \in [-2d_p^{\max} + d_m^{\min}, 2d_p^{\max} - d_m^{\min}]$ ,  $d_p^{\max}$  and  $d_m^{\min}$  are in per unit.
- $d_p^L$ : left drive-line, per unit pump volumetric displacement, where  $d_p \in [-d_p^{\max}, d_p^{\max}]$ ,  $d_p^{\max}$  is in per unit.
- $d_m^L$ : left drive-line, per unit motor volumetric displacement, where  $d_m \in [d_m^{\min}, d_m^{\max}]$ ,  $d_m^{\max}$  and  $d_m^{\min}$  are in per unit.
- $\omega_e$ : engine speed (also pump speed).
- $\omega_e^{ref}$ : engine rotational speed set-point.

- $\tau_e$ : engine torque in Nm.
- $dir_R$ : direction of the right track (1 or -1).
- $dir_L$ : direction of the left track (1 or -1).
- $dirs$ : direction of the sum of the right and left track (1 or -1).

### 6.3 Introduction

In this document we propose a first draft of heavy duty vehicle control architecture based on independent feedback control loops which can be summarized as follows

- A control loop which limits the maximum speed reached by the (*sum*) sum of the tracks speed, where for *sum* tracks speed it is intended  $v_{track}^{sum} = v_{track}^R + v_{track}^L$ . Supposing  $v_{track}^{ref}|_{sum}^{max} = v_{track}^{ref}|_R^{max} + v_{track}^{ref}|_L^{max}$  is the sum of the right and left maximum speed track reference (set-point). This control loop limits the maximum tracks speed sum which e.g. we can assume the following value  $v_{track}^{ref}|_{sum}^{max} = 11 \text{ km h}^{-1} + 11 \text{ km h}^{-1} = 22 \text{ km h}^{-1}$ .
- A (*diff*) difference tracks speed control or steering. Supposing  $v_{track}^{ref}|_{diff} = v_{track}^{ref}|_R - v_{track}^{ref}|_L$  the difference between the right and the left speed track reference (set-point) which results into a steering set-point. This control loop keeps the difference of the tracks speed to a given reference value and moreover saturates to a maximum value the steering speed.
- An *engine anti-stall*. This control loop enables an automatic total volumetric displacement reduction in order to keep the engine at the given value of speed set-point. The effect of the anti-stall is to reduce both (for each side left and right) the current volumetric displacement according the maximum engine torque available at a given engine speed set-point.
- Two *pressure limitation* control loops. These two regulators automatically reduce the corresponding volumetric displacement in order to keep the relative driveline pressure below a given maximum value. E.g. we can assume a delta pressure limit value of  $\Delta p^{lim} = 420 \text{ bar}$ .

### 6.4 Control architecture

#### 6.4.1 Introduction

The power-train control which we are going to describe in next sections can be summarized as shown in Figure 6.1. Three groups of quantities can be distinguished

- References
- Measures
- Control outputs

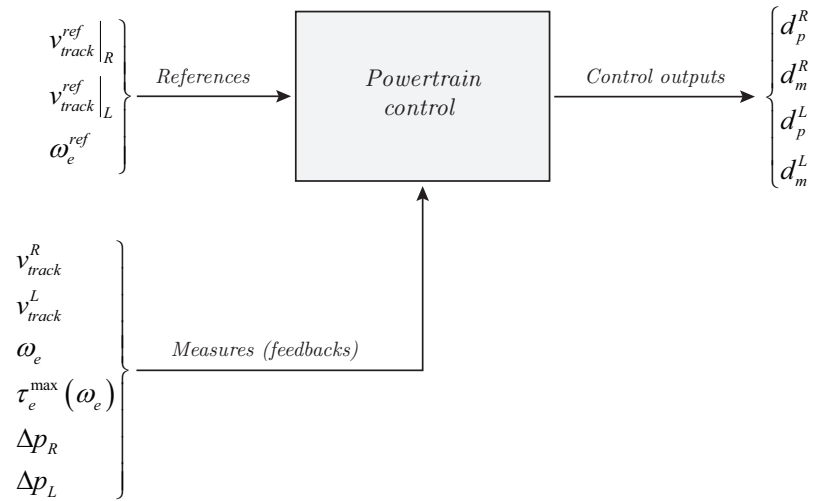


Figure 6.1: Power-train control overview.

As *References* are intended the right and left track speed targets, in  $\left[\text{km h}^{-1}\right]$ , and the engine rotational speed target, in  $\left[\text{min}^{-1}\right]$ .

As *Measures* are intended the right and left track speeds, in  $\left[\text{km h}^{-1}\right]$ , the engine rotational speed, in  $\left[\text{min}^{-1}\right]$ , the right and left drive-line delta pressure, in  $\left[\text{bar}\right]$ , and the available engine torque, in  $\left[\text{N m}\right]$ , derived from engine speed.

As *Control outputs* are intended the volumetric displacements of the hydraulic pumps and hydraulic motors.

In order to simplify the control architecture the following mathematical objects are defined:

- A **global** volumetric displacement (an object which include both motor and pump volumetric displacement) is created (see also Figure 6.2 and Figure 6.3). Let  $d$  be the **global** volumetric displacement, the terms  $d_m$  and  $d_p$  are derived as follows

$$\begin{cases} d_m = d_m^{\max} - [|d| - |d_p|] & \Rightarrow \quad d_m^{\min} \leq d_m \leq d_m^{\max} \\ d_p \Rightarrow -d_p^{\max} \leq d \leq d_p^{\max} \end{cases} \quad (6.4.1)$$

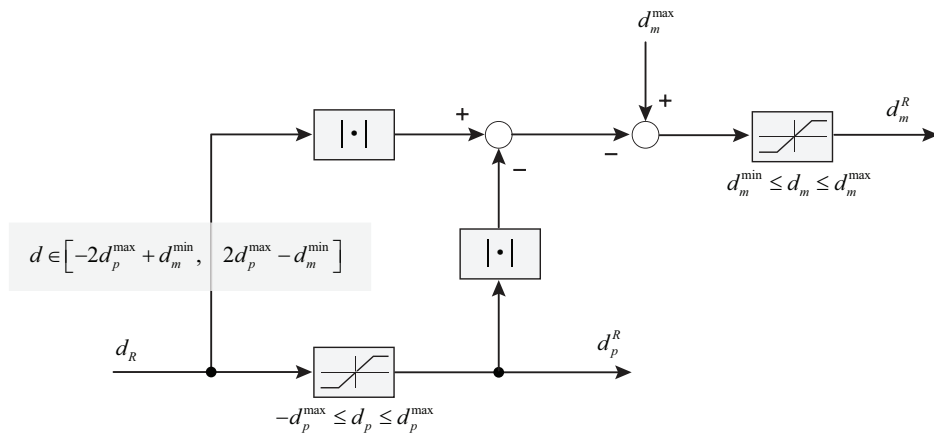


Figure 6.2: Total volumetric displacement for the right drive-line.

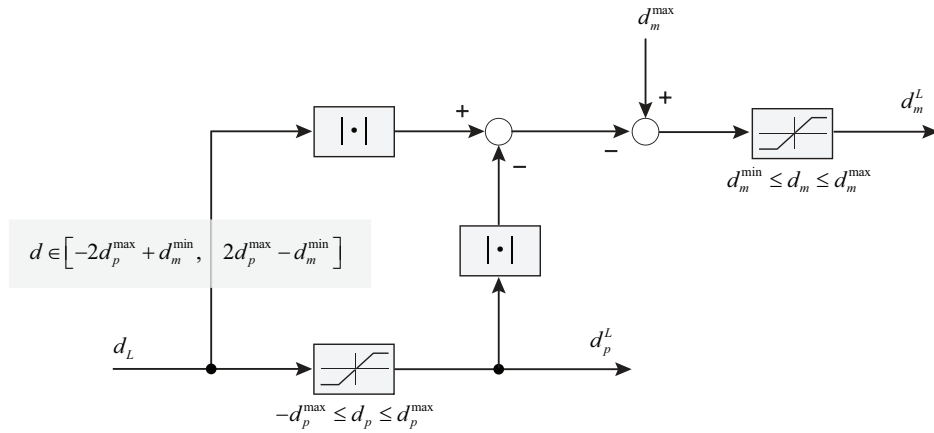


Figure 6.3: Total volumetric displacement for the left drive-line.

The construction of the **global** volumetric displacement is shown in Figure 6.6 Figure 6.8 and Figure 6.9.

Let  $d_R^{ctrl}$  and  $d_L^{ctrl}$  be the volumetric displacements which are generated by the *sum* and *diff* tracks speed loops.

Let  $d_R^{ff}$  and  $d_L^{ff}$  be the volumetric displacements which are generated as feed-forward from the tracks speed set-points as  $v_{track}^{ref}|_R$  and  $v_{track}^{ref}|_L$ .

The **global** volumetric displacements  $d_R$  and  $d_L$  are derived as follows

$$\begin{cases} d_R = d_R^{ctrl} + d_R^{ff} \\ d_L = d_L^{ctrl} + d_L^{ff} \end{cases} \quad (6.4.2)$$

- The **sum** and **diff** regulators are PI-based control loops, which require feedback defined as follows

$$\begin{aligned} v_{track}^{sum} &= v_{track}^R + v_{track}^L \\ v_{track}^{diff} &= v_{track}^R - v_{track}^L \end{aligned} \quad (6.4.3)$$

where

$$\begin{aligned} v_{track}^R &= \frac{1}{2} [v_{track}^{sum} + v_{track}^{diff}] \\ v_{track}^L &= \frac{1}{2} [v_{track}^{sum} - v_{track}^{diff}] \end{aligned} \quad (6.4.4)$$

- Two **global** volumetric displacement feed-forward as  $d_R^{ff}$  and  $d_L^{ff}$ . The construction of the feed-forward terms are here reported. Let  $v_{track}^{ref}$  be the speed track reference in  $\text{m s}^{-1}$  the equivalent hydraulic motor speed reference is given as follows

$$\omega_m^{ref} = \frac{v_{track}^{ref}}{R_{tg}} n_{tg} \quad (6.4.5)$$

Let  $\alpha_{ff}$  be the preliminary per unit volumetric displacement is given as follows

$$\alpha_{ff} = \frac{V_m^{nom}}{V_p^{nom}} \frac{1}{\eta_m^v \eta_p^v} \frac{\omega_m^{ref}}{\omega_e^{ref}} \quad (6.4.6)$$

or also

$$\alpha_{ff} = \left| \frac{1}{\eta_m^v \eta_p^v} \frac{1}{\omega_e^{ref}} \frac{V_m^{nom}}{V_p^{nom}} \frac{n_{tg}}{R_{tg}} v_{track}^{ref} \right| \quad (6.4.7)$$

the final formulation of the feed-forward  $d^{ff}$  can be represented as follows

$$d^{ff} = \begin{cases} 2 d_p^{max} - \frac{1}{\alpha_{ff}} & \text{if } \alpha_{ff} > d_p^{max} \\ \alpha_{ff} & \text{if } \alpha_{ff} \leq d_p^{max} \end{cases} \quad (6.4.8)$$

#### 6.4.2 Control layout

In this section the global control layout is depicted. Some fundamental points are here reported.

- The main speed level is achieved by a feed-forward inputs  $d_R^{ff}$  and  $d_L^{ff}$ , that means the main control is a open loop control. The external loops control just apply adjustment in order to avoid engine stall, over pressure and perform a synchronization among the two tracks. See Figure 6.6, Figure 6.8 and Figure 6.9.
- The speed track measure is not performed, but in its place, the driver gear (follower) rotational speeds  $\omega_l^R$  and  $\omega_l^L$  are measured. That means the overall quantities regarded  $v_{track}$  will be converted (in algebraic way) into quantities of the form  $\omega_l$ , as follows
  - The  $\omega_l^{sum} = \omega_l^R + \omega_l^L$  control loop limits the maximum vehicle speed.
  - The  $\omega_l^{diff} = \omega_l^R - \omega_l^L$  control loop maintains both tracks speed at the same level when not steering is required, and adjust the  $\omega_l^{diff}$  in case of steering demand.

During straight driving the  $\omega_l^{ref}|_{diff}$  reference is set to zero.

- An engine anti-stall control loop is implemented, where the actual engine torque is compared with the torque limit curve  $\tau_e(\omega_e)$  and the total volumetric displacement is properly compensated, see also Figure 6.8, Figure 6.9 and Figure 6.4.

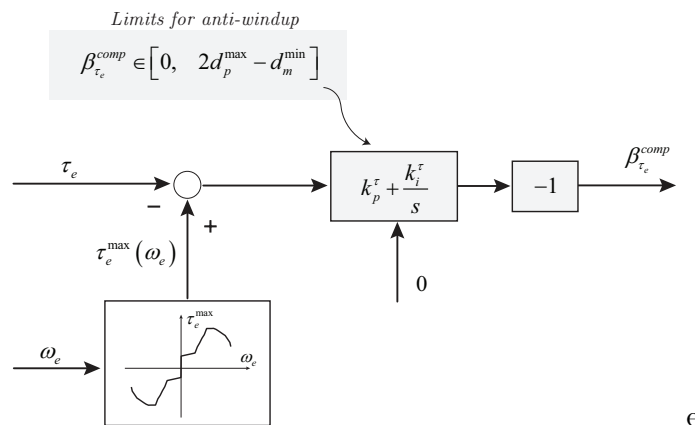


Figure 6.4: Engine anti-stall implementation.

- The limit drive line delta pressure is also constrained by proper compensation of the total volumetric displacement, in order to limit its maximum value, when operative field condition permits it, see also Figure 6.8, Figure 6.9 and Figure 6.5.

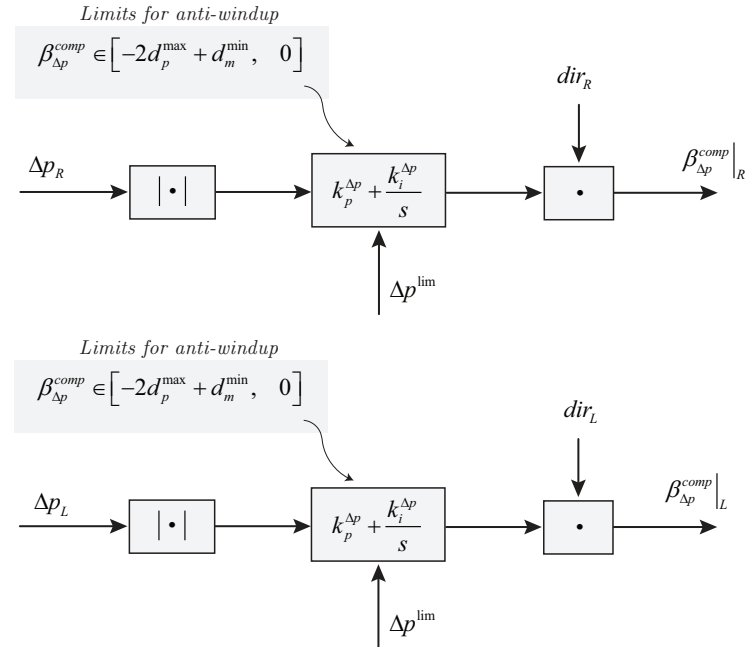


Figure 6.5: Drive line delta pressure limitation.

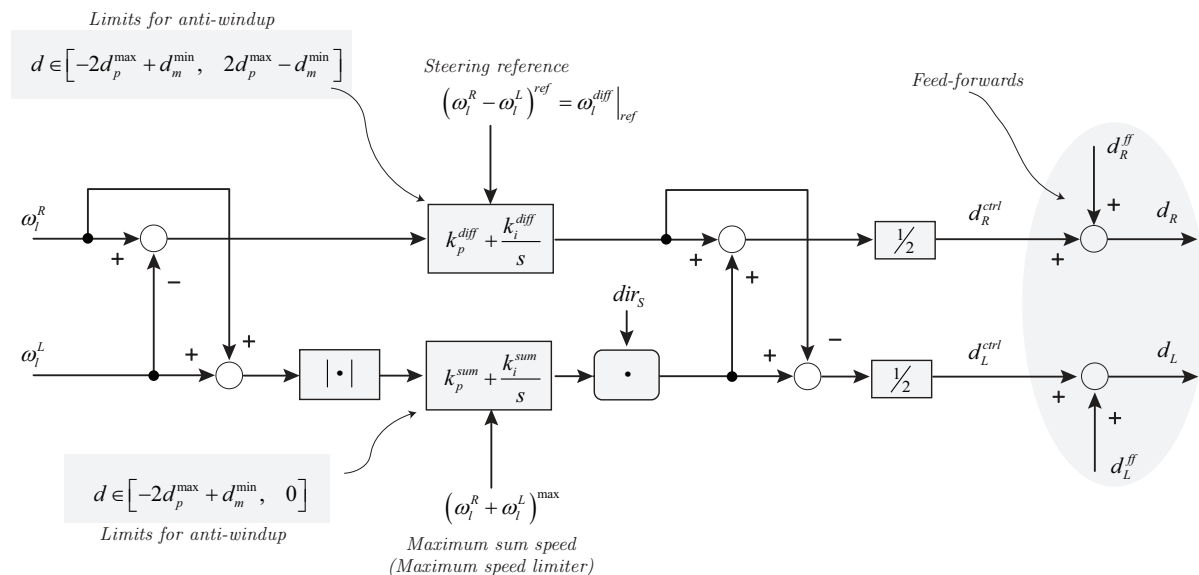


Figure 6.6: Steering and maximum speed limitation.

The global volumetric displacement is derived adding to the feed-forward and to the *sum* and *diff* control loops the *field* compensations. For field here the engine anti-stall and over-pressure compensation is intended. Figure 6.7 shows the global volumetric displacement architecture comprehensive of the *field* compensations.

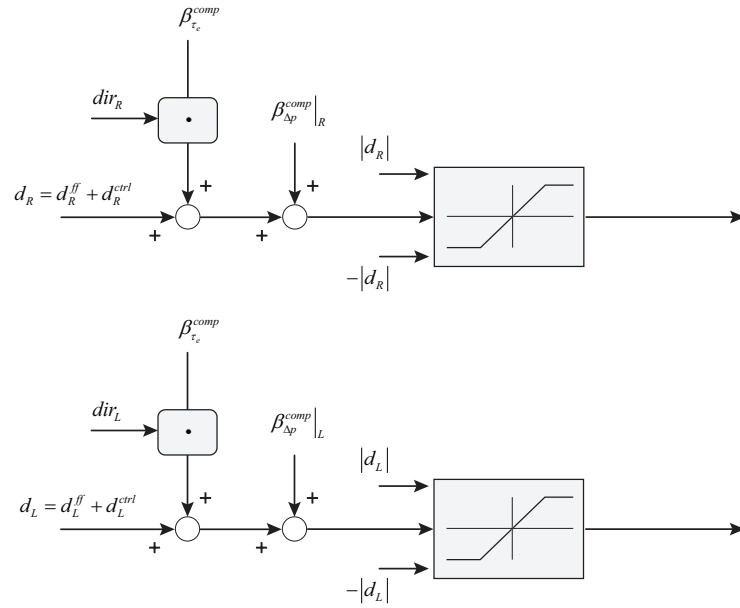


Figure 6.7: Global volumetric displacement construction comprehensives of the compensations.

*Total volumetric displacement and compensation for the Right Track*

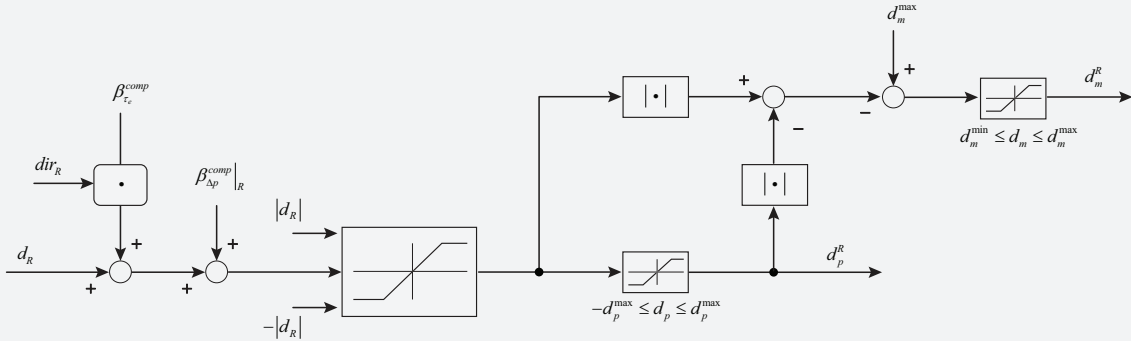


Figure 6.8: Architecture of the final volumetric displacement containing the engine stall and over-pressure compensation for right track.

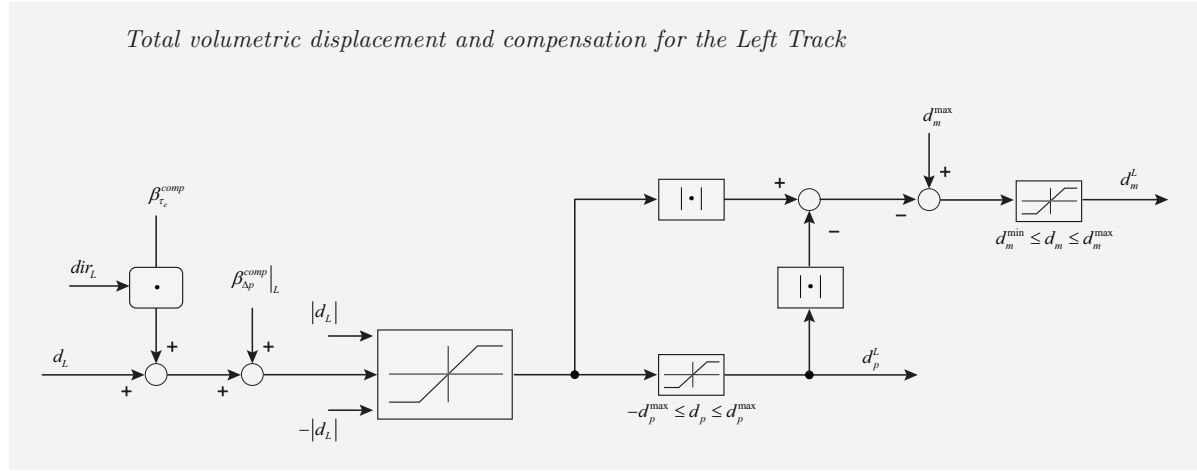


Figure 6.9: Architecture of the final volumetric displacement containing the engine stall and over-pressure compensation for left track.

## 6.5 Case study

The case study we are going to consider is a drive-train with the following data characteristics

- $V_m^{nom} = 252.8 \text{ cm}^3$
- $V_p^{nom} = 147.2 \text{ cm}^3$
- $R = 0.44056 \text{ m}$
- $n_{tg} = n_1/n_2 = 41.4$
- $v_{tr}^{max} = 11.0 \text{ km h}^{-1}$
- $\eta_p^m = 0.909$
- $\eta_p^v = 0.959$
- $\eta_m^m = 0.939$
- $\eta_m^v = 0.943$

### 6.5.1 Simulation results

#### 6.5.1.1 Scenario 1

In this scenario we are considering the following case

- Straight driving.
- Not homogeneous viscosity load on tracks.
- The total amount of load is enough to stall the engine.
- The maximum per drive-line load doesn't exceed the maximum admissible delta pressure.

Figure 6.10: Description of the test scenario 1.

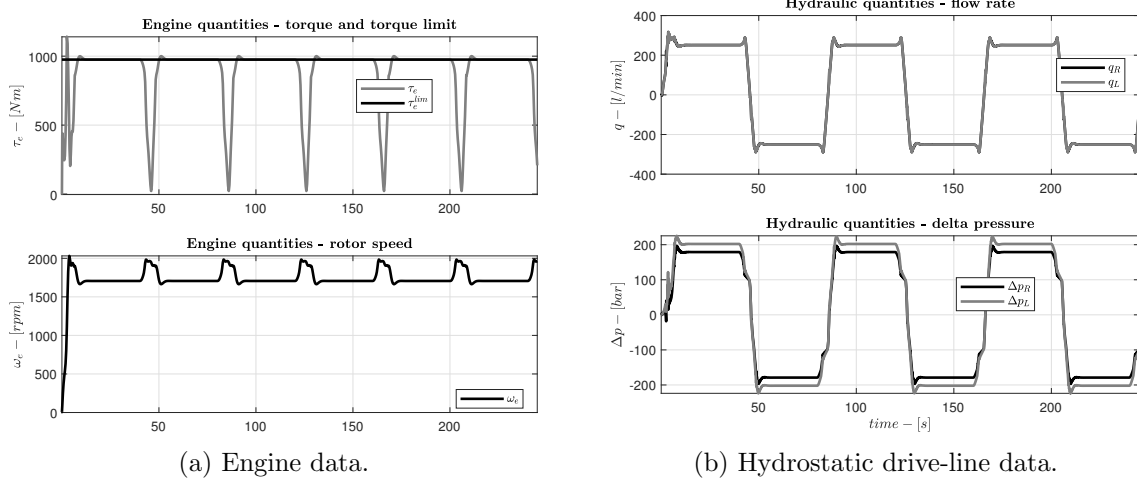


Figure 6.11: Simulation results scenario 1.

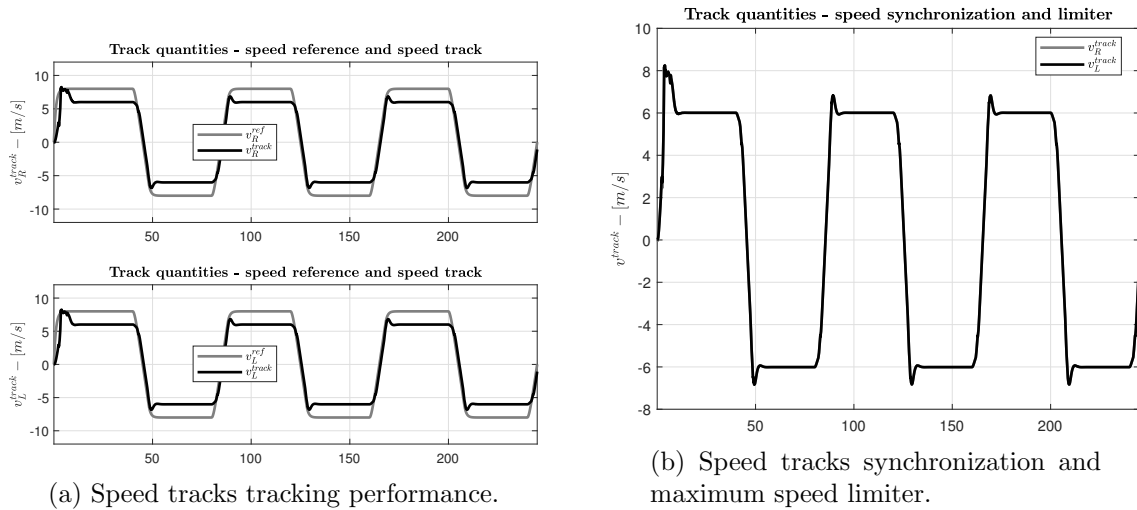


Figure 6.12: Simulation results scenario 1.

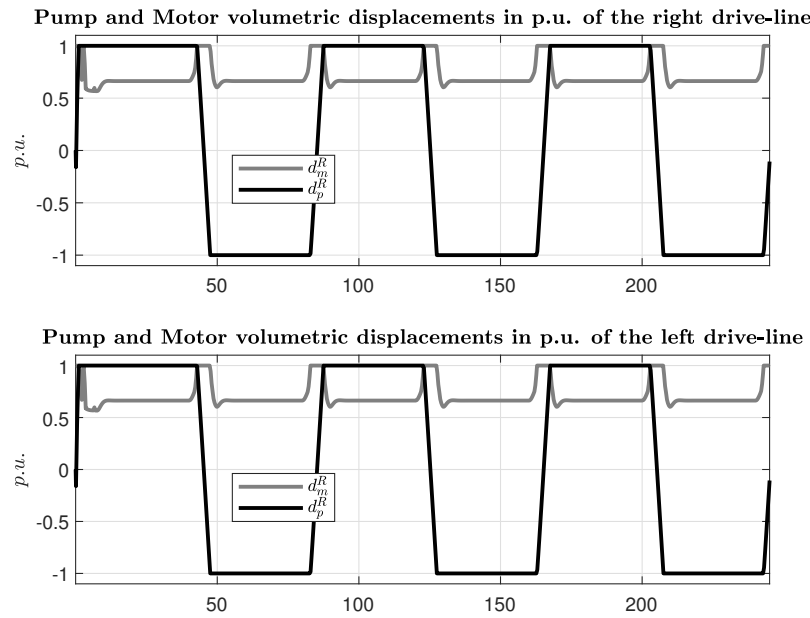


Figure 6.13: Volumetric displacements.

### 6.5.1.2 Scenario 2

In this scenario we are considering the following case

- Straight driving.
- Not homogeneous viscosity load on tracks.
- The total amount of load is enough to stall the engine.
- The maximum load on drive-line one (Right) exceed the maximum admissible delta pressure.

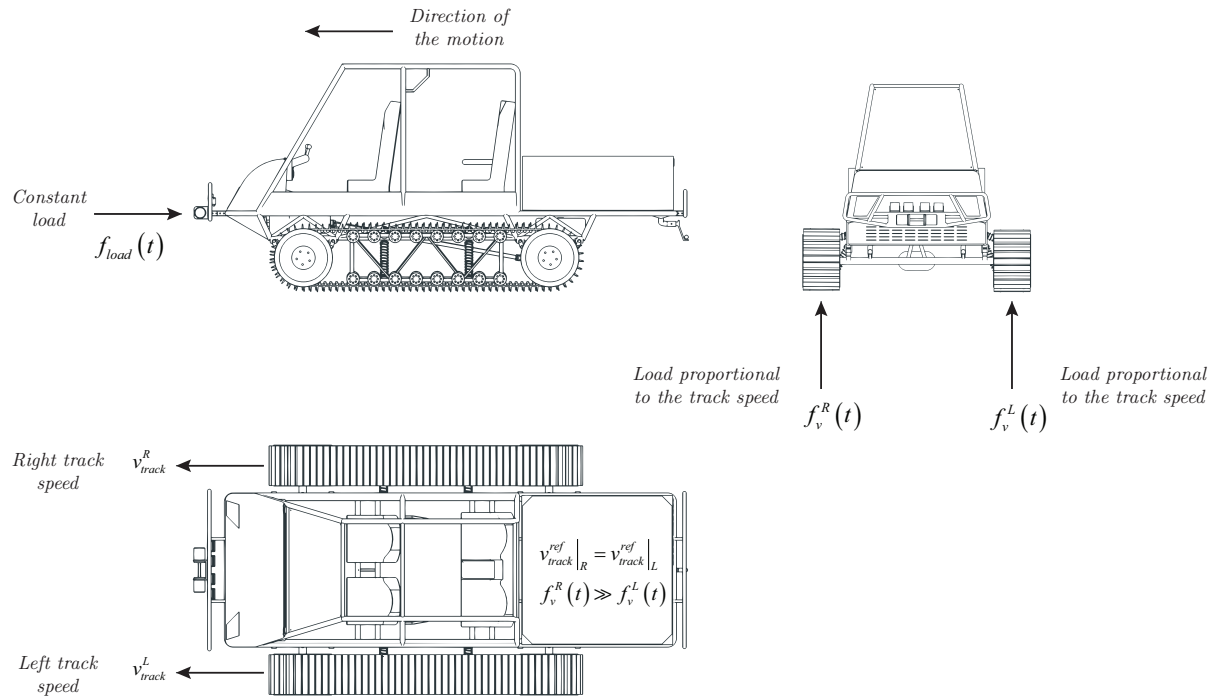


Figure 6.14: Description of the test scenario 2.

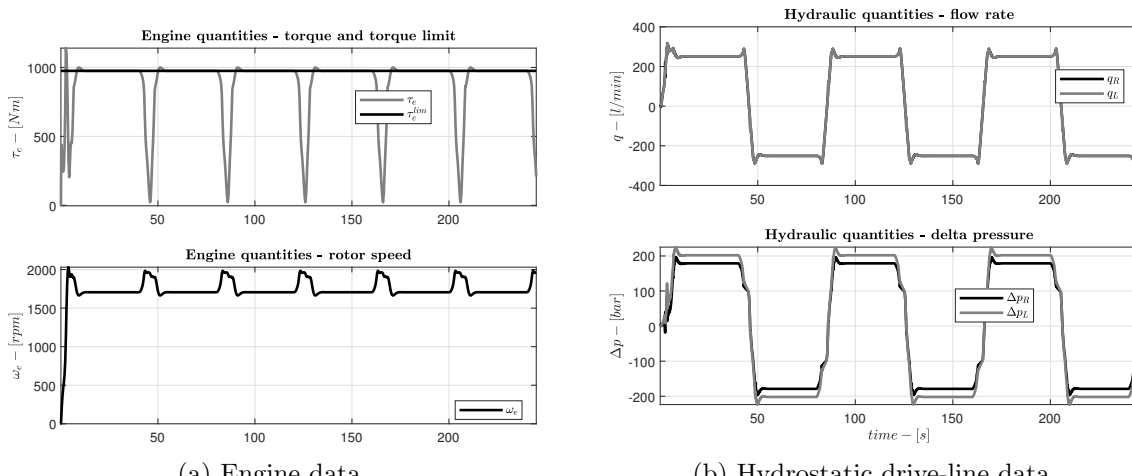


Figure 6.15: Simulation results scenario 2.

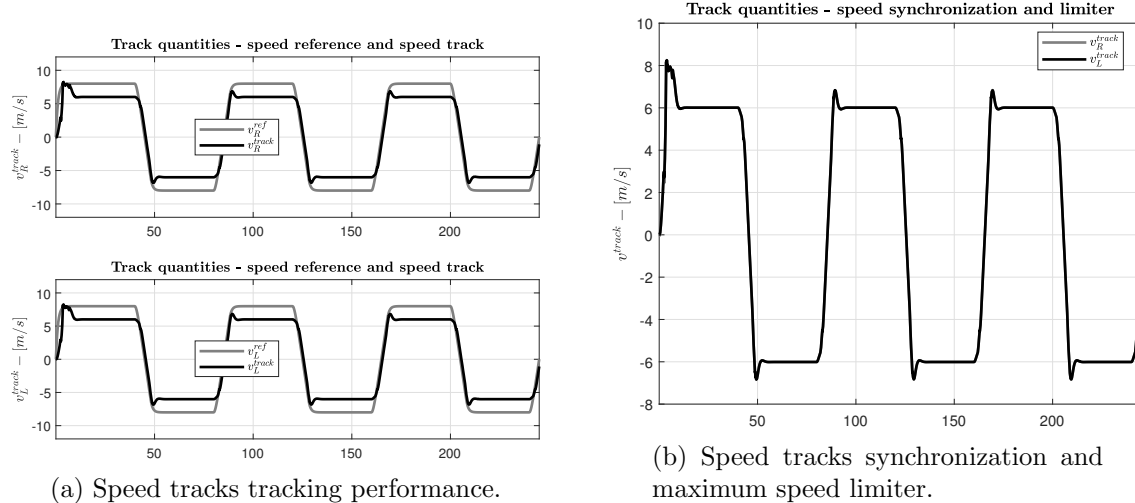


Figure 6.16: Simulation results scenario 2.

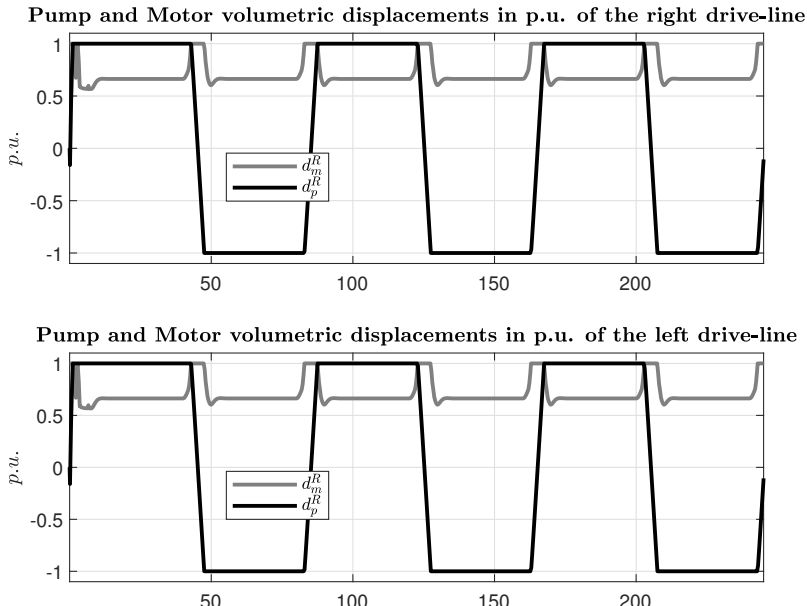


Figure 6.17: Volumetric displacements.

### 6.5.1.3 Scenario 3

In this scenario we are considering the following case

- Straight driving.
- Homogeneous negative load on both track (downhill scenario).
- The maximum negative load brings the vehicle in over-speed condition (over-speed management).

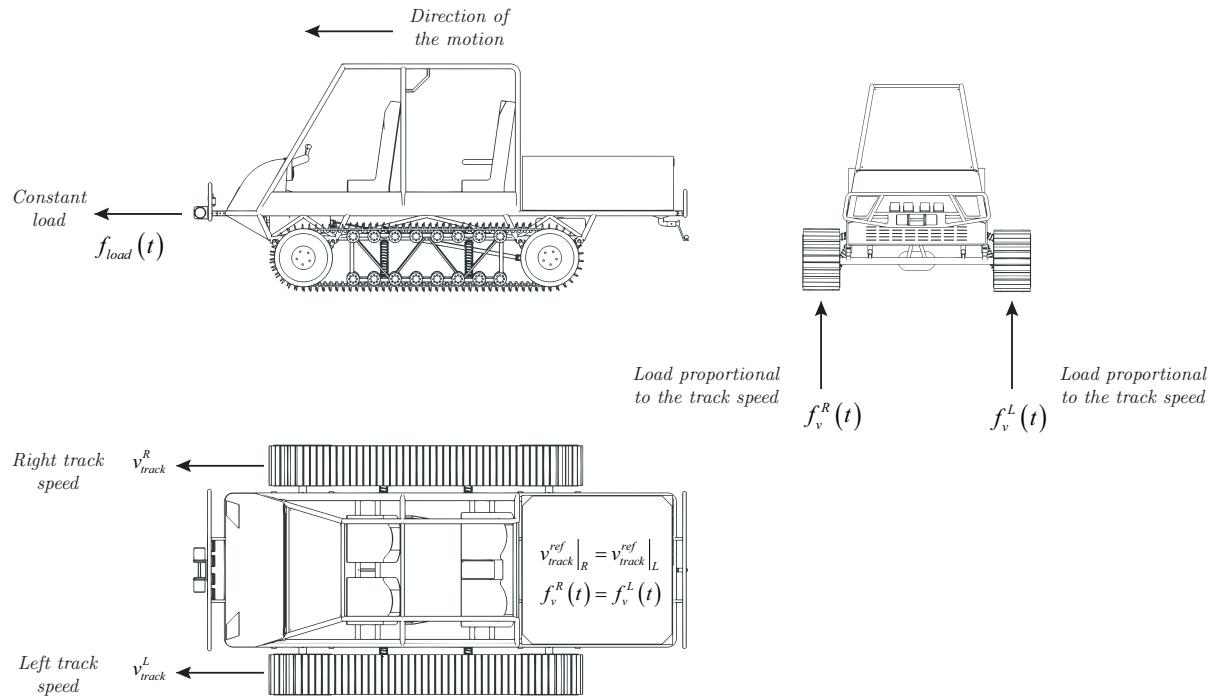


Figure 6.18: Description of the test scenario 3.

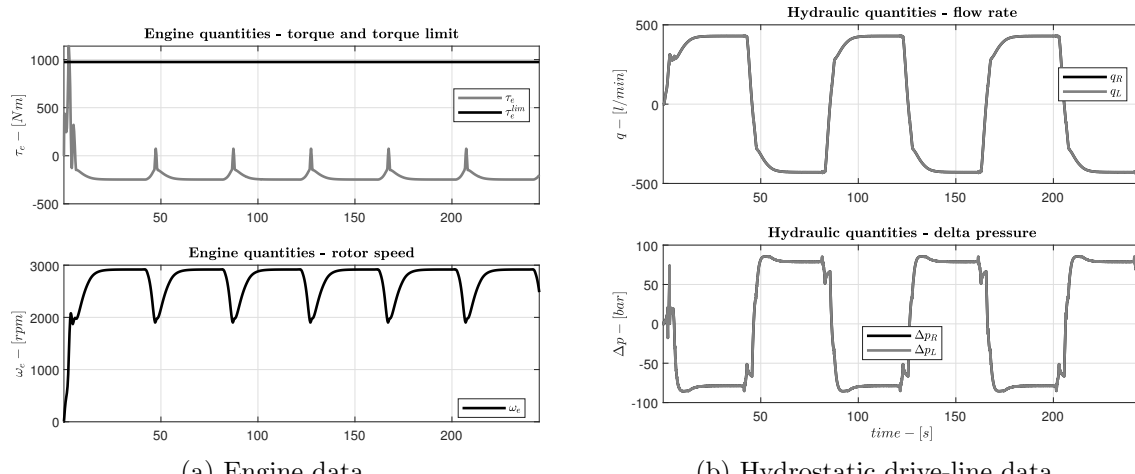


Figure 6.19: Simulation results scenario 3.

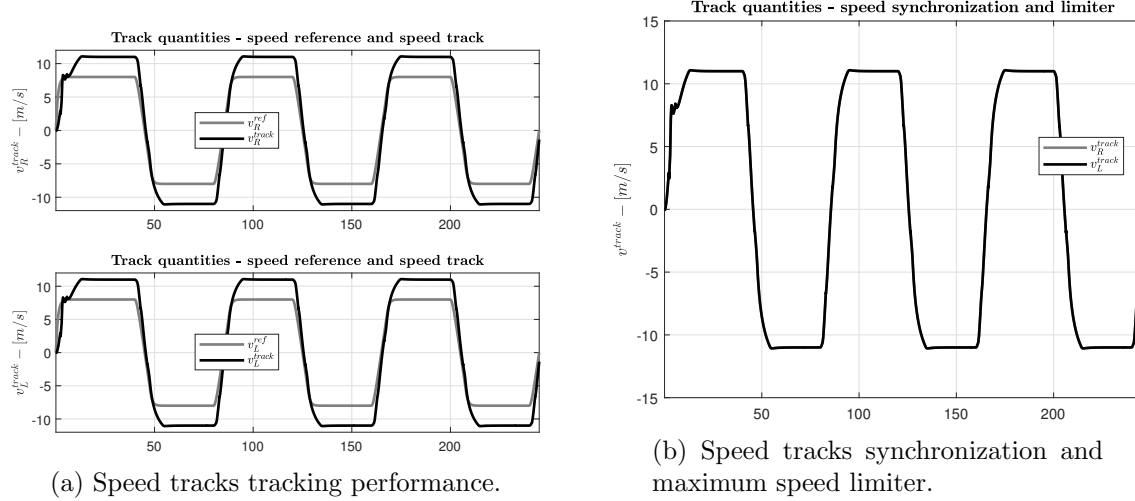


Figure 6.20: Simulation results scenario 3.

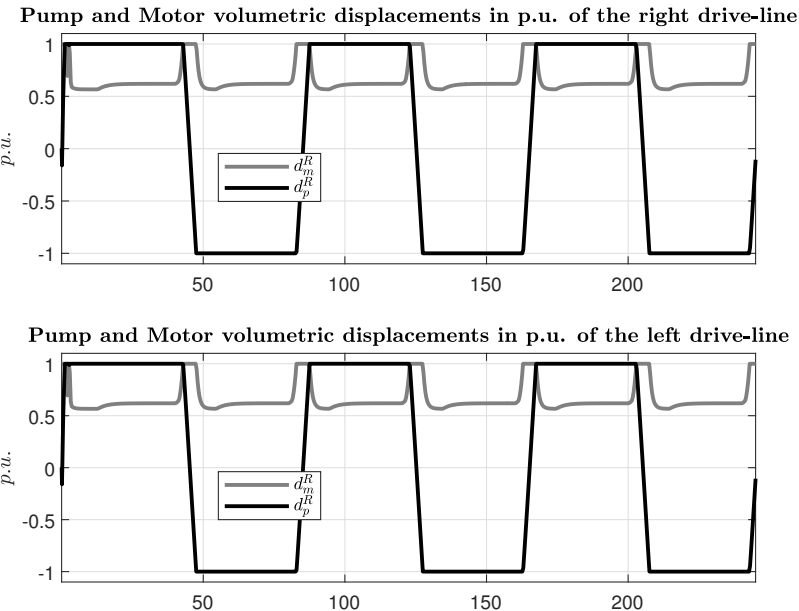


Figure 6.21: Volumetric displacements.

#### 6.5.1.4 Scenario 4

In this scenario we are considering the following case

- Steering driving.
- Not homogeneous viscosity load on tracks.
- The total amount of load is enough to stall the engine.
- The maximum load on drive-line one (Right) exceed the maximum admissible delta pressure.

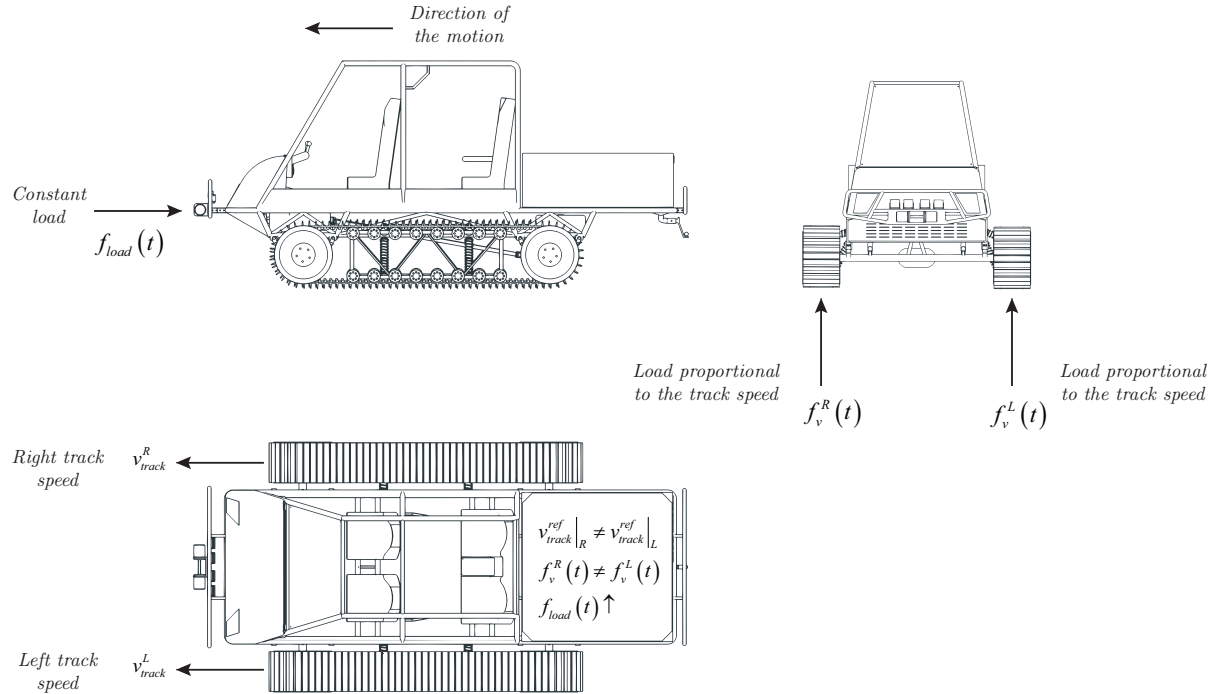


Figure 6.22: Description of the test scenario 4.

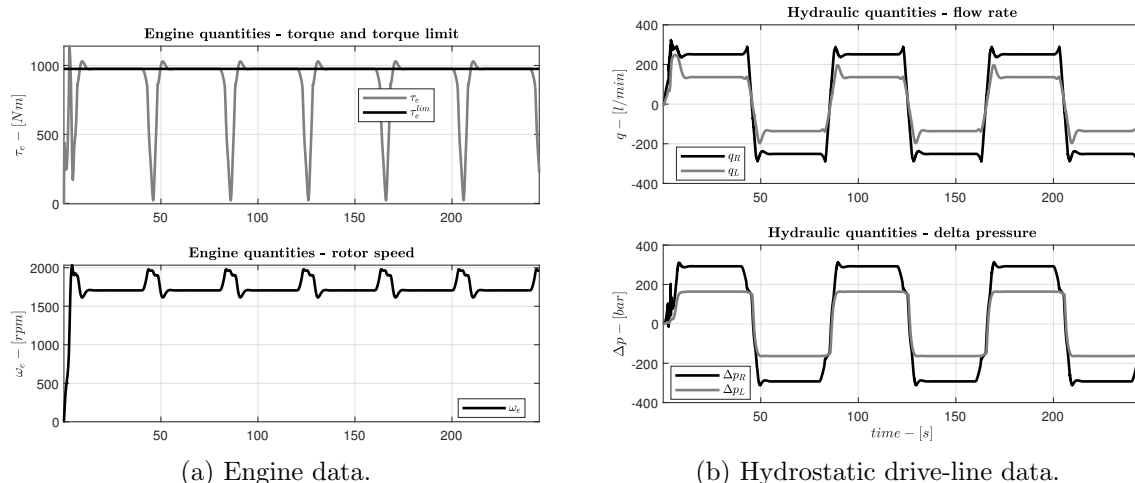


Figure 6.23: Simulation results scenario 3.

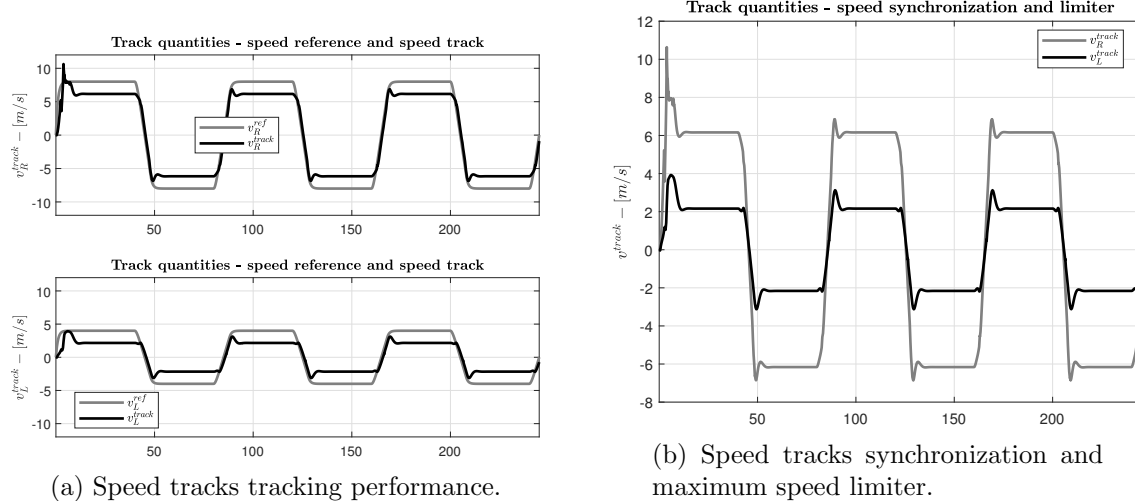


Figure 6.24: Simulation results scenario 3.

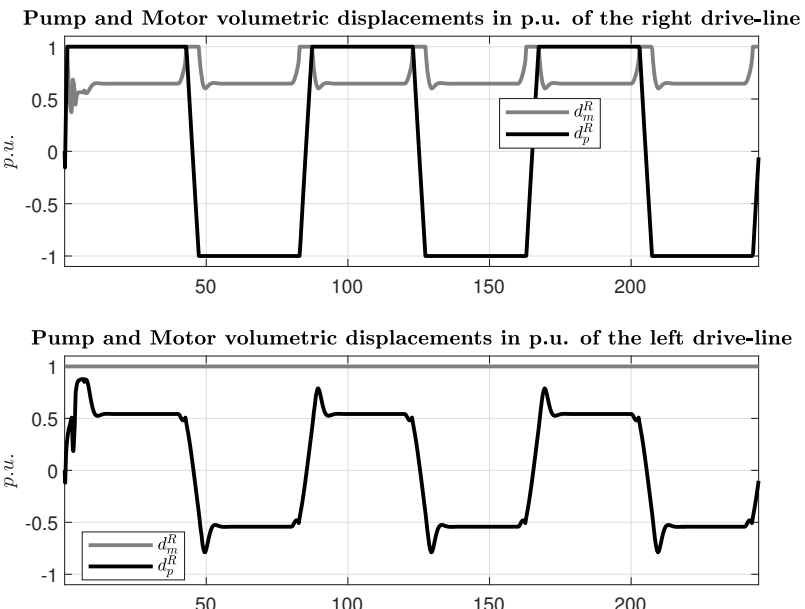


Figure 6.25: Volumetric displacements.

## **Part II**

# **Electrification of an Hydrostatic Power-train**

# Chapter 7

## Introduction

The electrification of the power-train consists in the replacement of the diesel engine and of the hydrostatic transmissions by a set of electrical equipment, consisting on:

- A fuel cell and its control system.
- A dc/dc converter and its control system.
- A battery and its battery management system.
- A braking unit and its control system.
- An inverter unit and its control system.
- A permanent magnet synchronous motor (PMSM).

Figure 7.1 shows the whole layout.

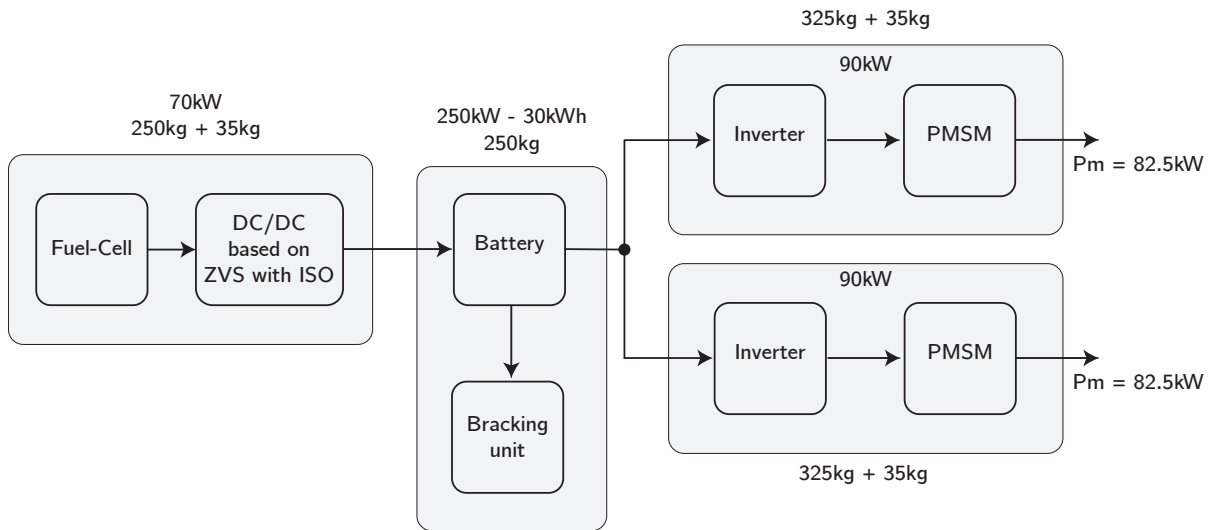


Figure 7.1: Electrical layout overview.

The dimensioning of the electrical equipment shall start from the torque-speed limit curve shown in Figure ??, where the sizing of the PMSM is directly affected. In addition, the motor control strategy (inverter control) which has been accounted will affect also the dimensioning

of the PMSM. The whole design is also strongly bounded by the constraints given by the semiconductor components which must be selected around a given set of industrial products.

In the following we will describe the physical model around each component, which the power-train consist of. We will start from the power source, which means the PEM fuel-cell, to arrive to the Lithium-ion battery and its DC/DC power supply equipment.

The last component is the **driver** unit which consists of an inverter, a PMSM and the motor control unit which plays a fundamental role in the whole design.

# Chapter 8

## Power source

### 8.1 The PEM fuel-cell

In this section we will describe the proton exchange membrane (PEM) fuel-cell or PEMFC in order to find a possible representation of its dynamic model in a **Simscape/Simulink** environment.

#### 8.1.1 Introduction

A fuel cell is a device in which a fuel is oxidized electrochemically to produce electric power. It has some characteristics of a battery, in fact, it consists of two electrodes separated by an electrolyte. However, the reactants are not stored in the cell but are fed to it continuously, and the products of reaction are continuously withdrawn. The fuel cell is thus not given an initial electric charge, and in operation it does not lose electric charge. It operates as a continuous-flow system as long as fuel and oxygen are supplied, and it produces a steady electric current. Compared to the conventional process of burning a fuel and extracting mechanical work via a heat engine to power a generator, fuel cells provide a more efficient means of converting the chemical energy available by oxidation of fuel into electrical energy.

In a fuel cell, the fuel, e.g. hydrogen, methane, butane, methanol, etc., makes intimate contact with an anode or fuel electrode, and oxygen (usually in air) makes intimate contact with a cathode or oxygen electrode. Half-cell reactions occur at each electrode, and their sum is the overall reaction. Several types of fuel cell exist, each characterized by a particular type of electrolyte.

Cells operating with hydrogen as fuel is shown in Figure 8.1.

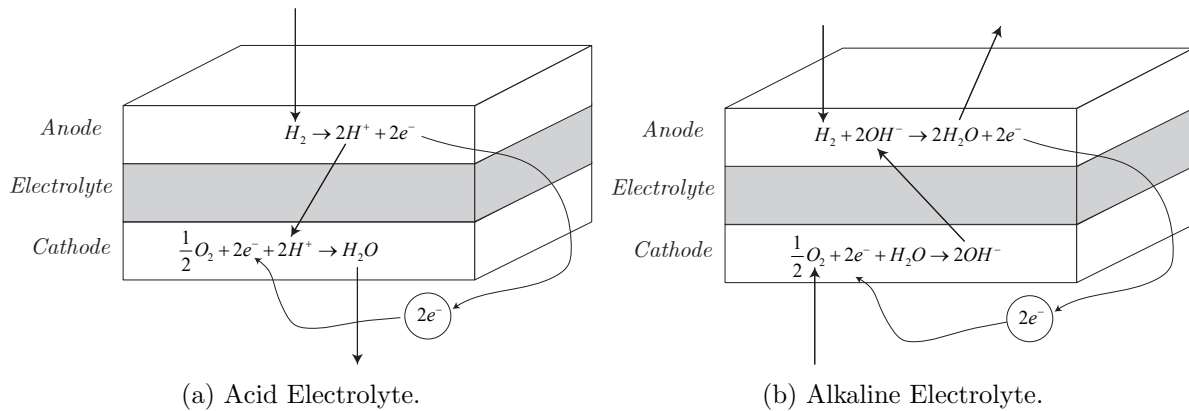


Figure 8.1: Schematic diagram of different fuel cells

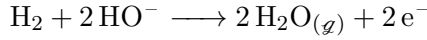
When the electrolyte is acid, the half-cell reaction occurring at the hydrogen electrode (anode) is:



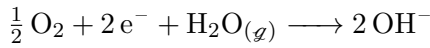
and that at the oxygen electrode (cathode) is



When the electrolyte is alkaline, the half-cell reaction at the anode is



and at cathode:



This of course is the *combustion reaction* of hydrogen, but combustion in the conventional sense of burning does not occur in the cell. In both cells electrons with negative charge ( $\text{e}^-$ ) are released at the anode, produce an electrical current in an external circuit, and are taken up by the reaction occurring at the cathode. The electrolyte does not allow the passage of electrons, but it provides a path migration of an ion from one electrode to the other. With an acid electrolyte, protons ( $\text{H}^+$ ) migrate from anode to cathode, whereas with an alkaline electrolyte hydroxyl ions ( $\text{OH}^-$ ) migrate from cathode to anode.

### 8.1.2 Background on electrochemical process

**According to the first law of thermodynamics**, the energy of a system (considered in the form of heat or work) is conserved, meaning that the energy can be neither created nor destroyed, but it can be converted from one type to another. The change in the system energy ( $dE$ ) is contributed by the heat entering the system ( $dQ$ ) and the work done by the system ( $dW$ ).

$$dE = dQ - dW \quad (8.1.1)$$

Note that work in the above equation is defined as work leaving the system. For a *simple system*, the total system energy is equal to the total system internal energy  $U$

$$E = U \quad (8.1.2)$$

In the following we only consider *simple systems*.

For a *control volume*, usually there is an expansion when heat is absorbed by the system at constant pressure. Part of the heat goes into internal energy and causes the system temperature to rise. The rest of the heat is used to expand the system against the pressure ( $p$ ). A property of the system, called *enthalpy H*, is used to represent the system state under a given condition. It is the sum of the system internal energy and the product of the system pressure and volume ( $V$ ).

$$H = U + PV \quad (8.1.3)$$

*Enthalpy* is independent of which way the system reaches its condition, and as a result, the product of the system pressure ( $p$ ) and volume ( $V$ ) is constant. Eq. (8.1.3) can therefore be written as

$$dH = dQ - dW \quad (8.1.4)$$

According to Eq. (8.1.4), any changes in enthalpy (state) of a system is a result of the difference between the change in the heat entering the system and the work leaving (done by) the system.

According to the first law of thermodynamics, work done by an ideal cyclic thermal process (heat engine), shown in Figure 8.2 can be defined by

$$W = Q_1 - Q_2 \quad (8.1.5)$$

where  $W$  is work done by the system to the outside and  $Q_1$  and  $Q_2$  are the heat entering and leaving the thermal process, respectively.

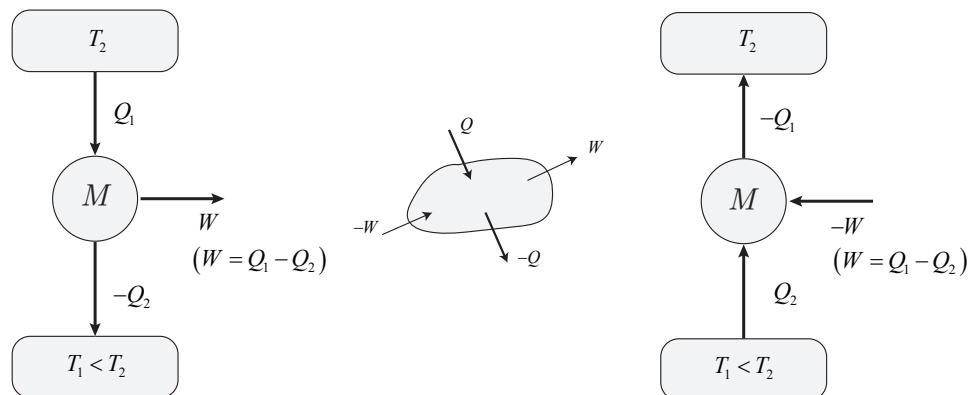


Figure 8.2: Thermal machines.

In 1842, French scientist Sadi Carnot presented the relationship between the heat entering and leaving ideal thermal processes and their corresponding temperatures,  $T_1$  and  $T_2$  as follows

$$\frac{Q_1}{T_1} = \frac{Q_2}{T_2} \quad (8.1.6)$$

The efficiency of the process then is

$$\eta_c = \frac{W}{Q_1} = \frac{Q_1 - Q_2}{Q_1} = 1 - \frac{T_2}{T_1} \quad (8.1.7)$$

It is clear from Eq. (8.1.7) that a higher efficiency can be obtained by having a larger difference between  $T_2$  and  $T_1$ . Another contribution from Carnot is that  $Q/T$  can be a state property of the system by showing the equivalence of  $Q_1/T_1$  and  $Q_2/T_2$ . Based on the Carnot's idea, Rudolf Clausius (a Polish scientist, 1822-1888) developed the concept of entropy and presented the second law of thermodynamics. This concept was introduced to indicate the degree of

disorder of a system. If the system is undergoing an infinitesimal reversible process with  $dQ$  heat entering the system at temperature  $T$ , then the infinitesimal change in its *entropy* ( $S$ ) is defined as

$$dS = \left. \frac{dQ}{T} \right|_{\text{rev}} \quad (8.1.8)$$

A reversible process is a process that can be reversed without leaving any traces to its environment. If a cyclic process only consists of reversible processes, then there is no entropy change after a cycle (i.e.  $\Delta S = 0$ ). On the contrary, if the cycle contains an irreversible process, then its entropy will change, which corresponds to work done (or received) by the system. Entropy is an important system property, which is very useful in describing a thermodynamic process. The temperature-entropy diagram for a Carnot Cycle is shown in Figure 8.3, where the area  $abcd$  represents work done by the system, when the system temperature goes from  $T_1$  to  $T_2$ . Note that  $\Delta S = 0$  when there is a change in temperature, but no work is done by the system.

The second law of thermodynamics, described by Clausius for a cyclic process, can be written in an infinitesimal form as follows

$$dS \geq \frac{dQ}{T} \quad (8.1.9)$$

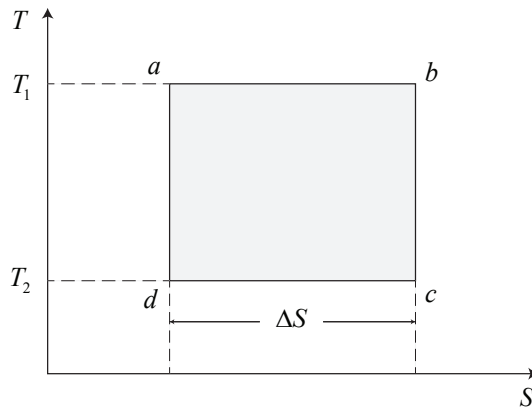


Figure 8.3: Temperature-entropy diagram for a Carnot cycle.

In Eq. (8.1.9), the equality sign applies to a reversible cyclic process and the inequality sign applies to an irreversible process. That is to say, for any irreversible process, change in work is done in the direction that change in entropy is greater than  $dQ/T$ . This means that heat cannot be transferred from a low temperature to a higher temperature without a need of work from outside. The second law also reveals that no real heat engine efficiency can reach 100% due to the increase of entropy. For an isolated system, the change of entropy will always be greater than equal to zero.

**The Gibbs free energy  $G$**  is defined as

$$G = H - TS = U + pV - TS \quad (8.1.10)$$

Differentiating Eq. (8.1.11) we obtain

$$dG = dH - (TdS + SdT) = dU + pdV + Vdp - (TdS + SdT) \quad (8.1.11)$$

Chemical reactions proceed toward the direction that minimizes the Gibbs energy. Therefore,  $dG$  is negative as a chemical reaction approaches its equilibrium point, and it will be zero

at the equilibrium point. According to the first law of thermodynamics, for a *simple system*, Eq. (8.1.11) can be rewritten as

$$dG = dH - (TdS + SdT) = dQ - dW + pdV + Vdp - (TdS + SdT) \quad (8.1.12)$$

For systems that are restricted to performing only expansion-type of work, we can write

$$dW = pdV \quad (8.1.13)$$

Also, the following condition holds if the process is reversible:

$$dQ = TdS \quad (8.1.14)$$

Substituting Eq. (8.1.13) and Eq. (8.1.14) into Eq. (8.1.12) we obtain

$$dG = Vdp - SdT \quad (8.1.15)$$

Solving the differential equation Eq. (8.1.15), Gibbs energy can be obtained at a given temperature ( $T$ ) and under any pressure.

$$G(T) = G^\circ(T) + nRT \log \left[ \frac{p}{p^\circ} \right] \quad (8.1.16)$$

In Eq. (8.1.16)  $G^\circ(T)$  is the standard Gibbs energy at temperature  $T$  and at  $p^\circ = 100 \text{ kPa}$ .

For an electrochemical reaction, the maximum work (electricity) is determined by the change in the Gibbs energy as the reactions change to products. It can be shown that the maximum electricity production ( $W_e$ ) is equal to the change in the Gibbs energy.

$$W_e = -\Delta G \quad (8.1.17)$$

In a chemical reaction, the change in enthalpy  $\Delta H$  due to the reaction can be written as

$$\Delta H = H_P - H_R = \sum_{P_i} N_{P_i} H_{P_i} - \sum_{R_j} N_{R_j} H_{R_j} \quad (8.1.18)$$

where  $H_P$  is the total enthalpy of the products and  $H_R$  is the total enthalpy of the reactants.  $N_{P_i}$  is the amount of moles of the  $i$ th species in the products and  $N_{R_j}$  is the amount of moles of the  $j$ th species in the reactants.

Accordingly,  $H_{P_i}$  and  $H_{R_j}$  are the molar enthalpies of the corresponding species, which can be represented as

$$H_{P_i} = (H_f^\circ + H - H^\circ)_{P_i} \quad (8.1.19)$$

In Eq. (8.1.19),  $H_f^\circ$  is the standard molar enthalpy of formation ( $\text{J mol}^{-1}$ ) and  $(H - H^\circ)$  is the molar enthalpy due to the temperature difference.

The change of entropy due to the reaction can be written as

$$\Delta S = S_P - S_R = \sum_{P_i} N_{P_i} S_{P_i} - \sum_{R_j} N_{R_j} S_{R_j} \quad (8.1.20)$$

where  $S_P$  is the total entropy of the products and  $S_R$  is the total entropy of the reactants.  $S_{P_i}$  ( $S_{R_j}$ ) is the molar entropy of the corresponding species. The change in Gibbs free energy due to the reaction ( $\Delta G$ ) can than be obtained from Eq. (8.1.10) as follows

$$\Delta G = \Delta G_P - \Delta G_R = \Delta H - T\Delta S \quad (8.1.21)$$

Two example reactions are given below for the formation of water, in vapor form and in liquid form, from hydrogen and oxygen, to show how the change in Gibbs energy (or electric energy) in a reaction can be calculated. The enthalpy and entropy values for water, hydrogen and oxygen used in the equations are given in Table 8.1. The reactions are assumed to happen under standard conditions ( $p = p^\circ$  and  $T = 298.15\text{ K}$ )

	Enthalpy, $H_f \left[ \text{kJ mol}^{-1} \right]$	Entropy, $S \left[ \text{J mol}^{-1} \text{K}^{-1} \right]$
$\text{H}_2\text{O}_{(\mathcal{G})}$	-241.8	188.7
$\text{H}_2\text{O}_{(\ell)}$	-285.8	69.9
$\text{H}_2$	0	130.6
$\text{O}_2$	0	205

Table 8.1: Standard thermodynamic properties (enthalpy and entropy).



In the formula shown in 8.1.22 and 8.1.23,  $(\mathcal{G})$  and  $(\ell)$  indicate that the reaction product is in gas or in liquid form, respectively. From Eq. (8.1.18) and Eq. (8.1.20), we have

$$\Delta H = H_P - H_R = (-241.8 - 0.0) = -241.8 \text{ kJ mol}^{-1}$$

$$\Delta S = S_P - S_R = (-188.7 - 130.6 - 0.5 \times 205) = -44.4 \text{ J mol}^{-1} \text{ K}^{-1}$$

Therefore, the change in the Gibbs energy of the reaction given in Eq. (8.1.17) is

$$\Delta G = \Delta H - T\Delta S = -241.8 - 298 \times (-44.4 \times 10^{-3}) = -228.57 \text{ kJ mol}^{-1}$$

For the reaction given in 8.1.23, we have

$$\Delta H = H_P - H_R = (-285.8 - 0.0) = -285.8 \text{ kJ mol}^{-1}$$

$$\Delta S = S_P - S_R = (-69.9 - 130.6 - 0.5 \times 205) = -163.2 \text{ J mol}^{-1} \text{ K}^{-1}$$

Therefore, the change in the Gibbs energy for the formation of water in vapor form (Eq. (8.1.17)) is

$$\Delta G = \Delta H - T\Delta S = -285.8 - 298 \times (-163.2 \times 10^{-3}) = -237.16 \text{ kJ mol}^{-1}$$

From the above examples, we can see that more work is done if the product ( $\text{H}_2\text{O}$ ) is in the liquid form.

### 8.1.3 The Nernst equation

Consider an electrochemical reaction under constant temperature and pressure, where reactants  $X$  and  $Y$  form products  $M$  and  $N$  as follows



where  $a$ ,  $b$ ,  $c$  and  $d$  are stoichiometric coefficients.

According to Eq. (8.1.21), the change in Gibbs energy of the reaction is

$$\Delta G = \Delta G_P - \Delta G_R = cG_M + dG_N - aG_X - bG_Y \quad (8.1.25)$$

The change in the Gibbs energy can also be calculated at different temperature and pressure as follows

$$\Delta G = \Delta G^\circ + RT \log \left[ \frac{\left( \frac{p_M}{p^\circ} \right)^c \left( \frac{p_N}{p^\circ} \right)^d}{\left( \frac{p_X}{p^\circ} \right)^a \left( \frac{p_Y}{p^\circ} \right)^b} \right] \quad (8.1.26)$$

or

$$\Delta G = \Delta G^\circ + RT \log \left[ \frac{\left( \frac{p_M^*}{p^\circ} \right)^c \left( \frac{p_N^*}{p^\circ} \right)^d}{\left( \frac{p_X^*}{p^\circ} \right)^a \left( \frac{p_Y^*}{p^\circ} \right)^b} \right] \quad (8.1.27)$$

where  $(^*)$  mean the **activity** of the respective reactant and/or product. For the case of gas behaving as **ideal gas**, it can be shown that

$$p^* = \frac{p}{p^\circ} \quad p^\circ = 100 \text{ kPa} \quad (8.1.28)$$

In Eq. (8.1.27)  $\Delta G^\circ$  is given as follows

$$\Delta G^\circ = cG_M^\circ + dG_N^\circ - aG_X^\circ - bG_Y^\circ \quad (8.1.29)$$

In an electrochemical reaction, work can be considered as the electrical energy delivered by the reaction. The electrochemical work is defined by

$$W_e = n_e F E \quad (8.1.30)$$

where  $n_e$  is the number of electrons participating in the reaction,  $F$  is the Faraday constant ( $98\,487 \text{ C mol}^{-1}$ ) and  $E$  is the potential difference across the electrodes.

According to Eq. (8.1.17), the change in Gibbs energy is the negative value of the work done by the reaction

$$\Delta G = -W_e = -n_e F E \quad (8.1.31)$$

Under standard condition, Eq. (8.1.31) can be written as

$$\Delta G^\circ = -W_e^\circ = -n_e F E^\circ \quad (8.1.32)$$

where  $E^\circ$  is the standard reference potential.

Using Eq. (8.1.31), the electrode voltage  $E$  can be calculated as follows

$$E = -\frac{\Delta G}{n_e F} = -\frac{\Delta G^\circ}{n_e F} - \frac{RT}{2F} \log \left[ \frac{\left( \frac{p_M^*}{p^\circ} \right)^c \left( \frac{p_N^*}{p^\circ} \right)^d}{\left( \frac{p_X^*}{p^\circ} \right)^a \left( \frac{p_Y^*}{p^\circ} \right)^b} \right] \quad (8.1.33)$$

Writing Eq. (8.1.33) in terms of standard reference potential  $E^\circ$ , the well-known electrochemical formula, the Nernst equation, for calculation of the potential difference between two electrodes can be derived

$$E = E^\circ - \frac{RT}{2F} \log \left[ \frac{\left( p_M^* \right)^c \left( p_N^* \right)^d}{\left( p_X^* \right)^a \left( p_Y^* \right)^b} \right] = E^\circ + \frac{RT}{2F} \log \left[ \frac{\left( p_X^* \right)^a \left( p_Y^* \right)^b}{\left( p_M^* \right)^c \left( p_N^* \right)^d} \right] \quad (8.1.34)$$

For fuel-cell with an overall reaction, given by Eq. (8.1.22) the voltage across the fuel cell electrodes (or the internal potential of the fuel cell) is given by

$$E = E^\circ + \frac{RT}{2F} \log \left[ \frac{p_{H_2}^* \cdot \left( p_{O_2}^* \right)^{\frac{1}{2}}}{p_{H_2O}^*} \right] \quad (8.1.35)$$

If the product ( $H_2O$ ) is in liquid form, given by the formula 8.1.23, the the fuel cell internal potential is

$$E = E^\circ + \frac{RT}{2F} \log \left[ p_{H_2}^* \cdot \left( p_{O_2}^* \right)^{\frac{1}{2}} \right] \quad (8.1.36)$$

#### 8.1.4 Dynamic model of PEM fuel-cell

For many practical applications the most satisfactory hydrogen/oxygen fuel cell is built around a solid polymer that serves as an acid electrolyte. Because it is very thin and conducts  $H^+$  ions or protons, it is known as a proton-exchange membrane (PEM). Each side of the membrane is bounded to a porous electrode loaded with an electrocatalyst such as finely divided platinum. The porous electrodes provide a very large surface area for reaction and accommodate the diffusion of hydrogen and oxygen into the cell and water liquid out of the cell. Cells can be stacked and connected in series to make very compact units with a desired terminal emf. They typically operate at temperature near 60 °C.

In order to build a dynamic model of a PEM fuel-cell stack, a preliminary mathematical approach is presented. To simplify the analysis, the following assumptions are made.

1. One-dimensional treatment.
2. Ideal and uniformly distributed gases.
3. Constant pressure in the fuel cell gas flow channels.
4. The fuel is humidified hydrogen, and the oxidant is humidified air.
5. On the anode side, the **water activity vapor pressure**<sup>1</sup> is 50% and on the cathode side, 100% of the saturated vapor pressure.

---

<sup>1</sup>  $x_{H_2O}^* = \frac{p_{H_2O}^*}{(p_{H_2O}^{sat})^*}$  where  $p_{H_2O}^*$  is the partial vapor pressure of water in the solution, and  $(p_{H_2O}^{sat})^*$  is the partial vapor pressure of pure water at the same temperature

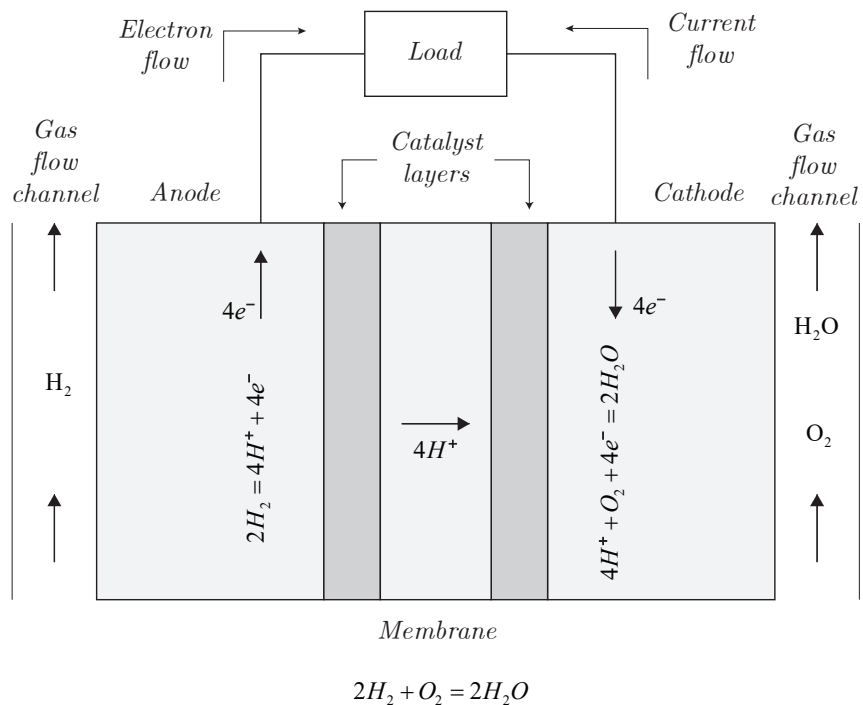


Figure 8.4: Schematic diagram and chemical reaction of PEMFC.

6. The PEMFC operates under  $100\text{ }^\circ\text{C}$  and the reaction product is in liquid phase.
7. Thermodynamics properties are evaluated at the average stack temperature. Temperature variations across the stack are neglected, and the overall specific heat capacity of the stack is assumed to be constant.
8. Parameters for individual cells can be lumped together to represent a fuel-cell stack.

A schematic diagram of a PEM fuel cell and its internal voltage drops are shown in Figure 8.5. In order to calculate the fuel-cell output voltage, the effective partial pressure of  $H_2$  and  $O_2$  need to be determined. In a gas mixture consisting of  $n$  specie, the diffusion of component  $i$  through the porous electrodes can be described by the Stefan-Maxwell formulation

$$\vec{\nabla}x_i = \frac{RT}{p} \sum_{j=1}^N \frac{x_i N_j - x_j N_i}{D_{i,j}} \quad (8.1.37)$$

where  $x_i$  ( $x_j$ ) is the mole fraction of the specie  $i$  ( $j$ );  $D_{i,j}$  is the diffusivity coefficient between the two species  $i$  and  $j$  [ $\text{m}^2\text{s}^{-1}$ ];  $N_i$  ( $N_j$ ) the superficial gas flow of species  $i$  ( $j$ ) in [ $\text{mol m}^{-2}\text{s}^{-1}$ ];  $R = 8.3143\text{ J mol}^{-1}\text{ K}^{-1}$  the gas constant;  $T [K]$  the gas temperature and  $p$  the overall pressure of gas mixture in [ $\text{Pa}$ ].

The **the effective partial pressures**<sup>2</sup> of hydrogen and oxygen are needed in order to calculate the PEMFC output voltage. At the anode channel, the gas stream is a mixture of  $H_2$  and  $H_2O(g)$ . The molar flux of water (in gas phase) normal to anode surface can be set to zero, according to hypothesis (1)-(3) given above.

<sup>2</sup>For gases, the activity is the effective partial pressure, and is usually referred to as *fugacity*.

According Eq. (10.2.3), assuming one dimensional (1-D) transport process along the  $x$  axis, as shown in Figure 8.5, the diffusion of water can be simplified as

$$\frac{dx_{H_2O}}{dx} = \frac{RT}{p_a} \left( \frac{x_{H_2O}N_{H_2} - x_{H_2}N_{H_2O}}{D_{H_2O,H_2}} \right) \quad (8.1.38)$$

where  $p_a$  is the overall gas pressure at the anode [Pa].

The molar flow of  $H_2$  can be determined by Faraday's Law

$$N_{H_2} = \frac{J}{2F} \quad (8.1.39)$$

where  $F \approx 96\,485 \text{ C mol}^{-1}$  is the Faraday constant and  $J$  is a current density [ $\text{A m}^2$ ].

By combining Eq. (10.2.4) and Eq. (10.2.5) and integrating the expression with respect to  $x$  from the anode channel to the catalyst surface, it gives

$$x_{H_2O}^* = \left( x_{H_2O}^{ch} \right)^* \exp \left( \frac{RTJ\ell_a}{2Fp_a D_{H_2O,H_2}} \right) \quad (8.1.40)$$

where  $\ell_a$  is the distance from anode surface to the reaction site [m]; superscript  $(^*)$ , denotes, as already seen, the activity<sup>3</sup>; superscript  $(^{ch})$  denotes the conditions at the anode or cathode channel.

According to the assumption (4) given above, the fuel consists only of hydrogen and water vapor. That is, at the anode,  $x_{H_2O}^* + x_{H_2}^* = 1$ . Therefore according to the uniformity of gas distribution along the  $x$ -axis (assumption - 2), the effective partial pressure of hydrogen  $H_2$  can be written as

$$p_{H_2}^* = \frac{p_{H_2O}^*}{x_{H_2O}^*} (1 - x_{H_2O}^*) \quad (8.1.41)$$

According to assumption (5),  $p_{H_2O}^*$  at the anode is  $0.5(p_{H_2O}^{sat})^*$ . Therefore,  $p_{H_2}^*$  is given as

$$p_{H_2}^* = 0.5(p_{H_2O}^{sat})^* \left( \frac{1}{x_{H_2O}^*} - 1 \right). \quad (8.1.42)$$

The gases flowing in the cathode channel are  $O_2$ ,  $N_2$ ,  $H_2O$  and  $CO_2$ . Using Eq. (10.2.3), the diffusion of  $H_2O(g)$  at the cathode side can be obtained from

$$\begin{aligned} \frac{dx_{H_2O}}{dx} &= \frac{RT}{p_c} \left( \frac{x_{O_2}N_{H_2O} - x_{H_2O}N_{O_2}}{D_{H_2O,O_2}} \right) \\ &= \frac{RT}{p_c} \left( \frac{-x_{H_2O}N_{O_2}}{D_{H_2O,O_2}} \right) \end{aligned} \quad (8.1.43)$$

where  $p_c$  is the overall gas pressure at the cathode [Pa].

---

<sup>3</sup>The thermodynamic activity of a species is a measure of the **effective concentration** of a species in a reacting system. By convention, it is a dimensionless quantity. The activity of pure substances in condensed phases (liquid or solid) is taken as unity. Activity depends principally on the temperature, pressure and composition of the system.

Similar to the analysis for anode, the activity coefficient of H<sub>2</sub>O, N<sub>2</sub> and CO<sub>2</sub> at the cathode catalyst interface can be derived as follows:

$$x_{H_2O}^* = \left(x_{H_2O}^{ch}\right)^* \exp\left(\frac{RTJ\ell_c}{4Fp_c D_{H_2O,O_2}}\right) \quad (8.1.44)$$

$$x_{N_2}^* = \left(x_{N_2}^{ch}\right)^* \exp\left(\frac{RTJ\ell_c}{4Fp_c D_{N_2,O_2}}\right) \quad (8.1.45)$$

$$x_{CO_2}^* = \left(x_{CO_2}^{ch}\right)^* \exp\left(\frac{RTJ\ell_c}{4Fp_c D_{CO_2,O_2}}\right) \quad (8.1.46)$$

where  $\ell_c$  is the distance from the cathode surface to the reaction site [m]; At the cathode the activity coefficient of O<sub>2</sub> is as follows

$$x_{O_2}^* = 1 - x_{H_2O}^* - x_{N_2}^* - x_{CO_2}^* \quad (8.1.47)$$

and the corresponding effective partial pressure of O<sub>2</sub> is

$$p_{O_2}^* = \frac{p_{H_2O}^*}{x_{H_2O}^*} x_{O_2}^* = \frac{p_{H_2O}^*}{x_{H_2O}^*} \left(1 - x_{H_2O}^* - x_{N_2}^* - x_{CO_2}^*\right). \quad (8.1.48)$$

According to assumption (5),  $p_{H_2O}^*$  at the cathode equals  $(p_{H_2O}^{sat})^*$  and the above equation can be written as

$$p_{O_2}^* = \left(p_{H_2O}^{sat}\right)^* \left(\frac{1 - x_{N_2}^* - x_{CO_2}^*}{x_{H_2O}^*} - 1\right). \quad (8.1.49)$$

where  $p_{H_2}^*$  and  $p_{O_2}^*$  are the partial pressure of the fuel and of the oxidant and will be used in the Nernst equation to find fuel-cell output voltage.

### 8.1.5 Material conservation

The instantaneous change in the effective partial pressure of hydrogen and oxygen can be determined through the ideal gas equations as follows

$$p^\circ \frac{V_a}{RT} \frac{dp_{H_2}^*}{dt} = M_{H_2,in} - M_{H_2,out} - \frac{i}{2F} = M_{H_2,net} - \frac{i}{2F} \quad (8.1.50)$$

$$p^\circ \frac{V_c}{RT} \frac{dp_{O_2}^*}{dt} = M_{O_2,in} - M_{O_2,out} - \frac{i}{4F} = M_{O_2,net} - \frac{i}{4F} \quad (8.1.51)$$

where  $V_a$  ( $V_c$ ) is the volume of the anode (cathode) channel [m<sup>3</sup>];  $M_{H_2} = H_2$ , mole flow rate [mol s<sup>-1</sup>];  $i$  the fuel cell current [A];  $M_{O_2} = O_2$ , mole flow rate [mol s<sup>-1</sup>]; subscripts  $(in)$ ,  $(out)$  and  $(net)$  denote the values related to input, output, and net.

At steady state, all partial pressures are considered to be kept constant, that is

$$\frac{dp_{H_2}^*}{dt} = \frac{dp_{O_2}^*}{dt} = 0 \quad (8.1.52)$$

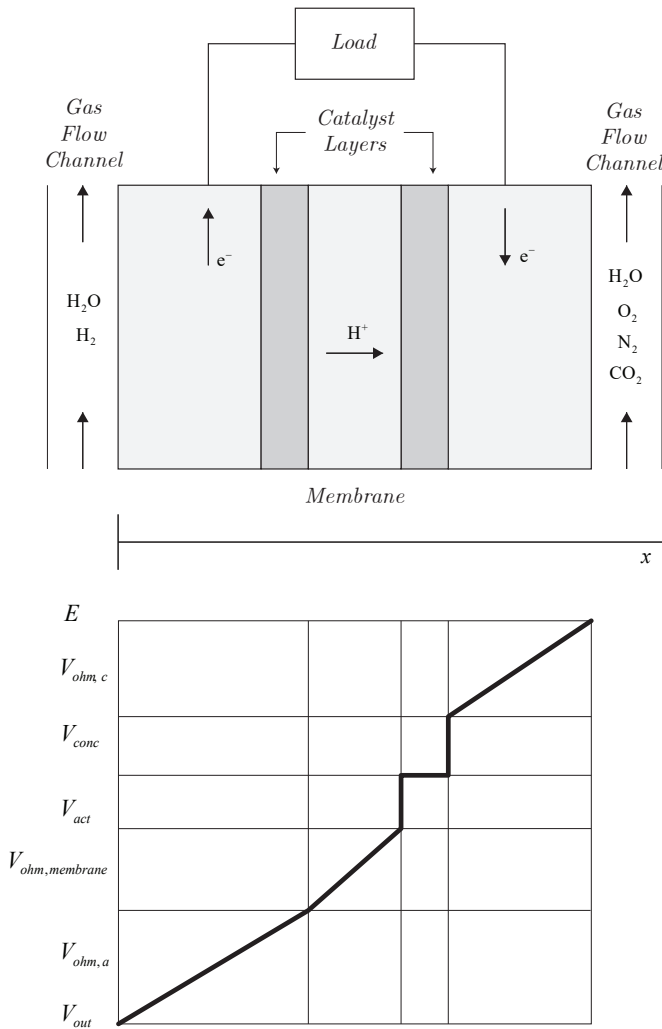


Figure 8.5: Schematic diagram of a PEM fuel cell and voltage drop across it.

Therefore, the net mole flow rates of H<sub>2</sub> and O<sub>2</sub> at steady state are

$$M_{H_2,net} = 2M_{O_2,net} = \frac{I}{2F} \quad (8.1.53)$$

Under transient state, there are delays between the change in load current and the flow of fuel (H<sub>2</sub>) and oxidant O<sub>2</sub>. Eq. (8.1.50) and Eq. (8.1.50) can be modeled by the following first order differential equations:

$$\begin{aligned} \tau_a \frac{dM_{H_2,net}}{dt} &= \frac{i}{2F} - M_{H_2,net} \\ \tau_c \frac{dM_{O_2,net}}{dt} &= \frac{i}{4F} - M_{O_2,net} \end{aligned} \quad (8.1.54)$$

Time constant  $\tau_a$  and  $\tau_c$  represent the fuel and oxidant flow delays (in seconds) at the anode and cathode respectively. The dynamic system of Eq. (8.1.54) will be used to determine the output voltage of the PEMFC.

### 8.1.6 PEMFC output voltage

According to assumption (5) the corresponding Nernst equation used to calculate the reversible potential is

$$E_{cell} = E_{0,cell} + \frac{RT}{2F} \log \left[ p_{H_2}^* \cdot (p_{O_2}^*)^{\frac{1}{2}} \right] \quad (8.1.55)$$

where  $E_{0,cell}$  is a function of temperature and can be expressed as follows

$$E_{0,cell} = E_{0,cell}^0 - k_E(T - 298) \quad (8.1.56)$$

where  $E_{0,cell}^0$  is the standard reference potential at standard state, 298 K and 101 325 Pa pressure.

To simplify the analysis, a voltage  $E_{d,cell}$  is considered to be subtracted from the right side of Eq. (8.1.55) for the overall effect of the fuel and oxidant delay. The steady state value of  $E_{d,cell}$  is zero, but it will show the influence of the fuel and oxidant delays on the fuel-cell output voltage during load transient. It can be written as

$$E_{d,cell} = \lambda_e \left[ i(t) - i(t) * \exp\left(-\frac{t}{\tau_e}\right) \right] \quad (8.1.57)$$

where  $*$  represent the convolution operator. Converting Eq. (8.1.57) to the Laplace domain, we get

$$E_{d,cell}(s) = \frac{\tau_e s}{\tau_e s + 1} \lambda_e I(s). \quad (8.1.58)$$

Eq. (8.1.58) is used for developing the model. The internal potential  $E_{cell}$  in Eq. (8.1.55) now becomes

$$E_{cell} = E_{0,cell} + \frac{RT}{2F} \log \left[ p_{H_2}^* \cdot (p_{O_2}^*)^{\frac{1}{2}} \right] - E_{d,cell} \quad (8.1.59)$$

where  $E_{cell}$  calculated from Eq. (8.1.59), is actually the open-circuit voltage of the fuel-cell. However, under normal operating conditions, the fuel-cell output voltage is less than  $E_{cell}$ . Activation loss, ohmic resistance voltage drop, and concentration over-potential are voltage drops across the fuel cell, as shown in Figure 8.5. Therefore

$$V_{cell} = E_{cell} - V_{act,cell} - V_{ohm,cell} - V_{conc,cell}. \quad (8.1.60)$$

The output voltage of the fuel-cell stack can be obtained as follows

$$V_{out} = N_{cell} V_{cell} = E - V_{act} - V_{ohm} - V_{conc}. \quad (8.1.61)$$

To calculate the fuel-cell output voltage, the following estimation are used:

1. *Activation voltage drop*: Tafel equation, given below, is used to calculate the activation voltage drop in a fuel cell

$$V_{act} = \frac{RT}{\alpha z F} \log \left( \frac{I}{I_0} \right) = T \cdot [a + b \log(I)] \quad (8.1.62)$$

On the other hand, an empirical equation for  $V_{act}$  is given in, where a constant ( $\eta_0$ ) is added to Eq. (8.1.62) as follows

$$V_{act} = \eta_0 + (T - 298) \cdot a + T \cdot b \log(I) = V_{act1} + V_{act2} \quad (8.1.63)$$

where  $V_{act1} = \eta_0 + (T - 298) \cdot a$  is the voltage drop affected only by the fuel cell internal temperature, while  $V_{act2} = T \cdot b \log(I)$  is both current and temperature dependent. The equivalent resistance of activation corresponding to  $V_{act2}$  is defined as

$$R_{act} = \frac{V_{act2}}{I} = \frac{T \cdot b \log(I)}{I} \quad (8.1.64)$$

2. *Ohmic voltage drop:* The ohmic resistance of a PEM fuel cell consists of the resistance of polymer membrane, the conducting resistance between the membrane and electrodes, and the resistances of electrodes. The overall ohmic voltage drop can be expressed as

$$V_{ohm} = V_{ohm,a} + V_{ohm,membrane} + V_{ohm,c} = IR_{ohm} \quad (8.1.65)$$

where  $R_{ohm}$  is also a function of current and temperature

$$R_{ohm} = R_{ohm,0} + k_{RI}I - k_{RT}T \quad (8.1.66)$$

where  $R_{ohm,0}$  is the constant part of the  $R_{ohm}$ .

3. *Concentration voltage drop:* During the reaction process, concentration gradients can be formed due to mass diffusion from the flow channel to the reaction sites (catalyst surface). At high current densities, slow transportation of reactants (products) to (from) the reaction sites is the main reason for the concentration voltage drop. Any water film covering the catalyst surfaces at the anode and cathode can be another contributor to this voltage drop. The concentration overpotential in the fuel-cell is defined as

$$V_{conc} = -\frac{RT}{zF} \log \frac{C_S}{C_B} \quad (8.1.67)$$

where  $C_S$  is the surface concentration and  $C_B$  is the bulk concentration. According to Fick's first law and Faraday's law, the above equation can be written as

$$V_{conc} = -\frac{RT}{zF} \log \left( 1 - \frac{I}{I_{limit}} \right) \quad (8.1.68)$$

The equivalent resistance for the concentration loss is

$$R_{conc} = \frac{V_{conc}}{I} = -\frac{RT}{zFI} \log \left( 1 - \frac{I}{I_{limit}} \right) \quad (8.1.69)$$

4. *Double-Layer charging effect:* In a PEM fuel cell, the two electrodes are separated by a solid membrane which only allows the  $H^+$  ions to pass, but blocks the electron flow. The electrons will flow from the anode through the external load and gather at the surface of the cathode, to which the protons of hydrogen will be attracted at the same time. Thus, two charged layers of opposite polarity are formed across the boundary between the porous cathode and the membrane. The layers, known as electrochemical double layer, can store electrical energy and behave like a super capacitor. The equivalent circuit of fuel cell considering this effect is given in Figure 8.6. In the circuit of Figure 8.6, the component  $C$  is the equivalent capacitor due to the double-layer charging effect. Since the electrodes of a PEM fuel cell are porous, the capacitance  $C$  is very large and can be in the order of several Farads.  $R_{act}$  and  $R_{conc}$  are equivalent resistance of activation and concentration voltage drops, which can be calculated according to Eq. (8.1.64) and Eq. (8.1.69). The voltage across  $C$  is

$$V_C = \left( I - C \frac{dV_C}{dt} \right) (R_{act} + R_{conc}) \quad (8.1.70)$$

The double-layer charging effect is integrated into the modeling, by using  $V_C$  instead of  $V_{act,2}$  and  $V_{conc}$ , to calculate  $V_{out}$ . The fuel cell output voltage now turns out to be

$$V_{out} = E - V_{act1} - V_C - V_{ohm} \quad (8.1.71)$$

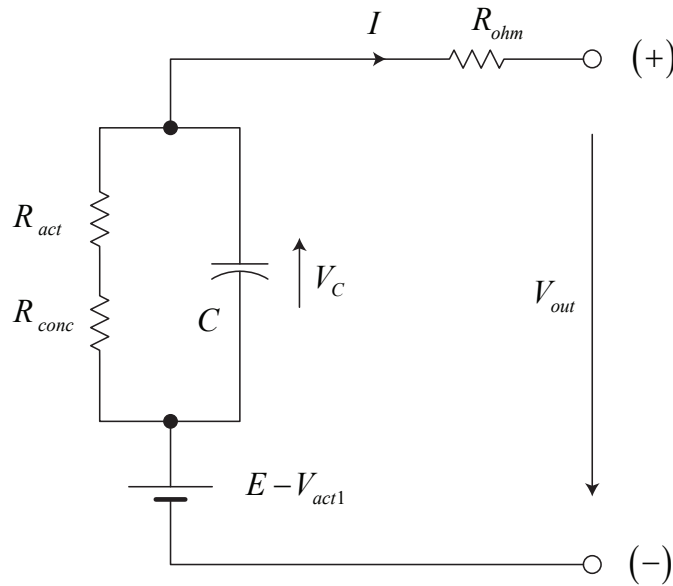


Figure 8.6: Equivalent circuit of the double-layer charging effect inside a PEMFC.

5. *Thermodynamic energy balance for PEMFC.* The net heat generation rate due to the chemical reaction inside the fuel cell, which causes its temperature rise or fall, can be written as

$$q_{net} = q_{chem} - q_{elec} - q_{sens+latent} - q_{loss} \quad (8.1.72)$$

where  $q_{net}$  is the net heat energy (J),  $q_{chem}$  the chemical (or heat) energy (J),  $q_{elec}$  the electrical energy (J),  $q_{sens+latent}$  the sensible and latent heat (J) and  $q_{loss}$  the heat loss (J).

From the power point of view we can write

$$\frac{dq_{net}}{dt} = \frac{dq_{chem}}{dt} - \frac{dq_{elec}}{dt} - \frac{dq_{sens+latent}}{dt} - \frac{dq_{loss}}{dt} \quad (8.1.73)$$

The power released due to chemical reaction due to the change in the enthalpy of the chemical reaction inside the fuel-cell ( $\Delta H$ ) can be written

$$\frac{dq_{chem}}{dt} = \frac{dn_{H_2,consumed}}{dt} \cdot \Delta H \quad (8.1.74)$$

where  $\frac{dn_{H_2,consumed}}{dt}$  is the consumption of  $H_2$ .

The maximum available electrical energy can be calculated from Gibbs free energy as follows

$$\Delta G = \Delta H - T\Delta S = \Delta G_0 - RT \log \left[ p_{H_2}^* \cdot (p_{O_2}^*)^{\frac{1}{2}} \right] \quad (8.1.75)$$

where  $\Delta G$  is the Gibbs free energy ( $J\text{mol}^{-1}$ );  $\Delta G_0$  the Gibbs free energy at standard condition (1 atm, 298 K).  $\Delta S$  the entropy change ( $J\text{mol}^{-1}\text{K}$ ).

The output electrical power can be written as

$$\frac{dq_{elec}}{dt} = V_{out} \cdot I \quad (8.1.76)$$

Sensible heat is the heat energy that is transferred by a body that has a temperature higher than its surroundings. Sensible heat transportation rate is the product of the species mol flow rate, its specific heat capacity, and its temperature and the room temperature. Latent heat is the amount of energy in the form of heat released or absorbed by a substance during a change of state or phase. heat of vaporization is used to indicate the amount of energy required when a substance changes its state into gas. Assuming the inlet temperature is the same of the room temperature, the sensible and latent heat absorbed during the process can be estimated by the following equation:

$$\frac{dq_{sens+latent}}{dt} = \frac{dn_{H_2,out}}{dt}(T - T_{room})C_{H_2} + \frac{dn_{O_2,out}}{dt}(T - T_{room})C_{O_2} + \frac{dn_{H_2O,generated}}{dt}(T - T_{room})C_{H_2O,l} + \frac{dn_{H_2O,generated}}{dt}H_V \quad (8.1.77)$$

where  $q_{sens+latent}$  is the sensible and latent heat (J),  $n_i$  the flow of species  $i$  ( $\text{mol s}^{-1}$ ),  $C_i$  the specific heat capacity of species  $i$  ( $\text{J mol}^{-1} \text{K}^{-1}$ ),  $H_V$  the vaporization heat of water ( $\text{J mol}^{-1}$ ) and  $T_{room}$  the room temperature (K).

The heat loss, which is mainly transferred by air convection, can be estimated as follows

$$\frac{dq_{loss}}{dt} = h_{cell}(T - T_{room})N_{cell}A_{cell} \quad (8.1.78)$$

where  $h_{cell}$  is the convective heat transfer coefficient ( $\text{W m}^{-2} \text{K}^{-1}$ ); it can be obtained through experiment.

At steady state, the fuel cell operates at constant temperature and  $q_{net} = 0$ . During transition, fuel cell temperature will rise or drop according to the fuel cell specific heat capacity and its net heat rate as follows

$$M_{FC}C_{FC}\frac{dT}{dt} = \frac{dq_{net}}{dt} \quad (8.1.79)$$

where the  $M_{FC}$  is the total mass of the fuel cell stack and  $C_{FC}$  is the overall specific heat capacity of the stack.

### 8.1.7 PEMFC model structure

A computer model can be developed for PEMFC based on its electrochemical and thermodynamic characteristics to predict the fuel cell dynamic response. The fuel cell output voltage is a function of temperature and load current. Since the fuel cell temperature and the voltage across the equivalent capacitance of double-layer charge effect are a function of time during a transient state, the resulting fuel cell output voltage is a dynamic quantity. Figure 8.7 shows a block diagram based on which a computer model can be developed for PEMFC. In this figure the input quantities are anode and cathode pressures, the initial fuel cell temperature and room temperature. At any given load current and time the internal temperature  $T$  is determined and both the load current and temperature are fed back to different blocks, which take part in the calculation of the fuel cell output voltage.

In the block diagram of Figure 8.7, mass diffusion equations are used to calculate the effective partial pressure of the hydrogen and oxygen. Then the Nernst equation and the overall fuel and oxidant delay effect are employed to determine the internal potential  $E$  of the fuel cell. The activation voltage drop equation, ohmic voltage drop equation, and concentration voltage drop equation together with the voltage of the equivalent capacitance of double-layer charge effect

are applied to determine the terminal output voltage of the PEMFC stack. Thermodynamic effect are also considered using energy balance equations.

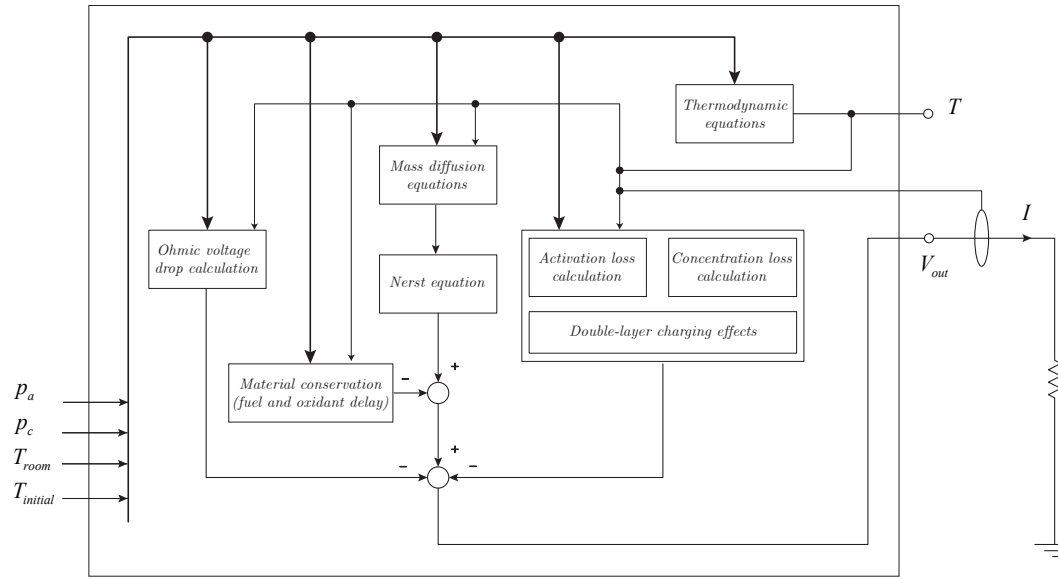


Figure 8.7: Block diagram for building a dynamic model of PEMFC.

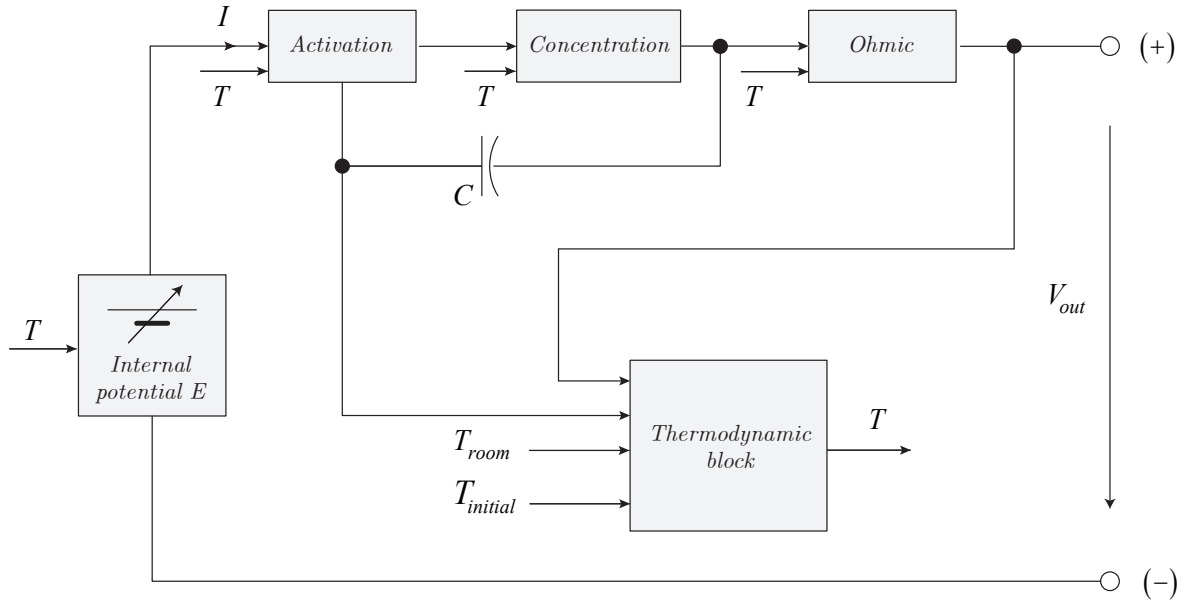


Figure 8.8: Block diagram for building an electrical circuit model for PEMFC.

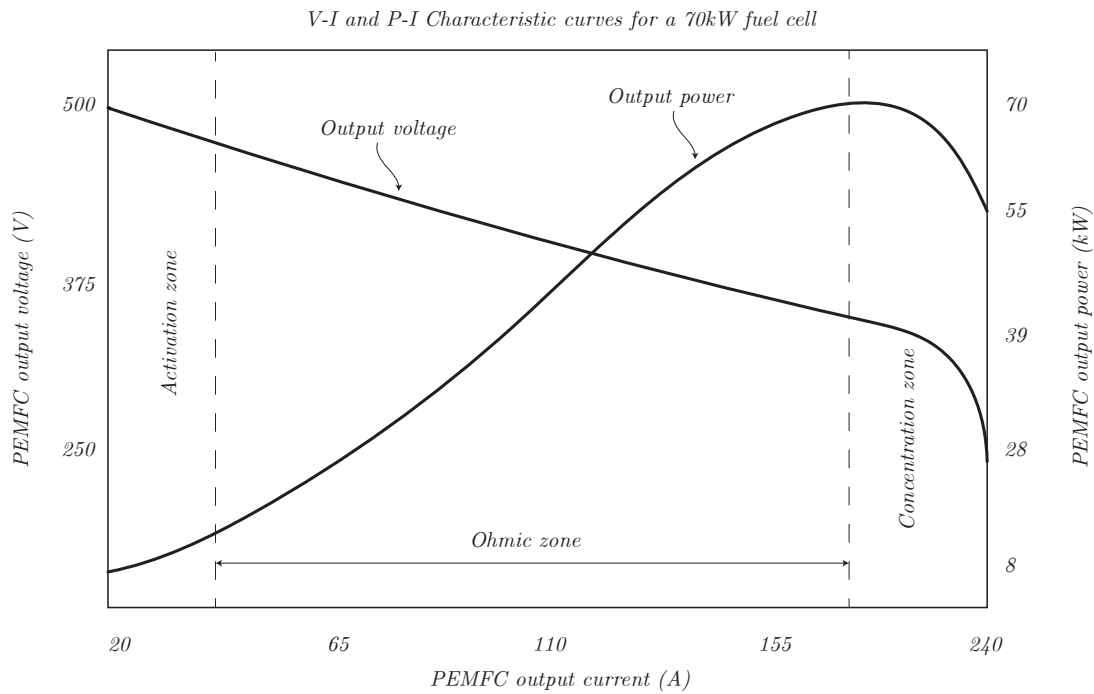


Figure 8.9:  $V - I$  and  $P - I$  characteristic curves for a 70 kW PEMFC.

### 8.1.8 The whole mathematical model of the PEMFC

The **OCV** (open circuit voltage) of the single cell and the transport equations can be summarized as follows

$$\left\{ \begin{array}{l} p^\circ \frac{V_a}{RT} \frac{dp_{H_2}^*}{dt} = M_{H_2,in} - M_{H_2,out} - \frac{i}{2F} = M_{H_2,net} - \frac{i}{2F} \\ p^\circ \frac{V_c}{RT} \frac{dp_{O_2}^*}{dt} = M_{O_2,in} - M_{O_2,out} - \frac{i}{4F} = M_{O_2,net} - \frac{i}{4F} \\ \tau_a \frac{dM_{H_2,net}}{dt} = \frac{i}{2F} - M_{H_2,net} \\ \tau_c \frac{dM_{O_2,net}}{dt} = \frac{i}{4F} - M_{O_2,net} \\ E_{cell} = E_{0,cell} + \frac{RT}{2F} \log \left[ p_{H_2}^* \cdot (p_{O_2}^*)^{\frac{1}{2}} \right] \\ E_{0,cell} = E_{0,cell}^0 - k_E(T - 298) \end{array} \right. \quad (8.1.80)$$

The additional voltage drops due to the current load effects are below summarized

$$\left\{ \begin{array}{l} V_{ohm} = V_{ohm,a} + V_{ohm,membrane} + V_{ohm,c} = IR_{ohm} \\ R_{ohm} = R_{ohm,0} + k_{RI}I - k_{RT}T \\ R_{conc} = \frac{V_{conc}}{I} = -\frac{RT}{zFI} \log \left( 1 - \frac{I}{I_{\text{limit}}} \right) \\ V_C = \left( I - C \frac{dV_C}{dt} \right) (R_{act} + R_{conc}) \\ V_{out} = E - V_{act1} - V_C - V_{ohm} \end{array} \right. \quad (8.1.81)$$

The elements of the equivalent circuit used to calculate the “load voltage” are time variant and are function of the load current  $i[\text{A}]$  and of the temperature  $T[\text{K}]$ .

# Chapter 9

## Energy storage

### 9.1 The fly-wheel equipment

### 9.2 The lithium-ion battery

In this section we are going to describe the lithium-ion cell operation using the simplified schematic of Figure 9.1. In the figure, the negative and positive electrodes are drawn as crystal structures comprising layers of electrode material. Lithium, drawn as small sphere, can be added to or removed from the space between layers. The lithium-ion cell used the method called **Intercalation** to store lithium charge-neutral atoms inside of the crystal structure.

Within the electrodes, lithium is stored as independent charge neutral atoms. Each lithium atom's valence electron is very loosely shared with neighboring atoms in the crystal structure. As such, the lithium is not tightly bonded in one place and is actually quite free to move around. Lithium enters and exits the surface of the electrodes, but diffuses within the layered open crystal structure to equalize the concentration of lithium within the vacant spaces of the electrode.

During discharge, lithium atoms at the surface of the negative electrode releases electrons - which travel through the external circuit - and become positive lithium ions,  $\text{Li}^+$  - which exit the crystal structure of the electrode and dissolve into the electrolyte. We can write  $\text{Li} \rightarrow \text{Li}^+ + \text{e}^-$ . Conversely, lithium ions proximate to the surface of the positive electrode receive electrons from the external circuit, and the resulting charge-neutral lithium atoms enter the crystal structure of the electrode. We can write  $\text{Li}^+ + \text{e}^- \rightarrow \text{Li}$ .

The process is completely reversible. Thus the lithium ions pass back and forth between the electrodes during charging and discharging. The intercalation mechanism is much gentler than an electromechanical reaction, so lithium-ion cells have much longer lives than other secondary cells.

The majority of commercial lithium-ion cells use some form of graphite ( $\text{C}_6$ ) for the negative-electrode material. Graphite comprises multiple graphene layers, in which hexagonal  $\text{C}_6$  structures are tightly bonded together. The graphene layers are stacked loosely on top of each other, held together only by weak van der Waals forces; lithium intercalates between these layers. The maximum amount of lithium that can be stored in graphite is one atom of lithium per six atoms of carbon; the minimum amount is zero. Therefore, when talking about the degree of lithiation of a graphite electrode, we use notation  $\text{Li}_x\text{C}_6$ , where  $0 \leq x \leq 1$ . Clearly, when viewed at the atomic level, there is either a single lithium atom or no lithium atom at all for any given  $\text{C}_6$  site.

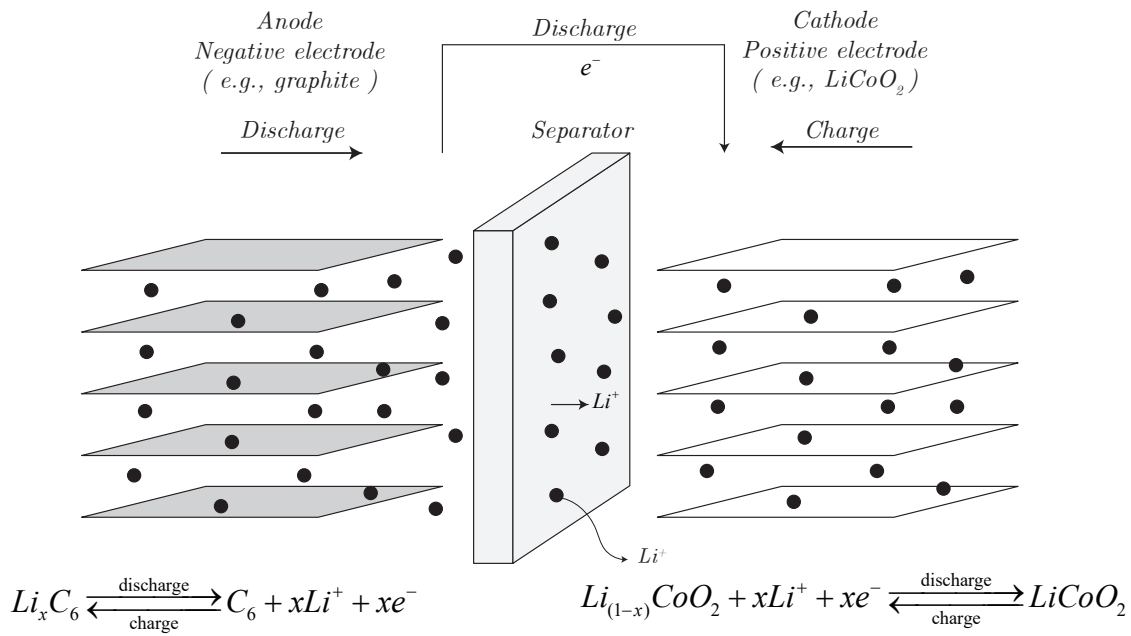


Figure 9.1: Schematic energy diagram of a lithium cell at open circuit.

But, when the entire electrode is considered, some fraction of the total number of  $\text{C}_6$  site is occupied and that fraction is the value of  $x$ . When the cell is charged the negative electrode is highly lithiated, and  $x$  is close to 1. When the cell is discharged, the negative electrode is largely depleted of lithium, and  $x$  is close to zero.

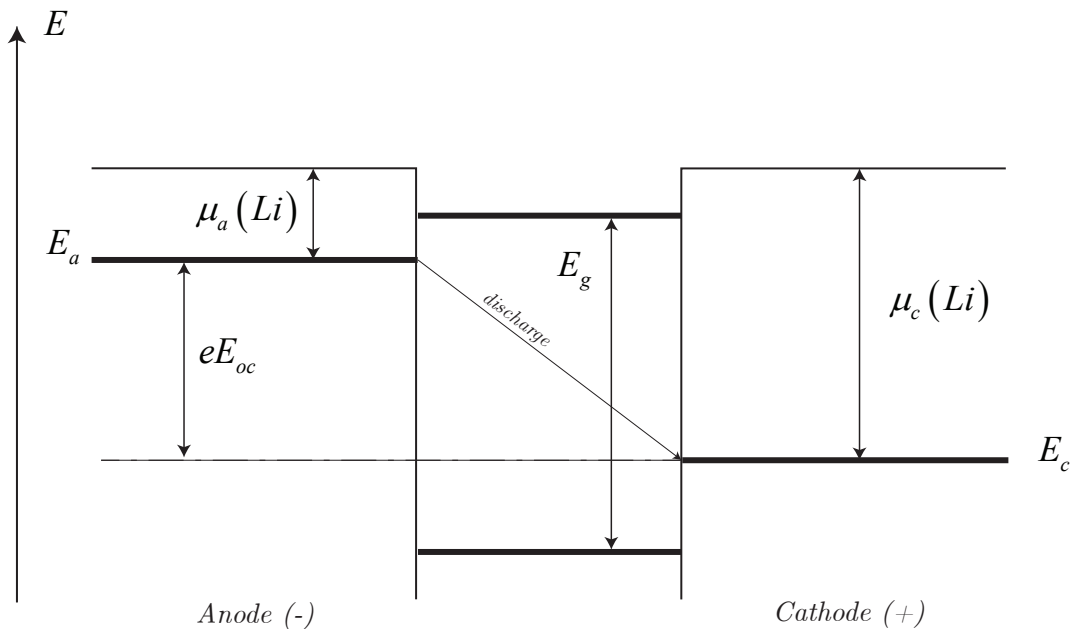


Figure 9.2: Schematic energy diagram of a lithium cell at open circuit.

### 9.2.1 The dynamical model of the lithium-ion battery

In this section we investigate a simpler approach to modeling cell operation, which uses an electrical-circuit analogy to define a *behavioural* or *phenomenological* approximation to how a cell's voltage responds to different input-current stimuli. Such models are called *equivalent-circuit models*.

From simple observation of the lithium-ion cell we can see that the open circuit voltage (*OCV*) is function of the state of charge (*SOC*) of the cell. The state of charge shall be considered a unit-less quantity and is denoted here as  $z(t)$ . To quantify the state of charge, we need to know how much charge a cell holds when it is fully charged versus how much charge remains when it is fully discharged.<sup>1</sup> So, we define the *total charge capacity* - or more simply the *total capacity* - of a cell to be the total amount of charge removed when discharging a cell from  $z = 100\%$  to  $z = 0\%$ . Total (charge) capacity is usually measured in ampere-hours ( $\text{A h}^{-1}$ ) and is denoted by the symbol  $Q$ . The value of total capacity is a parameter of the cell model; that is, it is a constant that may differ from cell to cell. Total capacity is not a function of temperature or current, although the total capacity of a cell does tend to decrease very gradually as the cell ages due to undesired parasitic chemical side reactions and structural breakdown of the cell's electrode materials<sup>2</sup>

We can model the state of charge using an ODE as follows

$$\frac{dz(t)}{dt} = -\frac{1}{Q}\eta(t)i(t) \quad (9.2.1)$$

where the sign of  $i(t)$  is positive when discharging. The current  $i(t)$  is measured in amperes,  $Q$  in coulombs (or A s). Both  $z(t)$  and  $\eta(t)$  are unitless.

The term  $\eta(t)$  is the *coulomb efficiency* or *charge efficiency* of the cell. We model  $\eta(t) = 1$  at time instants when the sign of current is positive (discharging), but  $\eta(t) \leq 1$  at time instants when the sign of current is negative (charging). When charging, most of the charge that passes through the cell participates in the desired chemical reactions, which do not increase the cell's state of charge (and often cause irreversible degradation to the cell as well).

---

<sup>1</sup>A *fully discharged* cell still has charge in it, but in general is never discharged beyond a certain point because that can cause damage and possibly a safety concern.

<sup>2</sup>The *total capacity* is different from a cell's *discharge capacity*. The latter is defined as the total amount of charge removed when discharging a cell at a constant rate from  $z = 100\%$  until the cell terminal voltage reaches some minimum cut-off voltage. This will occur before  $z = 0\%$  because real cells have internal resistance (and hence a voltage drop across the internal resistance). So, a cell's discharge capacities are always lower than its total capacity, unless discharge occurs at an infinitesimally slow rate.

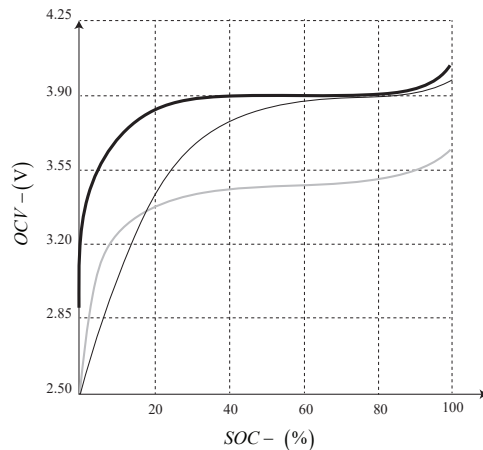


Figure 9.3: Open circuit voltage as a function of state of charge for different lithium-ion cell chemistries.

The  $OCV$  value for a cell are determined empirically at different  $SOC$  points. The valued can be stored in a look of table.

The open circuit voltage of a cell is a function of its state of charge as shown in Figure 9.3. There is some temperature dependence to this relationship - these curves are drawn for room temperature ( $25^\circ\text{C}$ ). Also, while these curves are drawn as function of the cell's state of charge, it is also common to see them expressed in terms of the cell's *depth of discharge (DOD)*. Depth of discharge is the converse of state of charge and is expressed either as a fraction or in ampere-hours.  $DOD = 1 - z(t)$  if it is being expressed as a fraction, and  $DOD = Q(1 - z(t))$  if being expressed in ampere-hours. The improved cell model, including open-circuit-voltage dependence on the cell's state of charge, is then depicted in Figure 9.4a, where the ideal voltage source is replaced by a controlled voltage source having value equal to  $OCV(z(t))$ . If temperature dependence is required, we instead use  $OCV(z(t), T(t))$ , where  $T(t)$  is the cell's internal temperature at time  $t$ .

time, we have

$$\begin{cases} \frac{dz(t)}{dt} = -\frac{1}{Q}\eta(t)i(t) \\ v(t) = OCV(z(t)) - i(t)R_0 \end{cases} \quad (9.2.2)$$

with this model, we see that  $v(t) > OCV(z(t))$  when  $i(t) < 0$  (i.e. when charging) and  $v(t) < OCV(z(t))$  when  $i(t) > 0$  (i.e. when discharging).

Finally, we note that the cell's resistance is often a function of the cell's state of charge and is always a function of the cell's internal temperature. The fidelity of the model's predictions will be enhanced if these dependencies are taken into account in  $R_0$ .

**Polarization** refers to any deviation of the cell's terminal voltage away from open-circuit voltage due to a passage of current through the cell. In the equivalent circuit model we have modeled instantaneous polarization via the  $i(t)R_0$  term. Real cells have more complex behaviour, where the voltage polarization slowly develops over time as current is demanded from the cell and then slowly decay over time when the cell is allowed to rest.

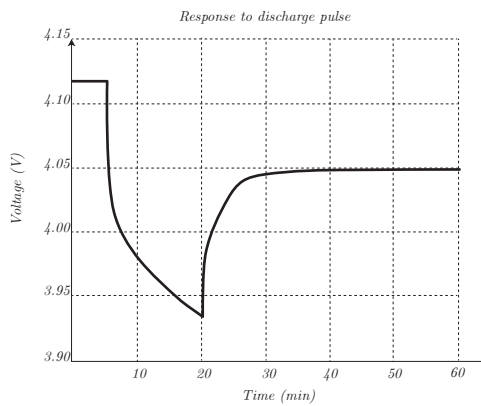


Figure 9.5 illustrates this slower behaviour. The voltage plotted in the figure corresponds to the following scenario:

1. the cell is at the rest for the first 5 minute, and the voltage is constant
2. the cell is then subjected to a discharge current pulse of constant magnitude from  $t = 5$  min until  $t = 20$  min
3. the load is removed and the cell is kept at rest for the remain of the test.

Figure 9.5: Behavior of the cell polarization, when a cell is subjected to a discharge pulse followed by a rest.

The model we have developed up to now is not able to explain the dynamic behaviour presents in the test shown in Figure 9.5.

The phenomenon shown in Figure 9.5 and which we witness every time we use a battery-powered device is mainly due to the slow diffusion process of lithium in lithium-ion cell, so we will refer to this slowly changing in a circuit using one or more parallel resistor-capacitor sub-circuits.

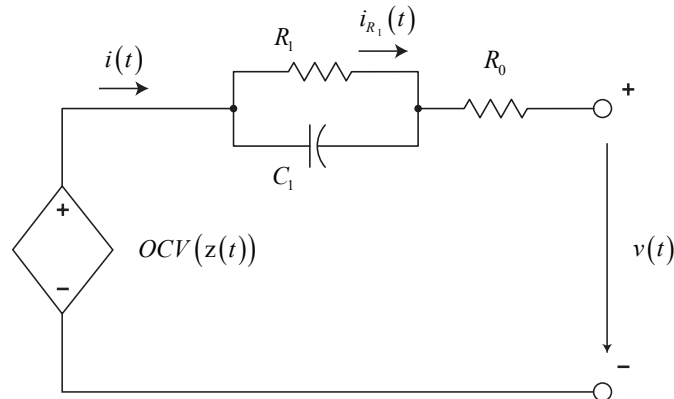


Figure 9.6: Circuit that models the diffusion voltage process.

The equivalent circuit model become as follows

$$\begin{cases} \frac{dz(t)}{dt} = -\frac{1}{Q}\eta(t)i(t) \\ \frac{di_{R_1}(t)}{dt} = -\frac{1}{R_1 C_1}(i_{R_1}(t) - i(t)) \\ v(t) = OCV(z(t)) - i_{R_1}(t)R_1 - i(t)R_0 \end{cases} \quad (9.2.3)$$

where its representation in discrete time domain becomes as follows

$$\begin{cases} z[k+1] = z[k] - \frac{t_s}{Q}\eta[k]i[k] \\ i_{R_1}[k+1] = \exp\left(-\frac{t_s}{R_1 C_1}\right)i_{R_1}[k] + \left[1 - \exp\left(-\frac{t_s}{R_1 C_1}\right)\right]i[k] \\ v[k] = OCV(z[k]) - R_1 i_{R_1}[k] - R_0 i[k] \end{cases} \quad (9.2.4)$$

Finally, we note that a cell's diffusion-voltage response is generally a function of the cell's state of charge and its internal temperature. If  $R_1$  and  $C_1$  are modeled as function of  $z(t)$  and  $T(t)$ , the model prediction can be improved.

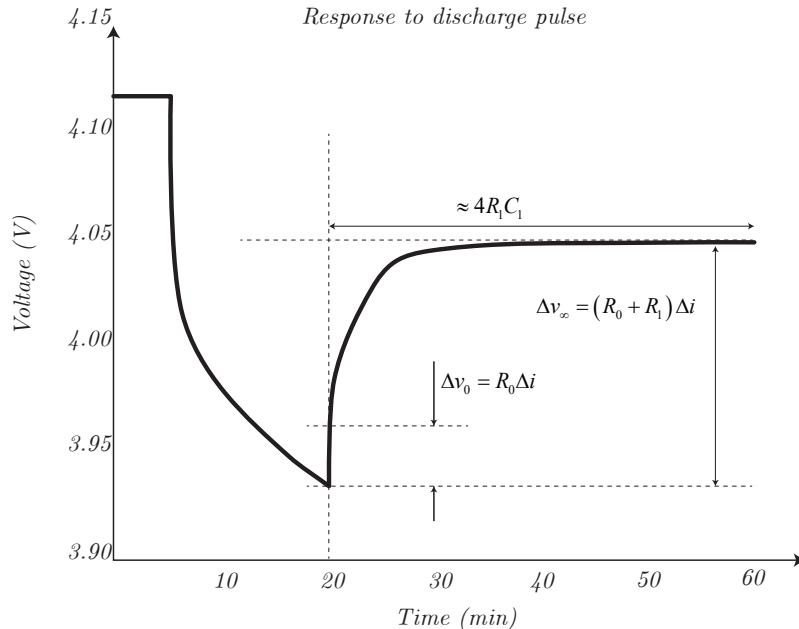


Figure 9.7: Measuring parameter values from a pulse response.

Now we are going to discuss about hysteresis behaviour if the cell. Considering a given  $OCV$  as function of the  $SOC$ , it can be observed that if we discharge a cell to 50%  $SOC$  and allow the cell to rest, the equilibrium voltage is lower than  $OCV$ . If we charge a cell to 50%  $SOC$  and allow the cell to rest, the equilibrium voltage is higher than  $OCV$ . These observations indicate that there is hysteresis in the cell terminal voltage.

Let  $h(z, t)$  be the dynamic hysteresis voltage as a function of  $SOC$  and time. We model the

change in hysteresis voltage as a function of change in *SOC* as follows

$$\frac{dh(z, t)}{dt} = \gamma \text{sign}(\dot{z}) [M(z, \dot{z}) - h(z, t)] \quad (9.2.5)$$

where  $M(z, \dot{z})$  is a function that gives the maximum polarization due to hysteresis as a function of *SOC* and the rate of charge od *SOC*. Specifically, we require that  $M(z, \dot{z})$  be positive for charge ( $\dot{z} > 0$ ) and negative for discharge ( $\dot{z} < 0$ ). The  $M(z, \dot{z}) - h(z, t)$  term is the differential equation states that the rate of change of hysteresis voltage is proportional to the distance of the present hysteresis value away from the major hysteresis loop, leading to a kind of exponential decay of voltage to the major loop. The term in front of this has a positive constant  $\gamma$  which tunes the rate of decay and  $\text{sign}(\dot{z})$ , which forces the equation to be stable both for charge and discharge.

To fit the differential equation for  $h(z, t)$  into our model, we must manipulate it to be a differential equation with respect to time, not with respect to *SOC*. We accomplish this by multiplying both side of the equation by  $dz/dt$

$$\frac{dh(z, t)}{dz} \frac{dz}{dt} = \gamma \text{sign}(\dot{z}) [M(z, \dot{z}) - h(z, t)] \frac{dz}{dt} \quad (9.2.6)$$

we use the chain rule to write the left-hand side of the equation as  $dh(z, t)/dt$  and we substitute  $dz/dt = -\eta(t)i(t)/Q$  into the right hand side, noting that  $\dot{z}\text{sign}(\dot{z}) = |\dot{z}|$ . Thus,

$$\frac{dh(t)}{dt} = - \left| \frac{\eta(t)i(t)\gamma}{Q} \right| h(t) + \left| \frac{\eta(t)i(t)\gamma}{Q} \right| M(z, \dot{z}). \quad (9.2.7)$$

This may be converted into a difference equation for our discrete-time application assuming  $i(t)$  and  $M(z, \dot{z})$  are constant over the sample period.

$$h[k+1] = \exp \left( - \left| \frac{\eta[k]i[k]\gamma t_s}{Q} \right| \right) h[k] + \left[ 1 - \exp \left( - \left| \frac{\eta[k]i[k]\gamma t_s}{Q} \right| \right) \right] M(z, \dot{z}). \quad (9.2.8)$$

Note that this is a nonlinear time-varying system as the factors multiplying the state and input change with  $i[k]$ . The simplest representation is when  $M(z, \dot{z}) = -M\text{sign}(i[k])$ , when

$$h[k+1] = \exp \left( - \left| \frac{\eta[k]i[k]\gamma t_s}{Q} \right| \right) h[k] - \left[ 1 - \exp \left( - \left| \frac{\eta[k]i[k]\gamma t_s}{Q} \right| \right) \right] M\text{sign}(i[k]). \quad (9.2.9)$$

With this representation  $-M \leq h[k] \leq M$  at all times, and  $h[k]$  has units of volts. When attempting to find the model parameters, we will find it valuable to rewrite this in an equivalent but slightly different representation, which has unitless hysteresis state  $-1 \leq h[k] \leq 1$ ,

$$h[k+1] = \exp \left( - \left| \frac{\eta[k]i[k]\gamma t_s}{Q} \right| \right) h[k] - \left[ 1 - \exp \left( - \left| \frac{\eta[k]i[k]\gamma t_s}{Q} \right| \right) \right] \text{sign}(i[k]). \quad (9.2.10)$$

$$\text{Hysteresis voltage} = Mh[k]. \quad (9.2.11)$$

This makes the output equation linear in  $M$ .

In addition to the type of dynamic hysteresis that changes as *SOC* changes, we also can model an instantaneous change in hysteresis voltage when the sign of the current changes.

$$s[k] = \begin{cases} \text{sign}(i[k]) & |i[k]| > 0 \\ s[k-1], & \text{otherwise} \end{cases} \quad (9.2.12)$$

Then the instantaneous hysteresis is modeled as

$$\text{Instantaneous hysteresis voltage} = M_0 s[k]. \quad (9.2.13)$$

and overall hysteresis is

$$\text{Hysteresis voltage} = M_0 s[k] + M h[k]. \quad (9.2.14)$$

### Enhanced self-correcting (ESC) model state equations

$$\begin{cases} z[k+1] = z[k] - \frac{t_s}{Q} \eta[k] i[k] \\ i_{R_1}[k+1] = \exp\left(-\frac{t_s}{R_1 C_1}\right) i_{R_1}[k] + \left[1 - \exp\left(-\frac{t_s}{R_1 C_1}\right)\right] i[k] \\ h[k+1] = \exp\left(-\left|\frac{\eta[k] i[k] \gamma t_s}{Q}\right|\right) h[k] - \left[1 - \exp\left(-\left|\frac{\eta[k] i[k] \gamma t_s}{Q}\right|\right)\right] \text{sign}(i[k]) \quad (9.2.15) \\ s[k] = \begin{cases} \text{sign}(i[k]) & |i[k]| > 0 \\ s[k-1], & \text{otherwise} \end{cases} \\ v[k] = OCV(z[k], T[k]) + M_0 s[k] + M h[k] - R_1 i_{R_1}[k] - R_0 i[k] \end{cases}$$

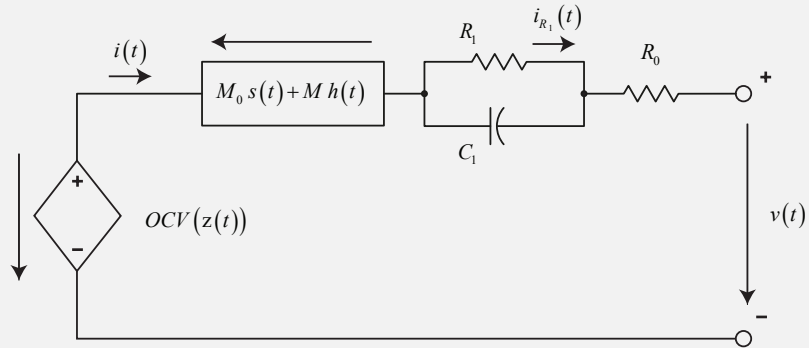


Figure 9.8: The enhanced self-correcting cell model equivalent circuit.

## 9.3 Battery management

### 9.3.1 Preliminaries

The primary purposes of a battery-management system (BMS) are:

- First and foremost, to protect the safety of the operator of the battery-powered system. The BMS must detect unsafe operating conditions and respond. This may demand disconnecting and isolating the battery pack from the load, warning the above operating system.

- Second, to protect cells of the battery pack from damage in abuse or failure cases. This may involve active intervention under software control, or specialized electronics that can detect failures and isolate the failing components from the rest of the battery pack and from the load it powers.
- Third, to prolong the life of the battery under normal operating cases. The BMS does so by coordinating with the controller of the load it powers, advising it of dynamic limits on power that can be sourced or sunk over some short future interval that ensures the battery pack will not be overcharged or overdischarged. It also controls the thermal-management system, ensuring that the battery pack is kept within its design operational-temperature range.
- Fourth, to maintain the battery pack in a state in which it can fulfil its functional design requirements. Thus, for example, it will not allow a battery pack to become so far discharged that it cannot deliver its rated discharge power, nor will it allow the pack to become so highly charged that it cannot receive its rated charge power at any point in time.

### 9.3.2 Battery state of charge estimator

State of charge estimation plays a fundamental role in the management of the battery. A not well fitted SOC estimator can reduce drastically the time life of the battery and bring it in a dangerous working area. According Figure 9.9 we can three main approach:

- model based control
- open loop control and coulomb counting
- data driven approach

It is clear than the only open loop approach or coulomb counting affect the estimation by a bias which increase long the time. The approach we will taken into account is the model based approach which can be made by a *cooperation* of control strategy among *model-based* and *open loop*.

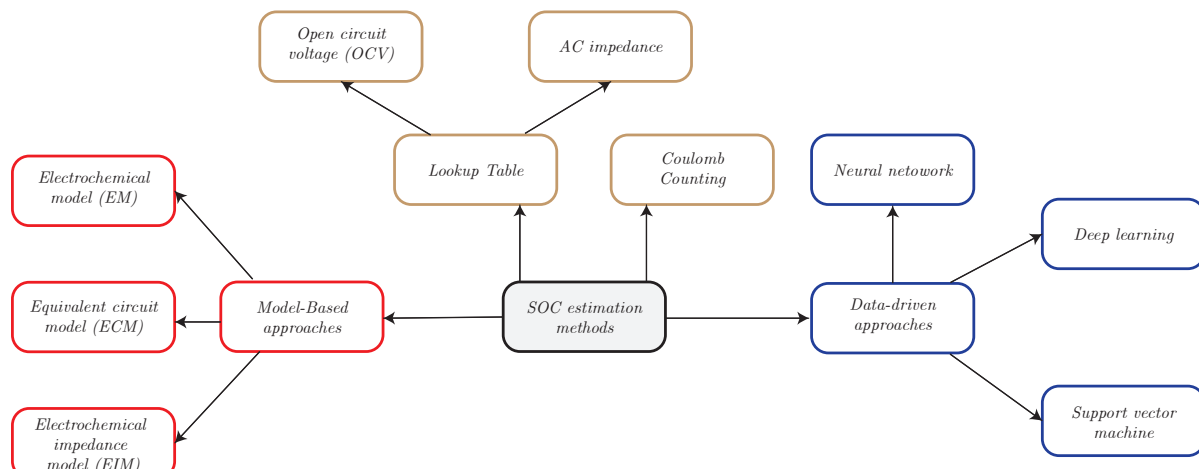


Figure 9.9: Classification of SOC estimation methods.

### 9.3.3 Model based SOC estimation with extended Kalman filter

See D. Bagnara *Advanced Control Engineering 2*, MCI 2022.

# Chapter 10

## The DC/DC converter

In this chapter two current controlled power supplies are described:

- zero voltage switching architecture. This architecture is relatively efficient, relatively compact, and implements an internal galvanic insulation;
- resonant zero current switching architecture. This architecture has a very high efficiency, is very compact, and implements an internal galvanic insulation;

### 10.1 Zero Voltage Switching Architecture

The DC/DC converter is basically the interface between the fuel-cell and the battery. According to the battery management control strategy and according to the control constraints due to the fuel cell a global fuel-cell/battery control shall be designed.

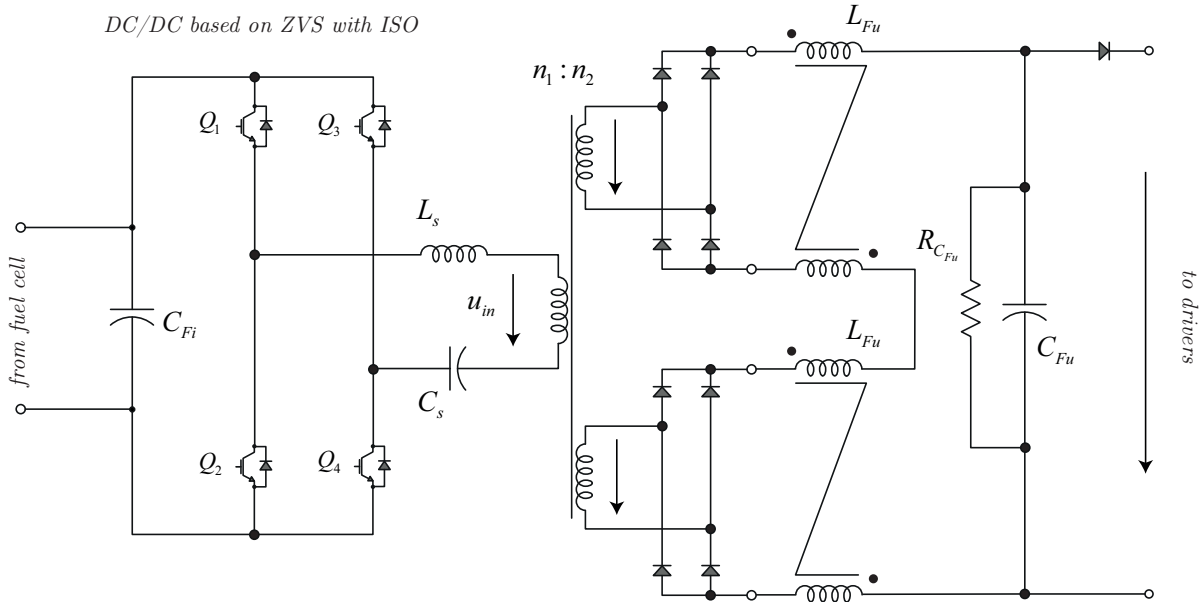


Figure 10.1: DC/DC converter based on galvanic insulated ZVS.

As general rule the battery charging process is performed at constant current until a certain amount to state of the charge of the battery and after that point the control of the ZVS

is performed at constant voltage. According these few rules we already can understand the necessity to control the DC/DC converter in both mode: current and voltage.

The ZVS converter is a special configuration which taking advantages from the parasitic collector-emitter capacitance  $C_{ce}$  of the IGBT is able to reduce the overall switching losses (commutation occurs at low  $V_{ce}$  voltage across the IGBT) given the possibility to increase the PWM frequency and reducing the dimensioning of the transformer used to introduce a galvanic insulation between the fuel cell and the rest of the power train.

The following components data can be taken into account (considering a PWM switching frequency of  $f_{PWM} = 20\text{ kHz}$ )

$C_{Fi} = 240\text{ }\mu\text{F}$	$u_{tr}^{1nom} = 400\text{ V}$	$u_{tr}^{2nom} = 438\text{ V}$	$u_{tr}^{3nom} = 438\text{ V}$
$n1 = 23$	$n2 = 21$	$n3 = 21$	$C_s = 180\text{ }\mu\text{F}$
$L_{Fu} = 500\text{ }\mu\text{H}$	$C_{Fu} = 3.3\text{ mF}$	$R_{CFu} = 2\text{ k}\Omega$	$L_s = 11.7\text{ }\mu\text{H}$

Table 10.1: Components data of the ZVS dc/dc converter.

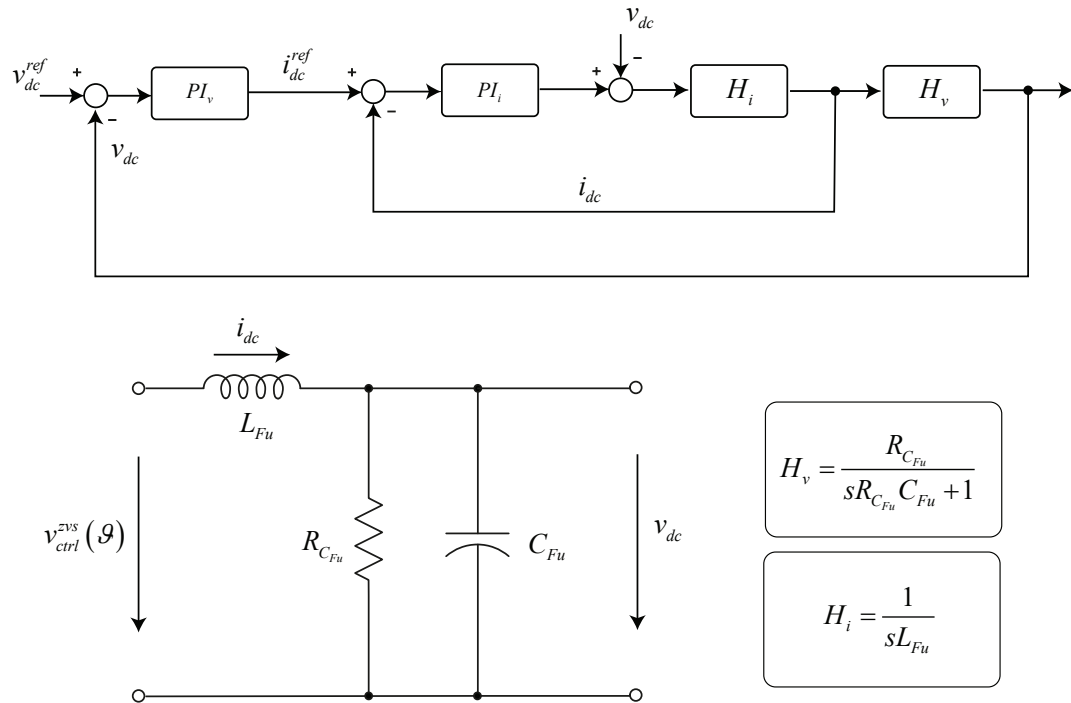


Figure 10.2: ZVS control architecture and equivalent control model.

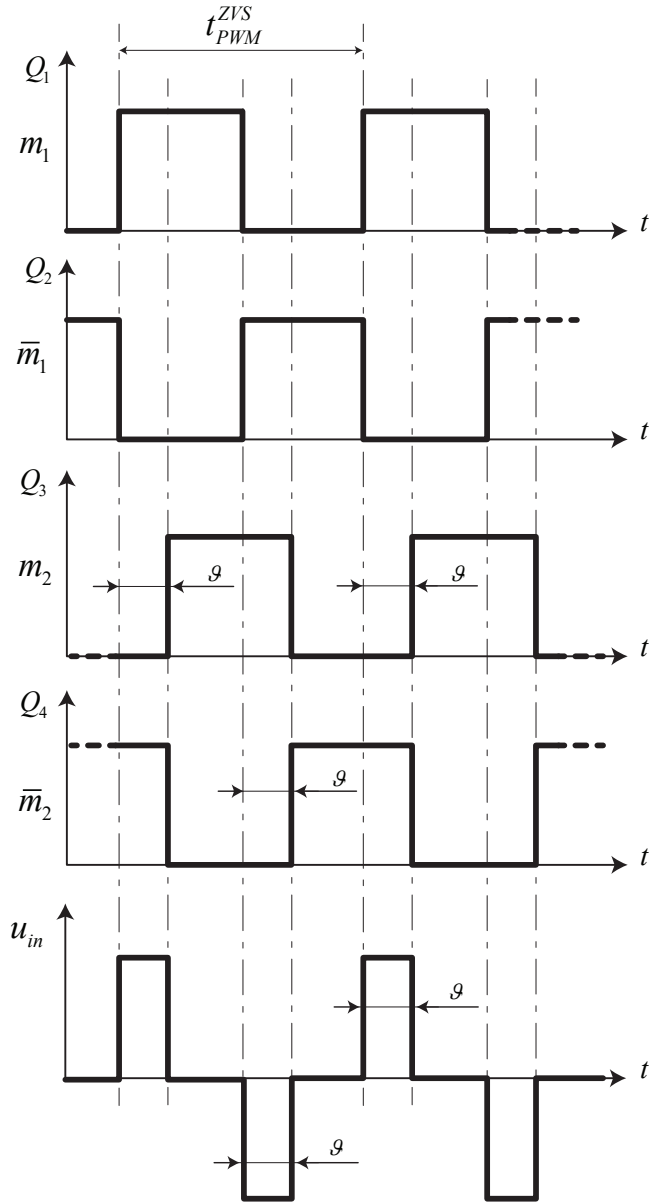


Figure 10.3: ZVS modulation strategy based on phase shift  $\vartheta$  of the leg  $Q_3Q_4$  respect to the leg  $Q_1Q_2$ .

Figure 10.3 shows the modulation strategy used at the H-bridge. Each leg of the H-bridge is commanded with a 50% duty cycle PWM, where we can call  $m_1$  and  $m_2$ . When the phase-displacement  $\vartheta$  between  $m_1$  and  $m_2$  the output voltage  $u_{in}$  is zero. As soon as the phase-displacement  $\vartheta$  become different from zero the output voltage  $u_{in}$  according to Figure 10.3. When the phase-displacement  $\vartheta$  reach the value of  $\pi$  the output voltage  $u_{in}$  reach its maximum value. From this short description of the working principle of the ZVS converter we can see the ZVS works like a *buck-converter*. As shown in Figure 10.1 the output voltage  $u_{in}$  passes through a transformer (in this case as step-up) in order to introduce a galvanic insulation and to adapt, the rectified voltage, to the constraints of the battery. The  $L_sC_s$  group is used to limit the current ripple and to remove any DC-voltage component which could saturate the transformer. In particular the resonance frequency  $f_0 = 1/(2\pi\sqrt{(L_sC_s)})$  of the LC group is kept 5 time slower than the PWM frequency of the H-bridge. At the output of the rectifier an *LRC* filter is placed. The aim of the *LRC* is to limit the voltage ripple creates a stable DC-voltage source for the inverter which are here connected. During the inverter operating most of the switching current is fed by the DClink capacitor and not by the battery. The battery should deliver the only DC components.

### 10.1.1 Control for ZVS converter

The equivalent plant model seen by the ZVS converter is shown in Figure 10.2, where the voltage plant can be defined as follows

$$H_v(s) = \frac{V_{dc}(s)}{I_{dc}(s)} = \frac{R_{C_{Fu}}}{sR_{C_{Fu}}C_{Fu} + 1} \quad (10.1.1)$$

and the current plant as follows

$$H_i(s) = \frac{I_{dc}(s)}{V_{ctrl}^{zvs}(s) - V_{dc}(s)} = \frac{1}{sL_{Fu}} \quad (10.1.2)$$

where  $v_{ctrl}^{zvs}(\vartheta(t))$  is the rectified voltage and is controlled by the phase-displacement  $\vartheta$ . Overall control can be implemented by a cascade PI control with a voltage outer loop and a inner current loop control as shown in Figure 10.2.

## 10.2 Resonant Zero Current Switching Architecture

A good and efficient DC/DC converter is the so called *Resonant Zero Current Switching*. This architecture permits to remove switching power losses due to the fact any switching occur at zero current, that means the corresponding switching energy are close to zero.

The use of the *ZCS* converter for battery charge make its design relatively straightforward due to the limited input and output voltage excursion in comparison to a generic wide range application.

### 10.2.1 Nomenclature

Here the list of variables and parameters used along the document:

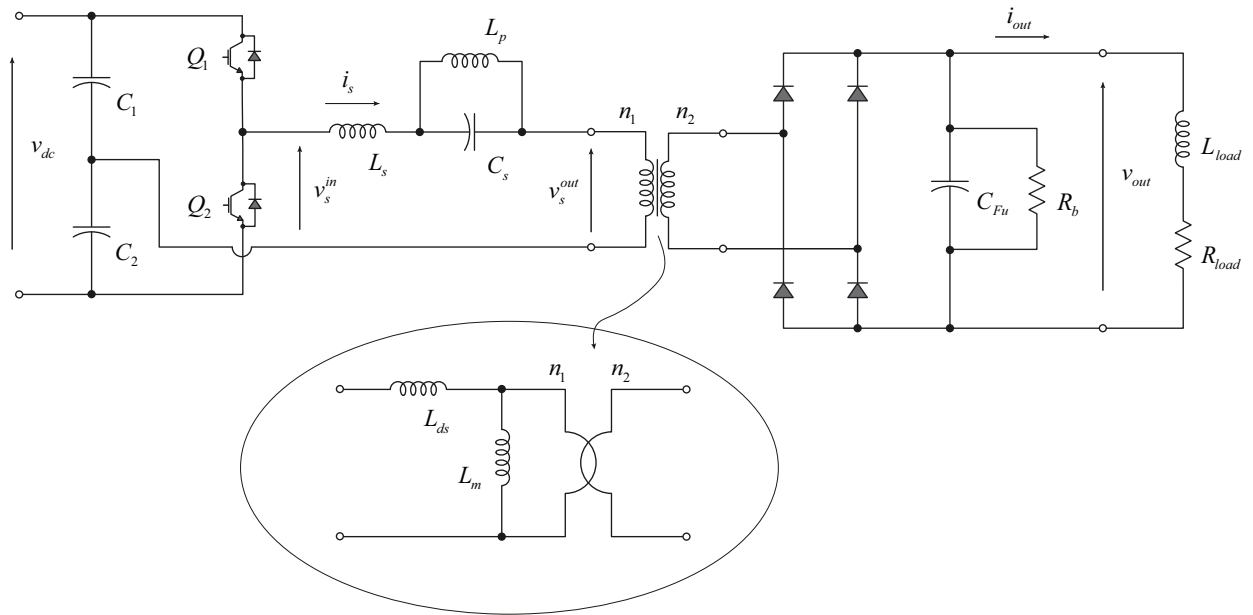
- $v_{rst}^{grid}$  [V]: grid phase voltage;
- $v_{dc}$  [V]: dc-link voltage;
- $i_s$  [A]: internal current of the resonant circuit;
- $v_s^{in}$  [V]: input voltage of the resonant circuit;
- $v_s^{out}$  [V]: output voltage of the resonant circuit;
- $v_{out}$  [V]: load voltage;
- $i_{out}$  [A]: load current;
- $C_1, C_2$  [F]: dc-link capacitors;
- $L_s$  [H]: series inductance of the resonant circuit;
- $L_p$  [H]: parallel inductance of the resonant circuit;
- $C_s$  [F]: series capacitance of the resonant circuit;
- $L_{ds}$  [H]: leakage inductance of the high-frequency single phase transformer;
- $L_m$  [H]: magnetization inductance of the high-frequency single phase transformer;

- $C_{Fu}$  [F]: output filter capacitance;
- $n_1$  [ ]: number of turns at primary side of the high-frequency single phase transformer;
- $n_2$  [ ]: number of turns at secondary side of the high-frequency single phase transformer;

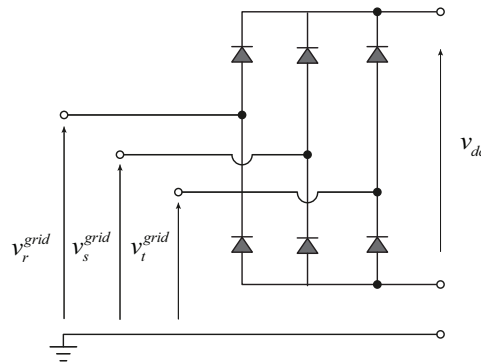
### 10.2.2 Model Description

In this section the electrical topology of the CLL-ZCS resonant converter is presented. Figure 10.4 shows the complete topology, where the following parts are depicted:

- an input stage uncontrolled rectifier (see Figure 10.4b) – AC/DC;
- an half bridge switching converter (see Figure 10.4a) – DC/AC;
- a double resonance circuit –  $C_s L_s L_p$ ;
- an high frequency transformer with scaling  $n_1/n_2$ ;
- an output stage uncontrolled rectifier – AC/DC;
- an output stage filter  $C_{Fu}$  with a bleeder load  $R_b$ ;



(a) CLL-ZCS resonant converter output stage.



(b) CLL-ZCS resonant converter input stage rectifier.

Figure 10.4: CLL-ZCS resonant converter.

During the normal operation, the half bridge generates a fixed  $t_{on}$  pulse with variable modulation index  $m = t_{on}/t_{sw}$  that means the switching frequency  $f_{sw} = 1/t_{sw}$  will be selected in a range between the minimum resonance frequency  $f_{sw}^{min} = f_{rp}$  and around half of the maximum resonance frequency  $f_{rs}$  i.e.  $f_{sw}^{max} \approx f_{rs}/2$ . The resonance block circuit is made by the coupling of two LC circuits:

- one series  $L_s C_s$ , which becomes a short-circuit at  $f_{rs}$  resonance frequency;
- one parallel  $L_p C_s$ , which becomes an open-circuit at  $f_{rp}$  resonance frequency;

The resonance block is also depicted in Figure 10.5a.

As above mentioned the resonance block can be splitted into two resonance  $LC$  circuits,

respectively as follows:

$$z_p(s) = \frac{sL_p}{s^2L_pC_s + 1} \quad (10.2.1)$$

$$z_s(s) = \frac{s^2L_sC_s + 1}{sC_s} \quad (10.2.2)$$

which results in the following boundary frequencies:

$$\omega_{rp}^2 L_p C_s - 1 = 0 \Rightarrow f_{rp} = \frac{1}{2\pi\sqrt{L_p C_s}} \quad (10.2.3)$$

$$\omega_{rs}^2 L_s C_s - 1 = 0 \Rightarrow f_{rs} = \frac{1}{2\pi\sqrt{L_s C_s}} \quad (10.2.4)$$

At frequency  $f_{rp}$  the transfer function between the resonance-circuit voltage input  $v_s^{in}$  and the resonance-circuit voltage output  $v_s^{out}$  results in a open circuit, while at the frequency  $f_{rs} \gg f_{rp}$  results in a short circuit.

Considering the equivalent circuit of Figure 10.5a, the transfer function between the voltage input  $v_s^{in}$ , and the voltage output  $v_s^{out}$  becomes as follows

$$H_v(v) = \frac{V_s^{out}(s)}{V_s^{in}(s)} = \frac{s^2 R_{load}^{eq} L_p C_s + R_{load}^{eq}}{s^3 R_{load}^{eq} L_s^{eq} L_p C_s + s^2 R_{load}^{eq} L_p C_s + s(L_s^{eq} + L_p) + R_{load}^{eq}} \quad (10.2.5)$$

where  $L_s^{eq} = L_s + L_{ds}$  and  $R_{load}^{eq} \approx \left(\frac{n_1}{n_2}\right)^2 R_{load}$ , and  $L_{ds}$  is the leakage transformer inductance.

Plotting the Bode diagram of Eq. (10.2.5) for different values of  $R_{load}^{eq}$  the curves reported in Figure 10.5b are obtained. As per Figure 10.5b the attenuation capacity of the *CLL* circuit is function of the load, if he load increases its impedance the corresponding attenuation curve will be pulled up toward a lower level of attenuation.

### 10.2.3 Modulation Strategy

Considering  $Q_1$  the gate command of the top switch and  $Q_2$  the gate command of the bottom switch, the modulation strategy is depicted in Figure 10.6. The resonance circuit is excited by a fixed  $t_{on}$  calculated as follows

$$t_{on} \approx \left(\sqrt{2}f_{rs}\right)^{-1} \quad (10.2.6)$$

the modulation takes its effect changing the timing where both gate command  $Q_1$  and  $Q_2$  are zero. The excitation pulse  $t_{on}$  is selected in order to guarantee the zero current switching.

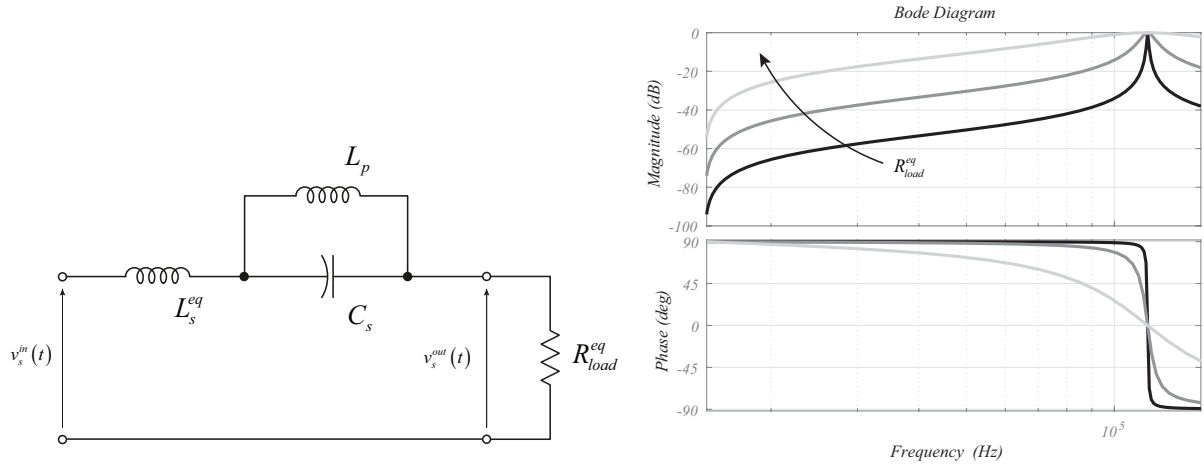


Figure 10.5: Resonance circuit analysis as function of the load.

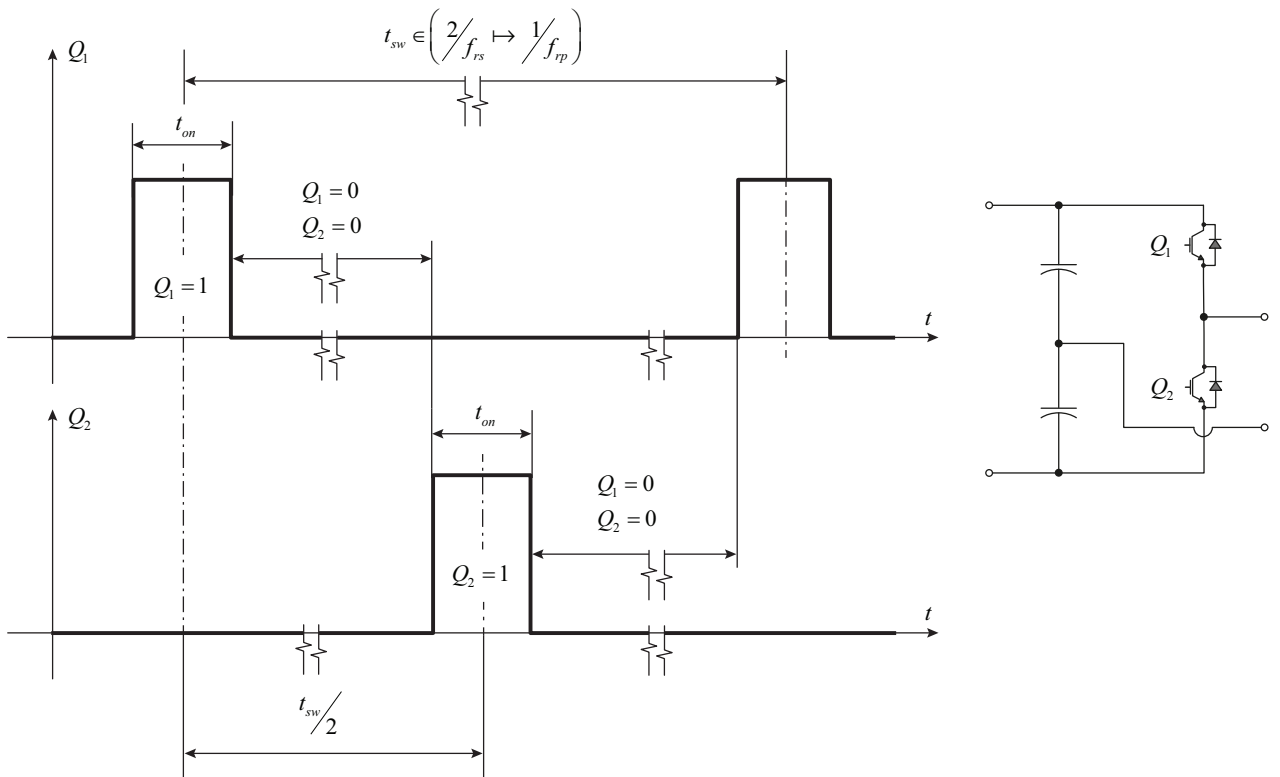


Figure 10.6: Description of the modulation law.

#### 10.2.4 Simulation results

# Chapter 11

## The Drivetrain

### 11.1 The Electrical Driver - Inverter

#### 11.1.1 General description

With the term **driver** we want to identify the part of the system which is involved into the prime-motion of the power trains, hence, the inverter and the permanent magnet synchronous motors (PMSMs).

The inverter itself is a DC/AC voltage source converter, which transform a DC voltage source into a AC fully controllable voltage source. In such a way we can control, in four quadrant mode, the motion of the PMSM.

The driver structure has been depicted in Figure 11.1. The inverter output voltage modulation is described in the Figures ??-???

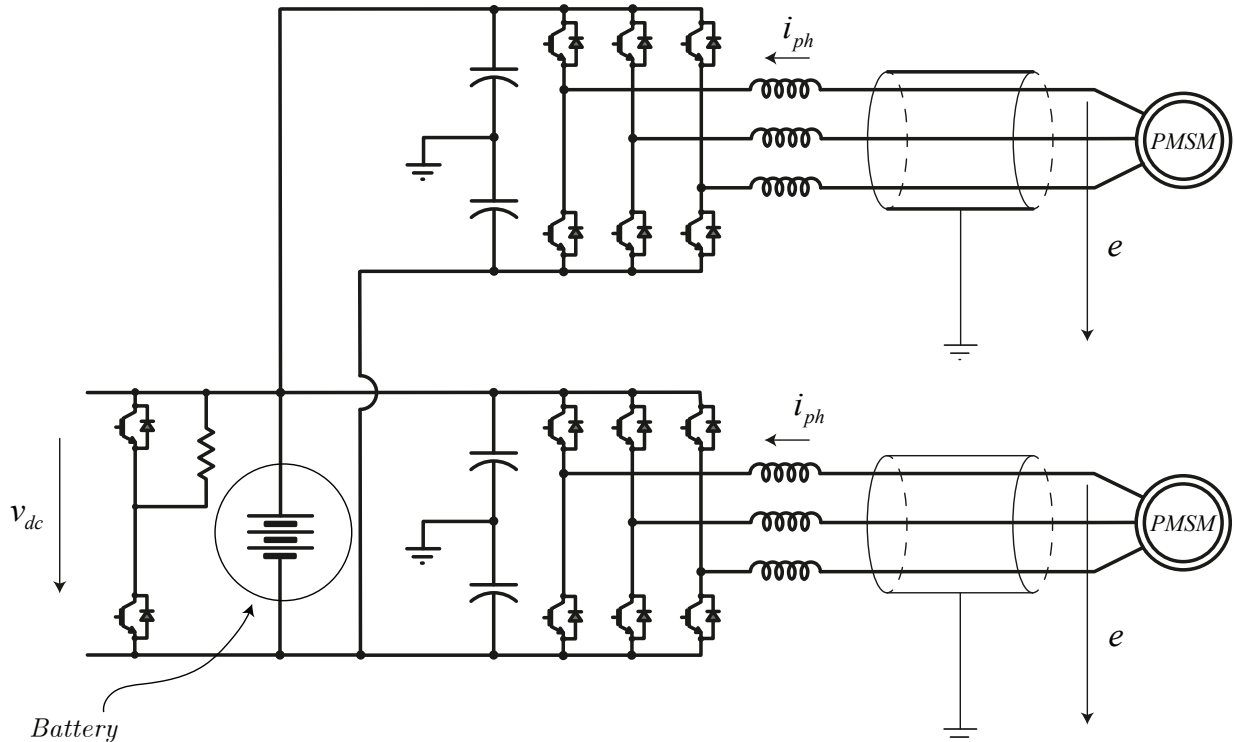


Figure 11.1: Driver description.

### 11.1.2 Space vector modulation

In this subsection a brief overview of the space vector modulation (*SVM*) is reported. Figure 11.2 depicts the voltages which a three phase inverter can actuate as function of the switches state in  $\alpha\beta$  fixed reference frame representation.

Figure 11.3 shows an example of a generic voltage actuation using a combination of adjacent state voltage vectors. The space vector hexagon can be divided into six sectors. For a given output voltage, the corresponding sector have to be identified. Once the sector is identified the “realization” of the output vector is made by a time combination of the adjacent three space vector voltages ( $\vec{v}_n$ ,  $\vec{v}_{n+1}$ , and  $\vec{v}_0$ ).

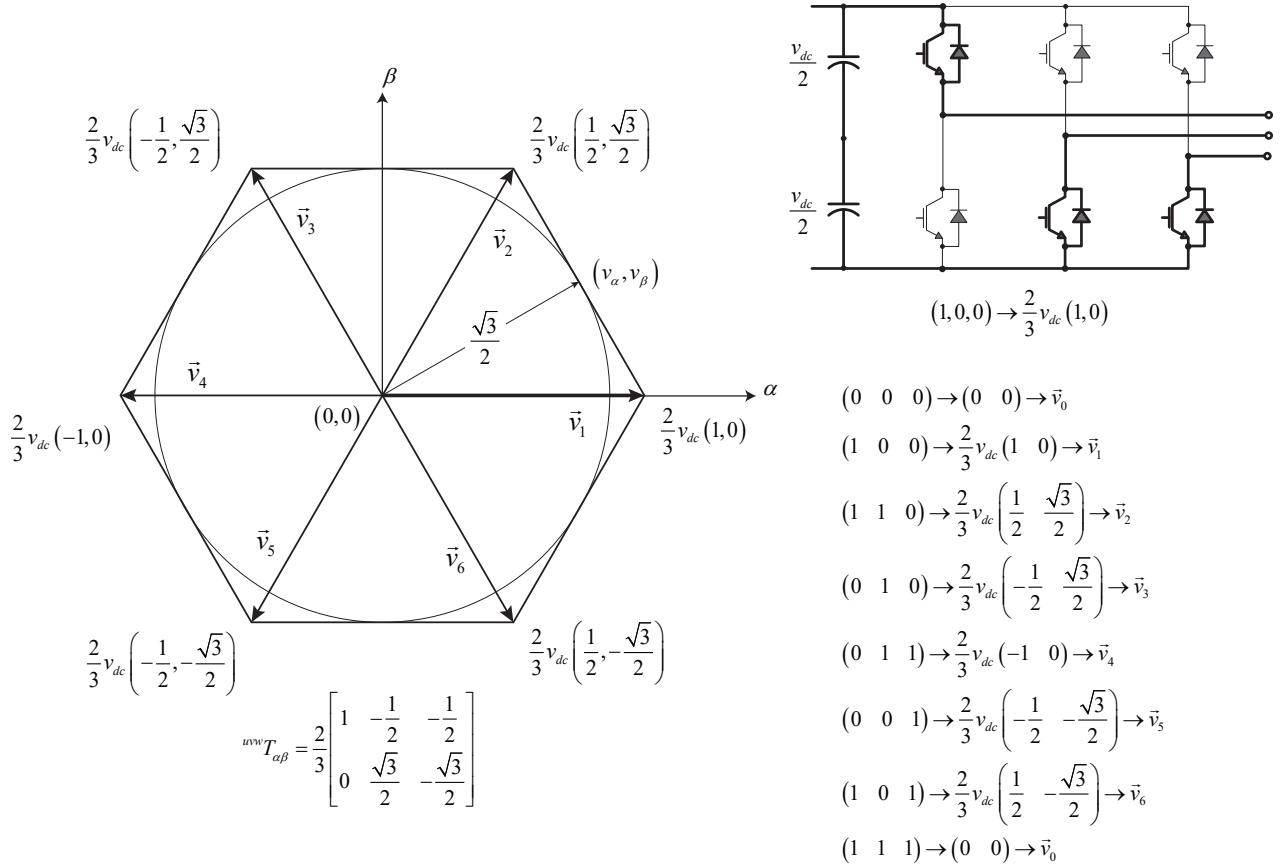


Figure 11.2: Representation of the space vector modulation and relation with inverter switches state.

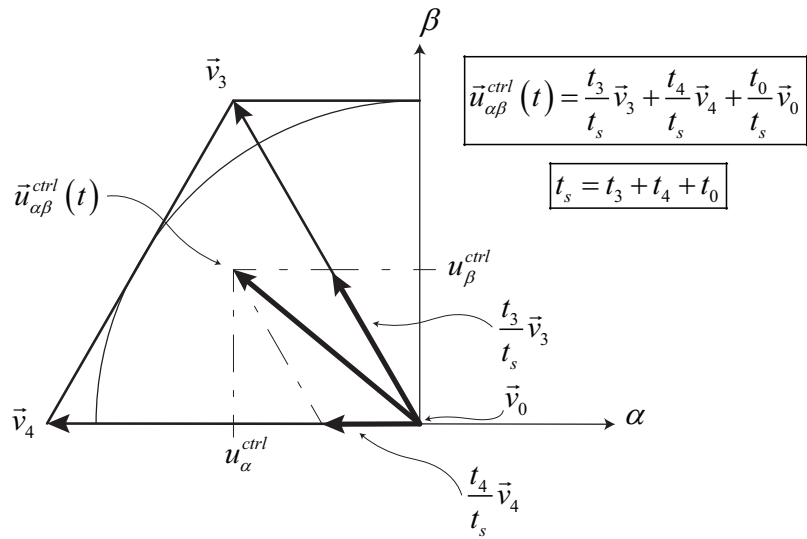


Figure 11.3: Space vector representation of a generic voltage vector  $\vec{u}_{\alpha\beta}$ .

Define  $t_s$  the switching period of the *SVM*, any vector  $\vec{v}_{\alpha\beta}$  (in some case the notation  $\vec{v}_{\xi\eta}$  is used) located in the sector  $n$  od the space vector hexagon can be “realized” by the time combination of the adjacent vectors ( $\vec{v}_n$ ,  $\vec{v}_{n+1}$ , and  $\vec{v}_0$ ), as follows

$$\vec{v}_{\alpha\beta} = \frac{t_n}{t_s} \vec{v}_n + \frac{t_{n+1}}{t_s} \vec{v}_{n+1} + \frac{t_0}{t_s} \vec{v}_0 \quad (11.1.1)$$

where  $t_n + t_{n+1} + t_0 = t_s$ .

In Figure 11.4–Figure 11.7 the relation between the state of the inverter switching bridge and the space voltage vector representation in  $\alpha\beta$  is depicted.

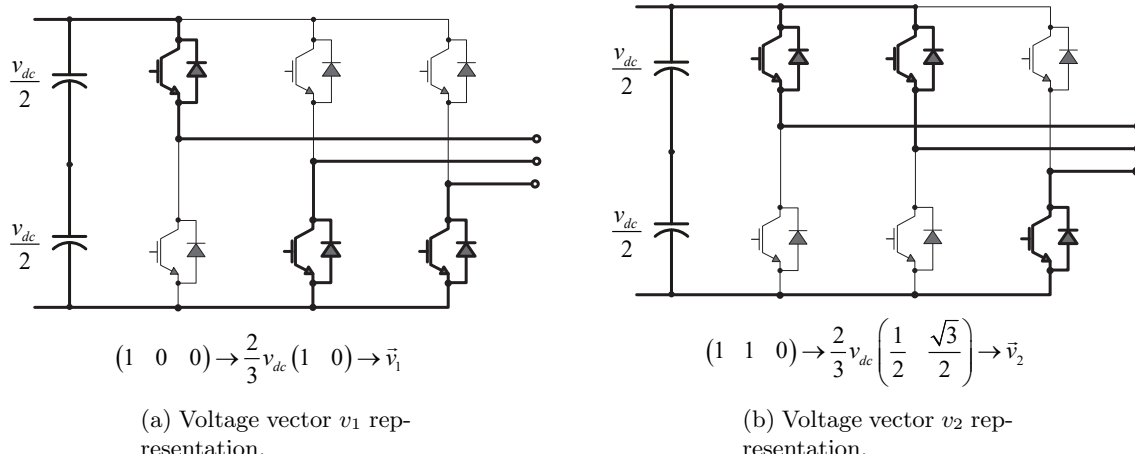
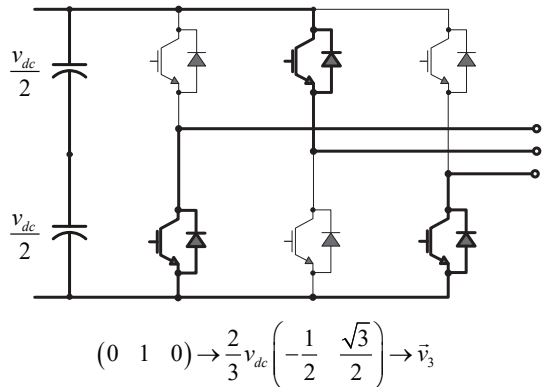
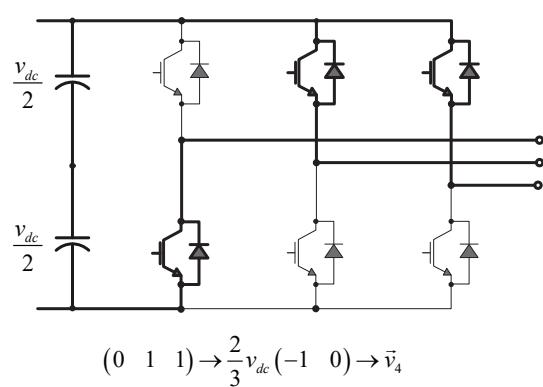


Figure 11.4: Inverter state representation of the voltages  $v_1$  and  $v_2$ .

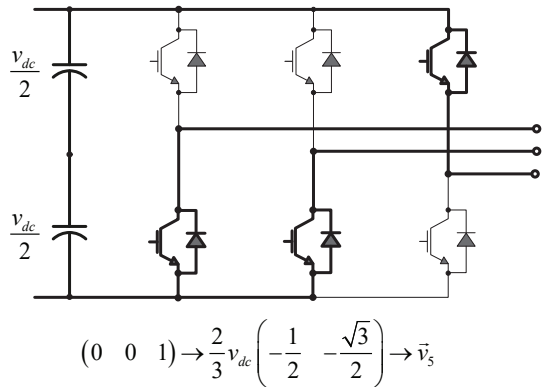


(a) Voltage vector  $v_3$  representation.

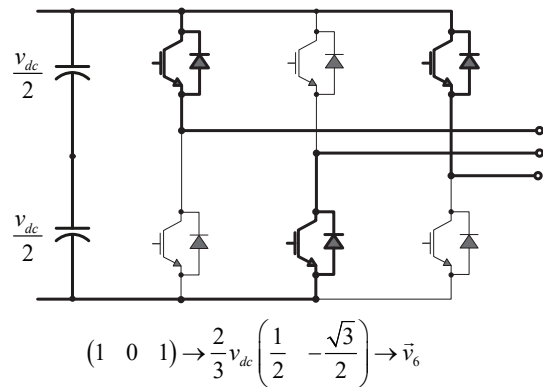


(b) Voltage vector  $v_4$  representation.

Figure 11.5: Inverter state representation of the voltages  $v_3$  and  $v_4$ .

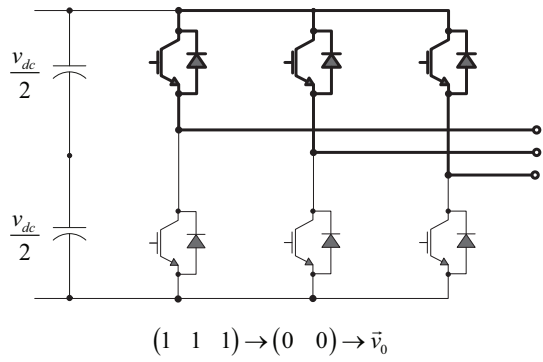


(a) Voltage vector  $v_5$  representation.

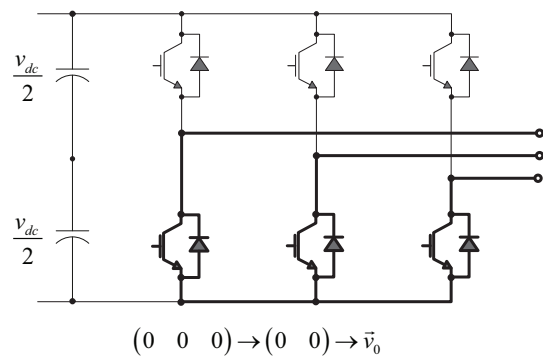


(b) Voltage vector  $v_6$  representation.

Figure 11.6: Inverter state representation of the voltages  $v_5$  and  $v_6$ .



(a) Voltage vector  $v_0$  representation - case 1.



(b) Voltage vector  $v_0$  representation - case 2.

Figure 11.7: Inverter state representations of the voltage  $v_0$ .

# Chapter 12

## Internal design of a permanent magnet synchronous machine (PMSM)

### 12.1 Preliminary dimensioning

According to the hydrostatic performance results, shown in Figure ??, the design of the PMSM, one for each drive line, shall be sized according the following constraints:

- $\hat{v}_{dc} = \hat{E}_{ph}\sqrt{3} = 800 \text{ V}$
- $\hat{\omega}_m = 3100 \text{ min}^{-1}$
- $\hat{\tau}_m = 1600 \text{ N m}$

where  $\hat{E}_{ph}$  is the maximum phase peak voltage at no-load (no-current). The constraint  $\hat{E}_{ph}$  is the maximum phase peak voltage occurs at maximum rotor speed in the case of no-load (or in general the inverter is not in the operative mode). The voltage limit  $\hat{E}_{ph}$  is correlated to the maximum DClink voltage permitted (with proper margin of safety) and the maximum phase peak voltage  $\hat{E}_{ph}$  is directly correlated to the maximum rotor speed as follows

$$\hat{E}_{ph} = p\hat{\omega}_m\hat{\psi}^M \quad (12.1.1)$$

where  $p$  is the number of pole pairs and  $\hat{\psi}^M$  is the rotor permanent magnet flux linked to the stator winding along the  $\tau/2$  region as shown in Figure 12.4. The equation of the torque as function of the phase current  $\hat{i}_q$  (here we suppose that  $\hat{i}_{ph} = \hat{i}_q$ ) is given as follows

$$\hat{\tau}_m = \frac{3}{2}p\hat{i}_q\hat{\psi}^M \quad (12.1.2)$$

Considering the following constraints

- $\hat{v}_{dc} = \hat{E}_{ph}\sqrt{3} = 800 \text{ V}$
- $\hat{\omega}_m = 3100 \text{ min}^{-1}$
- $\hat{\tau}_m = 1600 \text{ N m}$

- $D_{tg} = 41.4$

we obtain

$$\hat{\psi}^M = \frac{\hat{v}_{dc}}{\sqrt{3}p\hat{\omega}_m} = 0.356 \text{ Wb} \quad (12.1.3)$$

$$\hat{i}_q = \frac{2}{3} \frac{\hat{\tau}_m}{p\hat{\psi}^M} = \frac{2}{\sqrt{3}} \frac{\hat{\tau}_m \hat{\omega}_m}{\hat{v}_{dc}} = 750 \text{ A} \quad \text{for } \hat{v}_{dc} = 800 \text{ V} \quad (12.1.4)$$

the maximum permissible dc voltage will affect the sizing of the pmsm.

$$\hat{i}_q = \frac{2}{\sqrt{3}} \frac{\hat{\tau}_m \hat{\omega}_m}{\hat{v}_{dc}} = 750 \text{ A} \quad \text{for } \hat{v}_{dc} = 800 \text{ V} \quad (12.1.5)$$

$$\hat{i}_q = \frac{2}{\sqrt{3}} \frac{\hat{\tau}_m \hat{\omega}_m}{\hat{v}_{dc}} = 480 \text{ A} \quad \text{for } \hat{v}_{dc} = 1250 \text{ V}$$

all quantities here are in peak values (not-rms). At this stage the two fundamental quantities have been sized: a nominal current of the inverter and pmsm ( $\hat{i}_q$ ) and the nominal magnetic flux linked to the winding ( $\hat{\psi}^M$ ) which will affect the geometric sizing of the motor.

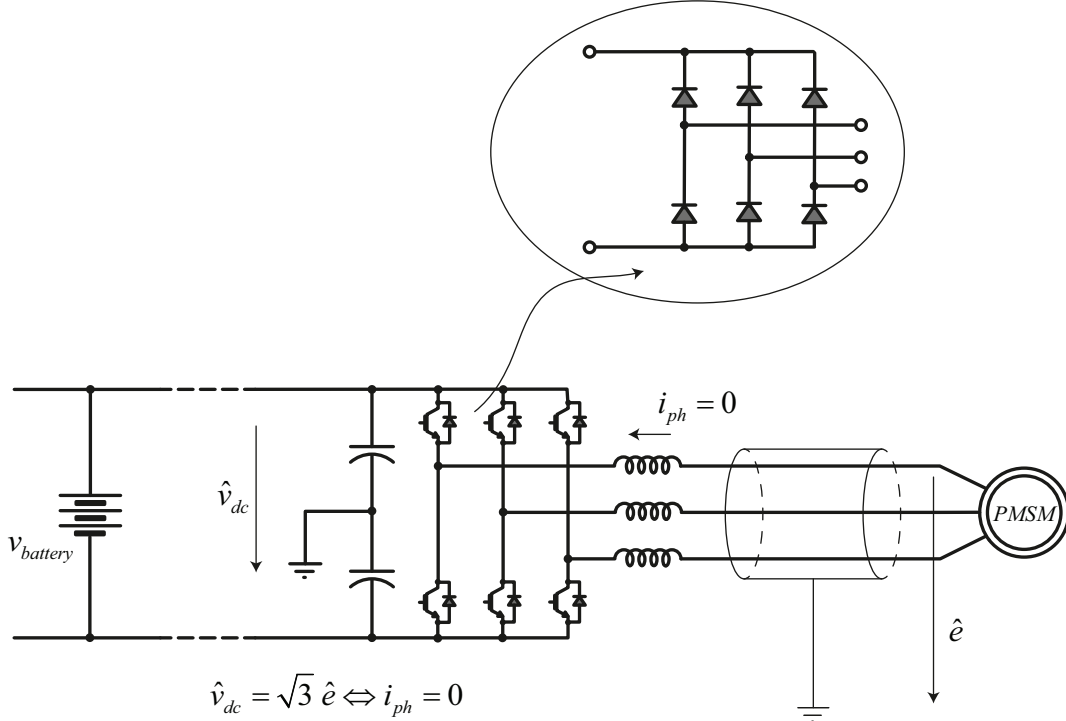


Figure 12.1: Inverter fault representation.

The two preliminaries design quantities have been calculated supposing a maximum motor terminal voltage of 566 V (line-rms). The designed current of 750 A is a value which will affect the thermal behaviour of the motor and it seems not to be of practical use. Hence the design of the PMSM will be carried out imposing an higher maximum terminal voltage

## 12.2 Basic of interior machine design

Before to start with the geometric sizing of the motor we want to select the material we intend to use.

- The stator and rotor are made by a pack of laminated crystal-oriented electrical steel: **Isovac 400 65A**.
- The rotor magnets are made by a NdFeB (**NdFe35**) considering a remain magnetic induction of  $B_r = 1.35 \text{ Wb m}^{-2}$  at the temperature of  $T = 20^\circ\text{C}$
- The stator windings are made by **aluminium** wire insulated by **mica**. Where  $\rho_{Cu} = 0.0275 \Omega \text{ mm}^2 \text{ m}^{-1}$  at  $T = 20^\circ\text{C}$ .

To size the pmsm we started from a “done” geometry (in term of rotor and stator diameters) e we scale the length of the motor according to the value of permanent magnet flux linked to the stator winding.

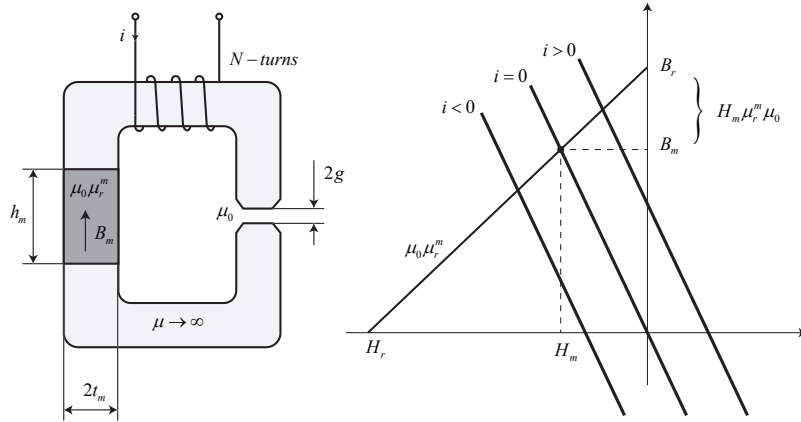


Figure 12.2: Permanent magnet operating point.

The rotor magnetic flux circuit can be approximated as reported in Figure 12.3 and Figure 12.2 by a simple magnetic circuit by the assumption of infinity permeability of the rotor and stator core. Applying Ampere's and Gauss's laws, to the case of no-current at the stator winding, we obtain the following constitutive equations<sup>1</sup>

$$2B_m h_m = B_g \frac{\pi D_r}{2p} \quad (12.2.1)$$

$$2H_m t_m + 2H_g g = 0 \quad (12.2.2)$$

from Figure 12.2 we can derive that

$$B_m = B_r + H_m \mu_r^m \mu_0 \Rightarrow H_m = \frac{B_m - B_r}{\mu_r^m \mu_0} \quad (12.2.3)$$

hence Eq. (12.2.1) can be written as follows

$$\frac{B_m - B_r}{\mu_r^m \mu_0} t_m + \frac{B_g}{\mu_0} g = 0 \Rightarrow B_g = B_r / \left( \frac{\pi D_r}{4p h_m} + \frac{g}{t_m} \mu_r^m \right) \quad (12.2.4)$$

where the permanent magnet flow linked to the stator winding is given as follows

$$\psi^M = B_g \frac{D_r \pi}{4p} L_{stack} N \quad (12.2.5)$$

<sup>1</sup>  $B_m h_m L_{stack} = B_g \frac{\pi D_r}{4p} L_{stack} \Rightarrow B_m h_m = B_g \frac{\pi D_r}{4p}$

From the air-gap magnetic field density  $B_g$  is also possible to evaluate the magnetic field density in the stator tooth and in the stator yoke applying Gauss's law. Figure 12.3a shows the behaviour of the  $\psi^M$  flow-stream along the magnetic circuit.

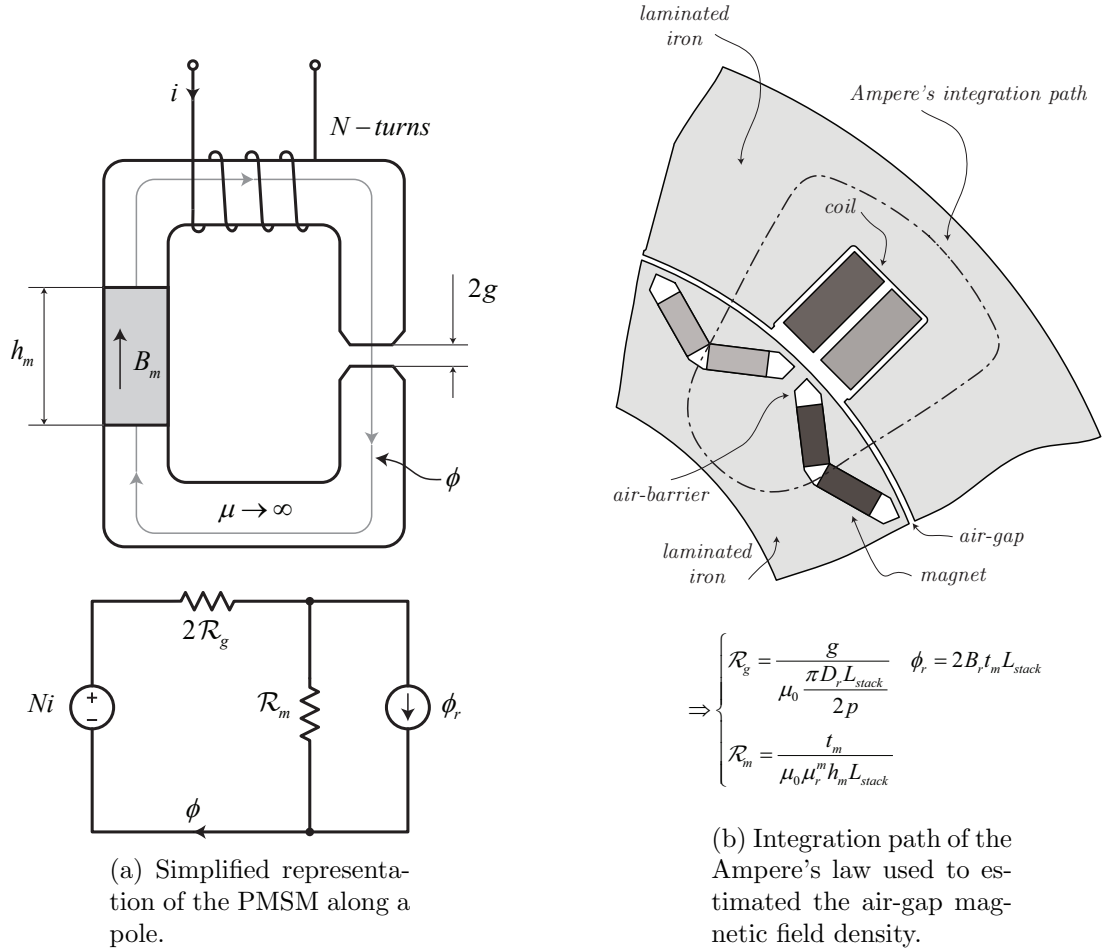


Figure 12.3: Magnetic circuit representation

The whole PMSM is depicted in Figure 12.5 which correspond to an eight poles forty eight slots. Following the drawing reported in Figure 12.4 we make a list of geometric parameters as follows

### 12.3 16 poles 12 slots solution

Figure 12.4 and Figure 12.5 show the whole geometric parameters which are involved in the design of the PMSM. The fixed geometric parameter as well as material properties are here summarized

- Number of slots  $N_{sl} = 12$ .
- Number of poles  $N_{2p} = 16$ .
- External stator diameter  $D_{se} = 640$  mm.

- Internal stator diameter  $D_{si} = 450$  mm.
- External rotor diameter  $D_{re} = 444$  mm.
- Internal rotor diameter  $D_{ri} = 310$  mm.
- Air-gap  $g = 3$  mm.
- Coil clearance  $t_{cl} = 5$  mm.
- Slot width  $d_{sl} = 50$  mm.
- Slot depth  $h_{sl} = 55$  mm.
- Single Magnet length  $h_m = 28$  mm.
- Single Magnet thickness  $t_m = 12$  mm.
- Magnet clearance  $t_{mb} = 12$  mm.
- Magnet position  $D_m = 358$  mm.
- Magnets angle  $\alpha_m = 75$  deg.
- Laminated Steel **Isovac 400 65A**.
- Coil conductor **Aluminium**.
- Magnet composition **NdFe35**.

The parameters which will be used for design are as follows

1. Length of the stator and rotor (we suppose same length)  $L_{stack}$ .
2. Number of turns  $N$ .
3. Winding connection: how coils are connected among them.
4. Class of insulation.

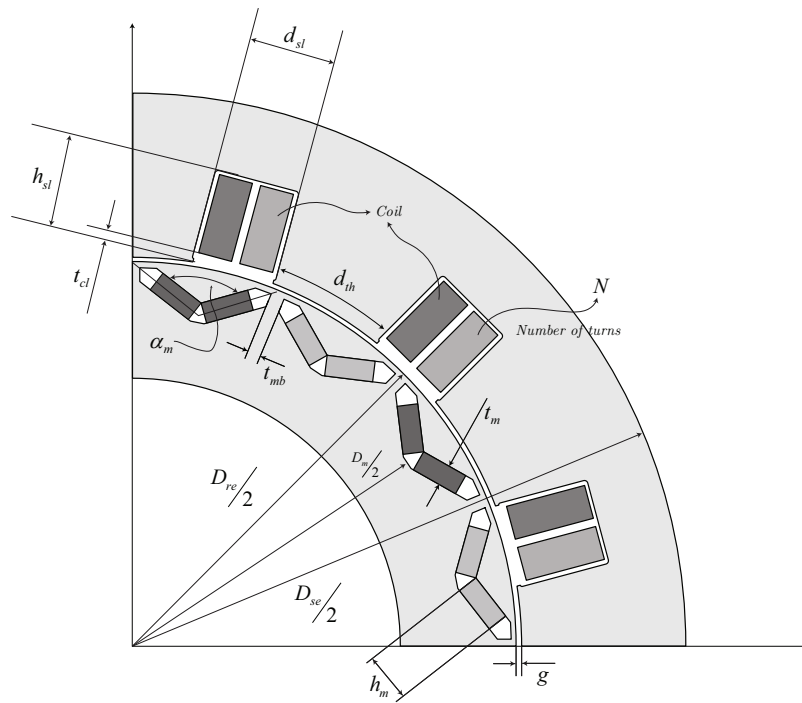


Figure 12.4: PMSM - description of the main “to be designed” geometric quantities.

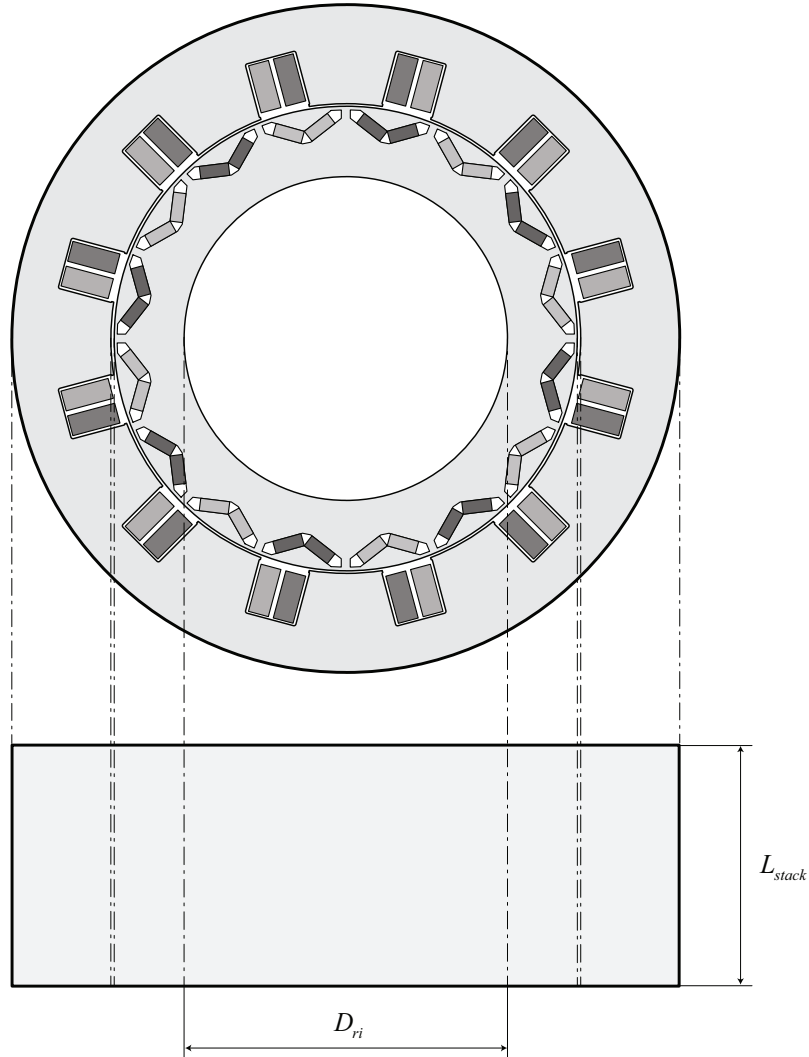


Figure 12.5: Internal permanent magnet synchronous machine.

From the above data is already possible to evaluate the flux density around the magnetic circuit of the motor, as follows (see also Figure 12.6)

#### Magnetostatic performance results at $T = 20^\circ\text{C}$

- $\tau = \frac{D_r \pi}{2p} = 87.77 \text{ mm}$  where  $D_r = \frac{D_{si} + D_{re}}{2}$
- $B_g = B_r \left( \frac{\pi D_r}{4p h_m} + \frac{g}{t_m} \mu_r^m \right)^{-1} = 0.77 \text{ Wb m}^{-2}$
- $B_{th} = B_g \frac{D_r \pi}{N_{sl} d_{th}} = 1.33 \text{ Wb m}^{-2}$
- $B_{yk} = B_g \frac{D_r \pi}{N_{sl}} \frac{1}{2h_{yk}} = 1.29 \text{ Wb m}^{-2}$

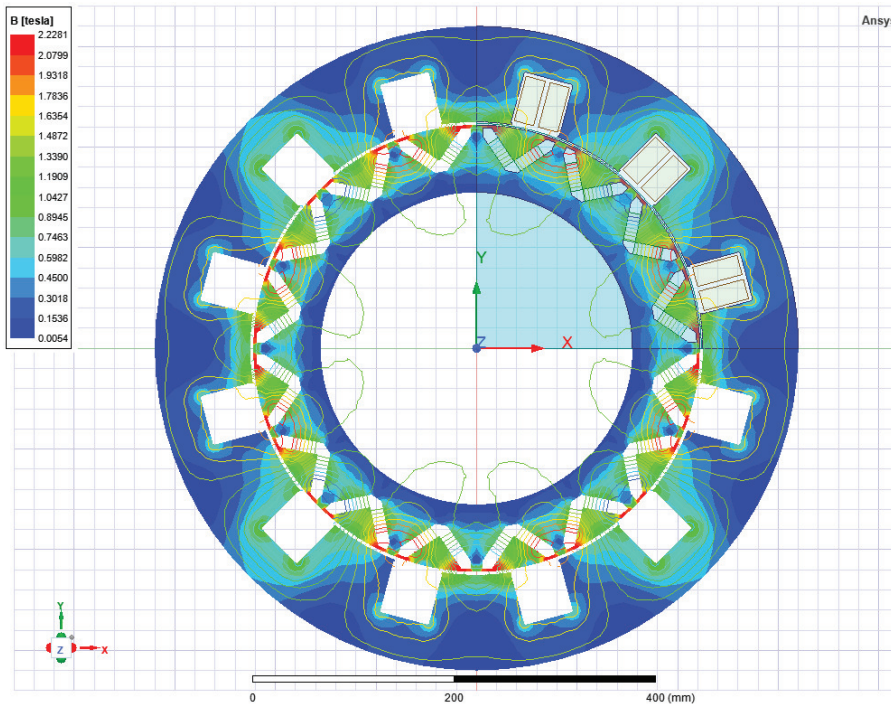


Figure 12.6: Magnetostatic analysis.

## 12.4 8 poles 12 slots solution

Figure 12.7 and Figure 12.8 show the whole geometric parameters which are involved in the design of the PMSM. The fixed geometric parameter as well as material properties are here summarized

- Number of slots  $N_{sl} = 12$ .
- Number of poles  $N_{2p} = 8$ .
- External stator diameter  $D_{se} = 640$  mm.
- Internal stator diameter  $D_{si} = 450$  mm.
- External rotor diameter  $D_{re} = 444$  mm.
- Internal rotor diameter  $D_{ri} = 310$  mm.
- Air-gap  $g = 3$  mm.
- Coil clearance  $t_{cl} = 5$  mm.
- Slot width  $d_{sl} = 55$  mm.
- Slot depth  $h_{sl} = 55$  mm.
- Single Magnet length  $h_m = 60$  mm.
- Single Magnet thickness  $t_m = 12$  mm.
- Magnet clearance  $t_{mb} = 12$  mm.

- Magnet position  $D_m = 358$  mm.
- Magnets angle  $\alpha_m = 150$  deg.
- Laminated Steel **Isovac 400 65A**.
- Coil conductor **Aluminium**.
- Magnet composition **NdFe35**.

The parameters which will be used for design are as follows

1. Length of the stator and rotor (we suppose same length)  $L_{stack}$ .
2. Number of turns  $N$ .
3. Winding connection: how coils are connected among them.
4. Class of insulation.

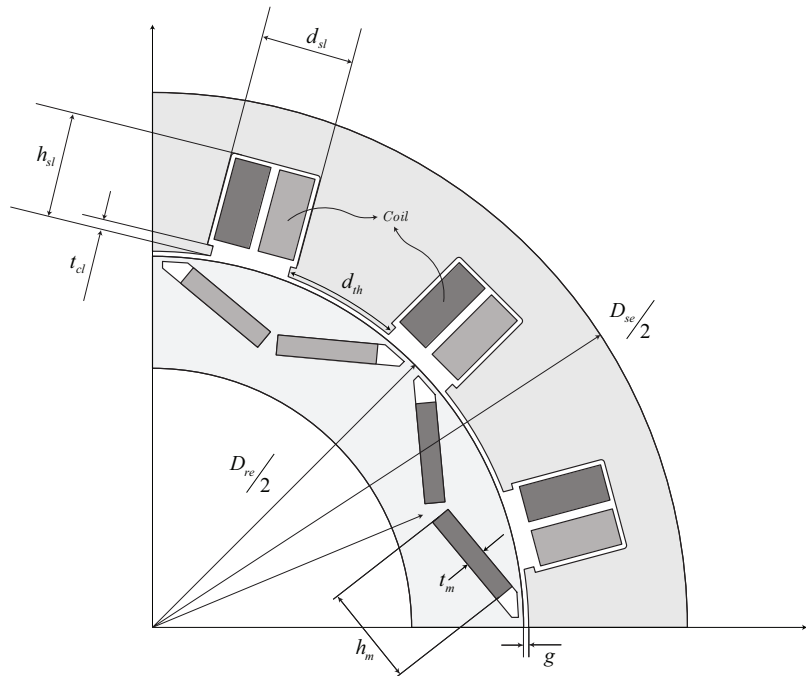


Figure 12.7: PMSM - description of the main “to be designed” geometric quantities.

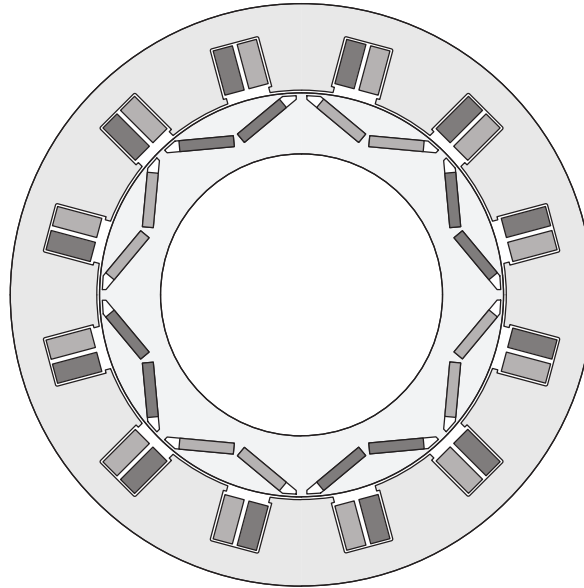


Figure 12.8: Internal permanent magnet synchronous machine.

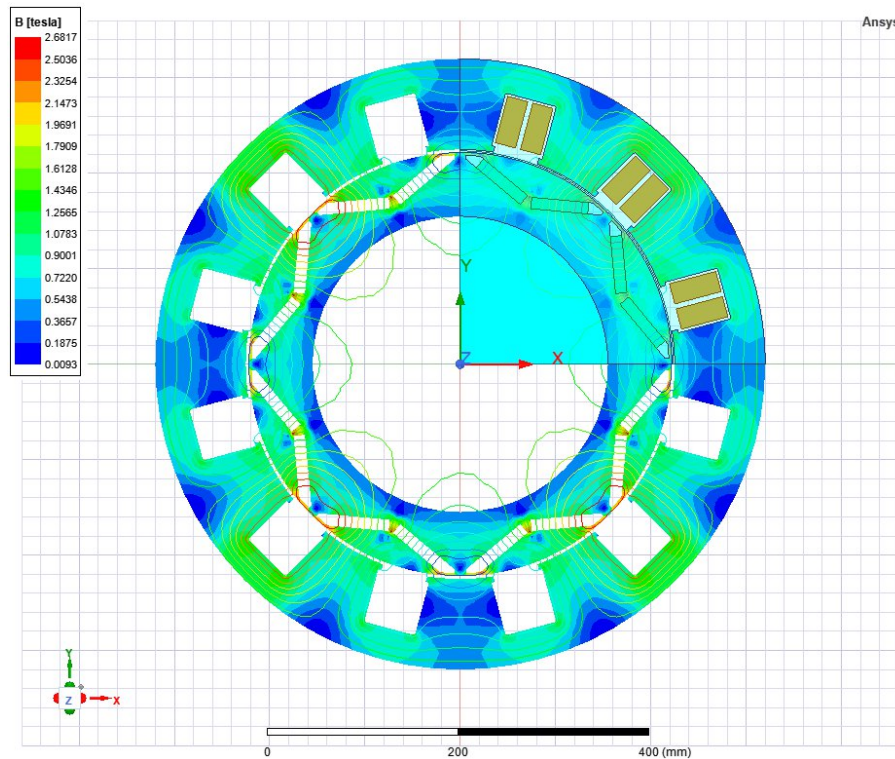


Figure 12.9: Magnetostatic Analysis.

From the above data is already possible to evaluate the flux density around the magnetic circuit of the motor, as follows (see also Figure 12.9)

#### Magnetostatic performance results at T = 20 °C

- $\tau = \frac{D_r \pi}{2p} = 175.54 \text{ mm}$  where  $D_r = \frac{D_{si} + D_{re}}{2}$

- $B_g = B_r \left( \frac{\pi D_r}{4p h_m} + \frac{g}{t_m} \mu_r^m \right)^{-1} = 0.79 \text{ Wb m}^{-2}$
- $B_{th} = B_g \frac{D_r \pi}{N_{sl}} \frac{1}{d_{th}} = 1.47 \text{ Wb m}^{-2}$
- $B_{yk} = B_g \frac{D_r \pi}{N_{sl}} \frac{1}{2h_{yk}} = 1.32 \text{ Wb m}^{-2}$

## 12.5 16 poles 12 slots solution

Figure 16.3 and Figure 16.3 show the whole geometric parameters which are involved in the design of the PMSM. The fixed geometric parameter as well as material properties are here summarized

- Number of slots  $N_{sl} = 12$ .
- Number of poles  $N_{2p} = 16$ .
- External stator diameter  $D_{se} = 640 \text{ mm}$ .
- Internal stator diameter  $D_{si} = 450 \text{ mm}$ .
- External rotor diameter  $D_{re} = 444 \text{ mm}$ .
- Internal rotor diameter  $D_{ri} = 310 \text{ mm}$ .
- Air-gap  $g = 3 \text{ mm}$ .
- Coil clearance  $t_{cl} = 5 \text{ mm}$ .
- Slot width  $d_{sl} = 50 \text{ mm}$ .
- Slot depth  $h_{sl} = 55 \text{ mm}$ .
- Single Magnet length  $h_m = 28 \text{ mm}$ .
- Single Magnet thickness  $t_m = 12 \text{ mm}$ .
- Magnet clearance  $t_{mb} = 12 \text{ mm}$ .
- Magnet position  $D_m = 358 \text{ mm}$ .
- Magnets angle  $\alpha_m = 75 \text{ deg}$ .
- Laminated Steel **Isovac 400 65A**.
- Coil conductor **Aluminium**.
- Magnet composition **NdFe35**.

The parameters which will be used for design are as follows

1. Length of the stator and rotor (we suppose same length)  $L_{stack}$ .
2. Number of turns  $N$ .
3. Winding connection: how coils are connected among them.

4. Class of insulation.

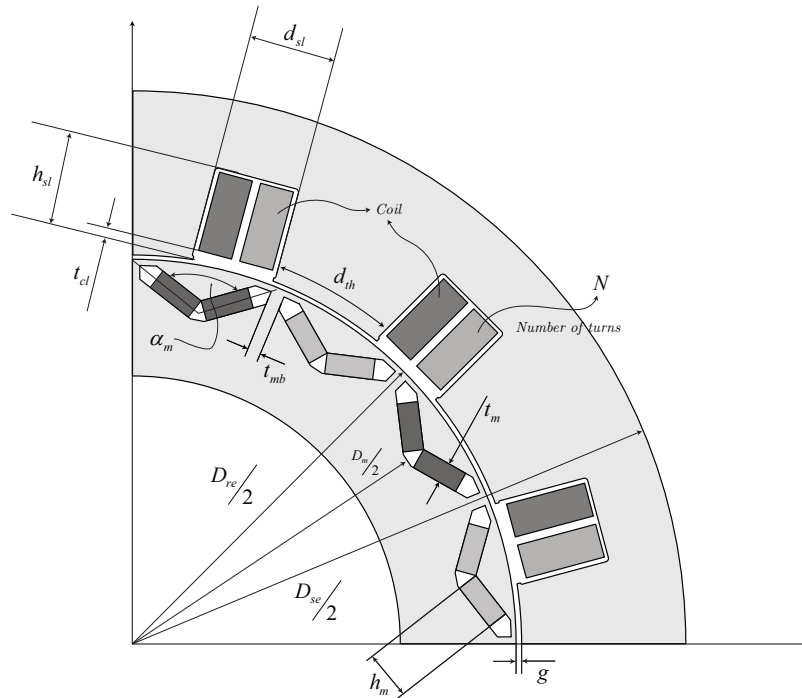


Figure 12.10: PMSM - description of the main “to be designed” geometric quantities.

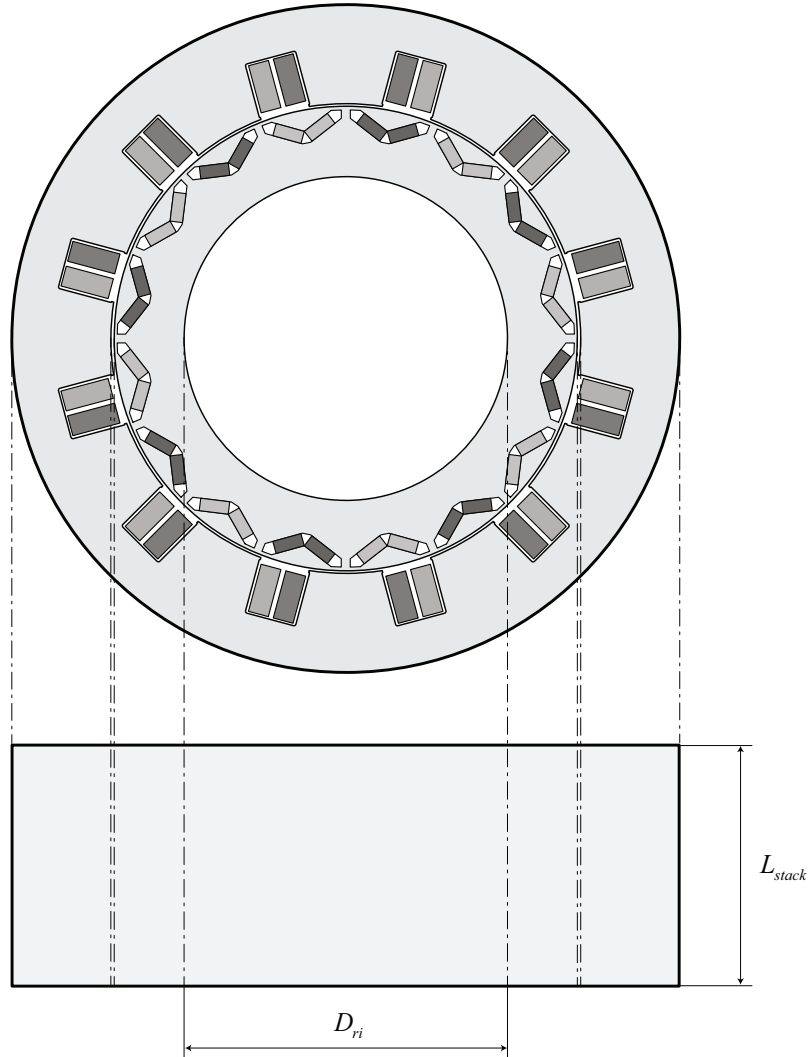


Figure 12.11: Internal permanent magnet synchronous machine.

From the above data is already possible to evaluate the flux density around the magnetic circuit of the motor, as follows (see also Figure 16.3)

#### Magnetostatic performance results at $T = 20^\circ\text{C}$

- $\tau = \frac{D_r \pi}{2p} = 87.77 \text{ mm}$  where  $D_r = \frac{D_{si} + D_{re}}{2}$
- $B_g = B_r \left( \frac{\pi D_r}{4p h_m} + \frac{g}{t_m} \mu_r^m \right)^{-1} = 0.77 \text{ Wb m}^{-2}$
- $B_{th} = B_g \frac{D_r \pi}{N_{sl} d_{th}} = 1.33 \text{ Wb m}^{-2}$
- $B_{yk} = B_g \frac{D_r \pi}{N_{sl}} \frac{1}{2h_{yk}} = 1.29 \text{ Wb m}^{-2}$

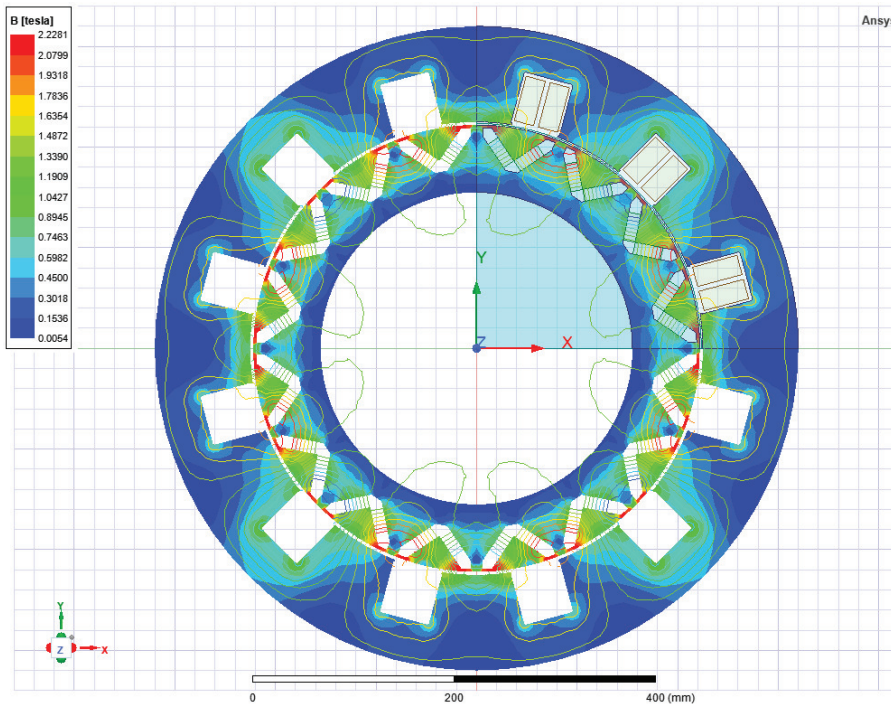


Figure 12.12: Magnetostatic analysis.

## 12.6 PMSM thermal model

The problem of temperature rise is twofold: first in motor, adequate heat removal is ensured by convection in air, conduction through the fastening surfaces of the machine and radiation to ambient. In machines with a high power densities, direct cooling methods can also be applied. Sometimes even the winding of the machine is made of copper pipe, though which the coolant flows during operation of the machine. The heat transfer of electrical machines can be analyzed adequately with a fairly simple equation for heat and fluid transfer. The most important factor in thermal design is, however, the temperature of ambient fluid, as it determines the maximum temperature rise with the heat tolerance of the insulation.

Second, in addition to the question of heat removal, the distribution of heat in different parts of the machine also has to be considered. This is a problem of heat diffusion, which is a complicated three-dimensional problem involving numerous elements such as the question of heat transfer from conductors over the insulation to the stator frame. The distribution of heat in the machine can be calculated when the distribution of losses in different part of the machine and the heat removal power are known. In transient, the heat is distributed completely differently than in the stationary state. It is possible to overload the motor considerably for a short period of time by storing the excess heat in the heat capacity of the machine which is function of the whole mass and materials.

The lifetime of the insulation can be estimated by statistical methods only.

## 12.7 Power losses

Power losses in electrical machines are composed of the following elements:

- resistive losses in stator and rotor conductor. In PMSM where no conductors are present

a residual amount of power losses is still available.

- iron losses in the magnetic circuit
- additional losses
- mechanical losses

Resistive losses in conductor are sometimes called Joule losses or copper losses, and therefore the subscript Cu is used for resistive losses.

### 12.7.1 Resistive losses (Copper power losses)

Resistive losses in a winding with  $m$  phases and current  $I$  are

$$P_{Cu} = mI^2R_{ac} \quad (12.7.1)$$

where  $R_{ac}$  is the resistance of the phase winding in AC mode where skin effect is taken into account, in fact for high frequency application the phase resistance at nominal frequency can be really different from the valued measured at DC.

### 12.7.2 Losses in iron circuit

In a PMSM the stator magnetic circuit experiences a sinusoidal flux which frequency depends on the rotation speed and on the number of pole pairs. The magnetic circuit of both stator and rotor are made by the packing of thin electrical insulated sheet (**magnetic sheet**).

The common thicknesses of the magnetic sheets are 0.2, 0.35, 0.5, 0.65, 1mm. Losses in an iron circuit are two different types, namely hysteresis losses and eddy current losses. The curves in Figure 12.13 illustrate half of a hysteresis loop for a magnetic material. Hysteresis in a material causes losses in an alternating field. First, a power loss caused by hysteresis will be investigated in iron, see Figure 12.13. When  $H$  increases from zero at point 1 to  $H_{max}$  at point 2, an energy per volume  $w$  absorbed in a unit volume is

$$w_1 = \int_{-B_r}^{B_{max}} HdB. \quad (12.7.2)$$

Correspondingly, when  $H \rightarrow 0$ , the dissipated energy is

$$w_2 = \int_{B_{max}}^{B_r} HdB. \quad (12.7.3)$$

The total hysteresis energy is calculated as a line integral, when the volume of the object is  $V$

$$W_{hy} = V \oint HdB. \quad (12.7.4)$$

The hysteresis energy of Eq. (12.7.4) is obtained by travelling around the hysteresis loop. With an alternating current, the loop is circulated constantly, and therefore the hysteresis dissipation power  $P_{hy}$  depends on the frequency  $f$ . When the area of the curve describes the hysteresis energy per volume  $w_{hy}$ , we obtain for the hysteresis power losses in volume  $V$

$$P_{hy} = fVw_{hy}. \quad (12.7.5)$$

Empirical equations yield an approximation for the hysteresis loss

$$P_{hy} = \eta V f(B_{max})^n \quad (12.7.6)$$

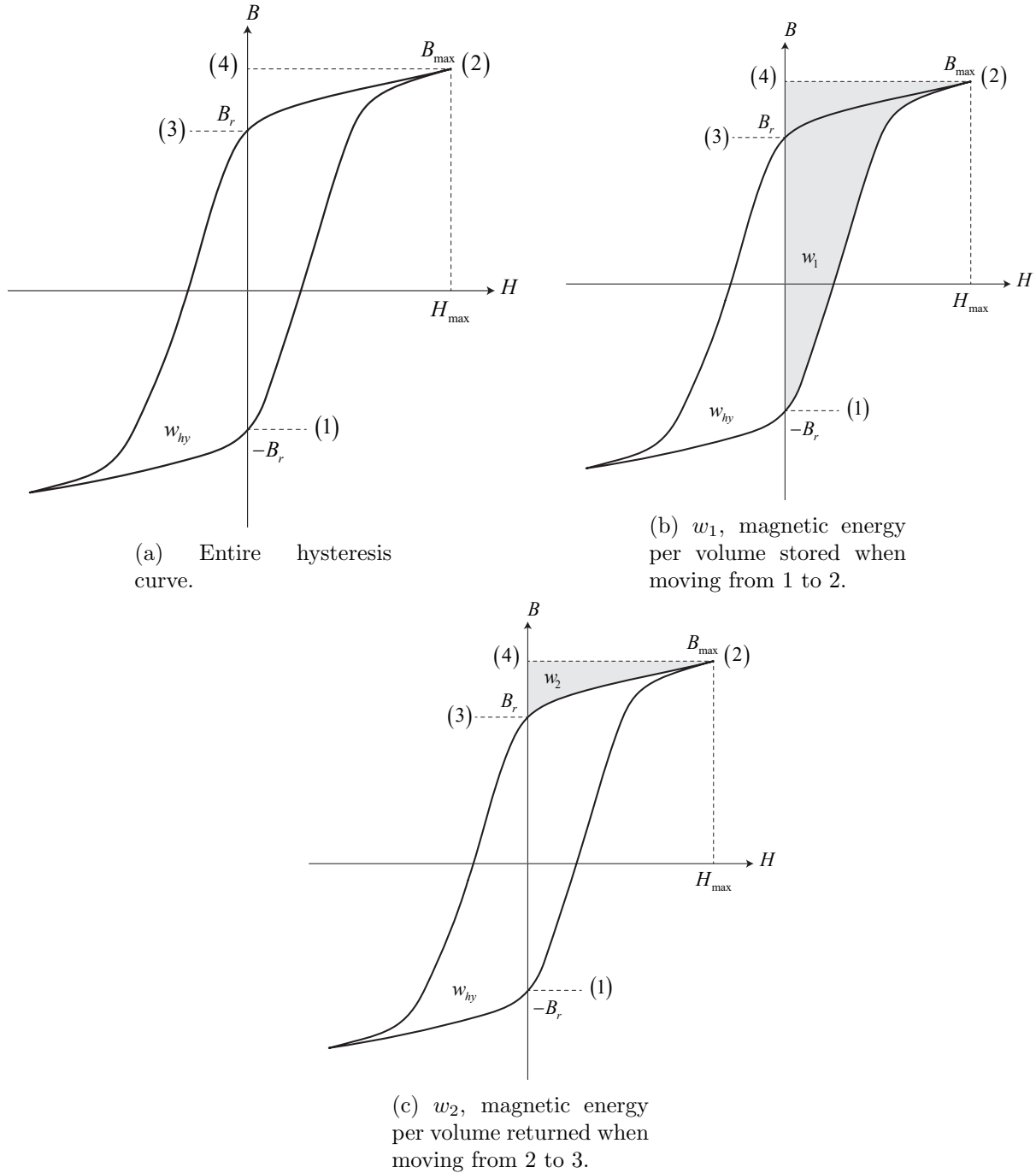


Figure 12.13: Determination of hysteresis loss.

where the exponential  $n$  varies typically over [1.5, 2.5],  $\eta$  being an empirical constant.

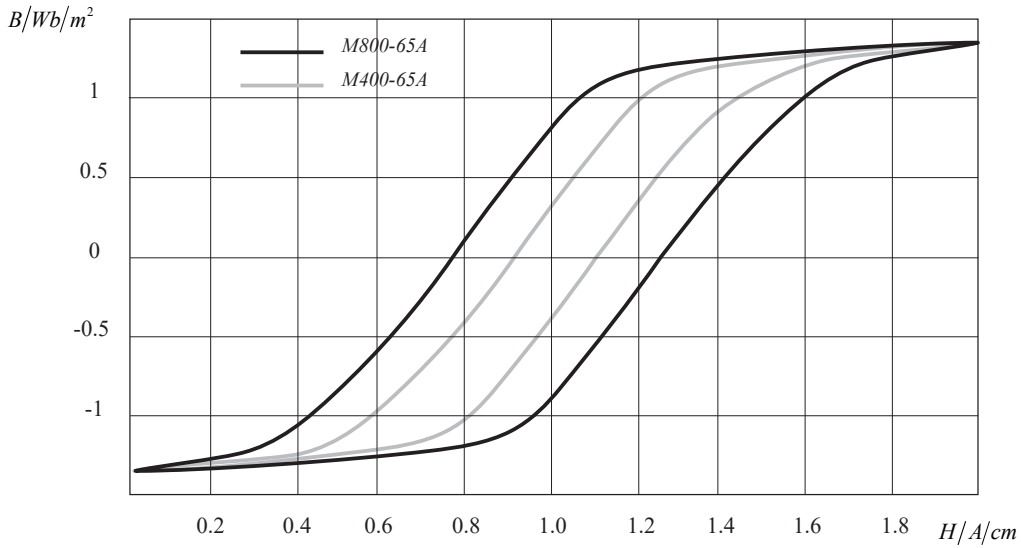


Figure 12.14: Approximate hysteresis curves of magnetic sheets.  $M400-65A$  contains more silicon than  $M800-65A$ , which is a common material in small motors.

In the case of an alternating flux in the iron core, the alternation of the flux induces voltages in the conductive core material. As a result, eddy currents occur in the core. These currents tend to resist changes in the flux. In solid objects, the eddy currents become massive and effectively restrict the flux from penetrating the material. The effects of the eddy currents is limited by using lamination or high resistivity compounds instead of solid ferromagnetic metal cores. Figure 12.15 depicts the hysteresis curves of two different magnetic sheets used in lamination.

Although magnetic cores are made of sheet, a thin sheet also enables eddy currents to occur when the flux alternates. The case of Figure 12.15, in which an alternating flux penetrates the core laminate, will now be investigated.

If a maximum flux density  $\hat{B}_m$  passes through the region 12341, the peak value for the flux of a parallelogram (dashed line) is obtained with the notation of Figure 12.15

$$\hat{\Psi} = 2hx\hat{B}_m \quad (12.7.7)$$

Since  $d \ll h$ , the effective value of the voltage induced in this path is, according to the induction law,

$$E = \frac{\omega \hat{B}_m}{\sqrt{2}} 2hx. \quad (12.7.8)$$

The resistance of the path in question depends on the specific resistivity  $\rho$ , the length of the path  $l$  and the area  $S$ . The lamination is thin compared with its other dimensions.

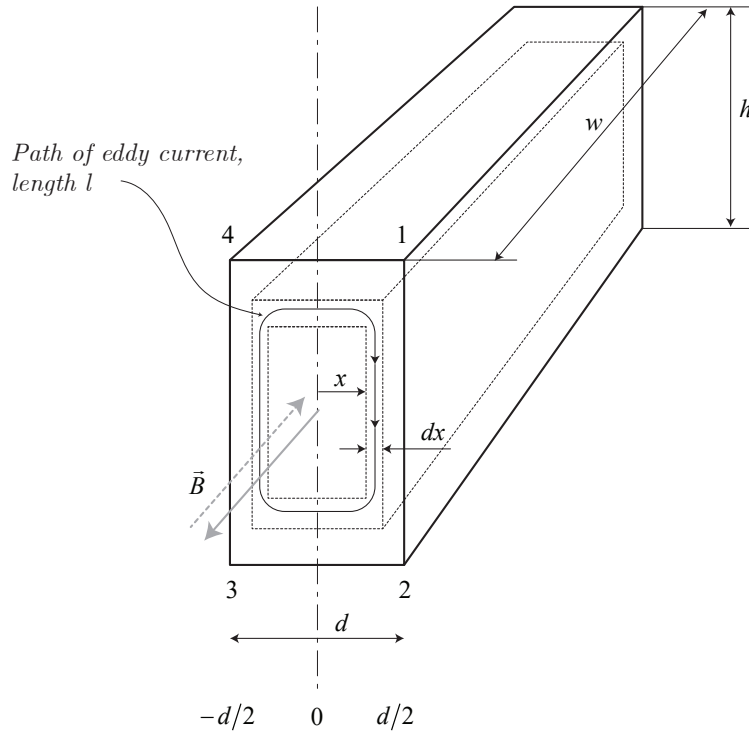


Figure 12.15: Eddy currents in a sheet material. The magnetic flux density  $B$  is varying in the directions given by the arrow and the corresponding eddy currents circulate around the magnetic flux. The eddy currents try, according to Lenz's law, to prohibit the flux from penetrating the lamination. The dashed line is for the magnetic sheet M400-65A and the solid line for the magnetic sheet M800-65A.

Hence, we may simply write for the resistance of the path  $l$

$$R = \frac{\rho l}{S} \approx \frac{2h\rho}{wdx}. \quad (12.7.9)$$

The flux density in the lamination creates a flux  $\Phi = xhB$ . The alternating flux creates a voltage  $-d\Phi/dt$  in the area observed. The induced voltage creates a current

$$dI = \frac{E}{R} = \frac{\frac{2\pi f \hat{B}_m}{\sqrt{2}} 2xh}{\frac{2h\rho}{wdx}} = \frac{2\pi f \hat{B}_m w x dx}{\sqrt{2}\rho} \quad (12.7.10)$$

the differential power loss being respectively

$$dP_{Fe,Ft} = EdI = \frac{(2\pi f \hat{B}_m)^2 w h x^2 dx}{\rho}. \quad (12.7.11)$$

The eddy current loss in the whole sheet is thus

$$P_{Fe,Ft} = \int_0^{d/2} dP_{Fe,Ft} = \frac{(2\pi f \hat{B}_m)^2 w h}{\rho} \int_0^{d/2} x^2 dx \quad (12.7.12)$$

Since  $whd = V$ , the volume of the laminate, the eddy current loss is

$$P_{Fe,Ft} = \frac{w h \pi^2 f^2 d^3 \hat{B}_m^2}{6\rho} = \frac{V \pi^2 f^2 \hat{B}_m^2}{6\rho} \quad (12.7.13)$$

Here we can see the radical influence of the sheet thickness  $d$  ( $P_{Fe} \approx d^3$ ), the peak value of the flux density  $\hat{B}_m$  and the frequency  $f$  on eddy current losses. Also, the resistivity  $\rho$  is of great significance. The measurements for silicon steel show that the eddy current loss is about 50% higher than the result given by Eq. (12.7.13).

The reason of this difference lies in the large crystal size of silicon steel. In general, we may state as the crystal size increase, the eddy current losses in the material increase as well. Eq. (12.7.13) can nevertheless be used as a guide when estimating eddy current losses for instance in the surrounding of a given operating point. Manufacturers usually give the losses of their materials per mass unit at a certain peak value of flux density and frequency, for instance  $P_{15} = 4 \text{ W kg}^{-1}$ ,  $B = 1.5 \text{ Wb m}^{-2}$ ,  $f = 50 \text{ Hz}$  or  $P_{10} = 1.75 \text{ W kg}^{-1}$ ,  $B = 1 \text{ Wb m}^{-2}$ ,  $f = 50 \text{ Hz}$ .

Figure 12.16 illustrates the iron losses in two electric sheets of equal thickness and different resistivity. The sheets are produced from the same materials as in the previous examples. The thickness of the sheets is 0.65 mm. The manufacturers usually give combined iron losses; in other words, eddy current losses and hysteresis losses are not separated. In manual calculations, the iron losses are found by dividing the magnetic circuit of the machine into  $n$  sections, in which the flux density is approximately constant. Once the masses  $m_{Fe,n}$  of the different area  $n$  have been calculated, the losses  $P_{Fe,n}$  of the different parts of the machine can be approximated as follows

$$P_{Fe,n} = P_{10} \left( \frac{\hat{B}_n}{1 \text{ Wb m}^{-2}} \right)^2 m_{Fe,n} \quad \text{or} \quad P_{Fe,n} = P_{15} \left( \frac{\hat{B}_n}{1.5 \text{ Wb m}^{-2}} \right)^2 m_{Fe,n} \quad (12.7.14)$$

Total losses can be calculated by summing the losses of different section  $n$ . A problem occurring in the calculation of losses in rotating machines is that the loss value  $P_{15}$  and  $P_{10}$  are valid only for a sinusoidally varying flux density. In rotating machines, however, pure sinusoidal flux variation never occurs in any part of the machine, but there are always rotating field that have somewhat different losses, practice, are higher than what obtained from calculation.

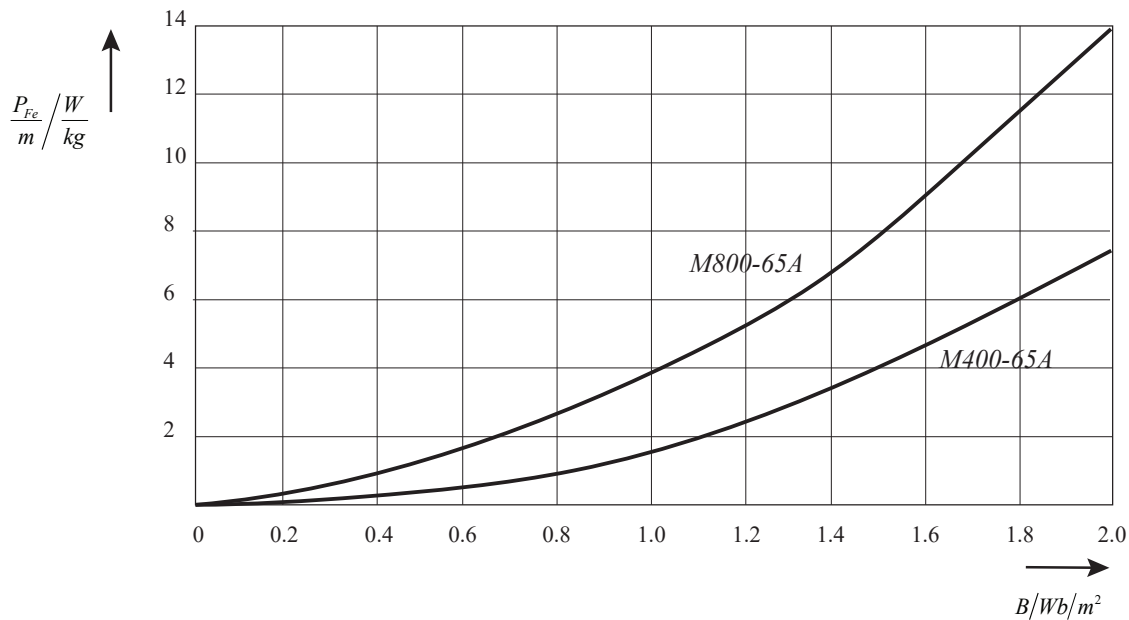


Figure 12.16: Iron losses of two different magnetic sheets at an alternating flux of 50 Hz as a function of the maximum value of flux density. The curves include both the hysteresis loss and the eddy current loss.

### 12.7.3 Additional losses

Additional losses lump together all the electromagnetic losses which are not included in the resistive losses and iron losses. They are very difficult to calculate and in general are assumed to be around 1 – 0.5% of the rated power (for the level of nominal power we are considering in this document).

### 12.7.4 Mechanical losses

Mechanical losses are consequence of bearing friction which depend on the shaft speed, bearing type, properties of the lubricant and load of the bearing. A formula for the bearing friction loss can be the following

$$P_{\nu, \text{bearing}} = \frac{1}{2} \omega_m \mu F D_{\text{bearing}} \quad (12.7.15)$$

where  $\omega_m$  is the angular frequency of the shaft,  $\mu$  the friction coefficient (for our case 0.02),  $F \approx gm_r$  the bearing load and  $D_{\text{bearing}}$  the bearing inner diameter.

### 12.7.5 Estimated temperature distribution

To extrapolate the temperature distribution inside of the motor a possible approach is to derive the thermal circuit model.

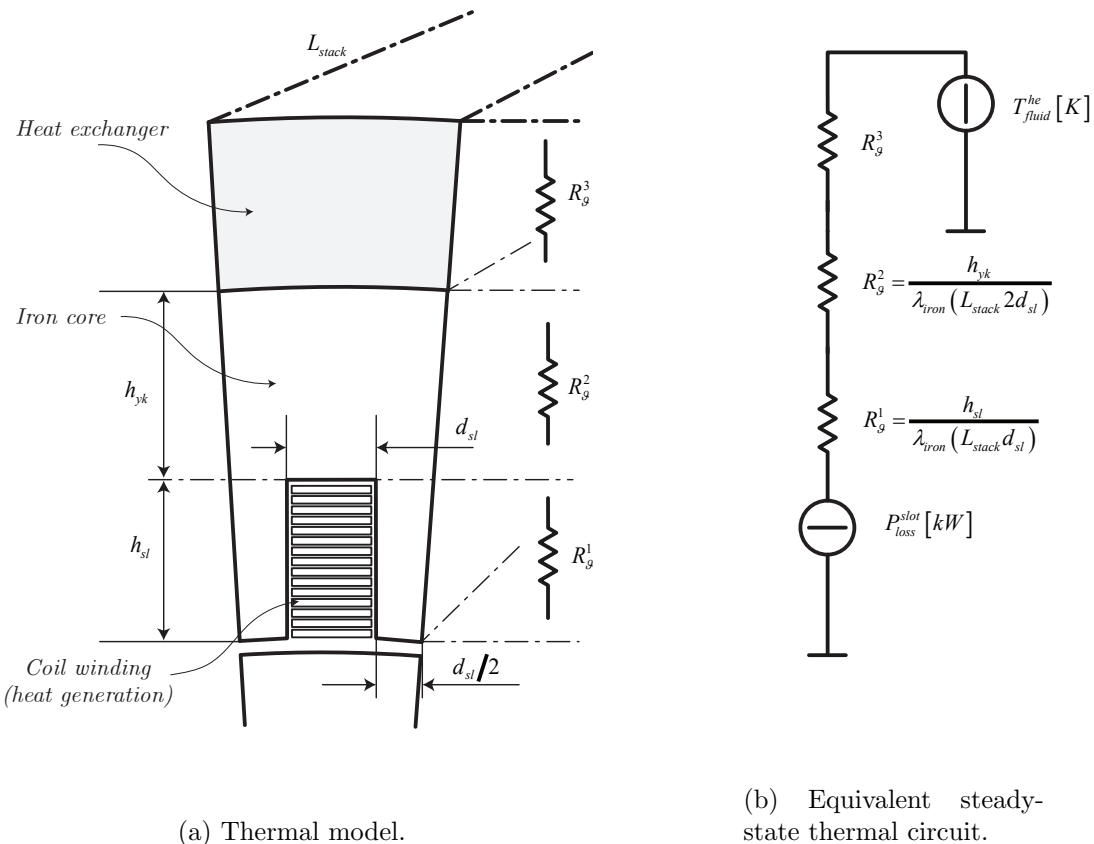


Figure 12.17: Per slot thermal model and equivalent steady-state thermal circuit of the PMSM.

To derive a thermal model we consider the smallest slide of PMSM, where heat generation and heat exchange is present. Figure 12.17a shows a possible thermal model representation, where the whole model is just the sum of 48 of these slides of motor. The quantitative analysis can be carried out considering the thermal circuit shown in Figure 12.17b where the thermal resistance are calculated from geometrical data and from the conductivity of the iron core which is around  $\lambda_{iron} = 30 \text{ W m}^{-1} \text{ K}^{-1}$ .

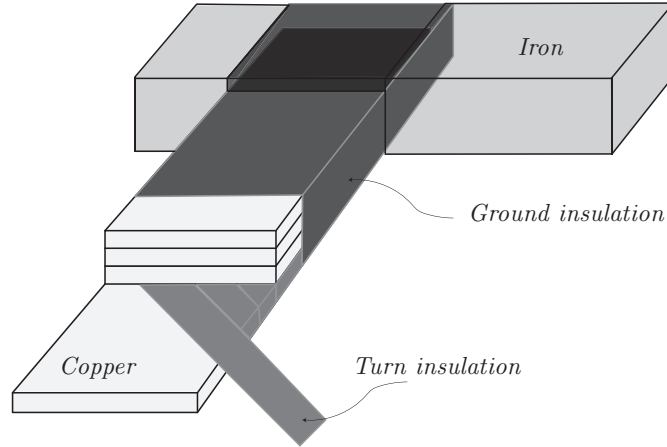


Figure 12.18: Typical coil insulation structure.

## Chapter 13

# Control based model of a PMSM

In this section the permanent magnet synchronous machine control based model is derived. The following model will be used as plant to be controlled in the model predictive and Kalman-filter application.

We can summarize the PMSM as a rotating permanent magnet coupled to three 120° shifted coils. During the rotation the time derivative of the magnetic flux linkages to the coils induces an electromagnetic force (emf) into the coils as

$$e(t) = -\frac{d\psi^r(t)}{dt}$$

. hence we can write the following generalized Kirchhoff's equations

$$\begin{cases} \vec{u}_{abc} - \mathbf{R}\vec{i}_{abc} - \frac{d\vec{\psi}_{abc}^s}{dt} = 0 \\ J\dot{\omega}_m = \tau_m - \tau_l \\ \dot{\theta} = \omega = p\omega_m \end{cases} \quad (13.0.1)$$

where  $\vec{u}_{abc} = [u_a(t) \ u_b(t) \ u_c(t)]^T$ ,  $\vec{i}_{abc} = [i_a(t) \ i_b(t) \ i_c(t)]^T$  are the three phase voltage and current vector and the magnetic flux  $\vec{\psi}_{abc}^s$  represent the stator magnetic flux linkages,  $p$  is the number of pole-pairs.

Recall that

$$\vec{u}_{abc}^s - \mathbf{R}\vec{i}_{abc}^s - \frac{d\vec{\psi}_{abc}^s}{dt} = 0 \leftrightarrow \vec{u}_{abc} - \mathbf{R}\vec{i}_{abc} - \frac{d\vec{\psi}_{abc}^s}{dt} = 0$$

The flux linkages may be written as

$$\vec{\psi}_{abc}^s = \mathbf{L}_s \vec{i}_{abc} + \vec{\psi}_{abc}^r \quad (13.0.2)$$

where  $\vec{\psi}_{abc}^r$  are the rotor flux linked to the stator generated by the rotor permanent magnets and where

$$\mathbf{L}_s = \begin{bmatrix} L_\mu + L_a - L_b \cos 2\theta & -\frac{1}{2}L_a - L_b \cos 2(\theta - \frac{\pi}{3}) & -\frac{1}{2}L_a - L_b \cos 2(\theta + \frac{\pi}{3}) \\ -\frac{1}{2}L_a - L_b \cos 2(\theta - \frac{\pi}{3}) & L_\mu + L_a - L_b \cos 2(\theta - \frac{2\pi}{3}) & -\frac{1}{2}L_a - L_b \cos 2(\theta + \pi) \\ -\frac{1}{2}L_a - L_b \cos 2(\theta + \frac{\pi}{3}) & -\frac{1}{2}L_a - L_b \cos 2(\theta + \pi) & L_\mu + L_a - L_b \cos 2(\theta + \frac{2\pi}{3}) \end{bmatrix} \quad (13.0.3)$$

is the stator inductance matrix.  $L_b$  is the anisotropic inductance term which is characteristic of internal permanent magnet machines.

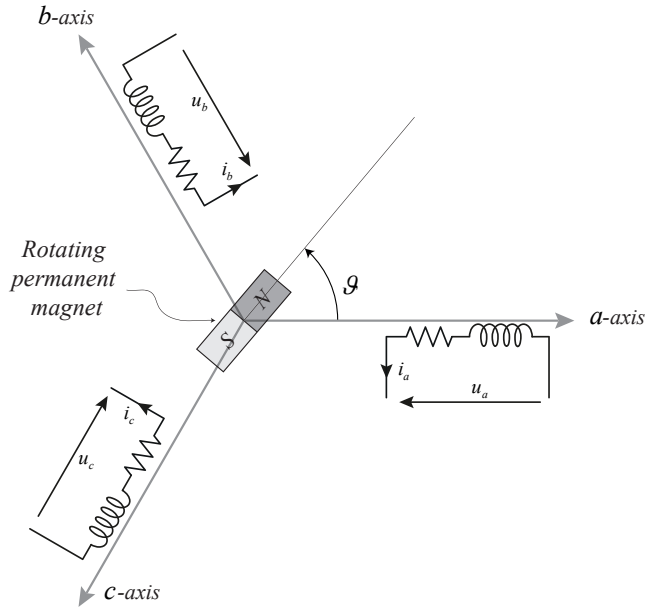


Figure 13.1: Stationary and rotating reference frame

In case of isotropic machine construction this term is null and the matrix of Eq. (13.0.3) becomes

$$\mathbf{L}_s = \begin{bmatrix} L_\mu + L_a & -\frac{1}{2}L_a & -\frac{1}{2}L_a \\ -\frac{1}{2}L_a & L_\mu + L_a & -\frac{1}{2}L_a \\ -\frac{1}{2}L_a & -\frac{1}{2}L_a & L_\mu + L_a \end{bmatrix} = \begin{bmatrix} L_s & L_m & L_m \\ L_m & L_s & L_m \\ L_m & L_m & L_s \end{bmatrix} \quad (13.0.4)$$

Where the term  $L_\mu$  is the leakage inductance and in general can be considered between one tenth and one twentieth of the synchronous inductance  $L_s \circ L_a$  and where  $L_m$  is the mutual inductance and is defined as negative value.

$$\begin{cases} \vec{u}_{abc} - \mathbf{R}\vec{i}_{abc} - \omega \frac{d\mathbf{L}_s}{d\theta} \vec{i}_{abc} - \mathbf{L}_s \frac{d\vec{i}_{abc}}{dt} - \frac{d\vec{\psi}_{abc}^r}{dt} = 0 \\ J\dot{\omega}_m = \tau_m - \tau_l \\ \dot{\vartheta} = \omega = p\omega_m \end{cases} \quad (13.0.5)$$

where

$$\begin{cases} \psi_a^r(t) = \Psi^M \cos(\theta) \\ \psi_b^r(t) = \Psi^M \cos(\theta - \frac{2\pi}{3}) \\ \psi_c^r(t) = \Psi^M \cos(\theta + \frac{2\pi}{3}) \end{cases} \quad (13.0.6)$$

where  $\Psi^M$  is the flux linkages generated by the permanent magnet.

### 13.1 PMSM model respect to a stationary reference frame

We are considering a 3-wire system which means we can apply the Kirchhoff condition  $x_a + x_b + x_c = 0$  that means we have three (not independent) vectors which lay in a plane (2-dimensions),

hence the whole three phase system can be written by the use of only one independent vector and can be represented by two coordinates  $(\alpha, \beta)$ . Applying the coordinates transformation  $\mathbf{T}_1$  defined as follows:

$$\mathbf{T}_1 = \frac{2}{3} \begin{bmatrix} 1 & -\frac{1}{2} & -\frac{1}{2} \\ 0 & \frac{\sqrt{3}}{2} & -\frac{\sqrt{3}}{2} \end{bmatrix} \quad \mathbf{T}_1^{-1} = \begin{bmatrix} 1 & 0 \\ -\frac{1}{2} & \frac{\sqrt{3}}{2} \\ -\frac{1}{2} & -\frac{\sqrt{3}}{2} \end{bmatrix} \quad (13.1.1)$$

$$\mathbf{T}_1 \mathbf{T}_1^{-1} = \mathbf{I}_2 \quad (13.1.2)$$

where

$$\vec{x}_{\alpha\beta} = \mathbf{T}_1 \vec{x}_{abc} \quad (13.1.3)$$

and

$$\mathbf{T}_1^{-1} \vec{x}_{\alpha\beta} = \vec{x}_{abc} \quad (13.1.4)$$

A graphical representation of the  $\alpha\beta$  reference frame is depicted in Figure 13.2.

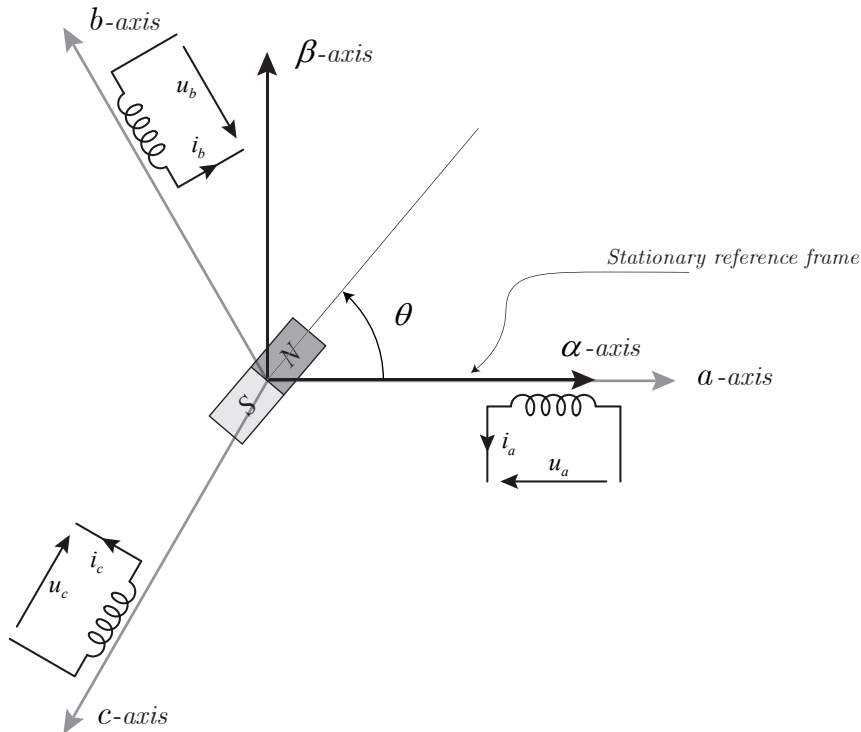


Figure 13.2: Stationary  $\alpha\beta$  reference frame

Applying the relation of Eq. (13.1.4) to the Eq. (13.0.2) we obtain

$$\mathbf{T}_1^{-1} \vec{u}_{\alpha\beta} - \mathbf{R} \mathbf{T}_1^{-1} \vec{i}_{\alpha\beta} - \omega \frac{d \mathbf{L}_s}{d\theta} \mathbf{T}_1^{-1} \vec{i}_{\alpha\beta} - \mathbf{L}_s \mathbf{T}_1^{-1} \frac{d \vec{i}_{\alpha\beta}}{dt} - \mathbf{T}_1^{-1} \frac{d \vec{\psi}_{\alpha\beta}^r}{dt} = 0$$

Multiplying left side for  $\mathbf{T}_1$  we obtain

$$\vec{u}_{\alpha\beta} - \mathbf{T}_1 \mathbf{R} \mathbf{T}_1^{-1} \vec{i}_{\alpha\beta} - \omega \frac{d}{d\theta} [\mathbf{T}_1 \mathbf{L}_s \mathbf{T}_1^{-1}] \vec{i}_{\alpha\beta} - \mathbf{T}_1 \mathbf{L}_s \mathbf{T}_1^{-1} \frac{d \vec{i}_{\alpha\beta}}{dt} - \frac{d \vec{\psi}_{\alpha\beta}^r}{dt} = 0$$

which results as follows

$$\vec{u}_{\alpha\beta} - \mathbf{R}^{\alpha\beta} \vec{i}_{\alpha\beta} - \omega \frac{d\mathbf{L}_s^{\alpha\beta}}{d\theta} \vec{i}_{\alpha\beta} - \mathbf{L}_s^{\alpha\beta} \frac{d\vec{i}_{\alpha\beta}}{dt} - \frac{d\vec{\psi}_{\alpha\beta}^r}{dt} = 0 \quad (13.1.5)$$

where

$$\frac{d\vec{\psi}_{\alpha\beta}^r}{dt} = \omega \begin{bmatrix} 0 & -1 \\ 1 & 0 \end{bmatrix} \vec{\psi}_{\alpha\beta}^r$$

in fact from Eq. (13.0.6) we can write as follows

$$\begin{cases} \psi_{\alpha}^r(t) = \Psi^M \cos \theta \\ \psi_{\beta}^r(t) = \Psi^M \sin \theta \end{cases} \quad (13.1.6)$$

which results in the following set of equations

$$\begin{cases} \vec{u}_{\alpha\beta} - \mathbf{R}^{\alpha\beta} \vec{i}_{\alpha\beta} - \omega \frac{d\mathbf{L}_s^{\alpha\beta}}{d\theta} \vec{i}_{\alpha\beta} - \mathbf{L}^{\alpha\beta} \frac{d\vec{i}_{\alpha\beta}}{dt} - \vec{\psi}_{\alpha\beta}^r = 0 \\ \frac{d\vec{\psi}_{\alpha\beta}^r}{dt} = \omega \begin{bmatrix} 0 & -1 \\ 1 & 0 \end{bmatrix} \vec{\psi}_{\alpha\beta}^r \\ J\dot{\omega} = \tau_m - \tau_l \\ \dot{\theta} = \omega \end{cases} \quad (13.1.7)$$

where

$$\mathbf{L}_s^{\alpha\beta} = \begin{bmatrix} L_\mu + \frac{3}{2}(L_a - L_b \cos 2\theta) & -\frac{3}{2}L_b \sin 2\theta \\ -\frac{3}{2}L_b \sin 2\theta & L_\mu + \frac{3}{2}(L_a + L_b \cos 2\theta) \end{bmatrix} \quad (13.1.8)$$

and

$$\frac{d\mathbf{L}_s^{\alpha\beta}}{d\theta} = 3L_b \begin{bmatrix} \sin 2\theta & -\cos 2\theta \\ -\cos 2\theta & -\sin 2\theta \end{bmatrix} \quad (13.1.9)$$

The isotropic ( $L_b = 0 \rightarrow d\mathbf{L}_s^{\alpha\beta}/d\theta = \mathbf{0}$ ) PMSM model respect to the stationary reference frame results as follows

$$\begin{cases} \vec{u}_{\alpha\beta}(t) - \mathbf{R}^{\alpha\beta} \vec{i}_{\alpha\beta}(t) - \mathbf{L}^{\alpha\beta} \frac{d\vec{i}_{\alpha\beta}(t)}{dt} - \omega(t) \begin{bmatrix} 0 & -1 \\ 1 & 0 \end{bmatrix} \vec{\psi}_{\alpha\beta}^r = 0 \\ \frac{d\vec{\psi}_{\alpha\beta}^r(t)}{dt} = \omega(t) \begin{bmatrix} 0 & -1 \\ 1 & 0 \end{bmatrix} \vec{\psi}_{\alpha\beta}^r(t) \\ \vec{\psi}_{\alpha\beta}^r(0) = [\Psi^M \ 0]^T \\ J\dot{\omega}_m(t) = \tau_m(t) - \tau_l(t) \\ \dot{\theta}(t) = \omega(t) = p\omega_m(t) \end{cases} \quad (13.1.10)$$

where  $\vec{\psi}_{\alpha\beta}^r = [\Psi^M \cos(\theta) \quad \Psi^M \sin(\theta)]^T$  and

$$\mathbf{R}^{\alpha\beta} = \begin{bmatrix} R & 0 \\ 0 & R \end{bmatrix}$$

$$\mathbf{L}^{\alpha\beta} = \begin{bmatrix} L_\alpha & 0 \\ 0 & L_\beta \end{bmatrix} = \frac{3}{2} \begin{bmatrix} L_\mu + L_a & 0 \\ 0 & L_\mu + L_a \end{bmatrix}$$

$\Psi^M$  is the amplitude of the permanent magnet flux as viewed from the stator phase winding and we assume constant.

## 13.2 PMSM model respect to a rotating reference frame

Consider now a new change of the reference frame, in particular, we are going to consider the a rotating reference frame. Let  $\theta_0$  the phase of a not stationary reference frame here called ( $dq$ ), the set of equations reported in Eq. 13.1.7 can now be written respect the rotating reference frame as follows

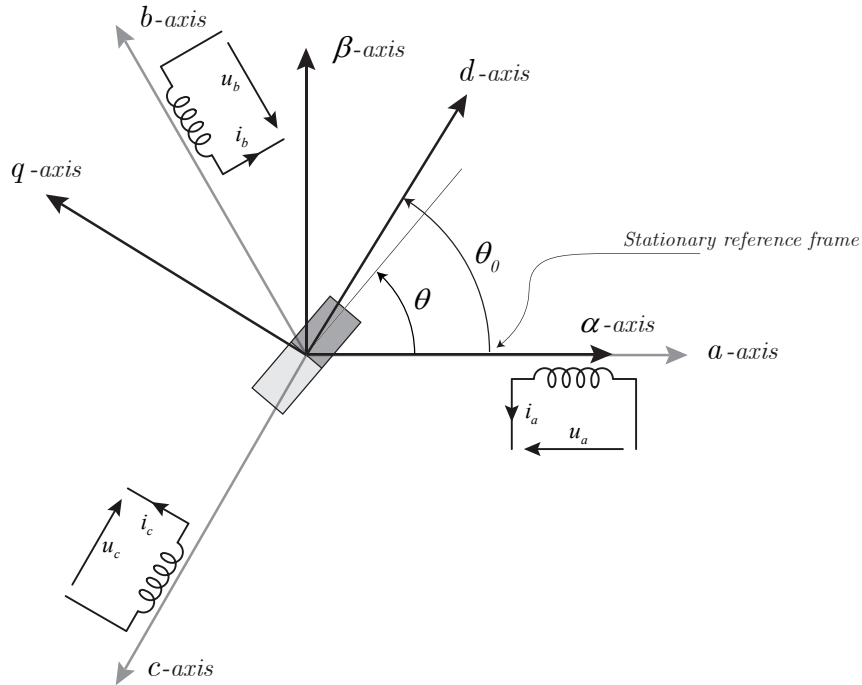


Figure 13.3: Rotating  $dq$  reference frame

$$\vec{x}_{dq} = \mathbf{T}_2 \vec{x}_{\alpha\beta} \quad (13.2.1)$$

$$\mathbf{T}_2^{-1} \vec{x}_{dq} = \vec{x}_{\alpha\beta} \quad (13.2.2)$$

where

$$\begin{aligned}\mathbf{T}_2(\theta_0) &= \begin{bmatrix} \cos(\theta_0) & \sin(\theta_0) \\ -\sin(\theta_0) & \cos(\theta_0) \end{bmatrix} \\ \mathbf{T}_2^{-1}(\theta_0) &= \begin{bmatrix} \cos(\theta_0) & -\sin(\theta_0) \\ \sin(\theta_0) & \cos(\theta_0) \end{bmatrix} \\ \mathbf{T}_2(\theta_0) \mathbf{T}_2^{-1}(\theta_0) &= \mathbf{I}_2 \\ \dot{\theta}_0 &= \omega_0\end{aligned}\tag{13.2.3}$$

Note that  $d\mathbf{T}_2(\theta_0)/dt \neq 0$

Hence applying the transformation  $\mathbf{T}_2(\vartheta_0)$  to the system represented by Eq. (13.1.7) results as follows

$$\mathbf{T}_2^{-1}\vec{u}_{dq} - \mathbf{R}^{\alpha\beta} \mathbf{T}_2^{-1}\vec{i}_{dq} - \omega \frac{d\mathbf{L}_s^{\alpha\beta}}{d\theta} \mathbf{T}_2^{-1}\vec{i}_{dq} - \mathbf{L}^{\alpha\beta} \frac{d(\mathbf{T}_2^{-1}\vec{i}_{dq})}{dt} - \frac{d(\mathbf{T}_2^{-1}\vec{\psi}_{dq}^r)}{dt} = 0$$

where

$$\frac{d\mathbf{T}_2^{-1}(\vartheta_0)}{dt} = -\omega_0 \begin{pmatrix} 0 & 1 \\ -1 & 0 \end{pmatrix} \mathbf{T}_2^{-1}(\vartheta_0)\tag{13.2.4}$$

left multiplying by  $\mathbf{T}_2$  we obtain the following terms

$$\begin{aligned}-\mathbf{T}_2\mathbf{L}^{\alpha\beta} \frac{d(\mathbf{T}_2^{-1}\vec{i}_{dq})}{dt} &= \\ = \omega_0 \mathbf{T}_2\mathbf{L}^{\alpha\beta} \begin{pmatrix} 0 & 1 \\ -1 & 0 \end{pmatrix} \mathbf{T}_2^{-1}\vec{i}_{dq} + \mathbf{T}_2\mathbf{L}^{\alpha\beta}\mathbf{T}_2^{-1} \frac{d\vec{i}_{dq}}{dt} & \\ \xrightarrow{\theta_0 \rightarrow \theta} \omega_0 \begin{pmatrix} 0 & L_d \\ -L_q & 0 \end{pmatrix} \vec{i}_{dq} + \mathbf{L}^{dq} \frac{d\vec{i}_{dq}}{dt} &\end{aligned}\tag{13.2.5}$$

where

$$\mathbf{L}^{dq} \xrightarrow{\theta_0 \rightarrow \theta} \begin{pmatrix} L_d & 0 \\ 0 & L_q \end{pmatrix} = \begin{pmatrix} L_\mu + \frac{3}{2}(L_a - L_b) & 0 \\ 0 & L_\mu + \frac{3}{2}(L_a + L_b) \end{pmatrix}\tag{13.2.6}$$

and

$$-\omega \mathbf{T}_2 \frac{d\mathbf{L}_s^{\alpha\beta}}{d\theta} \mathbf{T}_2^{-1}\vec{i}_{dq} = -\omega \mathbf{L}_m^{dq}\vec{i}_{dq} \xrightarrow{\theta_0 \rightarrow \theta} \omega \begin{pmatrix} 0 & 3L_b \\ 3L_b & 0 \end{pmatrix} \vec{i}_{dq}\tag{13.2.7}$$

Which results in the following set of equations

$$\begin{cases} \vec{u}_{dq} - \mathbf{R}^{dq} \vec{i}_{dq} - \omega \mathbf{L}_m^{dq}\vec{i}_{dq} + \omega_0 \begin{pmatrix} 0 & L_d \\ -L_q & 0 \end{pmatrix} \vec{i}_{dq} + \\ -\mathbf{L}^{dq} \frac{d\vec{i}_{dq}}{dt} + \omega_0 \begin{pmatrix} 0 & 1 \\ -1 & 0 \end{pmatrix} \vec{\psi}_{dq} + (\omega - \omega_0) \begin{pmatrix} 0 & 1 \\ -1 & 0 \end{pmatrix} \vec{\psi}_{dq}^r = 0 \\ \dot{\psi}_d^r = -(\omega - \omega_0) \psi_q^r \\ \dot{\psi}_q^r = (\omega - \omega_0) \psi_d^r \end{cases}$$

rearranging and approximating the term  $\omega \mathbf{L}_m^{dq} \vec{i}_{dq}$  to

$$-\omega \mathbf{L}_m^{dq} \vec{i}_{dq} \xrightarrow{\theta_0 \rightarrow \theta} \omega \begin{pmatrix} 0 & 3L_b \\ 3L_b & 0 \end{pmatrix} \vec{i}_{dq} = \omega \begin{pmatrix} 0 & L_q - L_d \\ L_q - L_d & 0 \end{pmatrix} \vec{i}_{dq}$$

we obtain the following set of equations

$$\left\{ \begin{array}{l} \vec{u}_{dq} - \mathbf{R}^{dq} \vec{i}_{dq} + \omega \begin{pmatrix} 0 & L_q - L_d \\ L_q - L_d & 0 \end{pmatrix} \vec{i}_{dq} + \omega_0 \begin{pmatrix} 0 & L_d \\ -L_q & 0 \end{pmatrix} \vec{i}_{dq} + \\ - \mathbf{L}^{dq} \frac{d\vec{i}_{dq}}{dt} + \omega \begin{pmatrix} 0 & 1 \\ -1 & 0 \end{pmatrix} \vec{\psi}_{dq}^r = 0 \\ \dot{\psi}_d^r = -(\omega - \omega_0) \psi_q^r \\ \dot{\psi}_q^r = (\omega - \omega_0) \psi_d^r \end{array} \right. \quad (13.2.8)$$

recall that  $3L_b = (L_q - L_d)$ .

The flux equations in Eq. (13.2.8) are derived as follows

$$\begin{aligned} \frac{d\vec{\psi}_{\alpha\beta}^r(t)}{dt} &= \omega(t) \begin{bmatrix} 0 & -1 \\ 1 & 0 \end{bmatrix} \vec{\psi}_{\alpha\beta}^r(t) \Rightarrow \\ \frac{d\mathbf{T}_2^{-1} \vec{\psi}_{dq}^r(t)}{dt} &= \omega(t) \begin{bmatrix} 0 & -1 \\ 1 & 0 \end{bmatrix} \mathbf{T}_2^{-1} \vec{\psi}_{dq}^r(t) \Rightarrow \\ -\omega_0 \begin{bmatrix} 0 & 1 \\ -1 & 0 \end{bmatrix} \mathbf{T}_2^{-1} \vec{\psi}_{dq}^r + \mathbf{T}_2^{-1} \frac{d\vec{\psi}_{dq}^r(t)}{dt} &= \omega(t) \begin{bmatrix} 0 & -1 \\ 1 & 0 \end{bmatrix} \mathbf{T}_2^{-1} \vec{\psi}_{dq}^r(t) \end{aligned} \quad (13.2.9)$$

Multiplying both terms per  $\mathbf{T}_2$  we obtain

$$\frac{d\vec{\psi}_{dq}^r(t)}{dt} = (\omega - \omega_0) \begin{bmatrix} 0 & -1 \\ 1 & 0 \end{bmatrix} \vec{\psi}_{dq}^r(t) \quad (13.2.10)$$

where  $\vec{\psi}_{dq}^r(t)$  is given as follows

$$\begin{aligned} \vec{\psi}_{dq}^r(t) &= \mathbf{T}_2 \vec{\psi}_{\alpha\beta}^r = \begin{bmatrix} \cos(\theta_0) & \sin(\theta_0) \\ -\sin(\theta_0) & \cos(\theta_0) \end{bmatrix} \begin{bmatrix} \Psi^M \cos(\theta_0) \\ \Psi^M \sin(\theta_0) \end{bmatrix} = \\ &= \Psi^M \begin{bmatrix} \cos \theta_0 \cos \theta + \sin \theta_0 \sin \theta \\ -\sin \theta_0 \cos \theta + \cos \theta_0 \sin \theta \end{bmatrix} = \Psi^M \begin{bmatrix} \cos(\theta - \theta_0) \\ \sin(\theta - \theta_0) \end{bmatrix} \end{aligned} \quad (13.2.11)$$

Considering the *DQ*-classical control, we can observe that, when the rotating reference frame (which is the frame where the controller is implemented) and the rotor reference frame are aligned ( $\theta_0 \rightarrow \theta$  and  $\omega_0 \rightarrow \omega$ ), all the inductance matrices become time-invariant and the flux components become  $\psi_q \rightarrow 0$ ,  $\psi_d \rightarrow \Psi^M$ .

The DQ-PMSM model for a generic rotating reference frame is here reported

$$\left\{ \begin{array}{l} \vec{u}_{dq} - \mathbf{R}^{dq} \vec{i}_{dq} + \omega \begin{pmatrix} 0 & L_q - L_d \\ L_q - L_d & 0 \end{pmatrix} \vec{i}_{dq} + \omega_0 \begin{pmatrix} 0 & L_d \\ -L_q & 0 \end{pmatrix} \vec{i}_{dq} \\ \quad - \mathbf{L}^{dq} \frac{d\vec{i}_{dq}}{dt} + \omega \begin{pmatrix} 0 & 1 \\ -1 & 0 \end{pmatrix} \vec{\psi}_{dq}^r = 0 \\ \dot{\psi}_d^r = -(\omega - \omega_0) \psi_q^r \\ \dot{\psi}_q^r = (\omega - \omega_0) \psi_d^r \\ \vec{\psi}_{dq}^r(0) = [\Psi^M \ 0]^T \\ J\dot{\omega}_m(t) = \tau_m(t) - \tau_l(t) \\ \dot{\vartheta}(t) = \omega(t) = p\omega_m(t) \end{array} \right. \quad (13.2.12)$$

where  $\vec{\psi}_{dq}^r = [\Psi^M \cos(\theta - \theta_0) \ \Psi^M \sin(\theta - \theta_0)]^T$  and

$$\mathbf{R}^{dq} = \begin{bmatrix} R & 0 \\ 0 & R \end{bmatrix}$$

$$\mathbf{L}^{dq} = \begin{bmatrix} L_d & 0 \\ 0 & L_q \end{bmatrix} = \begin{bmatrix} L_\mu + \frac{3}{2}L_s - \frac{L_b}{2} & 0 \\ 0 & L_\mu + \frac{3}{2}L_s + \frac{L_b}{2} \end{bmatrix}$$

$\Psi^M$  is the amplitude of the permanent magnet flux as viewed from the stator phase winding and we assume constant.

The DQ-PMSM model, when rotating reference frame coincides with the rotor reference frame  $\omega_0 \rightarrow \omega$ , can be written as follows

$$\left\{ \begin{array}{l} \vec{u}_{dq} - \mathbf{R}^{dq} \vec{i}_{dq} + \omega \begin{pmatrix} 0 & L_q \\ -L_d & 0 \end{pmatrix} \vec{i}_{dq} - \mathbf{L}^{dq} \frac{d\vec{i}_{dq}}{dt} + \omega \begin{pmatrix} 0 & 1 \\ -1 & 0 \end{pmatrix} \vec{\psi}_{dq}^r = 0 \\ \dot{\psi}_d^r = 0 \\ \dot{\psi}_q^r = 0 \\ \vec{\psi}_{dq}^r(0) = [\Psi^M \ 0]^T \\ J\dot{\omega}_m(t) = \tau_m(t) - \tau_l(t) \\ \dot{\vartheta}(t) = \omega(t) = p\omega_m(t) \end{array} \right. \quad (13.2.13)$$

where

$$\mathbf{R}^{dq} = \begin{bmatrix} R & 0 \\ 0 & R \end{bmatrix}$$

$$\mathbf{L}^{dq} = \begin{bmatrix} L_d & 0 \\ 0 & L_q \end{bmatrix} = \begin{bmatrix} L_\mu + \frac{3}{2}(L_a - L_b) & 0 \\ 0 & L_\mu + \frac{3}{2}(L_a + L_b) \end{bmatrix}$$

$\Psi^M$  is the amplitude of the permanent magnet flux as viewed from the stator phase winding and we assume constant.

### 13.3 PMSM torque derivation

#### Torque equation of the isotropic PMSM - stationary reference frame

Let  $E$  be the stored energy inside of the PMSM, it can be described as follows

$$E = \frac{3}{2} \left( \frac{1}{2} \vec{i}_{\alpha\beta}^T \mathbf{L}^{\alpha\beta} \vec{i}_{\alpha\beta} \right) + \frac{1}{2} J \omega_m^2$$

Applying the principle of energy conservation we can write

$$\frac{dE}{dt} = 0$$

$$\frac{dE}{dt} = \frac{3}{2} \left( \vec{i}_{\alpha\beta}^T \mathbf{L}^{\alpha\beta} \frac{d\vec{i}_{\alpha\beta}}{dt} \right) + J \omega_m \dot{\omega}_m = P_{in} - P_{out} - P_{loss} = 0$$

We can write

$$\begin{aligned} & \frac{3}{2} \left( \vec{i}_{\alpha\beta}^T \mathbf{L}^{\alpha\beta} \frac{d\vec{i}_{\alpha\beta}}{dt} \right) + J \omega_m \dot{\omega}_m = \\ & = \frac{3}{2} \left( \underbrace{u_\alpha i_\alpha + u_\beta i_\beta}_{=P_{in}} - \underbrace{R i_\alpha^2 - R i_\beta^2}_{=P_{loss}} - \underbrace{\omega [i_\alpha \quad i_\beta] \begin{bmatrix} 0 & -1 \\ 1 & 0 \end{bmatrix} [\psi_\alpha^r \quad \psi_\beta^r]^T}_{=\omega_m \tau_m} \right) + \omega_m \tau_m - \omega_m \tau_l \end{aligned}$$

But

$$\frac{3}{2} \left( \vec{i}_{\alpha\beta}^T \mathbf{L}^{\alpha\beta} \frac{d\vec{i}_{\alpha\beta}}{dt} \right) + J \omega_m \dot{\omega}_m = P_{in} - P_{out} - P_{loss}$$

Hence

$$P_{in} = \frac{3}{2} (u_\alpha i_\alpha + u_\beta i_\beta)$$

$$P_{out} = \omega_m \tau_l$$

$$P_{loss} = \frac{3}{2} (R i_\alpha^2 + R i_\beta^2)$$

The expression of the torque  $\tau_m$  becomes as follows

$$\tau_m = \frac{3}{2} p (\psi_\alpha^r i_\beta - \psi_\beta^r i_\alpha) \tag{13.3.1}$$

The full PMSM model respect to the stationary reference frame is as follows

$$\left\{ \begin{array}{l} \vec{u}_{\alpha\beta}(t) - \mathbf{R}^{\alpha\beta} \vec{i}_{\alpha\beta}(t) - \mathbf{L}^{\alpha\beta} \frac{d\vec{i}_{\alpha\beta}(t)}{dt} - \omega(t) \begin{bmatrix} 0 & -1 \\ 1 & 0 \end{bmatrix} \vec{\psi}_{\alpha\beta}^r = 0 \\ \frac{d\vec{\psi}_{\alpha\beta}^r(t)}{dt} = \omega(t) \begin{bmatrix} 0 & -1 \\ 1 & 0 \end{bmatrix} \vec{\psi}_{\alpha\beta}^r(t) \quad \vec{\psi}_{\alpha\beta}^r(0) = [\Psi^M \quad 0]^T \\ J\dot{\omega}_m(t) = \frac{3}{2}p \left[ \psi_{\alpha}^r(t)i_{\beta}(t) - \psi_{\beta}^r(t)i_{\alpha}(t) \right] - \tau_l(t) \\ \dot{\theta}(t) = \omega(t) = p\omega_m(t) \end{array} \right. \quad (13.3.2)$$

**Torque equation of the anisotropic PMSM - rotor reference frame**  
Let  $E$  be the stored energy inside of the PMSM, it can be described as follows

$$E = \frac{3}{2} \left( \frac{1}{2} \vec{i}_{dq}^T \mathbf{L}^{dq} \vec{i}_{dq} \right) + \frac{1}{2} J\omega_m^2$$

Applying the principle of energy conservation we can write

$$\begin{aligned} \frac{dE}{dt} &= 0 \\ \frac{dE}{dt} &= \frac{3}{2} \left( \vec{i}_{dq}^T \mathbf{L}^{dq} \frac{d\vec{i}_{dq}}{dt} \right) + J\omega_m \dot{\omega}_m = P_{in} - P_{out} - P_{loss} = 0 \end{aligned}$$

We can write as follows

$$\begin{aligned} &\frac{3}{2} \left( \vec{i}_{dq}^T \mathbf{L}^{dq} \frac{d\vec{i}_{dq}}{dt} \right) + J\omega_m \dot{\omega}_m = \\ &\underbrace{\frac{3}{2} (u_d i_d + u_q i_q)}_{=P_{in}} - \underbrace{\frac{3}{2} (R i_d^2 - R i_q^2)}_{=P_{loss}} + \\ &- \underbrace{\frac{3}{2} \left( \omega [i_d \quad i_q] \begin{bmatrix} 0 & -1 \\ 1 & 0 \end{bmatrix} [\psi_d^r \quad \psi_q^r]^T + \omega [i_d \quad i_q] \begin{bmatrix} 0 & -L_q \\ L_d & 0 \end{bmatrix} [i_d \quad i_q]^T \right)}_{=\omega_m \tau_m} + \\ &+ \omega_m \tau_m - \omega_m \tau_l \end{aligned}$$

But

$$\frac{3}{2} \left( \vec{i}_{dq}^T \mathbf{L}^{dq} \frac{d\vec{i}_{dq}}{dt} \right) + J\omega \dot{\omega} = P_{in} - P_{out} - P_{loss}$$

Hence

$$P_{in} = \frac{3}{2} (u_d i_d + u_q i_q)$$

$$P_{out} = \omega_m \tau_l$$

$$P_{loss} = \frac{3}{2} (R i_d^2 + R i_q^2)$$

The expression of the torque  $\tau_m$  becomes as follows

$$\tau_m = \frac{3}{2} p \left[ \psi_d^r i_q - \psi_q^r i_d + (L_d - L_q) i_d i_q \right] \xrightarrow{\theta_0 \rightarrow \theta} \frac{3}{2} p \left[ \Psi^M i_q + (L_d - L_q) i_d i_q \right] \quad (13.3.3)$$

The full PMSM model respect to the rotor reference frame is as follows

$$\left\{ \begin{array}{l} \vec{u}_{dq}(t) - \mathbf{R}^{dq} \vec{i}_{dq}(t) + \omega \begin{bmatrix} 0 & L_q \\ -L_d & 0 \end{bmatrix} \vec{i}_{dq} - \mathbf{L}^{dq} \frac{d\vec{i}_{dq}(t)}{dt} - \omega(t) \begin{bmatrix} 0 & -1 \\ 1 & 0 \end{bmatrix} \vec{\psi}_{dq}^r = 0 \\ \frac{d\vec{\psi}_{dq}^r(t)}{dt} = 0 \quad \vec{\psi}_{dq}^r(0) = [\Psi^M \quad 0]^T \\ J\dot{\omega}_m(t) = \frac{3}{2} p \left[ \Psi^M i_q + (L_d - L_q) i_d i_q \right] - \tau_l(t) \\ \dot{\theta}(t) = \omega(t) = p\omega_m(t) \end{array} \right. \quad (13.3.4)$$

## 13.4 Equivalent circuit of a PMSM

The DQ equivalent circuits of the PMSM is shown for both transient and steady state conditions.

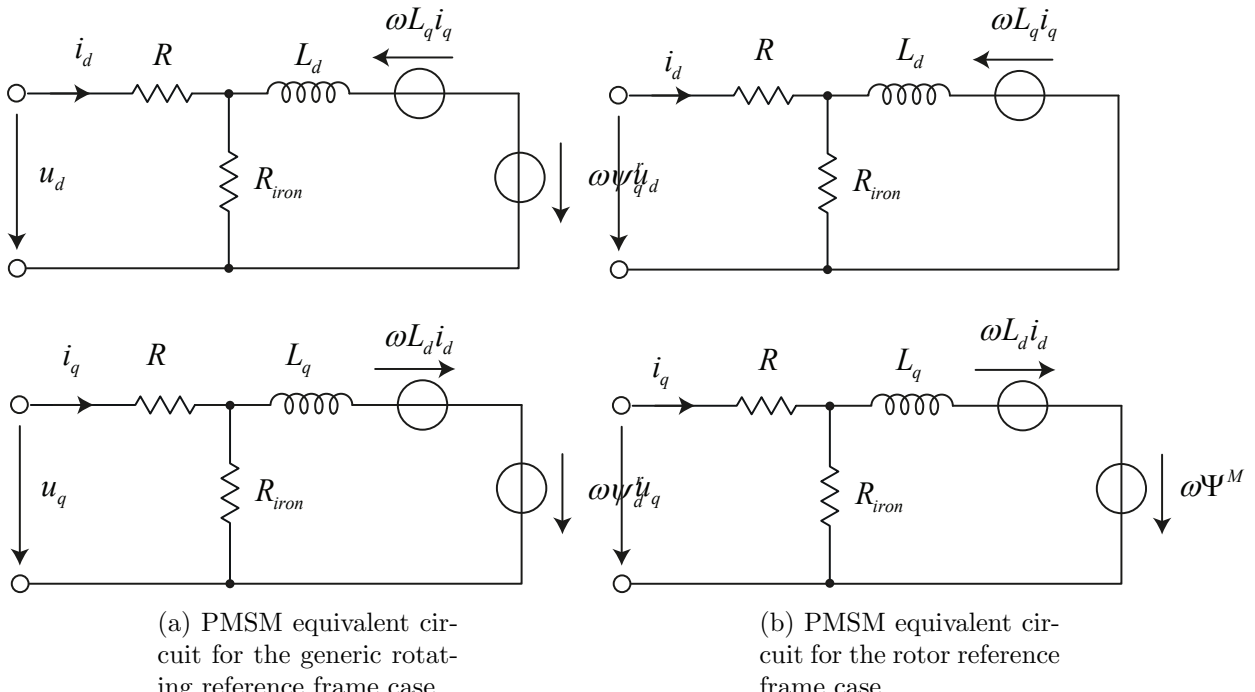


Figure 13.4: Rotating and rotor reference frame representation of the pmsm equivalent circuit.

# Chapter 14

## Control of a PMSM

### 14.1 Classical Field Oriented Control of a PMSM

The classical field oriented control (FOC) DQ-control of PMSMs in Figure 14.1 is depicted.

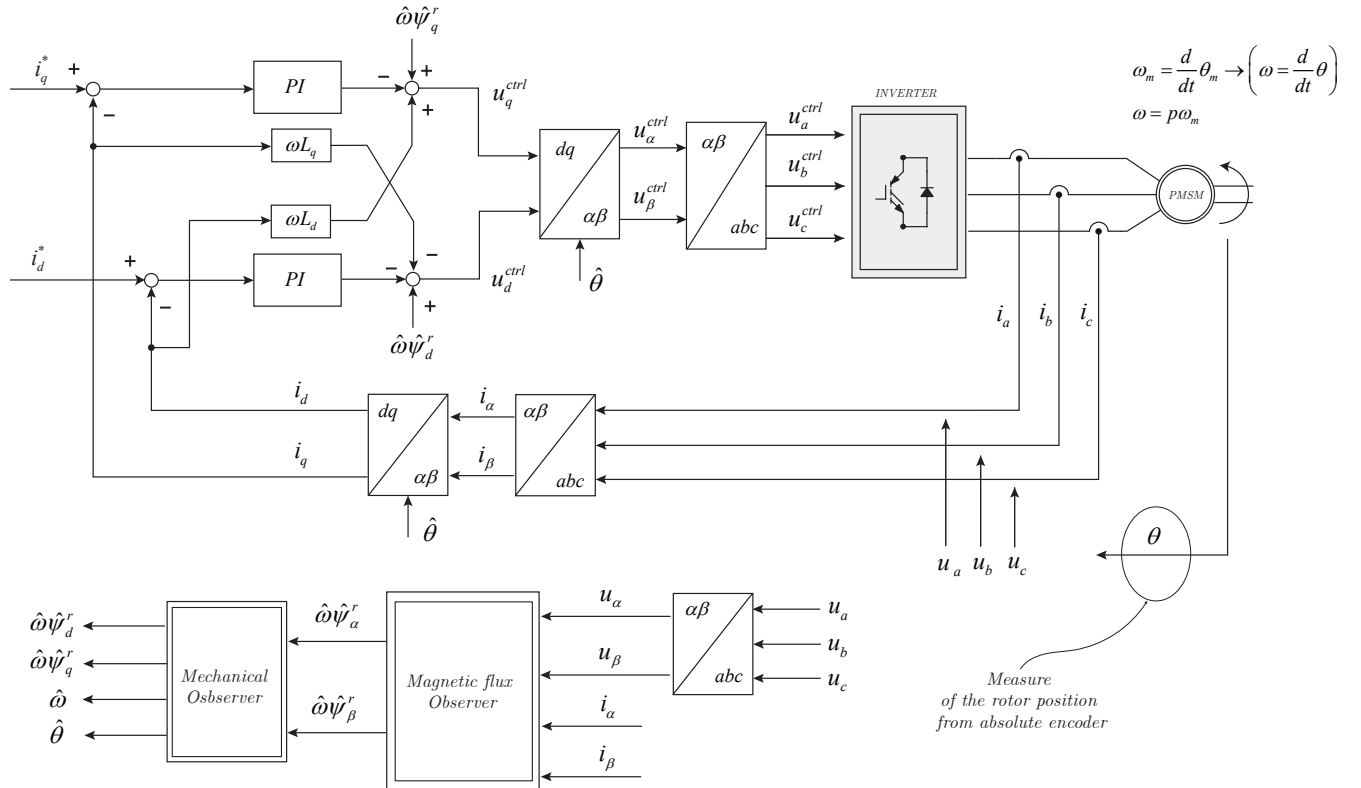


Figure 14.1: Internal current control of the classical FOC of a PMSM.

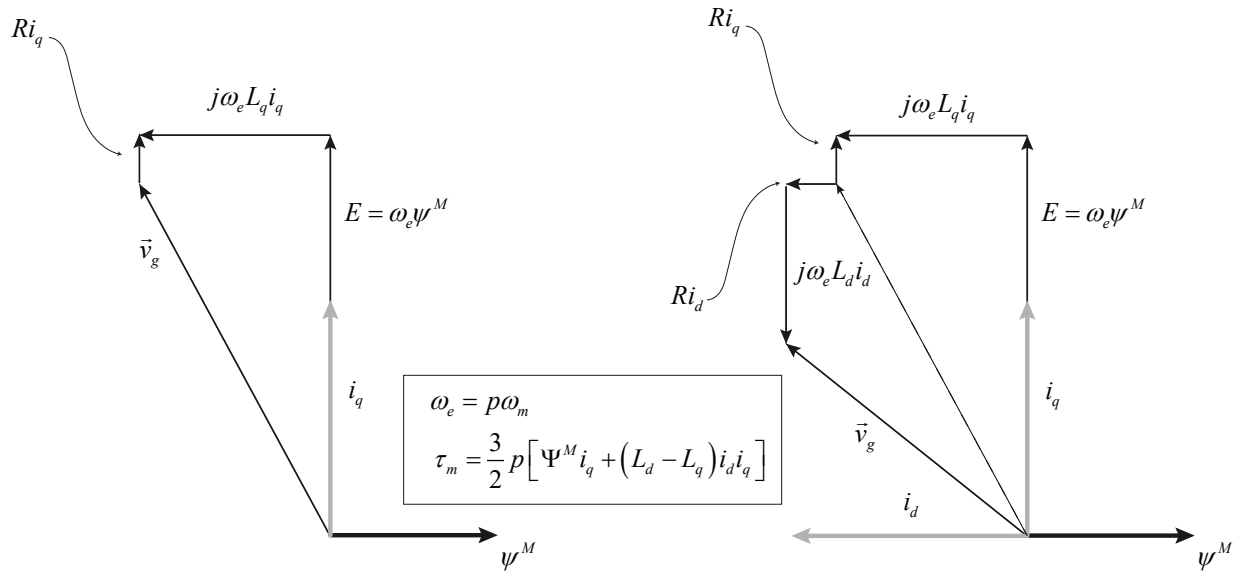


Figure 14.2: Vector diagram of the PMSM and effect of the  $i_d$  current component on the terminal voltage  $\vec{v}_g$ .

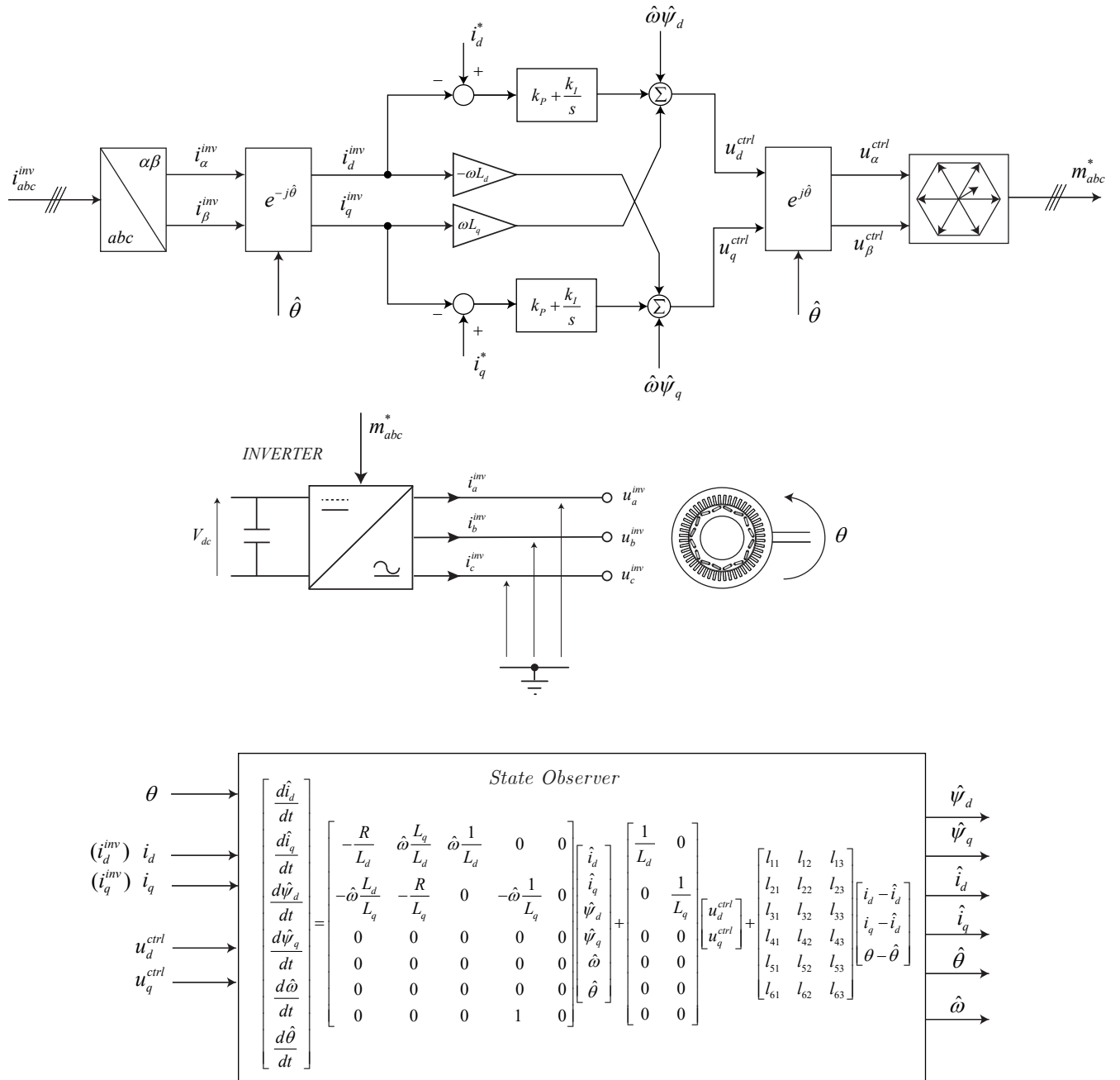


Figure 14.3: Another representation of the FOC of a PMSM with a state observer.

The **FOC** control strategy is based on the controlling of two current components. The two current components ( $i_d, i_q$ ) are derived by a proper transformation of the PMSM three phase current system into the  $dq$  reference frame. The knowledge of the rotor phase  $\theta$  play a fundamental role in the performance of the control system. A perfect knowledge of the rotor position  $\theta$  permits to decouple the control system into two current component where the  $Q$  axis concerns the generation of the torque and the  $D$  axis affect the value of the terminal voltage and can be properly set in order to extend the working operative are of the PMSMs as shown in Figure 14.2.

## 14.2 Normalization and control implementation.

Concerning the model representation and the control implementation we in front of two completely different approach. A model implementation is, in general, represented in SI unit and often in continuous time domain. On the other hand a control system as well as the state space representation of the dynamical system of the plant is, often, represented in per unit and in discrete time domain. The representation in per unit given many advantages in term of usability and *control gain stability* among different plants implementations.

The per unit representation of the model pass through the *normalization*, as follows

- Reference quantities

- $u_{bez}$  = is the peak phase voltage of the no-load voltage at nominal rotor speed  $\omega_m^{nom}$  of the motor in V
- $i_{bez}$  = is the peak phase nominal current of the motor in A
- $\omega_m^{nom}$  = is the nominal mechanical rotor speed of the motor in  $\text{rad s}^{-1}$
- $\omega_{bez} = p\omega_m^{nom}$  is the nominal electrical speed of the motor in  $\text{rad s}^{-1}$
- $X_{bez} = u_{bez}/i_{bez}$  = is the reference electrical impedance of the motor in  $\Omega$
- $L_{bez} = X_{bez}/\omega_{bez}$  = is the reference inductance of the motor in H
- $\psi_{bez} = u_{bez}/\omega_{bez}$  = is the reference flux of the motor in Wb

- Per unit quantities

- $R^{norm} = R/X_{bez}$  is the per unit phase resistance.
- $L_d^{norm} = L_d/L_{bez}$  is the per unit phase  $L_d$  inductance.
- $L_q^{norm} = L_q/L_{bez}$  is the per unit phase  $L_q$  inductance.
- $\omega^{norm} = p\omega_m/\omega_{bez}$  is the per unit electrical speed.
- $i_d^{norm} = i_d/i_{bez}$  is the per unit  $i_d$  current.
- $i_q^{norm} = i_q/i_{bez}$  is the per unit  $i_q$  current.
- $u_d^{norm} = u_d/u_{bez}$  is the per unit  $u_d$  voltage.
- $u_q^{norm} = u_q/u_{bez}$  is the per unit  $u_q$  voltage.
- $\psi_d^{norm} = \psi_d/\psi_{bez}$  is the per unit D-flux.
- $\psi_q^{norm} = \psi_q/\psi_{bez}$  is the per unit Q-flux.
- $\psi_M^{norm} = \Psi^M/\psi_{bez}$  is the per unit M-flux.

And the FOC control implementation become (in continuous time domain) - in the following we omit the term  $(^{norm})$  and we consider all as per unit quantities

$$\begin{cases} i_q^{ref} = k_p^w (\omega^{ref} - \omega) + i_q^i \\ \frac{di_q^i}{dt} = k_i^w (\omega^{ref} - \omega) \\ u_d = k_p^i (i_d^{ref} - i_d) + u_d^i - \omega \hat{\psi}_q - \omega L_q i_q \\ \frac{du_d^i}{dt} = k_i^i (i_d^{ref} - i_d) \\ u_q = k_p^i (i_q^{ref} - i_q) + u_q^i + \omega \hat{\psi}_d - \omega L_d i_d \\ \frac{du_q^i}{dt} = k_i^i (i_q^{ref} - i_q) \end{cases} \quad (14.2.1)$$

### 14.3 Model predictive control of a PMSM

The model predictive control, applied to PMSMs, permits to introduce some additional features and constraints in the optimization process which results in the following benefits

- naturally variable PWM - sand effect on sound emission
- possibility to implement a constraint to minimize the switching power losses of the inverter.

To implement a model predictive control we have to start writing down the PMSM model in discrete time domain.

#### 14.3.1 Discrete-time model

From the first four first order equations of Eq. (13.3.2)

$$\begin{cases} \vec{u}_{\alpha\beta}(t) - \mathbf{R}^{\alpha\beta} \vec{i}_{\alpha\beta}(t) - \mathbf{L}^{\alpha\beta} \frac{d\vec{i}_{\alpha\beta}(t)}{dt} - \omega(t) \begin{bmatrix} 0 & -1 \\ 1 & 0 \end{bmatrix} \vec{\psi}_{\alpha\beta}^r = 0 \\ \frac{d\vec{\psi}_{\alpha\beta}^r(t)}{dt} = \omega(t) \begin{bmatrix} 0 & -1 \\ 1 & 0 \end{bmatrix} \vec{\psi}_{\alpha\beta}^r(t) \quad \vec{\psi}_{\alpha\beta}^r(0) = [\Psi^M \quad 0]^T \end{cases} \quad (14.3.1)$$

we first write them in a canonical form as follows (we assume  $L_\alpha = L_\beta = L_s$  and  $R_\alpha = R_\beta = R_s$ )

$$\begin{cases} \frac{di_\alpha}{dt}(t) = -\frac{R_s}{L_s} i_\alpha(t) + \frac{\omega(t)}{L_s} \psi_\beta^r(t) + \frac{1}{L_s} u_\alpha(t) \\ \frac{di_\beta}{dt}(t) = -\frac{R_s}{L_s} i_\beta(t) - \frac{\omega(t)}{L_s} \psi_\alpha^r(t) + \frac{1}{L_s} u_\beta(t) \\ \frac{d\psi_\alpha^r}{dt}(t) = -\omega(t) \psi_\beta^r(t) \\ \frac{d\psi_\beta^r}{dt}(t) = \omega(t) \psi_\alpha^r(t) \end{cases} \quad (14.3.2)$$

which can be written as follows

$$\begin{aligned}\dot{\vec{x}}(t) &= \tilde{\mathbf{A}}(\vec{x})\vec{x}(t) + \tilde{\mathbf{B}}\vec{u}(t) \\ \vec{y}(t) &= \mathbf{C}\vec{x}(t)\end{aligned}\quad (14.3.3)$$

where ( $\vec{x} = [i_\alpha \ i_\beta \ \psi_\alpha^r \ \psi_\beta^r]^T$ )

$$\begin{aligned}\tilde{\mathbf{A}} &= \begin{bmatrix} -\frac{R_s}{L_s} & 0 & 0 & \frac{\omega}{L_s} \\ 0 & -\frac{R_s}{L_s} & -\frac{\omega}{L_s} & 0 \\ 0 & 0 & 0 & -\omega \\ 0 & 0 & \omega & 0 \end{bmatrix} \\ \tilde{\mathbf{B}} &= \begin{bmatrix} \frac{1}{L_s} & 0 \\ 0 & \frac{1}{L_s} \\ 0 & 0 \\ 0 & 0 \end{bmatrix}, \quad \mathbf{C} = \begin{bmatrix} 1 & 0 & 0 & 0 \\ 0 & 1 & 0 & 0 \end{bmatrix}\end{aligned}$$

By using the Euler approximation for the stator current derivatives for a sampling time  $t_s$ , that is,

$$\frac{di}{dt} \approx \frac{i(k+1) - i(k)}{t_s} \quad (14.3.4)$$

bring to the following approximated discretization

$$\begin{aligned}\mathbf{A}(\vec{x}) &= \mathbf{I} + \tilde{\mathbf{A}}(\vec{x})t_s \\ \mathbf{B}(\vec{x}) &= \tilde{\mathbf{B}}t_s\end{aligned}\quad (14.3.5)$$

which results into the following equations

$$\begin{cases} i_\alpha(k+1) = (1 - \frac{R_s}{L_s}t_s)i_\alpha(k) + \frac{\omega(k)}{L_s}t_s\psi_\beta^r(k) + \frac{t_s}{L_s}u_\alpha(k) \\ i_\beta(k+1) = (1 - \frac{R_s}{L_s}t_s)i_\beta(k) - \frac{\omega}{L_s}t_s\psi_\alpha^r(k) + \frac{t_s}{L_s}u_\beta(k) \\ \psi_\alpha^r(k+1) = -\omega(k)t_s\psi_\beta^r(k) \\ \psi_\beta^r(k+1) = \omega(k)t_s\psi_\alpha^r(k) \end{cases} \quad (14.3.6)$$

supposing the quantities  $\psi_\alpha^r(k)$  and  $\psi_\beta^r(k)$  have been estimated from a state observer such that  $\psi_\alpha^r(k) \rightarrow \hat{\psi}_\alpha^r(k)$  and  $\psi_\beta^r(k) \rightarrow \hat{\psi}_\beta^r(k)$  the model predictive current control (in the stationary reference frame) can be written as follows

$$\begin{cases} i_\alpha(k+1) = (1 - \frac{R_s}{L_s}t_s)i_\alpha(k) + \frac{\omega(k)}{L_s}t_s\hat{\psi}_\beta^r(k) + \frac{t_s}{L_s}u_\alpha(k) \\ i_\beta(k+1) = (1 - \frac{R_s}{L_s}t_s)i_\beta(k) - \frac{\omega}{L_s}t_s\hat{\psi}_\alpha^r(k) + \frac{t_s}{L_s}u_\beta(k) \end{cases} \quad (14.3.7)$$

Consider now, the rotor reference frame model of Eq. (13.3.4) here re-written (without mechanical equations)

$$\begin{cases} \vec{u}_{dq}(t) - \mathbf{R}^{dq} \vec{i}_{dq}(t) + \omega \begin{bmatrix} 0 & L_q \\ -L_d & 0 \end{bmatrix} \vec{i}_{dq} - \mathbf{L}^{dq} \frac{d\vec{i}_{dq}(t)}{dt} - \omega(t) \begin{bmatrix} 0 & -1 \\ 1 & 0 \end{bmatrix} \vec{\psi}_{dq}^r = 0 \\ \frac{d\vec{\psi}_{dq}^r(t)}{dt} = 0 \quad \text{where} \quad \vec{\psi}_{dq}^r(0) = [\Psi^M \quad 0]^T \end{cases} \quad (14.3.8)$$

Applying the same procedure as previously reported we obtain the following discrete-time model for the Kirchhoff's equations (as before we suppose flux have been estimated such that  $\psi_d^r(k) \rightarrow \hat{\psi}_d^r(k)$  and  $\psi_q^r(k) \rightarrow \hat{\psi}_q^r(k)$ ):

$$\begin{cases} i_d(k+1) = \left(1 - \frac{RL_d}{t_s}\right) i_d(k) + t_s \omega(k) \frac{L_q}{L_d} i_q(k) + \frac{t_s}{L_d} \omega(k) \hat{\psi}_q^r(k) + \frac{t_s}{L_d} u_d(k) \\ i_q(k+1) = \left(1 - \frac{RL_q}{t_s}\right) i_q(k) - t_s \omega(k) \frac{L_d}{L_q} i_d(k) - \frac{t_s}{L_q} \omega(k) \hat{\psi}_d^r(k) + \frac{t_s}{L_q} u_q(k) \end{cases} \quad (14.3.9)$$

when the flux observer will converge, the following relations are achieved

$$\begin{cases} \hat{\psi}_d^r(k) \rightarrow 0 \\ \hat{\psi}_q^r(k) \rightarrow \Psi^M \end{cases} \quad (14.3.10)$$

and the following representation can be considered

$$\begin{cases} i_d(k+1) = \left(1 - \frac{RL_d}{t_s}\right) i_d(k) + t_s \omega(k) \frac{L_q}{L_d} i_q(k) + \frac{t_s}{L_d} u_d(k) \\ i_q(k+1) = \left(1 - \frac{RL_q}{t_s}\right) i_q(k) - t_s \omega(k) \frac{L_d}{L_q} i_d(k) - \frac{t_s}{L_q} \omega(k) \Psi^M + \frac{t_s}{L_q} u_q(k) \end{cases} \quad (14.3.11)$$

These equations allow predictions of the stator currents to be calculated for each one of the seven voltage vectors generated by the inverter. The voltage vectors generated by the inverter are fixed in the rotor reference frame ( $dq$ ), but they are rotating in the stationary reference frame ( $\alpha\beta$ ), and are calculated as follows

$$\vec{u}_{\alpha\beta} = \vec{u}_{dq} e^{-j\theta} = \mathbf{T}_2^{-1} \vec{u}_{dq} \quad (14.3.12)$$

### 14.3.2 Control scheme

The control scheme for field oriented control (FOC) of the PMSM using predictive current control is shown in Figure 14.4. Here, a PI controller is used for speed control and generates the reference for the torque-producing current  $i_q^{ref}$ . A predictive current controller is used for tracking this current. In the predictive scheme, the discrete-time model of the machine is used for predicting the stator current components for the seven different voltage vectors generated by the inverter. The voltage vector that minimizes a cost function is selected and applied during a whole sampling interval.

The objective of the predictive current control scheme are summarized as follows:

- Torque current reference tracking
- Torque by ampere optimization

- Current magnitude limitation

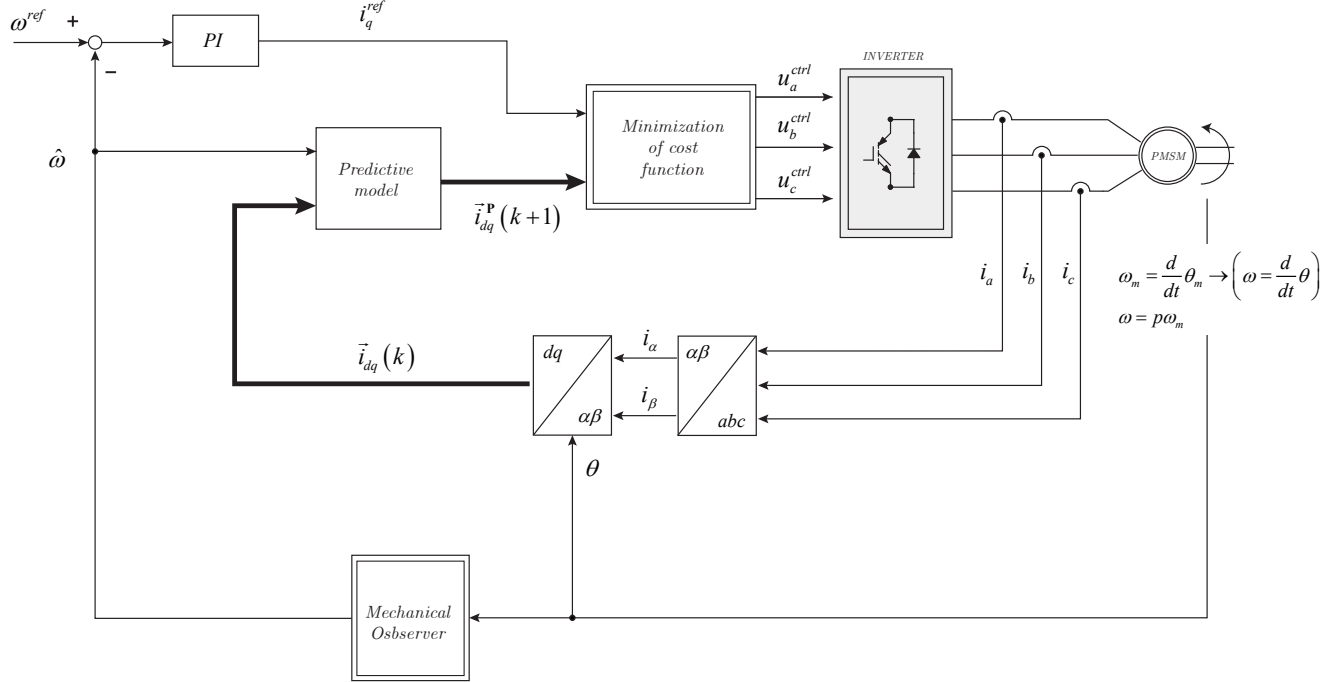


Figure 14.4: FOC of a PMSM using predictive current control.

The objectives can be expressed as the following cost function

$$g = \left[ i_d^P(k+1) \right]^2 + \left[ i_q^{ref} - i_q^P(k+1) \right]^2 + \hat{f}[i_d^P(k+1), i_q^P(k+1)] \quad (14.3.13)$$

where the first term represents the minimization of the reactive power, allowing the torque by ampere optimization, the second term is defined for tracking the torque-producing current and the last term is a nonlinear function for limiting the amplitude of the stator currents. This function is defined as

$$\hat{f}[i_d^P(k+1), i_q^P(k+1)] = \begin{cases} \infty & \text{if } |i_d^P| > i^{max} \text{ or } |i_q^P| > i^{max} \\ 0 & \text{if } |i_d^P| \leq i^{max} \text{ and } |i_q^P| \leq i^{max} \end{cases} \quad (14.3.14)$$

where  $i^{max}$  is the value of the maximum allowed stator current magnitude. In this way, if a given voltage vector generates predictive currents with a magnitude higher than  $i^{max}$  then the cost function will be  $g = \infty$ , and, in consequence, this voltage vector will not be selected.

## 14.4 Predictive speed control

One of the main advantages of MPC is the possibility to control several different variables using a single cost function. This makes possible the implementation of a predictive speed control while maintaining the stator currents under given conditions. It is desirable to consider a limitation on the magnitude of the currents and to optimize the control by ampere ratio (also called max torque per Ampere control strategy MTPA).

This application of MPC introduces some difficulties, such as the nonlinear model of the system, the large differences between the speed dynamics (mechanical dynamics) and the dynamics of the stator currents (electrical dynamics) and the quantization noise in the speed measurement.

#### 14.4.1 Discrete-time model

In order to perform a speed control using MPC, the mechanical equations must be included in the discrete-time equations used for calculation of the predictions. The machine model can be summarized in the form of the following space state equation:

$$\frac{d\vec{x}}{dt} = h(\vec{x}, \vec{u}) \quad (14.4.1)$$

where

$$\vec{x} = [i_d \ i_q \ \omega]^T \quad (14.4.2)$$

$$\vec{u} = [u_d \ u_q]^T \quad (14.4.3)$$

$$h(\vec{x}, \vec{u}) = \begin{bmatrix} -\frac{R}{L_d}i_d + \omega\frac{L_q}{L_d}i_q + \frac{1}{L_d}u_d \\ -\frac{R}{L_q}i_q - \omega\frac{L_d}{L_q}i_d - \frac{1}{L_q}\Psi^M\omega + \frac{1}{L_q}u_q \\ \frac{1}{J}\left(\frac{3}{2}p\Psi^M i_q - b\omega\right) \end{bmatrix} \quad (14.4.4)$$

In order to obtain a more accurate discrete-time model, a modified Euler integration method is used instead of the simple Euler approximation used in previous section. The discrete time model is defined as

$$\begin{cases} \hat{\vec{x}}(k|k) = \hat{\vec{x}}(k|k-1) + t_s h(\hat{\vec{x}}(k|k-1), \vec{u}(k|k)) \\ \hat{\vec{x}}(k+1|k) = \hat{\vec{x}}(k|k) + \frac{t_s}{2} \left[ h(\hat{\vec{x}}(k|k-1), \vec{u}(k|k)) + h(\hat{\vec{x}}(k|k), \vec{u}(k|k)) \right] \end{cases} \quad (14.4.5)$$

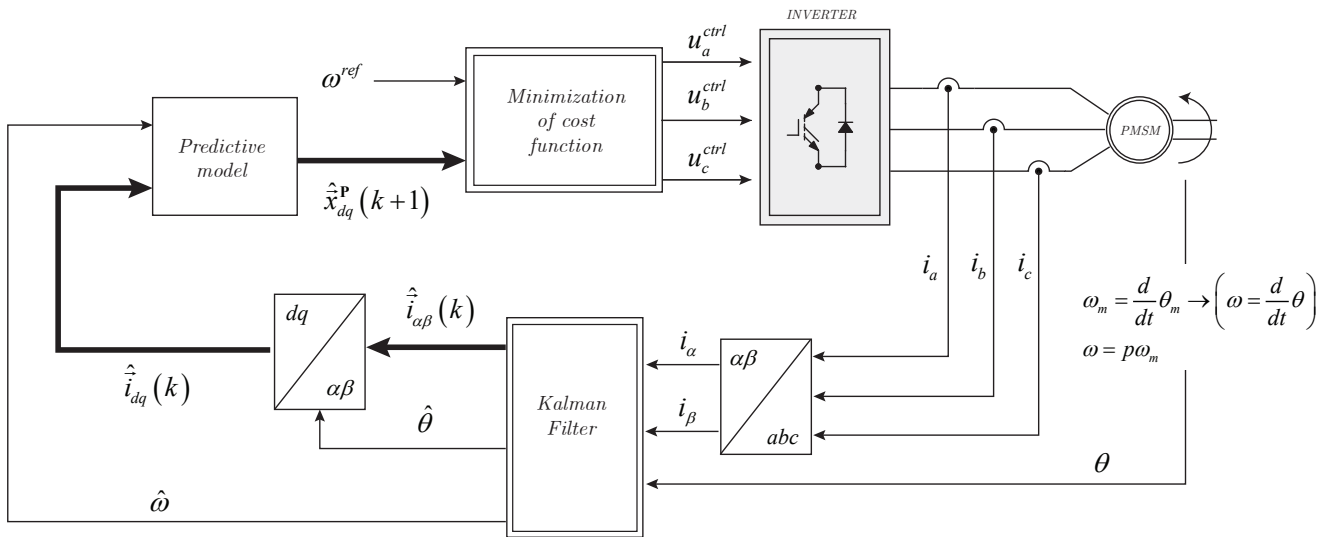
#### 14.4.2 Control scheme

A block diagram of the predictive speed control is shown in Figure 14.5. The discrete-time model of the machine is used for calculating predictions of the rotor speed and stator currents for the seven voltage vectors generated by the inverter. These predictions are evaluated by a cost function that defines the desired behaviour of the system. The voltage vector that minimizes this function is selected and applied to the machine terminals for a whole sampling interval.

Due to the noisy nature of the speed measurement and the high sampling frequencies that are usually needed in this kind of predictive control scheme, the use of an extended Kalman filter (EKF) was proposed for estimating the rotor speed.

The objectives of the predictive speed control scheme are summarized as follows

- Speed reference tracking
- Smooth behaviour of the electrical torque
- MTPA
- Current magnitude limitation



## Chapter 15

# Direct-Torque Control (DTC)

## Chapter 16

# Advanced Controls for PMSM Applications

### 16.1 PMSM Current Loci and Over-Speed Management

The control of a PMSM and in particular of an IPMSM where  $L_d$  and  $L_q$  are strongly different, has some degree of freedom concerning the set-point of the current  $i_d$ . As we will see, the current  $i_d$  can be used to coercive the terminal voltage (flux weakening, FW) of PMSM (which is subjected to the inverter constraints) to a given value. Moreover the a proper set of  $i_d$  current can be selected to optimize some properties of the PMSM like the maximum torque per ampere (MTPA) or the maximum torque per voltage (MTPV), or to minimize the copper power losses, or in flux weakening, etc.

In general an IPMSM is controlled by the MTPA and when it reach the maximum voltage (due to over-speed) the current loci  $i_d - i_q$  can be kept along a maximum voltage curve until a maximum current (circle -  $i_d - i_q$ ) is reached. When the current loci lays in a maximum current curve, the control can move along the limit curve until a different control strategy, like MTPV is adopted.

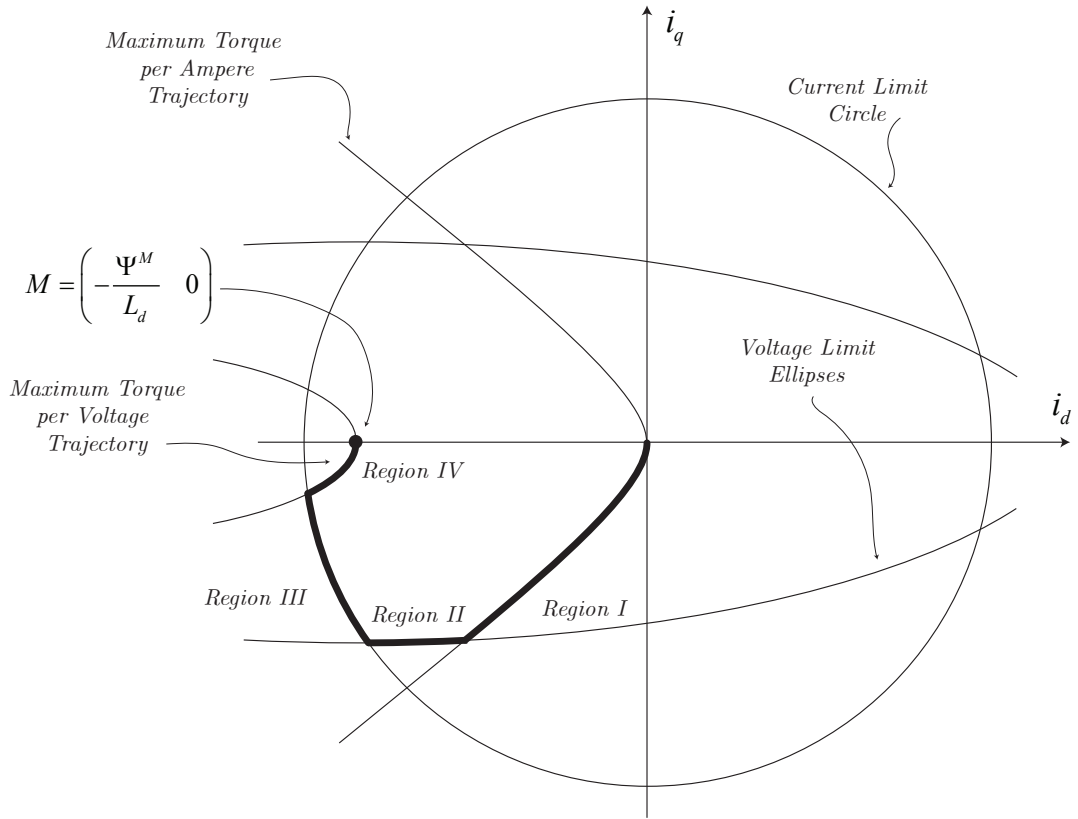


Figure 16.1: Current limit circle and voltage limit ellipses in  $i_d - i_q$  plane.

Another very common control strategy is the  $i_d = 0$  control, obviously this control is naturally the best choice for isotropic PMSM ( $L_d = L_q$ ), even if it is widely used in IPMSM. Using  $i_d = 0$  control in a IPMSM de-rate the effective efficiency of the system, requiring more current than what can be used in the case of a MTPA control.

Some current loci are shown in Figures 16.1 and 16.2

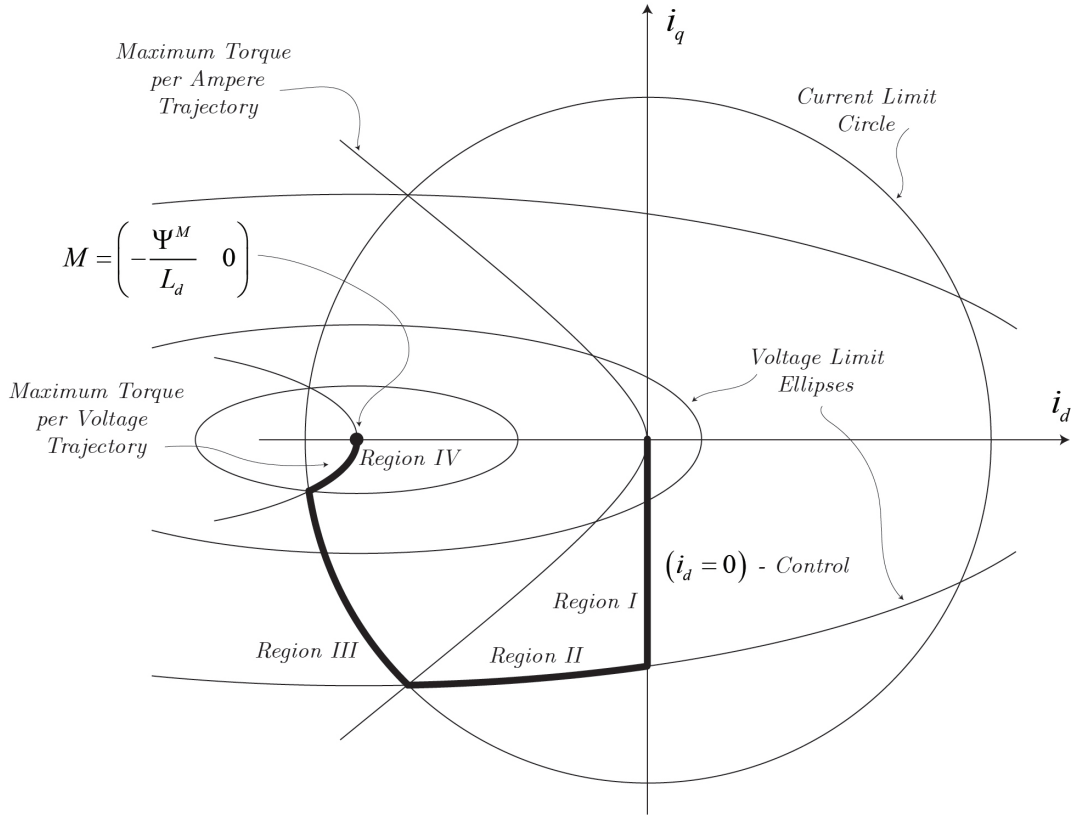


Figure 16.2: Some possible current control strategies and their properties.

The relation between  $d$ -axis and  $q$ -axis currents for the **maximum torque per ampere** (MTPA) condition is given as follows

$$\begin{cases} i_d^{ref} = \frac{\Psi^M}{2(Lq - Ld)} - \sqrt{\frac{(\Psi^M)^2}{4(Lq - Ld)^2} + i_q^2} \\ i_d^{ref} = \text{as per torque} \end{cases} \quad (16.1.1)$$

The optimal current vector by which the torque per flux linkage  $\psi_0 = \sqrt{(\Psi^M + L_d i_d)^+ (L_q i_q)^2}$  become maximal is given as follows

$$\begin{cases} i_d = -\frac{\Psi^M + \Delta\psi_d}{L_d} \\ i_q = \frac{1}{L_q} \sqrt{(\psi_0)^2 - (\Delta\psi_d)^2} \end{cases} \quad (16.1.2)$$

where

$$\Delta\psi_d = \frac{-L_q \Psi^M + \sqrt{(\Psi^M)^2 + 8(L_q - L_d)^2 \psi_0^2}}{4(L_q - L_d)} \quad (16.1.3)$$

The vector control based on Eq. (16.1.2) and 16.1.3 can be called *the maximum torque per flux linkage (MTPF) control*. This condition is equal to maximizing the torque to the voltage  $v_g$ , where  $v_g$  is defined as follows

$$v_g = \sqrt{\left(\omega\Psi^M + Ri_q + \omega L_d i_d\right)^2 + \left(Ri_d - \omega L_q i_q\right)^2} \quad (16.1.4)$$

thus this vector control is named *the maximum torque per voltage (MTPV) control*.

One of the most interesting and important  $i_d - i_q$  current loci is the *constant voltage* locus, where in Figure 16.2 is described like a ellipses. This current loci is very important and widely used in **generator mode** where the speed motor is imposed by the external system. Along this region (*region II*) the output voltage of the inverter (or of the terminals of the PMSM) is kept constant (in modulus) and the current vector is not more controlled but is free to rotate or move along this ellipses. This region is often used as **self field weakening control**, in fact, we can observe that in this condition the inverter is able to keep loaded the PMSM by automatically rotation of the motor current (the current is rotating out of control) in order to maintain the modulus of the terminal voltage constant and modifying the actual torque.

## 16.2 Robust field weakening control architecture

In this section a feedback (closed loop) field weakening control structure is proposed.

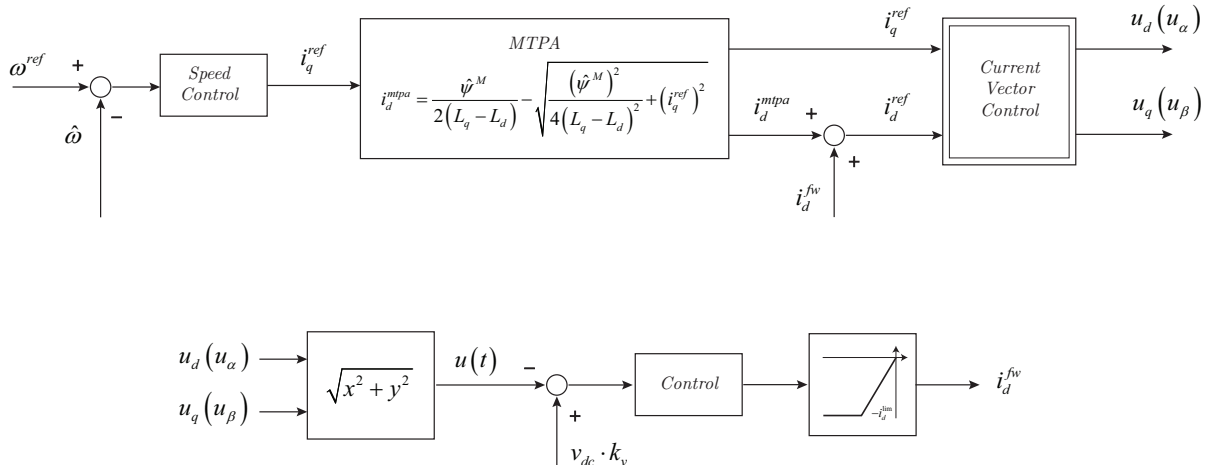


Figure 16.3: S.

## 16.3 Sensor-less (encoder-less) control structure with low rate failure synchronization at zero-speed

### 16.4 Safety and electromagnetic compatibility

### 16.5 Fault detection and fault tolerant control

# **Part III**

# **Case Study**

# Chapter 17

## Introduction

The Digital Twin Laboratory (here called DTL) is a project involved in the mathematical modelization of heavy duty vehicles. Heavy duty vehicles, in particular tracked vehicles, are in general constituted by the following parts

1. A prime mover which can be a diesel engine or an electrical motor
2. An hydrostatic transmission.
3. The hydrostatic transmission drives a wheel sprocket which is coupled to a track.
4. Ancillary components like shield and tiller based on hydrostatic transmissions and servos.

In alternative to the solution with diesel engine plus hydrostatic transmission a new generation of power-trains are going to be released in the mass market and they consist of a permanent magnet synchronous motor directly coupled to the wheel sprocket of each track, which is here called: *full electrification* (FE).

The aim of this document is to illustrate the mathematical model of all diesel engines involved into the project and also to formulate an equivalent electrical solution for each of them. In additional, solutions for full electrification will be also shown.

The following diesel engines will be investigated

- **Mercedes-Benz OM471** with  $P_{max} = 390 \text{ kW}$  at  $1600 \text{ min}^{-1}$  and with a maximum torque of  $\tau_{max} = 2600 \text{ N m}$  at  $1300 \text{ min}^{-1}$  and a maximum speed of  $2140 \text{ min}^{-1}$
- **Liebherr D934** with  $P_{max} = 170 \text{ kW}$  at  $1900 \text{ min}^{-1}$  and with a maximum torque of  $\tau_{max} = 1500 \text{ N m}$  at  $1300 \text{ min}^{-1}$  and a maximum speed of  $2500 \text{ min}^{-1}$
- **OM934** with  $P_{max} = 170 \text{ kW}$  at  $2000 \text{ min}^{-1}$  and with a maximum torque of  $\tau_{max} = 950 \text{ N m}$  at  $1700 \text{ min}^{-1}$  and a maximum speed of  $2600 \text{ min}^{-1}$

In additional, for each kind of heavy duty vehicle an full electric solutions will be shown. In order to create an homogeneous engineering a common geometrical solution will be proposed for each kind of motor size. The reached target in term of torque and maximum speed will be satisfy by proper dimensioning of length of the motor and number of turns of the coils. Additional information are available in Chapter ??

# Chapter 18

## Liebherr diesel engine D934

### 18.1 Technical data

In this section the main characteristics of the Liebherr D934 diesel engine are shown. Figure 18.1 shows the maximum torque curve (throttle at  $\theta = 100\%$ ) and the braking torque due to internal friction as function of the shaft rotating speed.

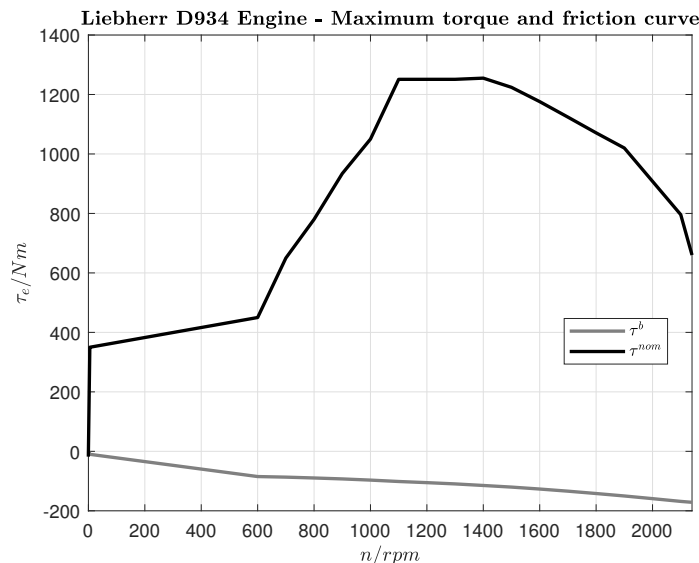


Figure 18.1: Liebherr diesel engine D934 - maximum torque curve.

Figure 18.2 shows the maximum power curve available at the engine shaft where the friction losses has been accounted.

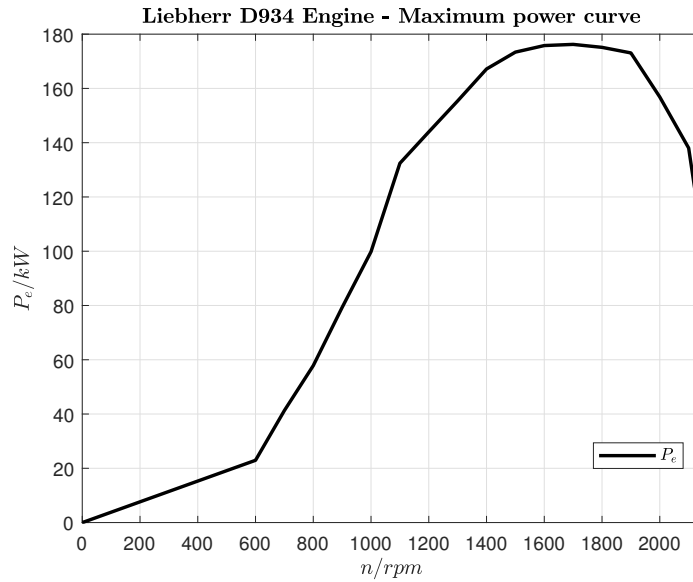


Figure 18.2: Liebherr diesel engine D934 - maximum power curve available at the crank-shaft.

Figure 18.3 shows a contour plot of the fuel consumption as function of the actual torque and rotor speed. Consumption is measured in g/kWh.

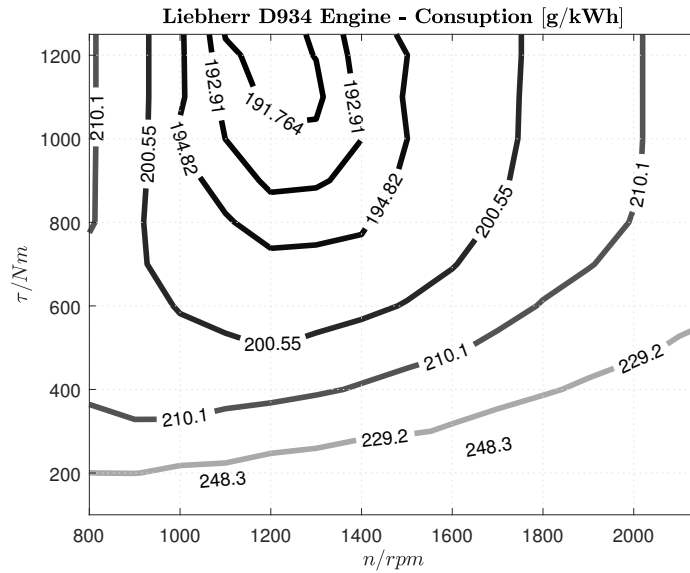


Figure 18.3: Liebherr diesel engine D934 - Consumption [g/kWh].

In the next figures the torque step responses at different rotor speed have been shown. Figure 18.4 shows the torque step response of the engine at rotor speed of  $n = 1400 \text{ min}^{-1}$

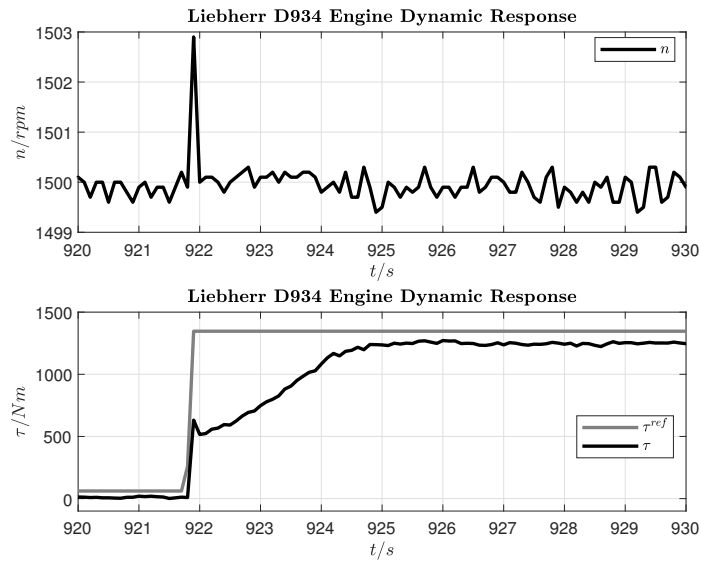


Figure 18.4: Liebherr diesel engine D934 - step response.

Figure 18.5 shows the torque step response of the engine at rotor speed of  $n = 1800 \text{ min}^{-1}$

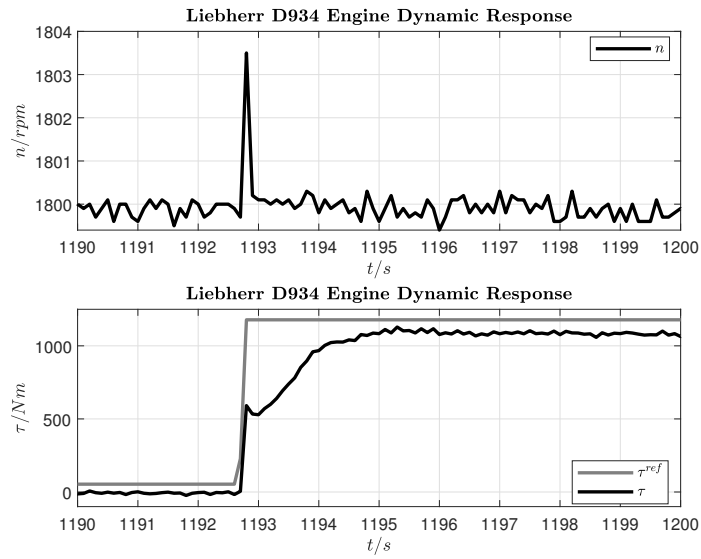


Figure 18.5: Liebherr diesel engine D934 - step response.

Figure 18.6 shows the torque step response of the engine at rotor speed of  $n = 2100 \text{ min}^{-1}$

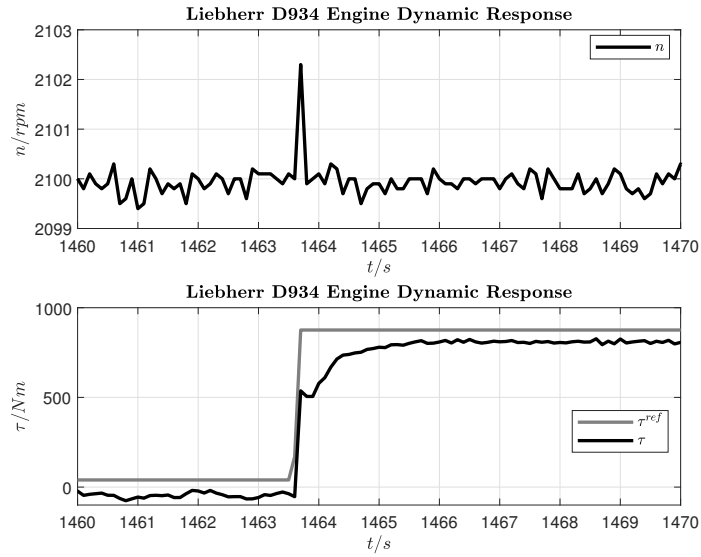


Figure 18.6: Liebherr diesel engine D934 - step response.

In the next section the equivalent mathematical model of the Liebherr D934 diesel engine will be proposed.

## 18.2 Equivalent model

In this section the description of the IC-engine is reported. The knowledge of the torque and power curve of the engine plays an important role in the performance of the engine anti-stall control.

In the following, we describe how the IC-engine has been modelized. We start to consider two curves:

- Torque curve: maximum torque available for a given rotor speed and maximum displacement of the throttle.
- Torque friction curve: torque generated by the friction for a given rotor speed. This friction is considered always present, for any value of the throttle. See also Figure 18.1

The mechanical model of the engine can be described as follows

$$J \frac{d\omega_e}{dt} = \theta_f(t) \tau^{nom}(\omega_e) + \tau^b(\omega_e) - \tau_{load} \quad (18.2.1)$$

where  $\tau^{nom}(\omega_e)$  and  $\tau^b(\omega_e)$  are shown in Figure 18.1 while  $\theta_f(t)$  is the throttle which is generated by the external speed loop control as shown in Figure 5.2 and  $J = 7.5 \text{ kg m}^{-2}$ .

The speed control is performed by a PI-controller and it adapts the throttle displacement in order to keep the request speed tracked.

An additional second order filter is taken into account in order to modelize additional dynamics.

The controller can be described as follows

$$\begin{cases} \tilde{\omega}_e(t) = \frac{1}{\omega_e^{\text{nom}}} (\omega_e^{\text{ref}} - \omega_e(t)) \\ \theta(t) = k_p \tilde{\omega}_e(t) + \theta^i(t) \\ \frac{d\theta^i}{dt}(t) = k_i \tilde{\omega}_e(t) \end{cases} \quad (18.2.2)$$

The control output  $\theta$  is passed through a second order filter:

$$\theta_f(s) = \frac{\omega_0^2}{s^2 + 2\zeta\omega_0 s + \omega_0^2} \theta(s) \quad (18.2.3)$$

where  $\zeta = 1$  and  $\omega_0 = 2\pi 25 \text{ Hz}$ .

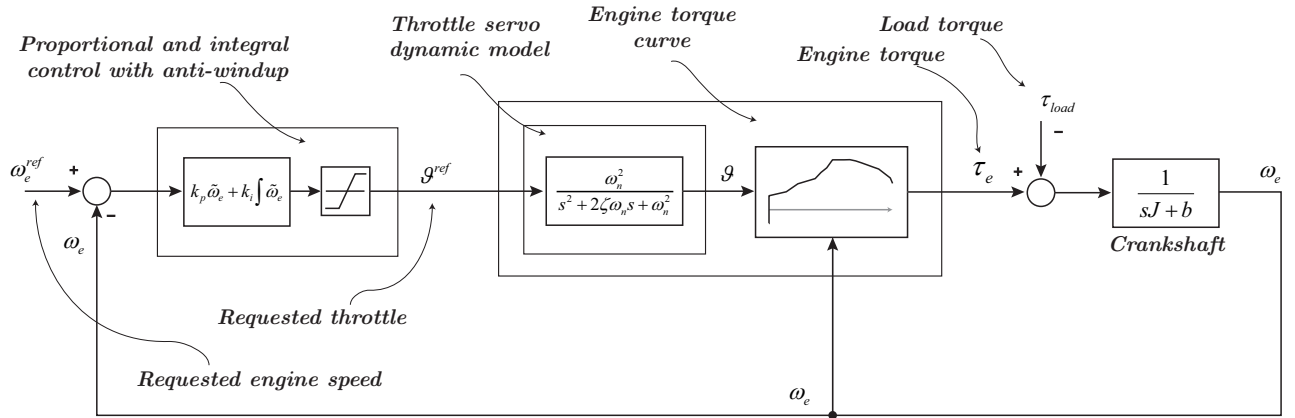


Figure 18.7: Engine model and control architecture.

## Chapter 19

# Case study for Liebherr diesel engine D934 electrification

Considering the above geometrical dimensions the case of  $\omega_m^{max} = 2140 \text{ min}^{-1}$ ,  $\hat{\omega}_m = 1500 \text{ min}^{-1}$ ,  $\hat{\tau}_m = 1250 \text{ N m}$  has been now taken into account, resulting in the following electrical and mechanical characteristics Settings of the variable design parameters

- $L_{stack} = 160 \text{ mm}$  machine length
- $N = 30$  number of turns per coil

**Performance results are as follows**

- The nominal torque is obtained at  $i_{phase} = 600 \text{ A}$  peak
- $\psi^M = 2B_g \frac{D_r \pi}{4p} L_{stack} N = 0.33 \text{ Wb}$  from analytical evaluation
- $\psi^M = 0.375 \text{ Wb}$  from Ansys analysis

The magnet flux linkage results in a value which is higher than the original target but can be evaluated during simulation performance its impact into the battery system during overspeed fault management.

- Slot current density :  $j_{sl} = 3.5 \text{ A mm}^{-2}$  at  $i_{ph}^{rms} = 424 \text{ A}$
- Phase resistance :  $R_s = 4.33 \text{ m}\Omega$  at  $T_{coil} = 75^\circ\text{C}$
- D-inductance :  $L_d = 650 \mu\text{H}$  at no-load ( $i_d = 0$ .  $i_q = 0$ )
- Q-inductance :  $L_q = 1.08 \text{ mH}$  at no-load ( $i_d = 0$ .  $i_q = 0$ )
- D-inductance :  $L_d = 668 \mu\text{H}$  at nominal current and MTPA ( $i_d = -300 \text{ A}$ .  $i_q = 520 \text{ A}$ )
- Q-inductance :  $L_q = 967 \mu\text{H}$  at nominal current and MTPA ( $i_d = -300 \text{ A}$ .  $i_q = 520 \text{ A}$ )
- Copper power losses :  $P_{Cu} = 1.7 \text{ kW}$  at  $i_{ph}^{rms} = 424 \text{ A}$  and  $\omega_m = 1500 \text{ min}^{-1}$
- Iron power losses :  $P_{Fe} = 1.68 \text{ kW}$  at  $\omega_m = 1500 \text{ min}^{-1}$  and MTPA ( $i_d = -300 \text{ A}$ )

- Stator mass (without chassis):  $m_s = 160 \text{ kg}$
- Rotor mass (without chassis):  $m_r = 100 \text{ kg}$
- Total motor mass (without chassis):  $m_t = 260 \text{ kg}$

### 19.0.1 Full torque ANSYS analysis

In the following section some additional simulation results have been shown. Simulations have been performed by ANSYS transient analysis and cover the condition of full torque nominal speed operating point. The aim of these simulations is to carry out the behaviour of the machine during maximum torque. The following quantities will be investigated:

- Torque ripple
- Machine inductances value and ripple
- Power losses

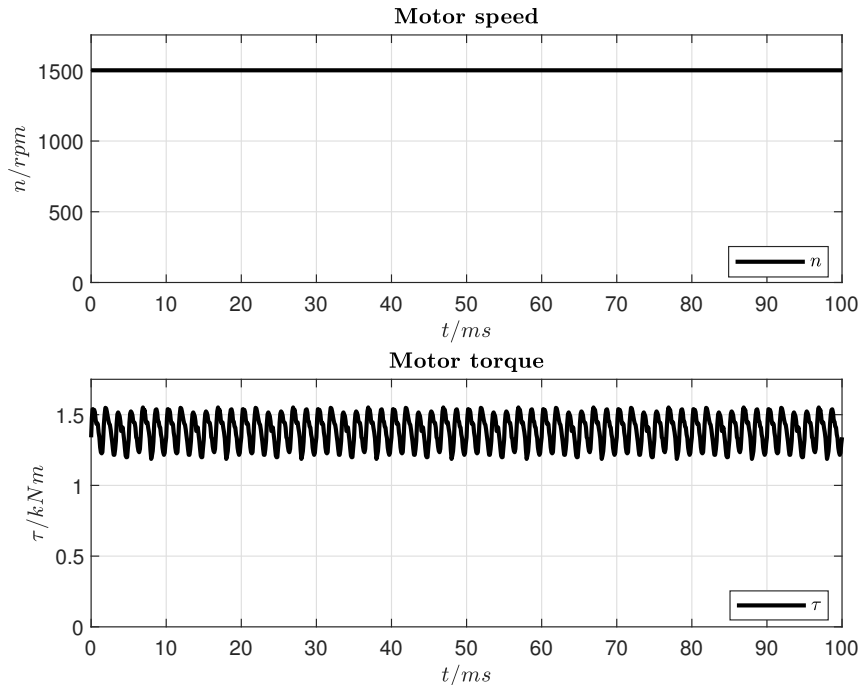


Figure 19.1: Speed and torque behaviour.

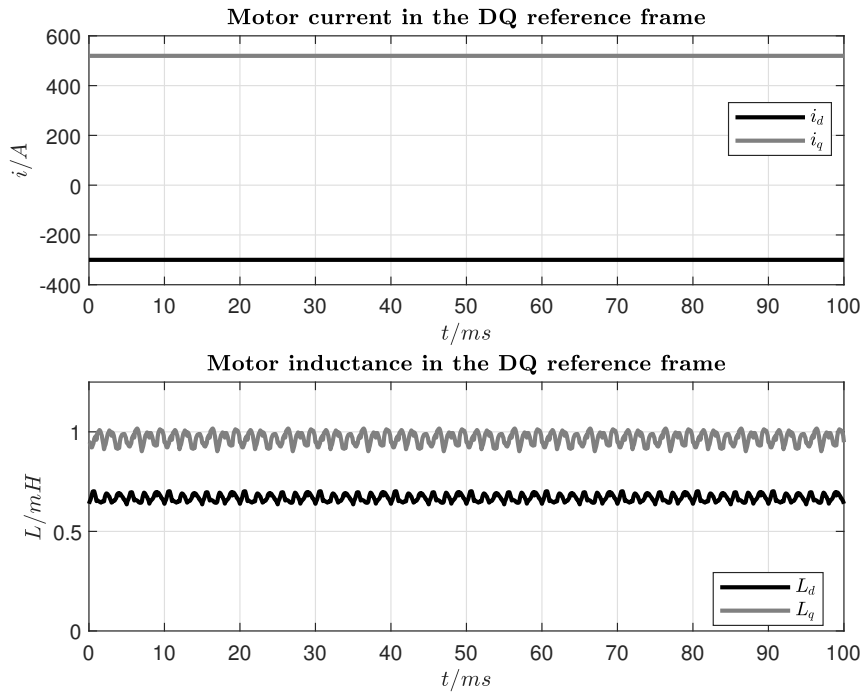


Figure 19.2: Motor current and motor inductances in the DQ reference frame at full load.

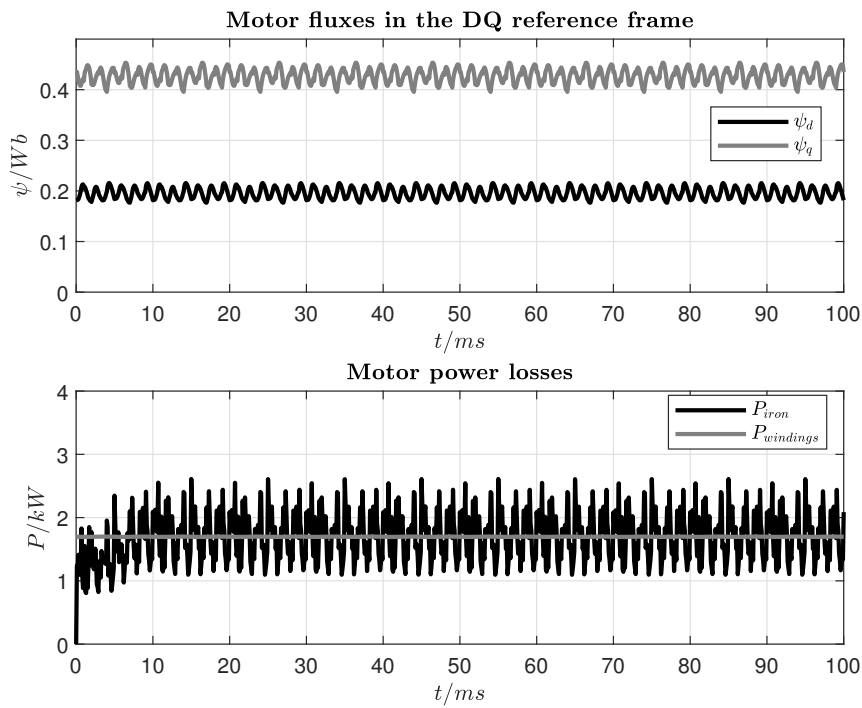


Figure 19.3: Motor fluxes in the DQ reference frame and power losses at full load.

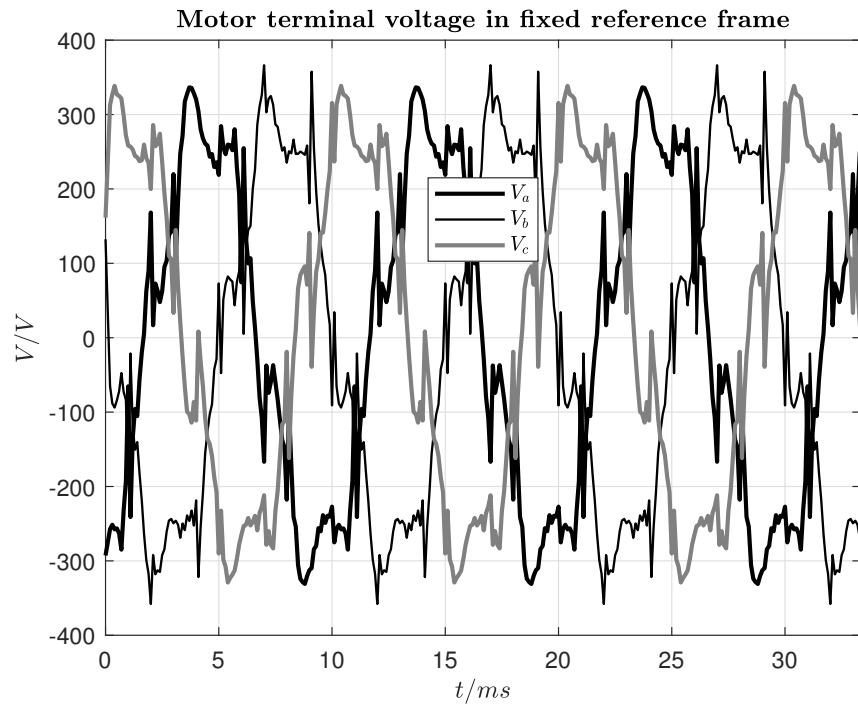


Figure 19.4: Motor terminal voltages at full load.

## Chapter 20

# Case study for Liebherr PR736 full electrification

The motor design we are here to illustrate concerns the full electrification of the PR736 heavy duty vehicle and its hydrostatic power-train. Figure 20.1 shows the torque-speed curve at the driver gear which is connected to the wheel sprocket of the track for one driveline.

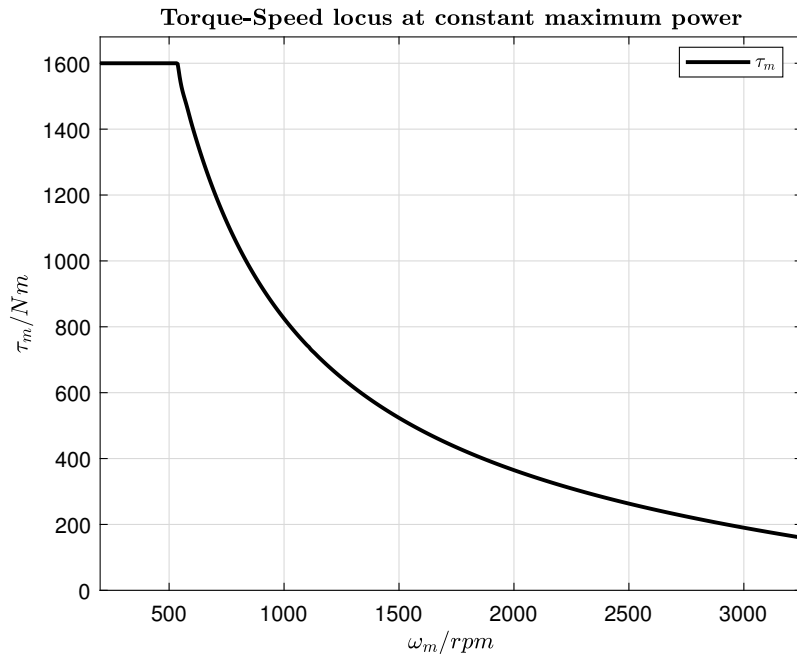


Figure 20.1: Torque speed limit curve.

The nominal power of the driveline is around  $P_{nom} = 85 \text{ kW}$ , the nominal torque is  $\tau_{nom} = 1600 \text{ N m}$  and the maximum speed is  $\omega_{max} = 3100 \text{ min}^{-1}$ .

The whole design results (which follow the chapter ??) are here reported.

Considering the above geometrical dimensions the case of  $\hat{\omega}_m = 3100 \text{ min}^{-1}$ ,  $\hat{\tau}_m = 1600 \text{ N m}$  has been now taken into account, resulting in the following electrical and mechanical characteristics Settings of the variable design parameters

- $L_{stack} = 160 \text{ mm}$  machine length

- $N = 50$  number of turns per coil

### Performance results are as follows

- The nominal torque is obtained at  $i_{phase} = 450$  A peak
- $\psi^M = 2B_g \frac{D_r \pi}{4p} L_{stack} N = 0.27$  Wb from analytical evaluation
- $\psi^M = 0.32$  Wb from Ansys analysis

The magnet flux linkage results in a value which is higher than the original target but can be evaluated during simulation performance its impact into the battery system during over-speed fault management.

- Slot current density :  $j_{sl} = 4.75$  A mm $^{-2}$  at  $i_{ph}^{rms} = 318$  A
- Phase resistance :  $R_s = 12.78$  m $\Omega$  at  $T_{coil} = 75$  °C
- D-inductance :  $L_d = 1.95$  mH at no-load ( $i_d = 0$ .  $i_q = 0$ )
- Q-inductance :  $L_q = 2.25$  mH at no-load ( $i_d = 0$ .  $i_q = 0$ )
- D-inductance :  $L_d = 1.85$  mH at nominal current and MTPA ( $i_d = -225$  A.  $i_q = 390$  A)
- Q-inductance :  $L_q = 2.0$  mH at nominal current and MTPA ( $i_d = -225$  A.  $i_q = 390$  A)
- Copper power losses :  $P_{Cu} = 2.65$  kW at  $i_{ph}^{rms} = 318$  A and  $\omega_m = 500$  min $^{-1}$
- Iron power losses :  $P_{Fe} = 650$  W at  $\omega_m = 500$  min $^{-1}$  and MTPA ( $i_d = -225$  A )
- Stator mass (without chassis):  $m_s = 160$  kg
- Rotor mass (without chassis):  $m_r = 90$  kg
- Total motor mass (without chassis):  $m_t = 250$  kg

#### 20.0.1 Full torque ANSYS analysis

In the following section some additional simulation results has been shown. Simulations have been performed by ANSYS transient analysis and cover the condition of full torque nominal speed operating point. The aim of these simulation is to carry out the behaviour of the machine during maximum torque. The following quantities will be investigated:

- Torque ripple
- Machine inductances value and ripple
- Power losses

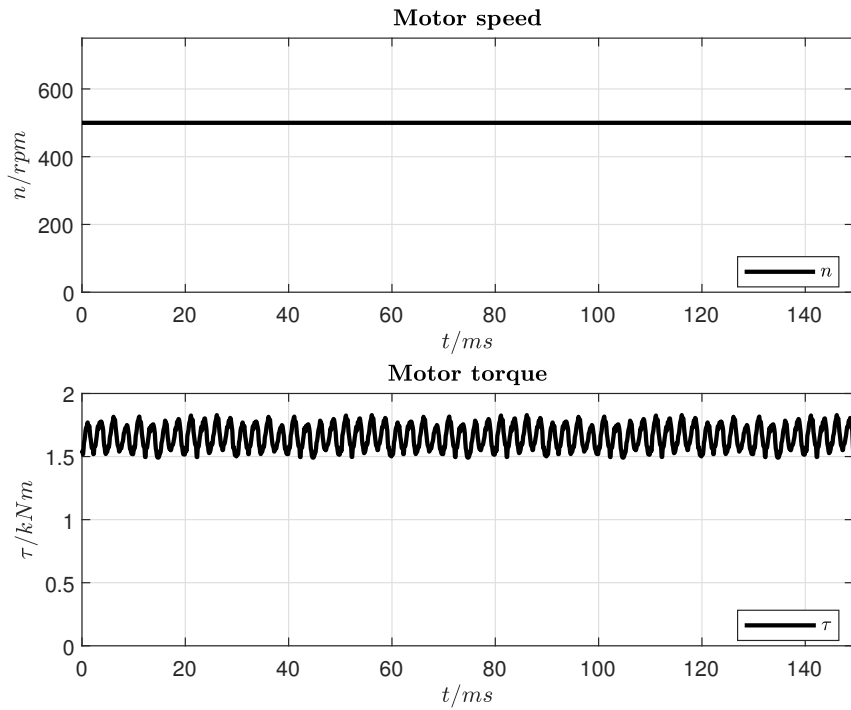


Figure 20.2: Speed and torque behaviour.

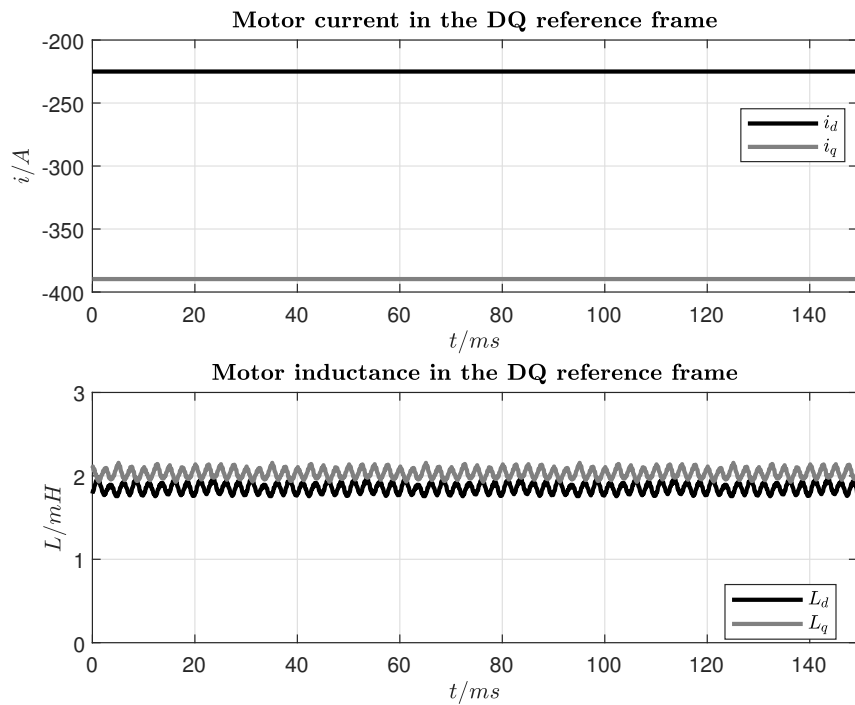


Figure 20.3: Motor current and motor inductances in the DQ reference frame at full load.

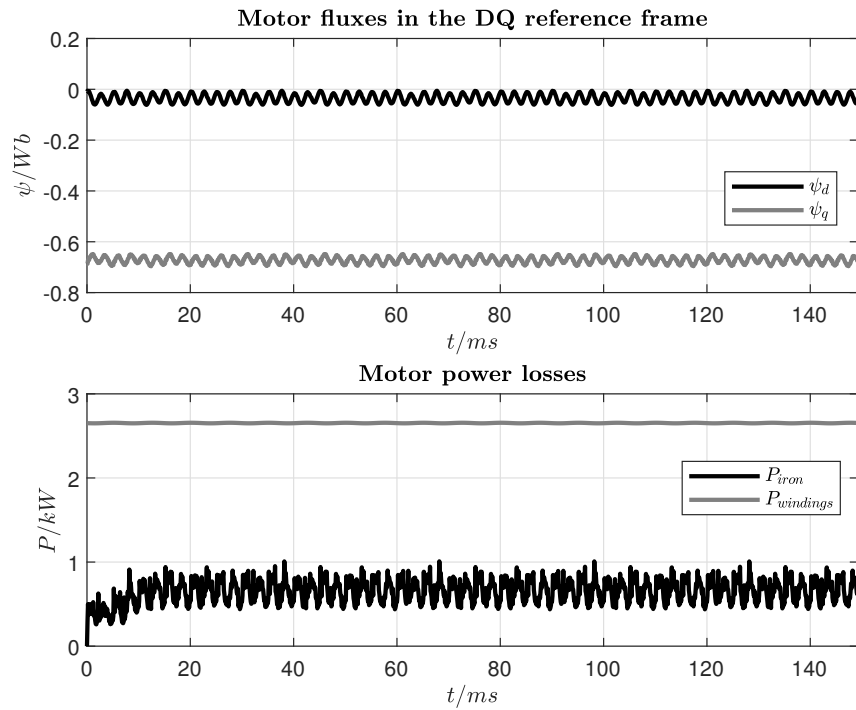


Figure 20.4: Motor fluxes in the DQ reference frame and power losses at full load.

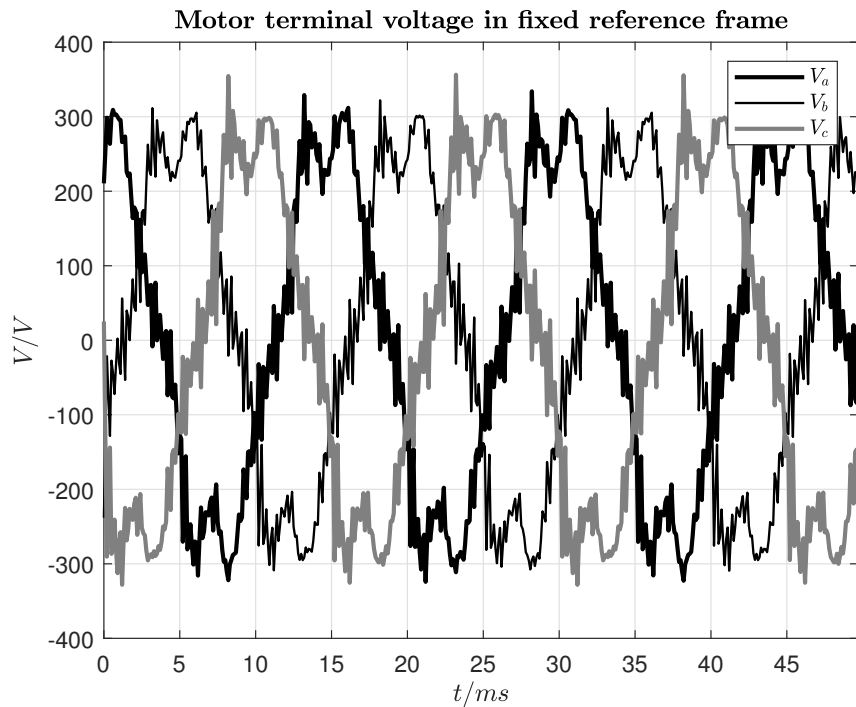


Figure 20.5: Motor terminal voltages at full load.

# Chapter 21

## Mercedes-Benz diesel engine OM471

### 21.1 Technical data

The following technical shall be taken into account

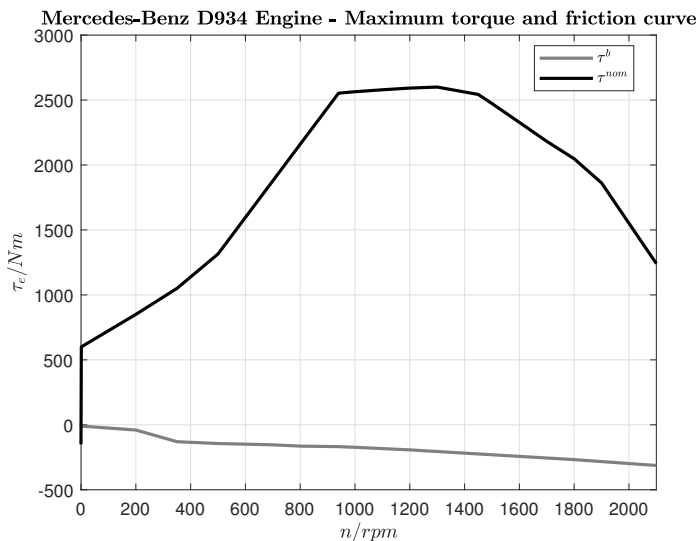


Figure 21.1: Mercedes-Benz diesel engine OM471 - maximum torque and friction curve.

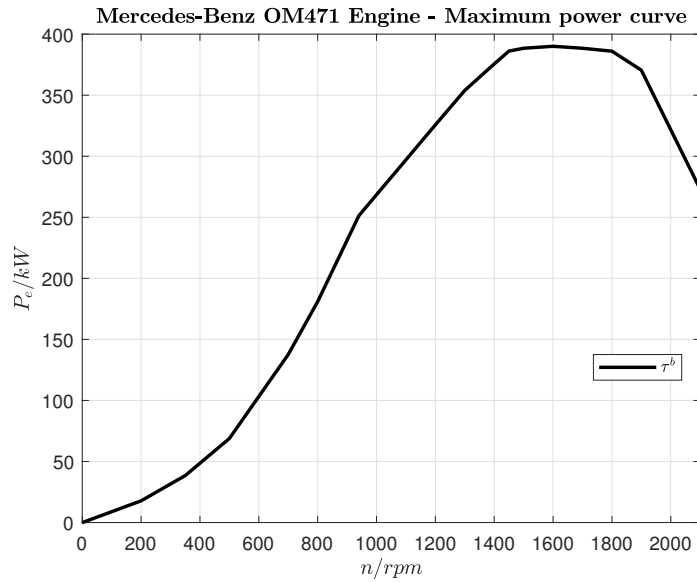


Figure 21.2: Mercedes-Benz diesel engine OM471 - maximum available power at the crankshaft.

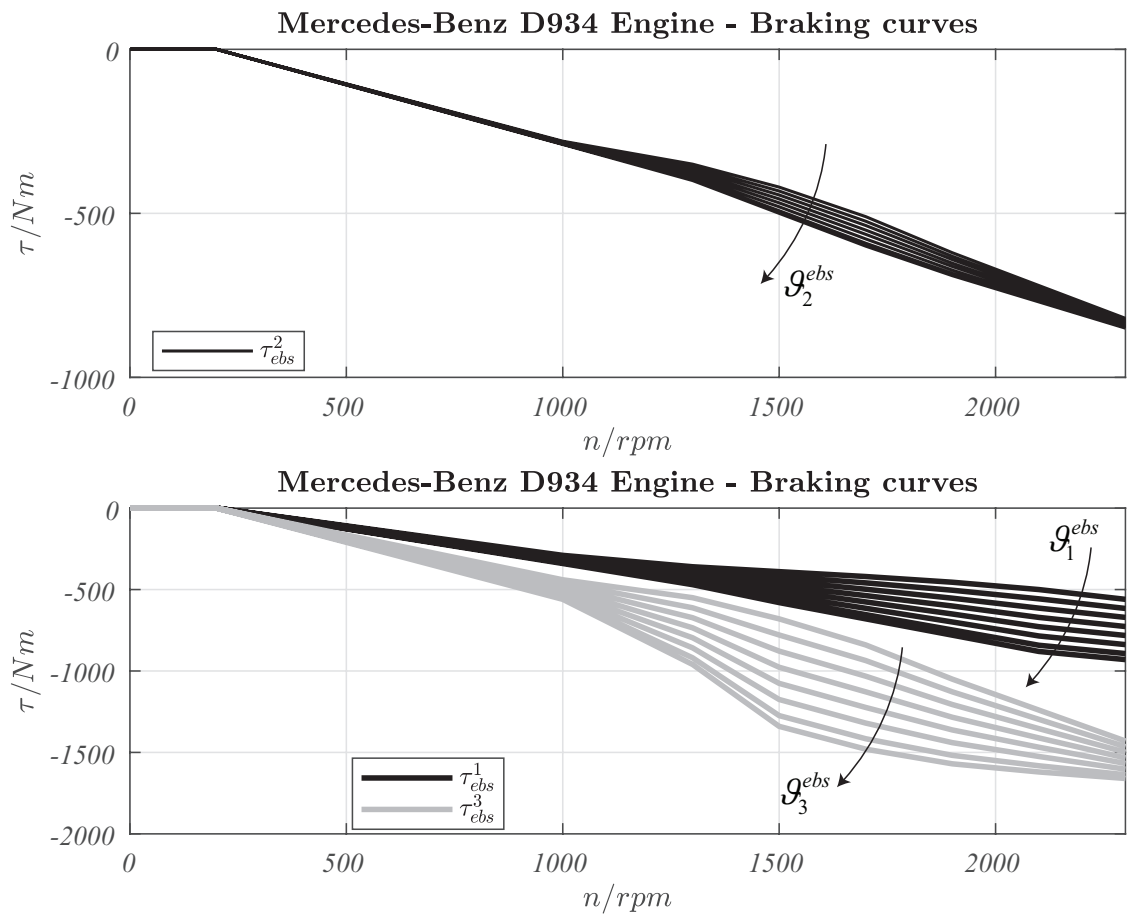


Figure 21.3: Mercedes-Benz diesel engine OM471 - braking curve.

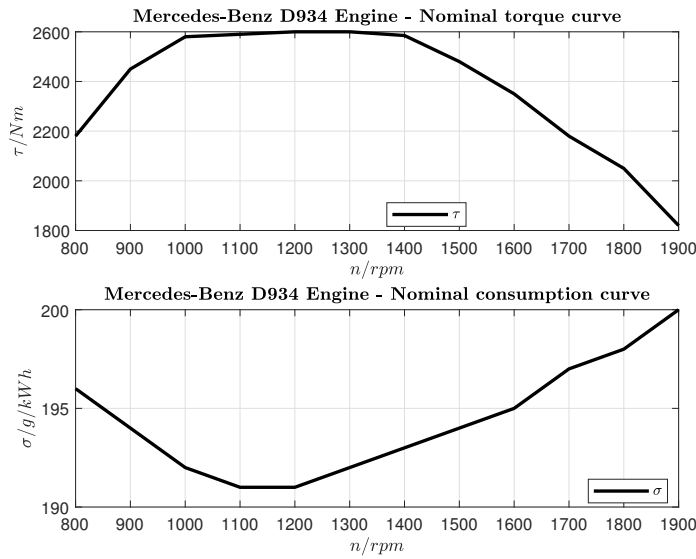


Figure 21.4: Mercedes-Benz diesel engine OM471 - Nominal consumption in [g/kWh].

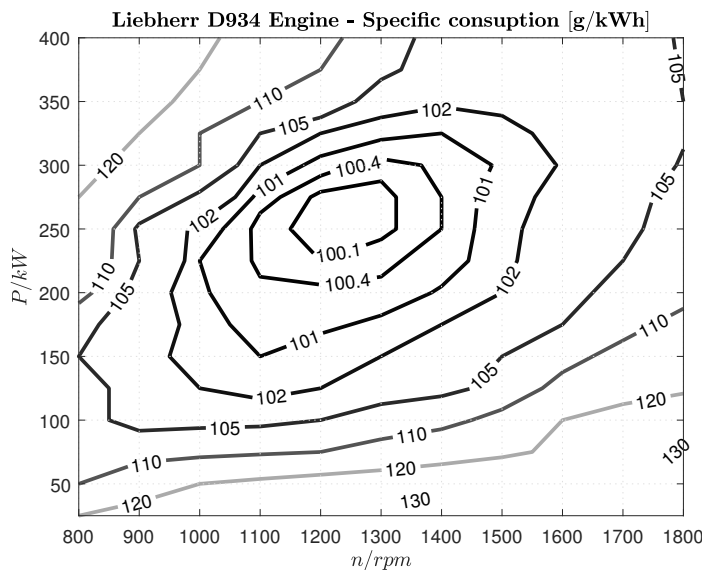


Figure 21.5: Mercedes-Benz diesel engine OM471 - Specific consumption in %.

## 21.2 Equivalent model

In this section the description of the IC-engine is reported. The knowledge of the torque and power curve of the engine plays an important role in the performance of the engine anti-stall control.

In the following, we describe how the IC-engine has been modelized. We start to consider two curves:

- Torque curve: maximum torque available for a given rotor speed and maximum displacement of the throttle.

- Torque friction curve: torque generated by the friction for a given rotor speed. This friction is considered always present, for any value of the throttle. See also Figure 18.1

The mechanical model of the engine can be described as follows

$$J \frac{d\omega_e}{dt} = \theta_f(t) \tau^{nom}(\omega_e) + \tau^b(\omega_e) - \tau_{load} \quad (21.2.1)$$

where  $\tau^{nom}(\omega_e)$  and  $\tau^b(\omega_e)$  are shown in Figure 18.1 while  $\theta_f(t)$  is the throttle which is generated by the external speed loop control as shown in Figure 5.2 and  $J = 7.5 \text{ kg m}^{-2}$ .

The speed control is performed by a PI-controller and it adapts the throttle displacement in order to keep the request speed tracked.

An additional second order filter is taken into account in order to modelize additional dynamics.

The controller can be described as follows

$$\begin{cases} \tilde{\omega}_e(t) = \frac{1}{\omega_e^{\text{nom}}} (\omega_e^{\text{ref}} - \omega_e(t)) \\ \theta(t) = k_p \tilde{\omega}_e(t) + \theta^i(t) \\ \frac{d\theta^i}{dt}(t) = k_i \tilde{\omega}_e(t) \end{cases} \quad (21.2.2)$$

The control output  $\theta$  is passed through a second order filter:

$$\theta_f(s) = \frac{\omega_0^2}{s^2 + 2\zeta\omega_0 s + \omega_0^2} \theta(s) \quad (21.2.3)$$

where  $\zeta = 1$  and  $\omega_0 = 2\pi 25 \text{ Hz}$ .

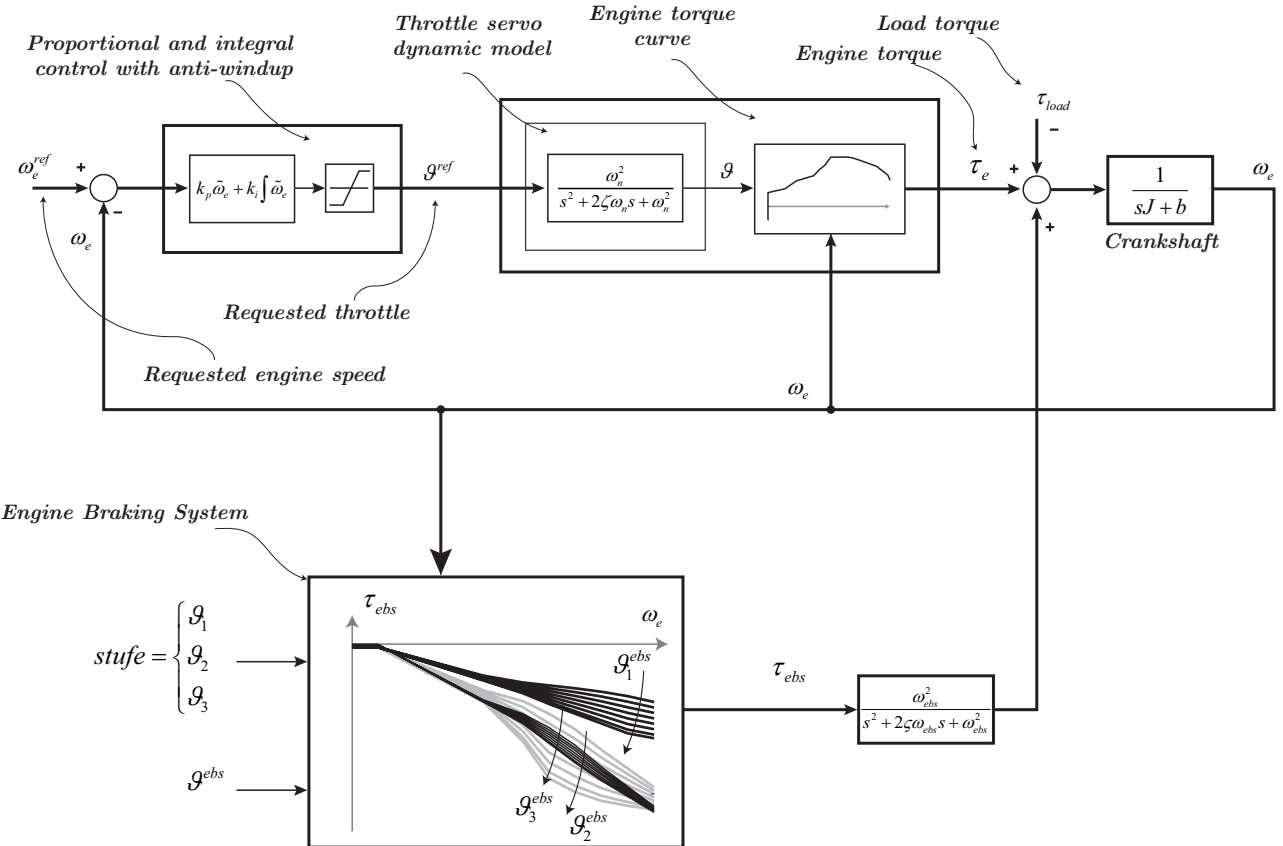


Figure 21.6: Engine model and control architecture.

## Chapter 22

# Case study for Mercedes-Benz diesel engine OM471 electrification

Considering the above geometrical dimensions the case of  $\omega_m^{max} = 2140 \text{ min}^{-1}$ ,  $\hat{\omega}_m = 1600 \text{ min}^{-1}$ ,  $\hat{\tau}_m = 2600 \text{ N m}$  has been now taken into account, resulting in the following electrical and mechanical characteristics Settings of the variable design parameters

- $L_{stack} = 320 \text{ mm}$  machine length
- $N = 24$  number of turns per coil

Performance results are as follows

- The nominal torque is obtained at  $i_{phase} = 750 \text{ A}$  peak
- $\psi^M = 2B_g \frac{D_r \pi}{4p} L_{stack} N = 0.53 \text{ Wb}$  from analytical evaluation
- $\psi^M = 0.6 \text{ Wb}$  from Ansys analysis

The magnet flux linkage results in a value which is higher than the original target but can be evaluated during simulation performance its impact into the battery system during overspeed fault management.

- Slot current density :  $j_{sl} = 3.5 \text{ A mm}^{-2}$  at  $i_{ph}^{rms} = 530 \text{ A}$
- Phase resistance :  $R_s = 4.36 \text{ m}\Omega$  at  $T_{coil} = 75^\circ\text{C}$
- D-inductance :  $L_d = 830 \mu\text{H}$  at no-load ( $i_d = 0$ .  $i_q = 0$ )
- Q-inductance :  $L_q = 1.38 \text{ mH}$  at no-load ( $i_d = 0$ .  $i_q = 0$ )
- D-inductance :  $L_d = 820 \mu\text{H}$  at nominal current and MTPA ( $i_d = -375 \text{ A}$ .  $i_q = 650 \text{ A}$ )
- Q-inductance :  $L_q = 1.21 \text{ mH}$  at nominal current and MTPA ( $i_d = -375 \text{ A}$ .  $i_q = 650 \text{ A}$ )
- Copper power losses :  $P_{Cu} = 2.6 \text{ kW}$  at  $i_{ph}^{rms} = 530 \text{ A}$  and  $\omega_m = 1600 \text{ min}^{-1}$
- Iron power losses :  $P_{Fe} = 3.8 \text{ kW}$  at  $\omega_m = 1600 \text{ min}^{-1}$  and MTPA ( $i_d = -375 \text{ A}$  )

- Stator mass (without chassis):  $m_s = 320 \text{ kg}$
- Rotor mass (without chassis):  $m_r = 200 \text{ kg}$
- Total motor mass (without chassis):  $m_t = 520 \text{ kg}$

### 22.0.1 Full torque ANSYS analysis

In the following section some additional simulation results have been shown. Simulations have been performed by ANSYS transient analysis and cover the condition of full torque nominal speed operating point. The aim of these simulations is to carry out the behaviour of the machine during maximum torque. The following quantities will be investigated:

- Torque ripple
- Machine inductances value and ripple
- Power losses

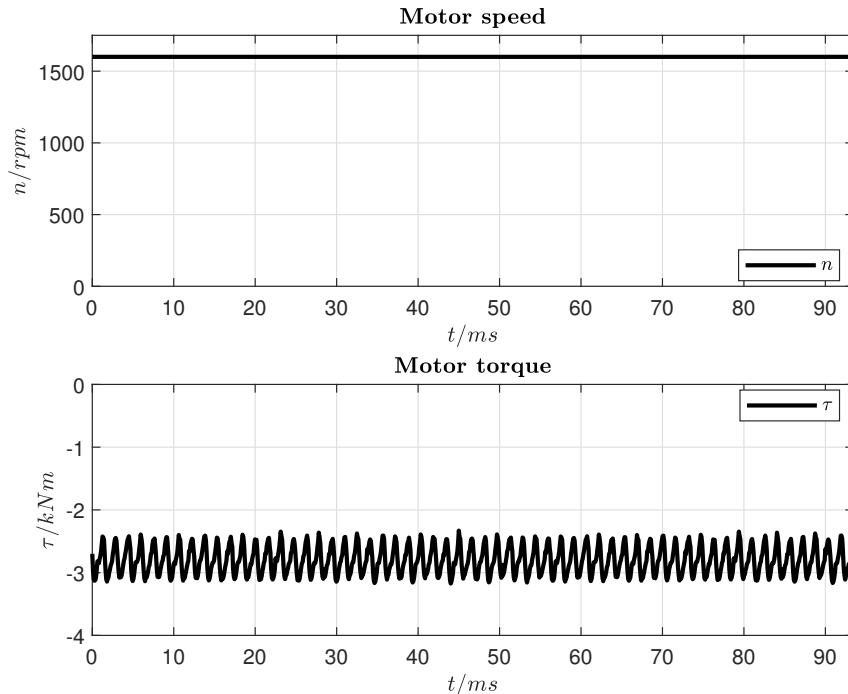


Figure 22.1: Speed and torque behaviour.

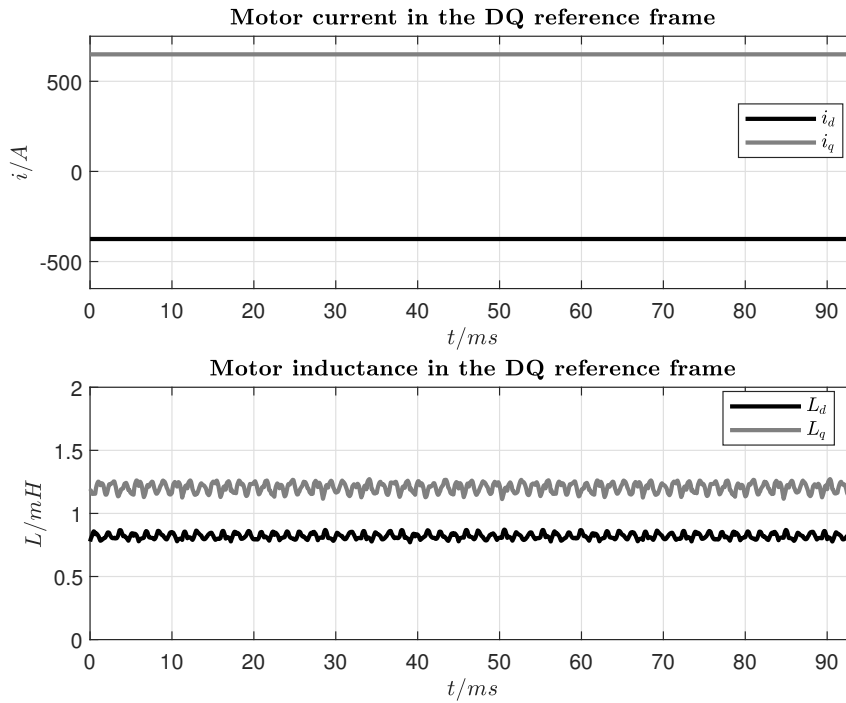


Figure 22.2: Motor current and motor inductances in the DQ reference frame at full load.

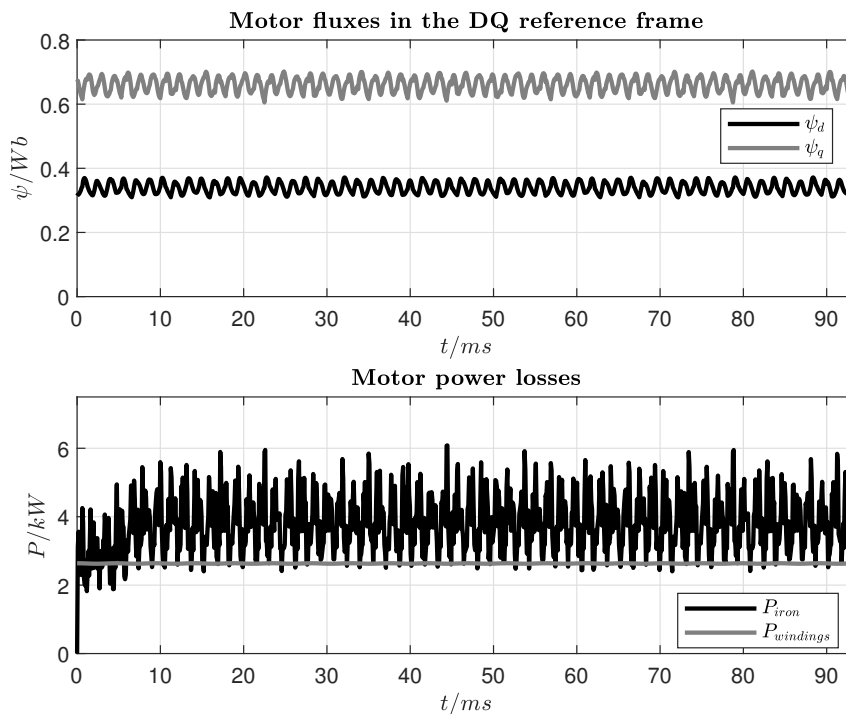


Figure 22.3: Motor fluxes in the DQ reference frame and power losses at full load.

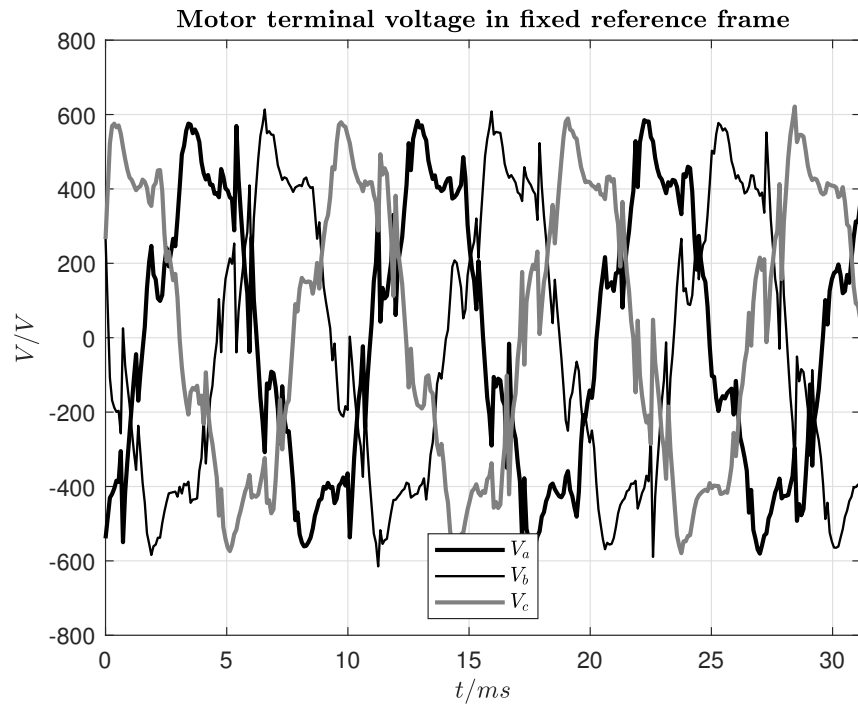


Figure 22.4: Motor terminal voltages at full load.

# **Part IV**

# **Appendix**

## Chapter 23

# Hydraulic Valve Piston Control

### 23.1 Introduction

In what follows we shell present how to model and implement an state feedback control for an hydro-static servo actuator. Figure 23.1 shows the structure of the system, where the main components are as follows:

- An hydraulic servo consisting of two chambers, one piston with symmetrical area coupled to a springs-damper system
- An hydraulic four ways valve
- An linear actuator based on permanent magnet which moves the spool of the hydraulic valve

The whole system perform the hydraulic valve piston. The control input is the voltage  $u_c(t)$  applied to the linear motor. The output, the quantity we want to control is the position of the piston.

By the four-way valve, we can regulate the flow of the hydraulic fluid from a generic ideal pressure source  $p_s$  toward the corresponding chamber (depending by the sign of valve position  $x_v$ ). The hydraulic fluid flowing into the chamber will increase the internal pressure and when the force actuated by the delta pressure over the piston areas overcomes the spring force the piston will move. To stand still in a position the valve orifice must be closed back in order to bring to zero the flows  $q_1(t)$  and  $q_2(t)$ .

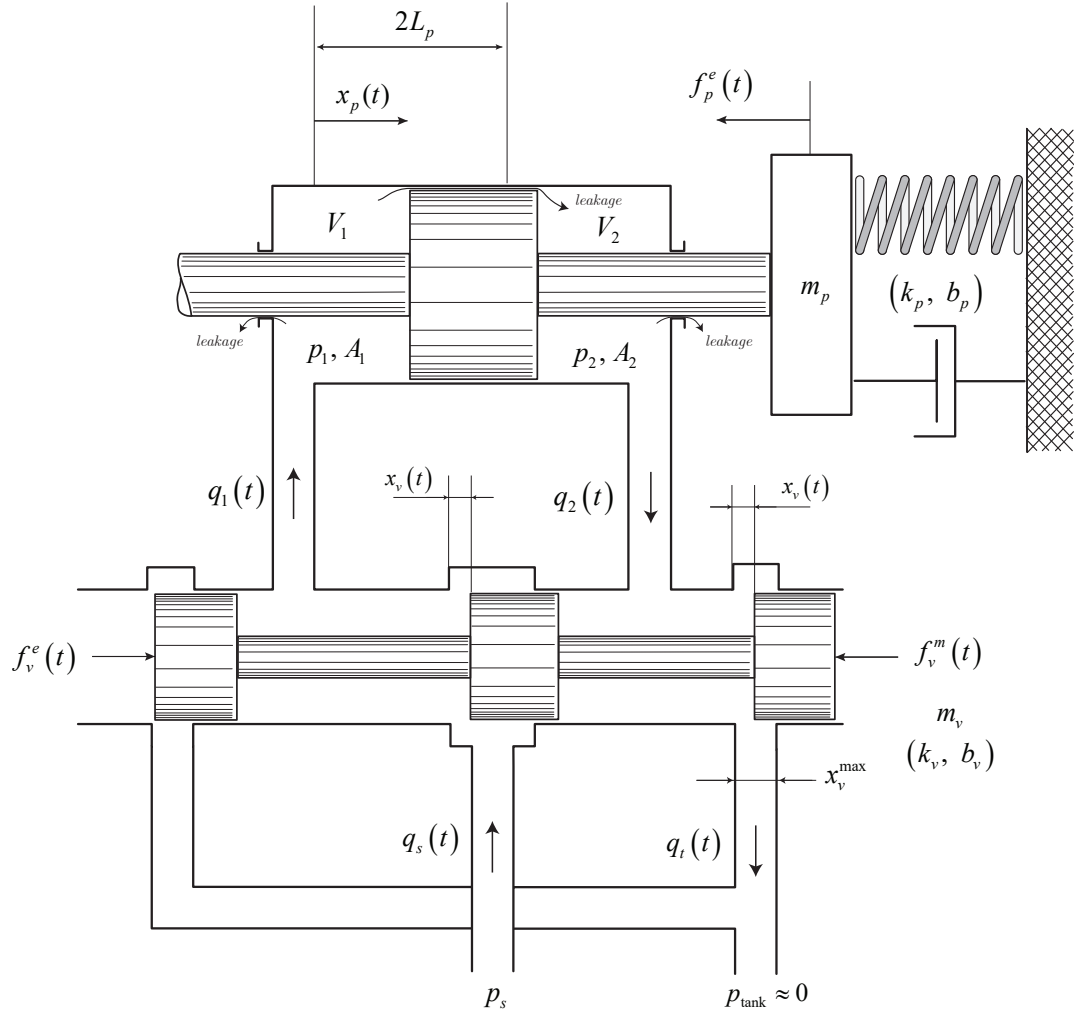


Figure 23.1: Four-way valve actuated piston during position changing.

For our analysis we suppose that the spool of the valve is governed by an electromagnetic linear actuator based on a permanent magnet, this permit to us to correlate the actuated force as linear function of the coil current  $f_v^m = k_f i_c$ . The spool of the valve is connected to a coil (with  $N_c$  turns) which is immersed in a constant magnetic field  $B^M$  generated by a permanent magnet. When a current is applied to the electromagnetic circuit a force is generated by the iteration of current and magnetic field resulting in a movement of the spool of the valve.

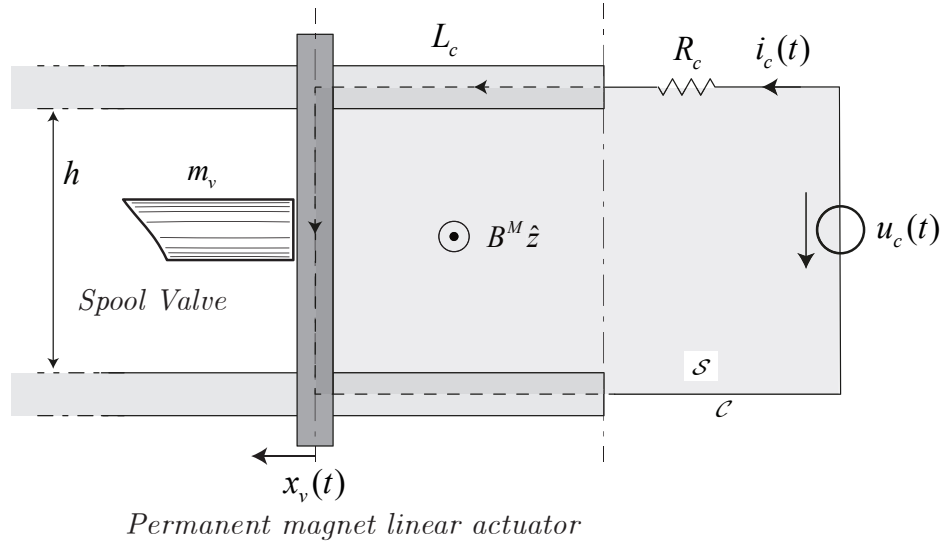


Figure 23.2: Permanent magnet spool valve actuator.

## 23.2 Model derivation

### 23.2.1 Permanent magnet actuator

In this section we are using the moving coil model (as shown in Figure 23.2) as linear permanent magnet motor. This approximation, of a more complex electromechanical actuator, is used for didactic way because the physics behind the system is still the same for a real pm-linear motor. The moving bar is consisting of  $N_c$  turns. The  $N_c$  turns are immersed into a constant and isotropic magnetic field  $\vec{B}^M$  which we suppose generated by a permanent magnet. When the moving coil is carrying a current  $i_c(t)$  the moving coil is subject to a force. In real implementation a linear motor is, in general, fed by a sin-wave current, but its transformation into the spool reference frame (like DQ transformation for rotating system) brings the overall model into a system where the final force applied to the spool of the valve is proportional to a current component, resulting in the form  $f_m^v(t) = k_f i_c(t)$ ,  $f_m^v(t)$  is the force applied to the spool.

To modelize a linear permanent magnet actuator we can start writing the Faraday's law

$$\oint_{\mathcal{C}} \vec{E} \cdot d\vec{l} = -\frac{d}{dt} \int_{\mathcal{S}} \vec{B} \cdot \hat{n} da \quad (23.2.1)$$

considering that the curve  $\mathcal{C}$  and the surface  $\mathcal{S}$  are fixed in space, the right term can also be written as follows

$$\frac{d}{dt} \int_{\mathcal{S}} \vec{B} \cdot \hat{n} da = \frac{d}{dt} \psi(i_c, x_v) \quad (23.2.2)$$

The term  $\psi(i_c, x_v)$  is the total flux linked to the circuit which can also be written as

$$\psi(i_c, x_v) = N_c \phi(i_c, x_v) \quad (23.2.3)$$

where  $N_c$  is an equivalent number of turns.

According to [J.R. Hendershot, 2010] the “flux rule” — that the emf in a circuit is equal to the rate of change of the magnetic flux through the circuit — applies whether the flux changes

because the field changes or because the circuit moves we can exploit the flux derivative as follows

$$\frac{d}{dt}\phi(i_c, x_v) = \frac{\partial\phi(i_c, x_v)}{\partial i_c} \frac{di_c(t)}{dt} + \frac{\partial\phi(i_c, x_v)}{\partial x_v} \frac{dx_v(t)}{dt} \quad (23.2.4)$$

the first term at the right side can be written as follows

$$\frac{\partial\phi(i_c, x_v)}{\partial x_v} \frac{dx_v(t)}{dt} = \frac{\partial Bx_v h}{\partial x_v} v_v(t) \approx B^M h v_v(t) \quad (23.2.5)$$

where  $h$  is the height of the coil and we suppose the magnetic field due to the current  $i_c(t)$  is negligible respect to  $B^M$  which is the magnitude of the permanent magnet magnetic field and it is considered a constant parameter.

The second term become

$$\frac{\partial\phi(i_c, x_v)}{\partial i_c} \frac{di_c(t)}{dt} = L'_c(x_v) \frac{di_c(t)}{dt} \approx L'_c \frac{di_c(t)}{dt} \quad (23.2.6)$$

Turning back to Eq. (23.2.1) we can write

$$\underbrace{\int_{(-)}^{(+)} \vec{E} \cdot d\vec{l}}_{\text{source}} + \underbrace{\int \vec{E} \cdot d\vec{l}}_{\text{resistor}} = -N_c B^M h v_v(t) - L_c \frac{di_c(t)}{dt} \quad (23.2.7)$$

where  $L_c = N_c L'_c$  and where

$$-u_c = \underbrace{\int_{(-)}^{(+)} \vec{E} \cdot d\vec{l}}_{\text{source}} \quad (23.2.8)$$

$$i_c R_c = \underbrace{\int \vec{E} \cdot d\vec{l}}_{\text{resistor}} \quad (23.2.9)$$

hence, we obtain the Kirchhoff's voltage law applied to the circuit as follows

$$u_c(t) - R_c i_c(t) - L_c \frac{di_c(t)}{dt} - N_c B^M h v_v(t) = 0 \quad (23.2.10)$$

To complete the linear pm-actuator model we must add the mechanical equations using the Newton's law. To apply the Newton's law we first must calculate the corresponding force actuated by the iteration between the current  $i_c$  and the magnetic field  $\vec{B}^M$ .

The expression of the force due to the current  $i_c$  in the magnetic field  $\vec{B}^M$  is evaluated as follows

$$\vec{f}(t) = i(t) \int_{\text{wire}} d\vec{l} \times \vec{B}^{\text{ext}} \quad (23.2.11)$$

where  $\vec{B}^{\text{ext}}$  is an external field. Applying the integration of Eq. (24.0.26) it results in the following equation (**integration path follows the current direction**)

$$f_v^m(t) = N_c i_c(t) \int_h^0 d\vec{l} \times \vec{B}^M = N_c B^M h i_c(t) \quad \text{positive x-direction} \quad (23.2.12)$$

where  $N_c$  is the number of turns linkage to the magnetic field. The complete set of system equations becomes

$$\begin{cases} \frac{dx_v(t)}{dt} = v_v(t) \\ \frac{dv_v(t)}{dt} = N_c \frac{B^M h}{m_v} i_c(t) - \frac{b_v}{m_v} v_v(t) - \frac{1}{m_v} f_v^e(t) \\ \frac{di_c(t)}{dt} = -\frac{R_c}{L_c} i_c(t) - \frac{1}{L_c} N_c B^M h v_v(t) + \frac{1}{L_c} u_c(t) \end{cases} \quad (23.2.13)$$

the first two equations represent the dynamic motion of the bar where the force  $f_v^m(t) = N_c B^M h i(t)$  is generated by the interaction of the current  $i_c(t)$  and the magnetic field  $\vec{B}^M$ . The third equation represents the Kirchhoff's voltage law of the electrical circuit which generates the current  $i_c(t)$  by applying the voltage  $u_c(t)$ . The equivalent auto-inductance  $L_c$  and the back-emf term,  $N_c B^M h v_v(t)$  represent the effect of the Faraday's law.

### 23.2.2 Four-ways valve piston actuated

As reported in Figure 23.1 the system we are going to describe is made by the coupling of a four-way valve and a double chambers piston. For model representation we are considering the overall leakage and offset orifices to be zero, moreover we are supposing the system is symmetrical  $A_1 = A_2$ , then, we can write the following set of continuity equations

$$\begin{cases} q_1(t) = \frac{dV_1(t)}{dt} + \frac{V_1(t)}{\beta} \frac{dp_1(t)}{dt} \\ -q_2(t) = \frac{dV_2(t)}{dt} + \frac{V_2(t)}{\beta} \frac{dp_2(t)}{dt} \end{cases} \quad (23.2.14)$$

The volume of the piston chambers may be written as follows (we are assuming the piston is centered)

$$\begin{cases} V_1(t) = V_0 + A_1 x_p(t) \\ V_2(t) = V_0 - A_2 x_p(t) \end{cases} \quad (23.2.15)$$

considering  $A_1 = A_2 = A$  we obtain

$$\begin{cases} V_1(t) = V_0 + A x_p(t) \\ V_2(t) = V_0 - A x_p(t) \end{cases} \quad (23.2.16)$$

and

$$\begin{cases} \frac{dV_1(t)}{dt} = A v_p(t) \\ \frac{dV_2(t)}{dt} = -A v_p(t) \end{cases} \quad (23.2.17)$$

which bring to the following state equations

$$\begin{cases} \frac{dp_1(t)}{dt} = \beta \left[ \frac{q_1(t) - Av_p(t)}{V_0 + Ax_p(t)} \right] \\ \frac{dp_2(t)}{dt} = \beta \left[ \frac{Av_p(t) - q_2(t)}{V_0 + A(-x_p(t))} \right] \\ \frac{dv_p(t)}{dt} = \frac{1}{m_p} \left[ A(p_1(t) - p_2(t)) - b_p v_p(t) - k_p x_p(t) - f_p^e(t) \right] \\ \frac{dx_p(t)}{dt} = v_p(t) \end{cases} \quad (23.2.18)$$

where  $\rho = 850 \text{ kg m}^{-3}$  is the density of the fluid,  $\beta = 1.2 \times 10^9 \text{ Pa}$  is the bulk modulus,  $x_v$  is the valve orifice where we suppose the orifice area is  $x_v \cdot x_v^{\max}$ ,  $k_p$  is the spring coefficient,  $b_p$  the damping coefficient and  $m_p$  the mass of the piston. Like in most of the hydraulic system the ratio between force and mass is very high that means the inertia effects are in general less significant.

Due to compressibility effect the flow  $q_1(t)$  and the flow  $q_2(t)$  are different as consequence of the conservation of the mass flow between chamber 1 and chamber 2.

The first two equations of Eq. (23.2.18) represent the state equation of the pressure of the chambers. The flow  $q_1(t)$  is function of the delta pressure between a orifice, hence we can write the following relations

$$q_1(t) = \begin{cases} x_v x_v^{\max} \sqrt{\frac{2}{\rho}} \sqrt{|p_s - p_1|} \operatorname{sign}(p_s - p_1) & \text{for } x_v > 0 \\ x_v x_v^{\max} \sqrt{\frac{2}{\rho}} \sqrt{|p_1 - p_{\text{tank}}|} \operatorname{sign}(p_1 - p_{\text{tank}}) & \text{for } x_v < 0 \end{cases} \quad (23.2.19)$$

while  $q_2(t)$  is given the following relations

$$q_2(t) = \begin{cases} x_v x_v^{\max} \sqrt{\frac{2}{\rho}} \sqrt{|p_2 - p_{\text{tank}}|} \operatorname{sign}(p_2 - p_{\text{tank}}) & \text{for } x_v > 0 \\ x_v x_v^{\max} \sqrt{\frac{2}{\rho}} \sqrt{|p_2 - p_s|} \operatorname{sign}(p_s - p_2) & \text{for } x_v < 0 \end{cases} \quad (23.2.20)$$

Moreover, according Figure 23.1 we have to consider the following relations:

$$x_v > 0 \Rightarrow \begin{cases} q_s(t) = q_1(t) \\ q_t(t) = q_2(t) \end{cases} \quad (23.2.21)$$

$$x_v < 0 \Rightarrow \begin{cases} q_s(t) = -q_2(t) \\ q_t(t) = -q_1(t) \end{cases} \quad (23.2.22)$$

and

$$x_v = 0 \Rightarrow \begin{cases} q_s(t) = 0 \\ q_t(t) = 0 \end{cases} \quad (23.2.23)$$

The pressure source  $p_s$  is generated by a pressure controlled pump. This model is not here described but is available in the released simscape library.

### 23.2.3 The whole model

The final system is made the union between the pm-magnet actuator and the double chamber piston and it consists of seven ordinary differential equations, as follows

$$\left\{ \begin{array}{l} \frac{dx_v(t)}{dt} = v_v(t) \\ \frac{dv_v(t)}{dt} = N_c \frac{B^M h}{m_v} i_c(t) - \frac{b}{m_v} v_v(t) \\ \frac{di_c(t)}{dt} = -\frac{R_c}{L_c} i_c(t) - \frac{1}{L_c} N_c B^M h v_v(t) + \frac{1}{L_c} u_c(t) \\ \frac{dp_1(t)}{dt} = \beta \left[ \frac{q_1(t) - Av_p(t)}{V_0 + Ax_p(t)} \right] \\ \frac{dp_2(t)}{dt} = \beta \left[ \frac{Av_p(t) - q_2(t)}{V_0 + A(-x_p(t))} \right] \\ \frac{dv_p(t)}{dt} = \frac{1}{m_p} \left[ A(p_1(t) - p_2(t)) - b_p v_p(t) - k_p x_p(t) - f_p^e(t) \right] \\ \frac{dx_p(t)}{dt} = v_p(t) \end{array} \right. \quad (23.2.24)$$

where

$$q_1(t) = \begin{cases} x_v x_v^{\max} \sqrt{\frac{2}{\rho}} \sqrt{|p_s - p_1|} \operatorname{sign}(p_s - p_1) & \text{for } x_v > 0 \\ x_v x_v^{\max} \sqrt{\frac{2}{\rho}} \sqrt{|p_1 - p_{\text{tank}}|} \operatorname{sign}(p_1 - p_{\text{tank}}) & \text{for } x_v < 0 \end{cases} \quad (23.2.25)$$

$$q_2(t) = \begin{cases} x_v x_v^{\max} \sqrt{\frac{2}{\rho}} \sqrt{|p_2 - p_{\text{tank}}|} \operatorname{sign}(p_2 - p_{\text{tank}}) & \text{for } x_v > 0 \\ x_v x_v^{\max} \sqrt{\frac{2}{\rho}} \sqrt{|p_2 - p_s|} \operatorname{sign}(p_s - p_2) & \text{for } x_v < 0 \end{cases} \quad (23.2.26)$$

the disturbance

$$f_v^e(t)$$

applied to the spool of the valve has been omitted because is considered negligible, while the disturbance

$$f_p^e(t)$$

applied to the piston is taken into account.

While the pm-actuator is represented by a liner time invariant system, the double chamber piston is a non-linear system. In order to implement a state feedback control strategy we have to linearize the model around a steady state point. Due to the complexity of the model, the resulting linearized model is still complex. A possible different approach could be to evaluate the time response of the system when is driven by a step input signal. This approach will be carried out in the next section.

### 23.2.3.1 System parameters

- Permanent magnet actuator
  - $B^M = 1 \text{ Wb m}^{-2}$
  - $m_v = 0.05 \text{ kg}$
  - $L_c = 10 \text{ mH}$
  - $R_c = 10 \Omega$
  - $b_v = 2 \times 10^3 \text{ N s m}^{-1}$
  - $h = 0.05 \text{ m}$
  - $x_v^{\max} = 2.75 \text{ mm}$
  - $N_c = 1000$
  - $u_c^{\max} = 25 \text{ V}$
- Four-way valve bi-chambers piston with load
  - $\beta = 1.2 \times 10^9 \text{ Pa}$
  - $\rho = 850 \text{ kg m}^{-3}$
  - $D_1 = 0.1 \text{ m}$
  - $D_2 = 0.1 \text{ m}$
  - $L_p = 1 \text{ m}$
  - $m_p = 25 \text{ kg}$
  - $k_p = 100 \text{ kN m}$
  - $b_p = 200 \text{ N s m}^{-1}$

### 23.2.4 System approximation

In the following section we try to find a way to represent the physical system with a simpler model which cover its main dynamic. Applying test signal to the input  $u_c(t)$  we evaluate the behaviour of the output  $x_p(t)$  in such a way to try to write down a possible approximated linear representation of the form  $X_p(s) = H_s(s)U_c(s)$  where  $U_c(s)$  is the applied voltage in the Laplace domain and  $X_p(s)$  is the piston position also in the Laplace domain.

In order to identify the system a set of different test signals are applied. As shown in the Figure 23.3, from the time response of the physical system we can approximate the seven order model by a simpler double integrator, hence the transfer function the system could be modeled as follows

$$X_p(s) = k \frac{1}{s^2} U_c(s) \quad (23.2.27)$$

where the value of the parameters  $k$  can be determined experimentally. Once the parameters  $k$  have been identified the model representation is ended. In order to implement a state feedback control with a state observer the state space representation of the model must be taken into account.

The transfer function

$$H(s) = k \frac{1}{s^2}$$

can be represented in state space form using the controllable canonical form as follows

$$\tilde{\mathbf{A}} = \begin{bmatrix} 0 & 1 \\ 0 & 0 \end{bmatrix} \quad \tilde{\mathbf{B}} = \begin{bmatrix} 0 \\ 1 \end{bmatrix} \quad \mathbf{C} = [k \ 0] \quad (23.2.28)$$

Resulting in the following system

$$\begin{aligned} \dot{\vec{x}}(t) &= \tilde{\mathbf{A}}\vec{x}(t) + \tilde{\mathbf{B}}u(t) \\ y(t) &= \mathbf{C}\vec{x}(t) \end{aligned} \quad (23.2.29)$$

where  $u(t) = u_c(t)$  and  $y(t) = x_p(t)$ .

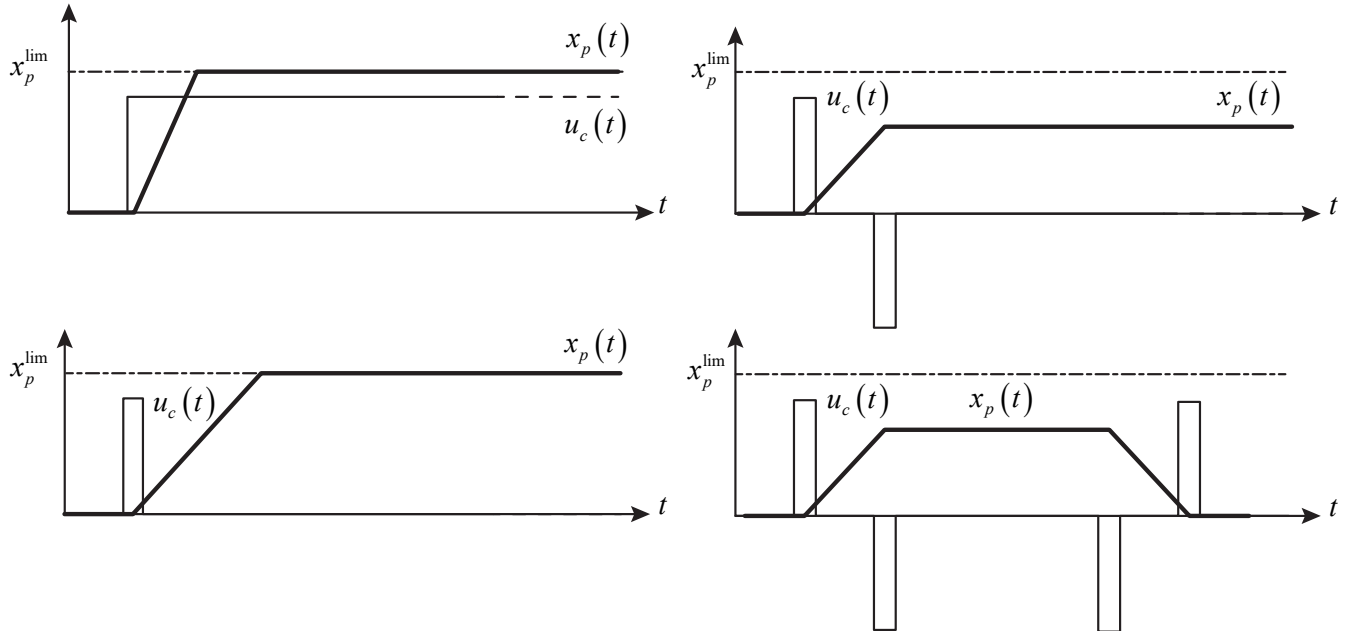


Figure 23.3: Description of the test signals used for system identification and linearization.

### 23.3 Control implementation

In this laboratory course we want to show how to implement a controller in both time domains: continuous and discrete time. The discrete time control implementation will be done using a direct C-code using the C-caller function. The C-caller function permit to use the proper code implementation and can be a very useful strategy to generate a very robust code with minimum of bugs. As already mention the control system strategy is based on state feedback control and state observer as shown in Figure 23.4 for the continuous time domain and as shown in Figure 23.5 for the discrete time domain.

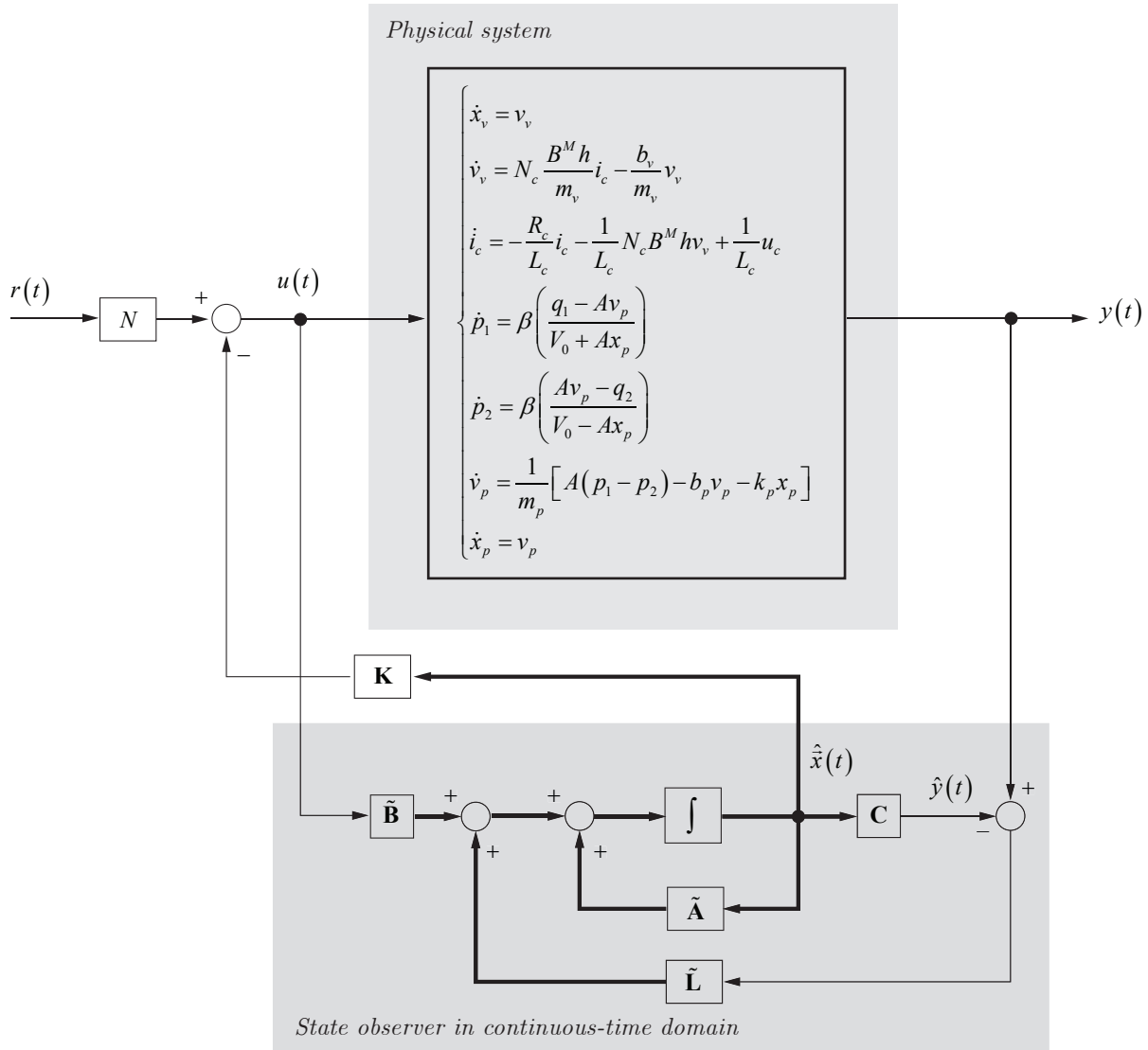


Figure 23.4: Control system layout based on state feedback and state observer for the continuous time domain.

In the next sections we will present the design of these controllers.

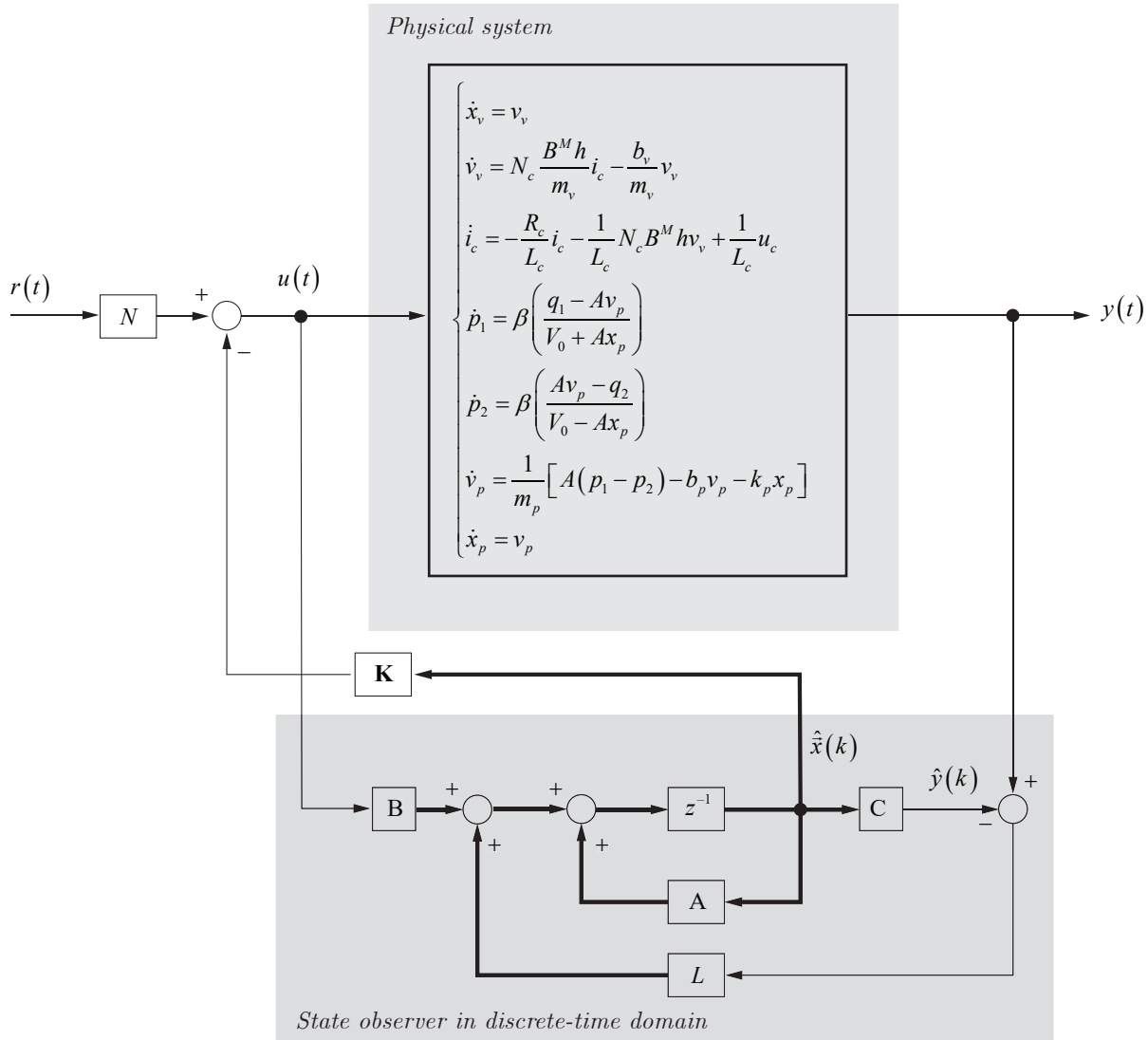


Figure 23.5: Control system layout based on state feedback and state observer for the discrete time domain.

### 23.3.1 Continuous-time domain

The first implementation will be carried out in continuous time domain. This is a good method to verify the feasibility of our control strategy. The control strategy layout is reported in Figure 23.7 where the physical system is represented with its linear approximation. The linear approximation is only used to design the controller. Once the controller is designed it will be implemented in the full-order system shown in Figure 23.4.

Pole placement problem can be solved easily with **Matlab** by two commands: `acker()` or `place()` for the computation of the feedback-gain matrix  $\mathbf{K}$ . The command `acker()` is based on Ackermann's formula. This command applies to single input system only. The desired closed-loop poles can include multiple poles (pole located at the same place).

If the system involves multiple inputs, for a specified set of closed-loop poles the state-feedback gain matrix  $\mathbf{K}$  is not unique and we have an additional freedom to choose  $\mathbf{K}$ . There are many approaches to constructively utilize this additional freedom to determine  $\mathbf{K}$ . One

common use is to maximize the stability margin. The pole placement based on this approach is called the robust pole placement. The matlab command for the robust pole placement is `place()`.

Although the command `place` can be used for both single-input and multiple-input systems, this command requires that the multiplicity of poles in the desired closed-loop poles be no greater than the rank of  $\mathbf{B}$ . That is, if matrix  $\mathbf{B}$  is an  $n \times 1$  matrix, the command `place()` requires that there be no multiple poles in the set of desired close-loop poles.

For single input systems, the commands `acker()` and `place()` yield the same  $\mathbf{K}$ .

To use the command `acker`, we first enter the following matrices

$$\mathbf{A} \quad \mathbf{B} \quad \mathbf{P}_{sf}$$

where  $\mathbf{P}_{sf}$  is the matrix consisting of the desired closed-loop poles such that

$$\mathbf{P}_{sf} = \begin{bmatrix} p_1^{sf} & p_2^{sf} & \cdots & p_n^{sf} \end{bmatrix}$$

The matrix  $\mathbf{K}$  can be derived by the command

$$\mathbf{K} = \text{acker}(\mathbf{A}, \mathbf{B}, \mathbf{P}_{sf});$$

Once the feedback-gain matrix  $\mathbf{K}$  has been design, the scaling matrix  $N$  shall be calculated.

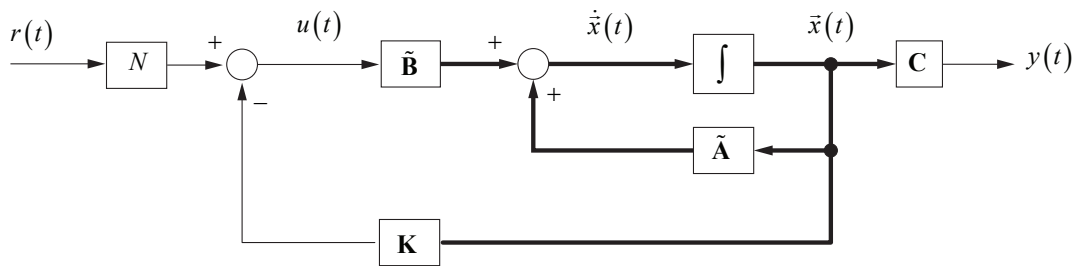


Figure 23.6: State feedback control.

Considering Figure 23.6 we can write the following equation

$$\dot{\vec{x}}(t) = \tilde{\mathbf{A}}\vec{x}(t) + \tilde{\mathbf{B}}(Nr(t) - \mathbf{K}\vec{x}(t)) \quad (23.3.1)$$

In steady state condition we can suppose  $\dot{\vec{x}}(t) = 0$  and Eq. (23.3.1) becomes

$$0 = \tilde{\mathbf{A}}\vec{x}_\infty + \tilde{\mathbf{B}}(Nr_\infty - \mathbf{K}\vec{x}_\infty) \quad (23.3.2)$$

or

$$\vec{x}_\infty = -(\tilde{\mathbf{A}} - \tilde{\mathbf{B}}\mathbf{K})^{-1}\tilde{\mathbf{B}}Nr_\infty \quad (23.3.3)$$

and in steady state we want to satisfy the following condition  $y_\infty = r_\infty$

$$y_\infty = \mathbf{C}\vec{x}_\infty = -\mathbf{C}(\tilde{\mathbf{A}} - \tilde{\mathbf{B}}\mathbf{K})^{-1}\tilde{\mathbf{B}}Nr_\infty = r_\infty \quad (23.3.4)$$

which brings to the following definition of  $N$  ( $N$  is scalar)

$$N = -\frac{1}{\mathbf{C}(\tilde{\mathbf{A}} - \tilde{\mathbf{B}}\mathbf{K})^{-1}\tilde{\mathbf{B}}} \quad (23.3.5)$$

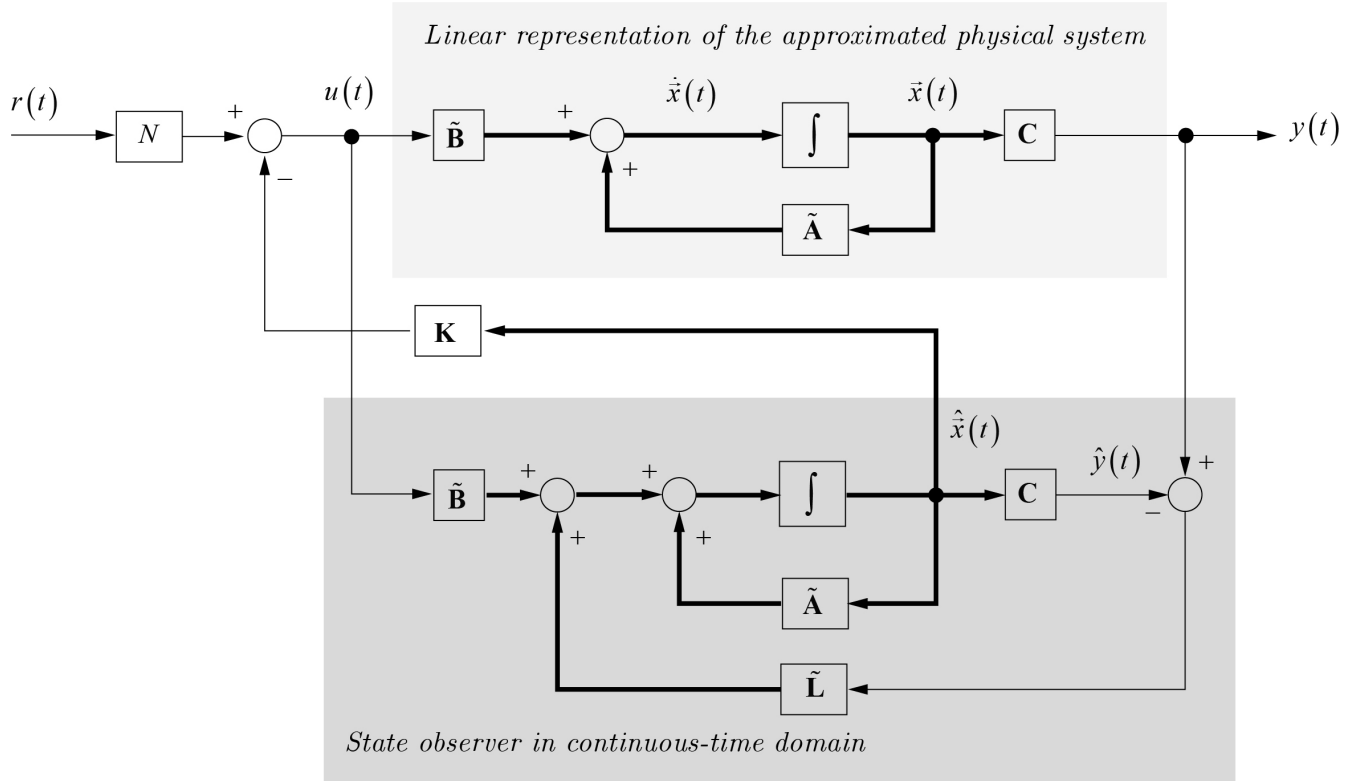


Figure 23.7: Control system layout of the approximated model in continuous time domain.

Regarding the observer block we can consider the following system equation:

$$\begin{aligned}\dot{\hat{x}}(t) &= \tilde{\mathbf{A}} \hat{x}(t) + \tilde{\mathbf{B}} u(t) + \tilde{\mathbf{L}} (\vec{y}(t) - \hat{y}(t)) \\ \hat{y}(t) &= \mathbf{C} \hat{x}(t)\end{aligned}\tag{23.3.6}$$

where  $\tilde{\mathbf{L}}$  matrix gain is obtained by the pole placement procedure.

Let  $\mathbf{P}_{obs}$  be the desired poles regarding the state observer where

$$\mathbf{P}_{obs} = [p_1^{obs} \ p_2^{obs} \ \cdots \ p_n^{obs}]$$

the matrix gain  $\tilde{\mathbf{L}}$  can be determined by the `acker` command in matlab:

```
L = (acker(A', C', Pobs))';
```

### 23.3.2 Discrete-time domain

In this section we shall explain how to converter a continuous time domain system into a discrete time domain. This transformation is of fundamental importance for the implementation of the control into digital micro-controller. Currently most of the control implementation are based on micro-controller or FPGA. Analog controller, which emulate a real continuous time domain, are in minority. Moreover direct code generation is also very common in particular for modern advanced control system. In section ?? a short review concerning the concept of the discretization of state space system is reported.

The state space representation in the discrete-time domain of the system

$$\begin{aligned}\dot{\vec{x}}(t) &= \tilde{\mathbf{A}}\vec{x}(t) + \tilde{\mathbf{B}}u(t) \\ y(t) &= \mathbf{C}\vec{x}(t)\end{aligned}\tag{23.3.7}$$

where

$$\tilde{\mathbf{A}} = \begin{bmatrix} 0 & 1 \\ 0 & 0 \end{bmatrix} \quad \tilde{\mathbf{B}} = \begin{bmatrix} 0 \\ 1 \end{bmatrix} \quad \mathbf{C} = [k \ 0] \tag{23.3.8}$$

is the following (consider  $t_s$  as sampling time)

$$\begin{aligned}\vec{x}(k+1) &= \mathbf{A}\vec{x}(k) + \mathbf{B}u(k) \\ y(k) &= \mathbf{C}\vec{x}(k)\end{aligned}\tag{23.3.9}$$

where  $u(k) = u_c(k)$  and  $y(k) = x_p(k)$  and where

$$\begin{aligned}\mathbf{A} &= \mathbf{I} + \tilde{\mathbf{A}}t_s \\ \mathbf{B} &= \tilde{\mathbf{B}}t_s\end{aligned}\tag{23.3.10}$$

Equation (23.3.8) and equation (23.3.9) represent the same physical model where the first one is in the continuous-time domain while the second one is in the discrete-time domain.

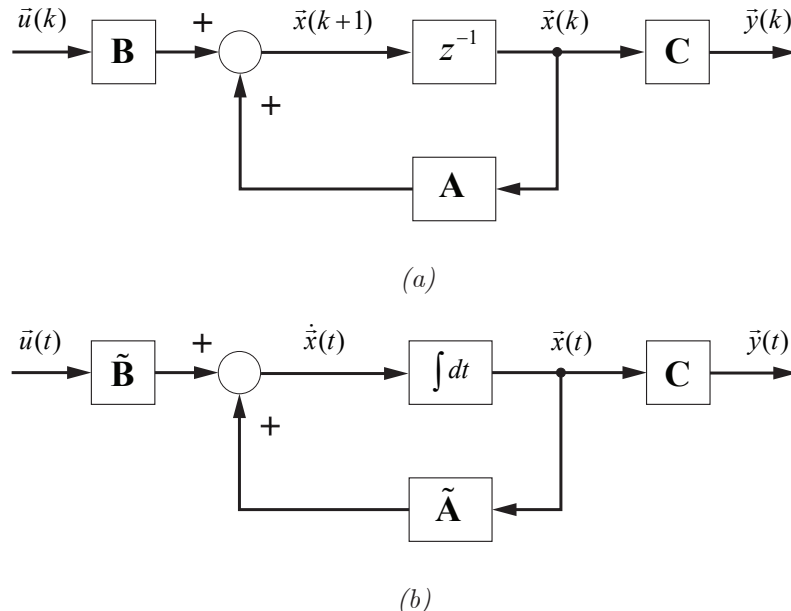


Figure 23.8: State space representation of a same system: (b) continuous-time domain case; (a) discrete-time domain case.

Regarding the observer block we can consider the following system equation:

$$\begin{aligned}\hat{\vec{x}}(k+1) &= \mathbf{A}\hat{\vec{x}}(k) + \mathbf{B}u(k) + \mathbf{L}(\vec{y}(k) - \hat{\vec{y}}(k)) \\ \hat{\vec{y}}(k) &= \mathbf{C}\hat{\vec{x}}(k)\end{aligned}\tag{23.3.11}$$

where  $\mathbf{L}$  matrix gain is obtained by the `acker` command in Matlab by a proper transformation of the desired poles from  $s$  plane to  $z$  plane, by the formula

$$\mathbf{P}_{obs}^d = \exp(\mathbf{P}_{obs} t_s)$$

and then apply the command:

```
Ld = (acker(Ad', C', Pdobs))';
```

For the discrete-time domain the poles used for state observer must be located inside the unit circle of the  $z$ -plane, see also Figure 23.9, in fact, the discretization process maps stable poles located into the left hand side of the  $s$  plane into stable poles located inside the unit circle of the  $z$  plane.

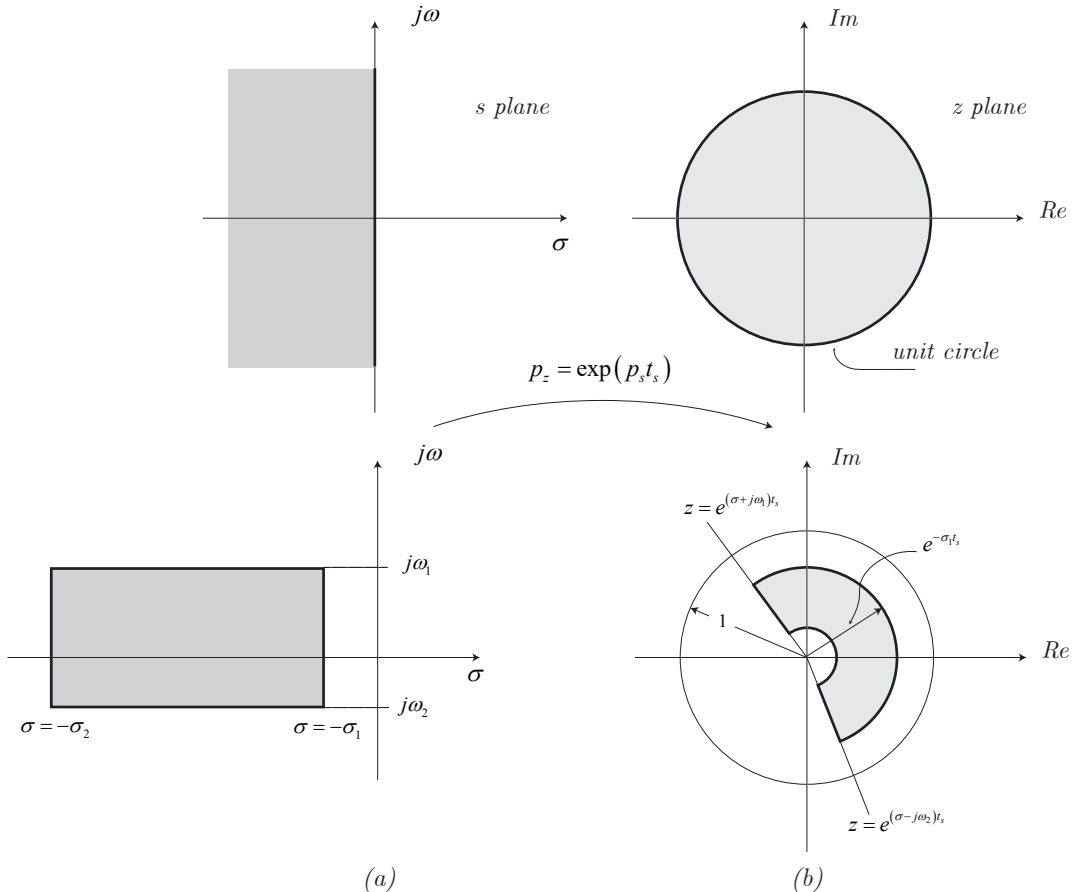


Figure 23.9: (a) Region bounded by lines  $\omega = \omega_1$ ,  $\omega = -\omega_2$ ,  $\sigma = -\sigma_1$  and  $\sigma = -\sigma_2$  in the  $s$ -plane; (b) the corresponding region in the  $z$  plane.

The realized control system is shown in Figure 23.10

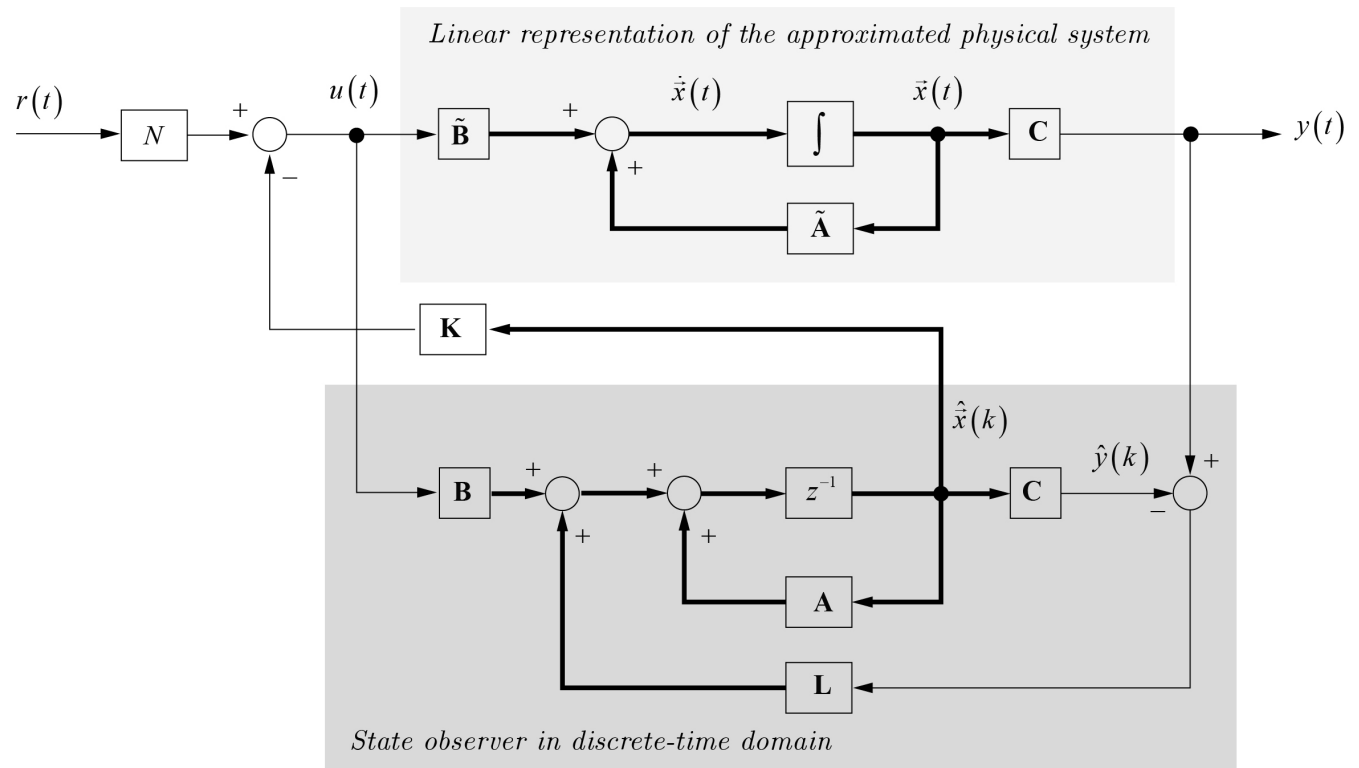


Figure 23.10: Control system layout for the discrete-time domain case.

## Chapter 24

# Moving Coil

The moving coil was already studied at the beginning of this document. Here we want to represent the moving coil model using a different approach, we would like to use a more mathematical (and less physical) approach to show a more formal representation. Most of the following material has been taken from the monumental work of **[J. Pyrhönen, 2008]**.

We define two reference frames: one stationary  $\mathcal{O}$  and one which lies on the moving coil  $\mathcal{O}'$  and we define the following meaning of the electrical field  $\vec{E}$  induced across the coil

- $\vec{E}'$  is the induced electrical field observed from the moving reference frame  $\mathcal{O}'$ .
- $\vec{E}$  is the induced electrical field observed from the stationary reference frame  $\mathcal{O}$ .

The Faraday's law applied to such that circuit can be written as follows

$$\oint_{\mathcal{C}} \vec{E}' \cdot d\vec{l} = -\frac{d}{dt} \int_{\mathcal{S}} \vec{B} \cdot \hat{n} da \quad (24.0.1)$$

where  $\vec{E}'$  is the electrical field applied to the coil respect the moving reference frame.

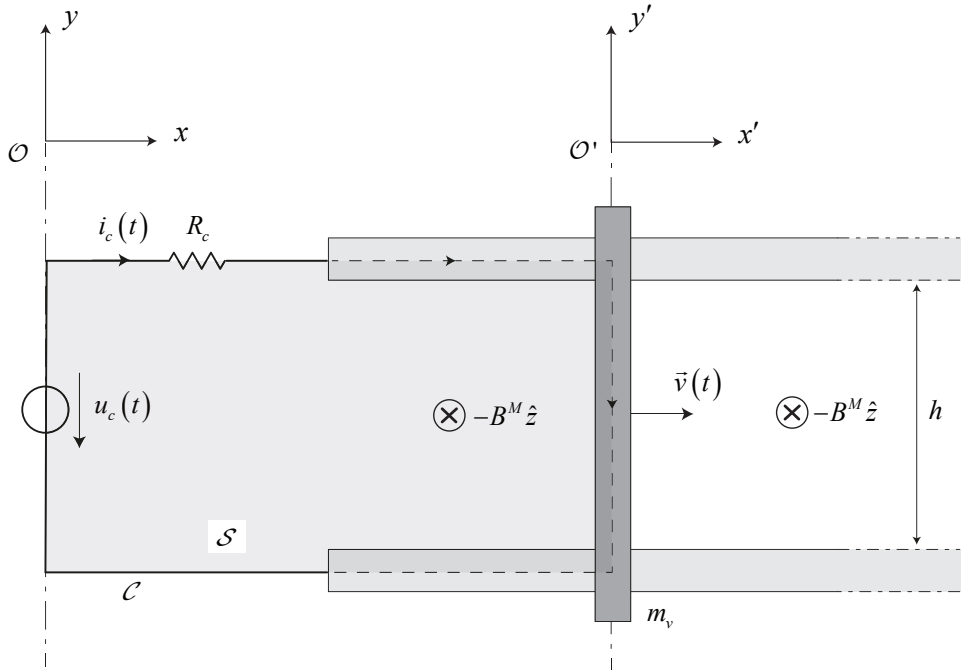


Figure 24.1: Moving coil actuator.

The circuit is moving at a certain speed  $\vec{v}$ , hence, the total time derivation of the linkage flux at the right hand side of Eq. (24.0.1) shall take into account that the linkage flux can change due to change of  $\vec{B}$  and due to the change of the contour  $\mathcal{C}$  (or  $\mathcal{S}$ ) due to the movement of the coil.

The total time derivative<sup>1</sup> of the flux through the moving coil is (see [J. Pyrhönen, 2008])

$$\frac{d}{dt} \int_{\mathcal{S}} \vec{B} \cdot \hat{n} da = \int_{\mathcal{S}} \frac{\partial \vec{B}}{\partial t} \cdot \hat{n} da + \oint_{\mathcal{C}} (\vec{B} \times \vec{v}) \cdot d\vec{l} \quad (24.0.2)$$

Hence Eq. (24.0.1) can now be written in the form

$$\oint_{\mathcal{C}} [\vec{E}' - \vec{v} \times \vec{B}] \cdot d\vec{l} = \int_{\mathcal{S}} \frac{\partial \vec{B}}{\partial t} \cdot \hat{n} da \quad (24.0.3)$$

Eq. (24.0.3) can also be obtained as follows (see also Figure 24.2)

$$\oint_{\mathcal{C}} \vec{E}' \cdot d\vec{l} = -\frac{d}{dt} \int_{\mathcal{S}} \vec{B} \cdot \hat{n} da = -\frac{1}{dt} \left[ \int_{\mathcal{S}(t+dt)} \vec{B}(t+dt) \cdot \hat{n} da - \int_{\mathcal{S}(t)} \vec{B}(t) \cdot \hat{n} da \right] \quad (24.0.4)$$

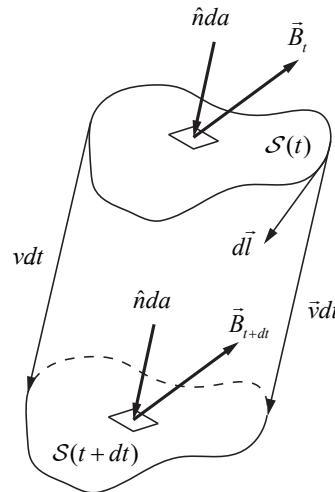


Figure 24.2: Evaluation of the  $D\vec{B}/Dt$ .

where

$$\vec{B}(t+dt) = \vec{B}(t) + \frac{\partial \vec{B}}{\partial t} dt \quad (24.0.5)$$

<sup>1</sup>The concept of the convective derivative can be used

$$\frac{d}{dt} = \frac{\partial}{\partial t} + \vec{v} \cdot \vec{\nabla}$$

we obtain that

$$\frac{d\vec{B}}{dt} = \frac{\partial \vec{B}}{\partial t} + (\vec{v} \cdot \vec{\nabla}) \vec{B} = \frac{\partial \vec{B}}{\partial t} + \vec{\nabla} \times (\vec{B} \times \vec{v}) + \vec{v} (\vec{\nabla} \cdot \vec{B})$$

where  $\vec{v}$  is considered a constant vector. Applying Stokes theorem we obtain Eq. (24.0.2)

The second term of Eq. (24.0.4) become

$$\begin{aligned} & -\frac{1}{dt} \left[ \int_{\mathcal{S}(t+dt)} \left( \vec{B}(t) + \frac{\partial \vec{B}}{\partial t} \right) \cdot \hat{n} da - \int_{\mathcal{S}(t)} \vec{B}(t) \cdot \hat{n} da \right] = \\ & -\frac{1}{dt} \left[ \int_{\mathcal{S}(t)} \vec{B}(t+dt) \cdot \hat{n} da - \int_{\mathcal{S}(t)} \vec{B}(t) \cdot \hat{n} da \right] - \int_{\mathcal{S}(t+dt)} \frac{\partial \vec{B}}{\partial t} \cdot \hat{n} da \end{aligned} \quad (24.0.6)$$

The first term at the right side of the equation represents the variation of the flux of  $\vec{B}$  due to the only change of the surface, and we can write

$$-\frac{1}{dt} \left[ \int_{\mathcal{S}(t)} \vec{B}(t+dt) \cdot \hat{n} da - \int_{\mathcal{S}(t)} \vec{B}(t) \cdot \hat{n} da \right] = \oint_{\mathcal{C}} (\vec{v} \times \vec{B}) \cdot d\vec{l} \quad (24.0.7)$$

while the second term represent the variation of the flux due to the change of the vector  $\vec{B}$

$$\int_{\mathcal{S}(t+dt)} \frac{\partial \vec{B}}{\partial t} \cdot \hat{n} da = \int_{\mathcal{S}(t)} \frac{\partial \vec{B}}{\partial t} \cdot \hat{n} da \quad dt \rightarrow 0 \quad (24.0.8)$$

and we obtain the Eq. (24.0.3).

Now we apply the Faraday's law to the circuit respect the stationary reference frame  $\mathcal{O}$  and by the fact that the circuit  $\mathcal{C}$  and the surface  $\mathcal{S}$  are fixed respect to the same stationary reference frame  $\mathcal{O}$  the Faraday's law can be written in the form

$$\oint_{\mathcal{C}} \vec{E} \cdot d\vec{l} = - \int_{\mathcal{S}} \frac{\partial \vec{B}}{\partial t} \cdot \hat{n} da \quad (24.0.9)$$

Galilean invariance Eq. (24.0.3) and Eq. (24.0.9) must be equal, hence results that the electrical field of the coil measured respect to  $\mathcal{O}$  can be expressed as (see also section 25)

$$\boxed{\vec{E} = \vec{E}' - \vec{v} \times \vec{B}} \quad (24.0.10)$$

Hence the Faraday's law applied to the moving coil

$$\boxed{\oint_{\mathcal{C}} \vec{E}' \cdot d\vec{l} = - \frac{d}{dt} \int_{\mathcal{S}} \vec{B} \cdot \hat{n} da} \quad (24.0.11)$$

where the circuit  $\mathcal{C}$  and the surface  $\mathcal{S}$  are not considered fixed, can be written in the form

$$\boxed{\oint_{\mathcal{C}} [\vec{E}' - \vec{v} \times \vec{B}] \cdot d\vec{l} = \int_{\mathcal{S}} \frac{\partial \vec{B}}{\partial t} \cdot \hat{n} da} \quad (24.0.12)$$

where the circuit  $\mathcal{C}$  and the surface  $\mathcal{S}$  can be considered fixed but where we already account the speed of the coil.

From another, but equivalent, point of view, we can suppose to freeze, at a certain instant, the circuit and to define the contour  $\mathcal{C}$  and its surface  $\mathcal{S}$  as fixed respect to the stationary reference frame. Even if the contour  $\mathcal{C}$  and the surface  $\mathcal{S}$  are fixed in the space, the charge present into the coil is subjected to a vector speed  $\vec{v}$  and hence is subjected to a force  $\vec{f} = q(\vec{E} + \vec{v} \times \vec{B})$  respect to the reference frame  $\mathcal{O}$ , from Galilean invariance we can impose that

$\vec{f} = \vec{f}' = q\vec{E}'$  which results in  $\vec{E}' = \vec{E} + \vec{v} \times \vec{B}$ . That means, the induced electrical field along the coil seen from a stationary reference frame is given by

$$\vec{E} = \vec{E}' - \vec{v} \times \vec{B} \quad (24.0.13)$$

For ideal conductive coil we can write

$$\vec{E} = -\vec{v} \times \vec{B}.$$

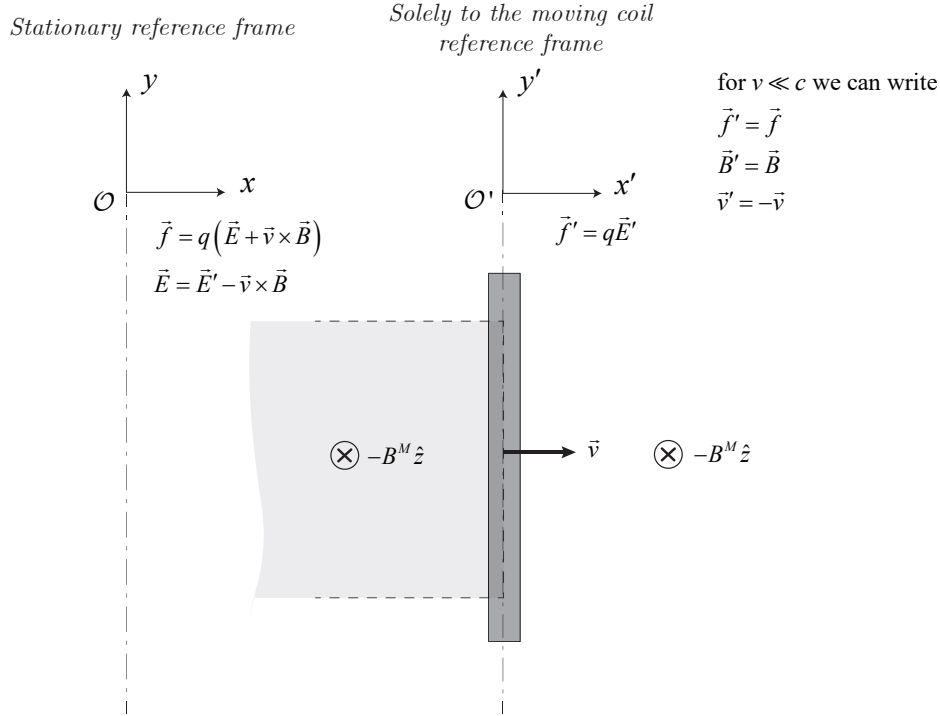


Figure 24.3: Lorentz force applied to the coil charge due to effect of the speed.

Now we can write the vector  $\vec{B}$  as a superposition of two fields: the  $\vec{B}_i$  due to the current  $i(t)$  and the external field  $\vec{B}^M$  which is supposed to be constant and isotropic,

$$\vec{B}(t) = \vec{B}_i(t) + \vec{B}^M$$

Therefore, the last term in Eq. (24.0.12) can be rewritten as

$$\int_{\mathcal{S}} \frac{\partial \vec{B}}{\partial t} \cdot \hat{n} da = \int_{\mathcal{S}} \frac{\partial \vec{B}_i}{\partial t} \cdot \hat{n} da + \int_{\mathcal{S}} \frac{\partial \vec{B}^M}{\partial t} \cdot \hat{n} da \quad (24.0.14)$$

where

$$\frac{\partial \vec{B}^M}{\partial t} = 0 \quad (24.0.15)$$

$$\frac{\partial \vec{B}_i}{\partial t} = \frac{\partial \vec{B}_i(i)}{\partial i} \frac{di(t)}{dt} \quad (24.0.16)$$

Hence Eq. (24.0.14) can be written as

$$\int_{\mathcal{S}} \frac{\partial \vec{B}}{\partial t} \cdot \hat{n} da = \int_{\mathcal{S}} \left[ \frac{\partial \vec{B}_i(i)}{\partial i} \frac{di(t)}{dt} \right] \cdot \hat{n} da = \frac{\partial \phi(i)}{\partial i} \frac{di(t)}{dt} = L \frac{di(t)}{dt} \quad (24.0.17)$$

where  $\mathcal{S}$  is considered constant and  $\partial\phi(i)/\partial i = L$  is the definition of inductance.

Now we apply Eq. (24.0.12) in clockwise around the contour  $\mathcal{C}$  of the Figure 24.1 and we consider the case that the coil is composed of  $N_c$  turns

$$\psi(t) = N_c \phi(t) = N_c \int_S \vec{B} \cdot d\vec{s} \quad (24.0.18)$$

$$L_c = N_c L$$

we obtain

$$\underbrace{\int_{(-)}^{(+)} \vec{E} \cdot d\vec{l}}_{\text{source}} + \underbrace{\int \vec{E} \cdot d\vec{l}}_{\text{resistor}} + \underbrace{\int \vec{E}' \cdot d\vec{l}}_{\text{coil}} = -\frac{d}{dt} \int_S \vec{B} \cdot \hat{n} da. \quad (24.0.19)$$

or

$$\underbrace{\int_{(-)}^{(+)} \vec{E} \cdot d\vec{l}}_{\text{source}} + \underbrace{\int \vec{E} \cdot d\vec{l}}_{\text{resistor}} + \underbrace{\int [\vec{E}' - \vec{v}_v \times \vec{B}^M N_c] \cdot d\vec{l}}_{\text{coil}} = -L_c \frac{di_c(t)}{dt}. \quad (24.0.20)$$

The integrals over the fixed components (source and resistor) follow from Equations

$$-u_c = \underbrace{\int_{(-)}^{(+)} \vec{E} \cdot d\vec{l}}_{\text{source}} \quad (24.0.21)$$

$$i_c R_c = \underbrace{\int \vec{E} \cdot d\vec{l}}_{\text{resistor}} \quad (24.0.22)$$

Concerning the coil we consider the case where the whole resistance is accounted in  $R_c$  and we set  $\vec{E}' = \vec{J}/\sigma = 0$ , we obtain

$$u_c(t) - i_c(t) R_c - L_c \frac{di_c}{dt} + \int_{\text{coil}} (\vec{v}_v \times \vec{B}^M N_c) \cdot d\vec{l} = 0 \quad (24.0.23)$$

We are considering the case where  $\vec{v}_v = v_v \hat{x}$ ,  $\vec{B}^M = -B^M \hat{z}$  and  $d\vec{l} = dy \hat{y}$ . Therefore  $(\hat{x} \times \hat{z} = -\hat{y})$ ,

$$\int_{\text{coil}} (\vec{v}_v \times \vec{B}^M N_c) \cdot d\vec{l} = \int_h^0 v_v B^M N_c dy = -N_c B^M h v_v(t) \quad (24.0.24)$$

we obtain

$$\boxed{u_c(t) - i_c(t) R_c - L_c \frac{di_c(t)}{dt} - N_c B^M h v_v(t) = 0} \quad (24.0.25)$$

To complete the linear pm-actuator model we must add the mechanical equations using the Newton's equation. To apply the Newton's law we first must calculate the corresponding force actuated by the iteration between the current  $i_c$  and the magnetic field  $\vec{B}^M$ .

The expression of the force due to the current  $i_c$  in the magnetic field  $\vec{B}^M$  is evaluated as follows

$$\vec{f}(t) = i(t) \int_{\text{wire}} d\vec{l} \times \vec{B}^{\text{ext}} \quad (24.0.26)$$

where  $\vec{B}^{\text{ext}}$  is an external field. Applying the integration of Eq. (24.0.26) it results in the following equation (**integration path follows the current direction**)

$$f_v^m(t) = N_c i_c(t) \int_h^0 d\vec{l} \times \vec{B}^M = N_c B^M h i_c(t) \quad \text{positive x-direction} \quad (24.0.27)$$

where  $N_c$  by the number of turns linkage to the magnetic field. The complete set of system equations becomes

$$\begin{cases} \frac{dx_v(t)}{dt} = v_v(t) \\ \frac{dv_v(t)}{dt} = N_c \frac{B^M h}{m_v} i_c(t) - \frac{b_v}{m_v} v_v(t) - \frac{1}{m_v} f_v^e(t) \\ \frac{di_c(t)}{dt} = -\frac{R_c}{L_c} i_c(t) - \frac{1}{L_c} N_c B^M h v_v(t) + \frac{1}{L_c} u_c(t) \end{cases} \quad (24.0.28)$$

the first two equations represent the dynamic motion of the bar where the force  $f_v^m(t) = N_c B^M h i(t)$  is generated by the interaction of the current  $i_c(t)$  and the magnetic field  $\vec{B}^M$ . The third equation represents the Kirchhoff's voltage law of the electrical circuit which generates the current  $i_c(t)$  by applying the voltage  $u_c(t)$ . The equivalent auto-inductance  $L_c$  and the back-emf term,  $N_c B^M h v_v(t)$  represent the effect of the Faraday's law.

## Chapter 25

# Moving reference frames

In our study of electromechanical devices we will need to determine the voltage induced in a coil as it moves through a stationary magnetic field. This requires an understanding of quasi-static field theory as observed in two different inertial reference frames (in motion relative to one another). For our purposes, an inertial reference frame is one that moves with constant velocity. In this section, we derive the transformation laws for quasi-static fields as observed in two different inertial reference frames.

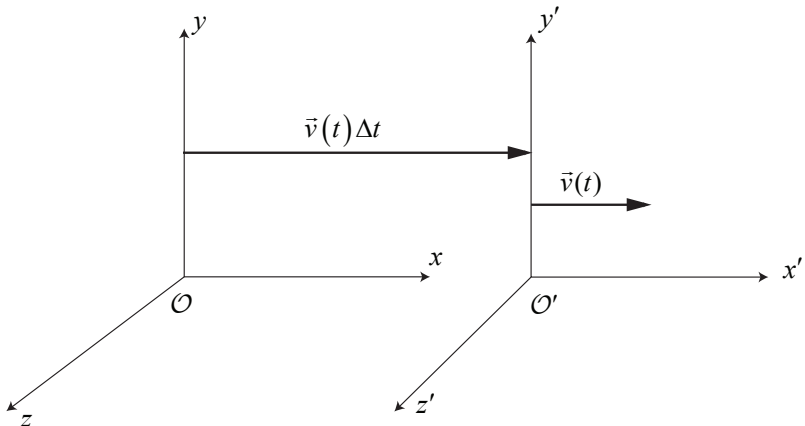


Figure 25.1: Inertial reference frames in relative motion along one axis.

Consider two inertial reference frames, a stationary “laboratory” reference frame  $\mathcal{O}$  with coordinates  $(x, y, z, t)$  and a moving reference frame  $\mathcal{O}'$  with coordinates  $(x', y', z', t')$ . Frame  $\mathcal{O}'$  moves with velocity  $\vec{v}$  with respect to  $\mathcal{O}$  as shown in Figure 25.1. Observers in  $\mathcal{O}$  and  $\mathcal{O}'$  measure different values for the electromagnetic fields. Rigorous comparison of these measurements can be made if one knows how fields transform from  $\mathcal{O}$  to  $\mathcal{O}'$  or vice versa. The transformation laws follow from the theory of special relativity.

The basic postulates of special relativity are as follows:

1. The law of physics are the same in all inertial reference frames.
2. Observer in inertial reference frames measure the same value for the speed of light.

The first postulate implies that the quasi-static field equations must have the same form in both  $\mathcal{O}$  and  $\mathcal{O}'$  as shown in the following equations

### Quasi-Static Equations

**Reference frame  $\mathcal{O}$** 

$$\begin{aligned}\vec{\nabla} \times \vec{H} &= \vec{J} \\ \vec{\nabla} \cdot \vec{B} &= 0 \\ \vec{\nabla} \times \vec{E} &= -\frac{\partial \vec{B}}{\partial t} \\ \vec{\nabla} \cdot \vec{J} &= 0\end{aligned}\tag{25.0.1}$$

**Reference frame  $\mathcal{O}'$** 

$$\begin{aligned}\vec{\nabla}' \times \vec{H}' &= \vec{J}' \\ \vec{\nabla}' \cdot \vec{B}' &= 0 \\ \vec{\nabla}' \times \vec{E}' &= -\frac{\partial \vec{B}'}{\partial t} \\ \vec{\nabla}' \cdot \vec{J}' &= 0\end{aligned}\tag{25.0.2}$$

Here  $\vec{\nabla}'$  is the gradient operator with respect to the  $(x', y', z', t')$  coordinate

$$\vec{\nabla}' = \frac{\partial}{\partial x'} \vec{i}' + \frac{\partial}{\partial y'} \vec{j}' + \frac{\partial}{\partial z'} \vec{k}'$$

our goal is to determine the transformation laws for the field going from  $\mathcal{O}$  to  $\mathcal{O}'$  and vice versa. We can determine these if we know the transformation relations for the coordinate variables. These follow from the second postulate of the special relativity and are given by

$$\begin{aligned}t' &= \gamma(t - \beta x/c) \\ x' &= \gamma(x - \beta ct) \\ y' &= y \\ z' &= z\end{aligned}\tag{25.0.3}$$

where

$$\gamma = \frac{1}{\sqrt{1 + \beta^2}}$$

and

$$\beta = \frac{v}{c}$$

Here,  $c$  is the speed of the light in a vacuum. We are interested in low-velocity electromechanical devices for which  $u \ll c$ . Therefore

$$\beta \approx 0$$

and

$$\gamma \approx 1.$$

Substituting the above approximations Eq. (25.0.3) reduce to the Galilean transform relation

$$\begin{aligned}t' &= t \\ x' &= x - vt \\ y' &= y \\ z' &= z\end{aligned}\tag{25.0.4}$$

This analysis generalized to the case of an arbitrary velocity as shown in Figure 25.2.

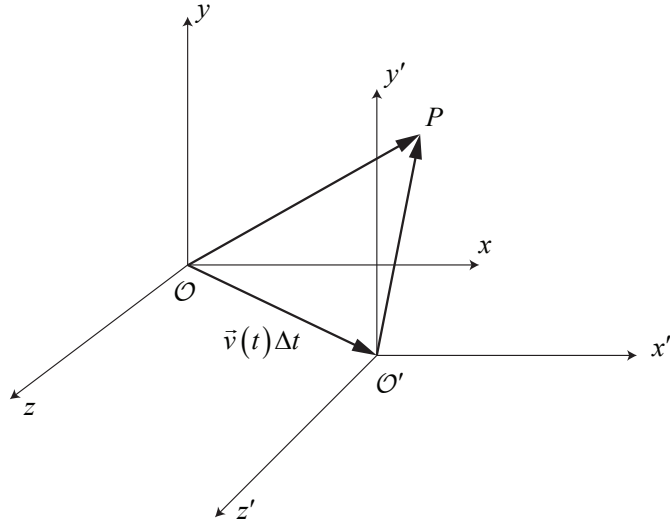


Figure 25.2: Inertial reference frames in relative motion.

For this case we find that

$$\begin{aligned} t' &= t \\ x' &= x - v_x t \\ y' &= y - v_y t \\ z' &= z - v_z t \end{aligned} \tag{25.0.5}$$

Now that we know the transform relations for the coordinates, we can determine the corresponding relations for the field equations. These will ultimately enable us to compare the fields in the two reference frames. We start by considering a scalar-valued function  $f'$  of the **primed** coordinates,  $f'(x', y', z')$ . By virtue of Eq. (25.0.5),  $f'$  can be considered to be a function of the **unprimed** coordinates,

$$f'(x', y', z') = f'(x'(x, t), y'(y, t), z'(z, t)),$$

We use the chain rule to determine the derivatives of  $f'$  with respect to the **unprimed** coordinates. We consider spatial derivatives first and find that

$$\frac{\partial f'}{\partial x} = \frac{\partial f'}{\partial x'} \frac{\partial x'}{\partial x} = \frac{\partial f'}{\partial x'}.$$

It follows that

$$\vec{\nabla} f' = \vec{\nabla}' f'.$$

Next, we consider the time derivative. From the chain rule we have

$$\begin{aligned} \frac{\partial f'}{\partial t} &= \frac{\partial f'}{\partial t'} \frac{\partial t'}{\partial t} + \frac{\partial f'}{\partial x'} \frac{\partial x'}{\partial t} + \frac{\partial f'}{\partial y'} \frac{\partial y'}{\partial t} + \frac{\partial f'}{\partial z'} \frac{\partial z'}{\partial t} = \\ &= \frac{\partial f'}{\partial t'} - \frac{\partial f'}{\partial x'} v_x - \frac{\partial f'}{\partial y'} v_y - \frac{\partial f'}{\partial z'} v_z \end{aligned} \tag{25.0.6}$$

where

$$\begin{aligned}\frac{\partial t'}{\partial t} &= 1; & \frac{\partial x'}{\partial t} &= -v_x; \\ \frac{\partial y'}{\partial t} &= -v_y; & \frac{\partial z'}{\partial t} &= -v_z;\end{aligned}\tag{25.0.7}$$

Eq. (25.0.6) can be rewritten as

$$\frac{\partial f'}{\partial t} = \frac{\partial f'}{\partial t'} - \vec{v} \cdot (\vec{\nabla}' f') \tag{25.0.8}$$

or

$$\frac{\partial f'}{\partial t'} = \frac{\partial f'}{\partial t} + \vec{v} \cdot (\vec{\nabla} f') \tag{25.0.9}$$

The relations 25.0.8 and 25.0.9 relate the derivatives in  $\mathcal{O}$  and in  $\mathcal{O}'$  for scalar-valued function. A similar analysis applies to vector-valued function. Let  $\vec{A}'(x', y', z', t')$  be a vector-valued function of the **primed** coordinate variables.

This can also be considered to be a vector-valued function of the **unprimed** coordinates

$$\vec{A}'(x', y', z', t') = \vec{A}'(x'(x, t), y'(y, t), z'(z, t))$$

It is easy to check that

$$\vec{\nabla}' \cdot \vec{A}' = \vec{\nabla} \cdot \vec{A}' \tag{25.0.10}$$

and that

$$\vec{\nabla}' \times \vec{A}' = \vec{\nabla} \times \vec{A}'. \tag{25.0.11}$$

Similarly, by taking the time derivative we find that

$$\frac{\partial \vec{A}'}{\partial t'} = \frac{\partial \vec{A}'}{\partial t} + (\vec{v} \cdot \vec{\nabla}) \vec{A}'. \tag{25.0.12}$$

Suppose that the **unprimed** frame is the fixed or laboratory frame. Then, from the left-hand side of Eq. (25.0.12) it is clear that the right-hand side is *the rate of change with respect to time of  $\vec{A}'$  for an observer moving with velocity  $\vec{v}$* . This derivative, written in terms of the coordinates  $(x, y, z, t)$  of the fixed reference frame, is called *substantial derivative*

$$\boxed{\frac{D\vec{A}'}{Dt'} = \frac{\partial \vec{A}'}{\partial t} + (\vec{v} \cdot \vec{\nabla}) \vec{A}'}. \quad (\text{respect to } \mathcal{O}')$$

(25.0.13)

Eq. (25.0.12) can be written in different form. Because  $\vec{v}$  is constant and by the identity

$$\vec{\nabla} \times (\vec{A} \times \vec{B}) = (\vec{B} \cdot \vec{\nabla}) \vec{A} - (\vec{A} \cdot \vec{\nabla}) \vec{B} + \vec{A}(\vec{\nabla} \cdot \vec{B}) - \vec{B}(\vec{\nabla} \cdot \vec{A}) \tag{25.0.14}$$

makes it possible to write Eq. (25.0.12) in the form

$$\frac{\partial \vec{A}'}{\partial t'} = \frac{\partial \vec{A}'}{\partial t} + \vec{v}(\vec{\nabla} \cdot \vec{A}') - \vec{\nabla} \times (\vec{v} \times \vec{A}'), \tag{25.0.15}$$

Finally, substitute Eqs. 25.0.10, 25.0.11 and 25.0.15 into the quasi-static equations for  $\mathcal{O}'$  in 25.0.2 we obtain

$$\vec{\nabla}' \times \vec{H}' = \vec{J}' \Rightarrow \vec{\nabla} \times \vec{H}' = \vec{J}' \quad (\text{respect to } \mathcal{O}') \tag{25.0.16}$$

$$\vec{\nabla}' \cdot \vec{B}' \Rightarrow \vec{\nabla} \cdot \vec{B}' = 0 \quad (\text{respect to } \mathcal{O}') \tag{25.0.17}$$

$$\vec{\nabla}' \times \vec{E}' = -\frac{\partial \vec{B}'}{\partial t'} \Rightarrow \vec{\nabla} \times (\vec{E}' - \vec{v} \times \vec{B}') = -\frac{\partial \vec{B}'}{\partial t} \quad (\text{respect to } \mathcal{O}') \quad (25.0.18)$$

$$\vec{\nabla}' \cdot \vec{J}' \Rightarrow \vec{\nabla} \cdot \vec{J}' = 0 \quad (\text{respect to } \mathcal{O}') \quad (25.0.19)$$

We have used  $\vec{\nabla} \cdot \vec{B}' = 0$  in the equation 25.0.18.

It has been postulated that equations 25.0.16-25.0.19 describe the same physical laws as

$$\vec{\nabla} \times \vec{H} = \vec{J} \quad (\text{respect to } \mathcal{O}) \quad (25.0.20)$$

$$\vec{\nabla} \cdot \vec{B} = 0 \quad (\text{respect to } \mathcal{O}) \quad (25.0.21)$$

$$\vec{\nabla} \times \vec{E} = -\frac{\partial \vec{B}}{\partial t} \quad (\text{respect to } \mathcal{O}) \quad (25.0.22)$$

$$\vec{\nabla} \cdot \vec{J} = 0 \quad (\text{respect to } \mathcal{O}) \quad (25.0.23)$$

A comparison of Eqs. (25.0.16)-(25.0.19) and Eq. (25.0.20)-25.0.23 shows that a consistent set of transformations which satisfies this requirement is:

### Transformation Relations

$$\vec{H} = \vec{H}' \quad (25.0.24)$$

$$\vec{B} = \vec{B}' \quad (25.0.25)$$

$$\vec{E} = \vec{E}' - \vec{v} \times \vec{B} \quad (25.0.26)$$

$$\vec{J} = \vec{J}' \quad (25.0.27)$$

In Eqs. (25.0.24) - (25.0.27) the variables  $(\vec{H}, \vec{B}, \vec{E}, \vec{v}, \vec{J})$  are measured in the stationary reference frame  $\mathcal{O}$  and the variables  $(\vec{H}', \vec{B}', \vec{E}', \vec{J}')$  are measured in the moving frame  $\mathcal{O}'$ . For these relations to hold, the variables must be compared **at the same physical point in space**. For example, from Eqs. 25.0.5 and 25.0.26 we have

$$\begin{aligned} \vec{E}'(x', y', z', t') &= \vec{E}(x - v_x t, y - v_y t, z - v_z t, t) \\ &\quad + \vec{v} \times \vec{B}(x - v_x t, y - v_y t, z - v_z t, t). \end{aligned}$$

Notice that we have assumed that  $\vec{v}$  is a constant (independent of position).

The relations (25.0.24) - (25.0.27) give the transformations for the fields and the source. However, we still need to know the constitutive relations in  $\mathcal{O}$  and  $\mathcal{O}'$ . We apply a general principle that says that the constitutive relations for moving media are the same as for stationary media when they are written in terms of the fields defined in an inertial reference frame moving with the media. For example for a linear, homogeneous and isotropic media at rest in  $\mathcal{O}'$  we have  $\vec{J}' = \sigma \vec{E}'$  and  $\vec{B}' = \mu \vec{H}'$ . However, in  $\mathcal{O}$  (which is moving with respect to the media) the relations are modified by virtue of Eqs. (25.0.24) - (25.0.27). Specifically, we find that

**Constitutive Relations****Reference frame  $\mathcal{O}$** 

$$\vec{J} = \sigma(\vec{E} + \vec{v} \times \vec{B})$$

$$\vec{B} = \mu \vec{H}$$

**Reference frame  $\mathcal{O}'$** 

$$\vec{J}' = \sigma \vec{E}'$$

(25.0.28)

$$\vec{B}' = \mu \vec{H}'$$

## **Part V**

# **ANSYS Tutorial for PMSM design**

## Chapter 26

# Nomenclature and Scope of the document

The document wants to give a basic level guide for the design of IPMSM (interior permanent magnet synchronous machine) using ANSYS RMxpert and ANSYS Maxwell (Electronic).

- The ANSYS toolbox RMxpert will be used to design the PMSM from specifics geometries already available in toolbox.
- The ANSYS toolbox Maxwell will be used to perform FEM (finite element method) analysis.

Along the document, the following notation will be used:

- RMB : *right mouse button*;
- LMB : *left mouse button*;
- DLMB : *double left mouse button*;
- → : *go to*.

Moreover, achievements as well as important steps will be marked with a grey box:

e.g.

# Chapter 27

## RMxprt Toolbox for IPMSM

### 27.1 Introduction

**RMxprt** is a ANSYS Electronics toolbox used for the design of different typologies of motors: based on induction principle as well as based on permanent magnets.

In the following will be considered the design of a synchronous motor based on interior permanent magnet. As case study we design an IPMSM with the following characteristics

<b>Rated Power</b>	200 kW
at motor speed	1500 min <sup>-1</sup> (rpm)
<b>Rated Torque</b>	1250 N m
at motor speed	1500 min <sup>-1</sup> (rpm)
<b>Rated Speed</b>	
maximum motor speed	2140 min <sup>-1</sup> (rpm)
nominal motor speed	1500 min <sup>-1</sup> (rpm)
<b>Number of Poles</b>	8
<b>Number of Slots</b>	12

Table 27.1: PMSM Data as Case Study.

### 27.2 Setup of RMxprt design

Here, the preliminary steps for the setup of the RMxprt tool design.

- From ANSYS Workbench → DLMB **RMxprt**
  - From *Project Schematic-RMxprt Design* DLMB *setup*.
- From **RMxprt** → **Project Manager** → **MaxwellProject** → RMB on **RMxprtDesign1** and select: *Machine Type...*

- From *Design Flow* select: *Generate RMxprt Solutions*.
- From *Machine Type* select: *General*.
- From the bottom window select: *Synchronous Machines* → *IPM Synchronous Machine*.
- Press OK.

After these preliminary steps, specific icons list will be appeared in the tree of the *RMxprtDesign1*. The following steps shall be done.

- LMB on *Machine* and select:

Parameter	Input
Source Type	AC
Structure	Inner Rotor
Stator Type	SLOT_AC
Rotor Type	PM_INTERIOR

Table 27.2: Machine setup.

- LMB on *Machine-Stator* and select:

Parameter	Input
Number of Poles	8
Number of Slots	12
Circuit Type	Y3
Slot Type	4
Position Control	unchecked

Table 27.3: Machine-Stator setup.

- LMB on *Machine-Stator-Core* and select:

Parameter	Input
Outer Diameter	640 mm
Inner Diameter	450 mm
Length	160 mm
Stacking Factor	0.95
Steel Type	isovac 400 65A
Press Board Thickness	0 mm
Magnetic Press Board	unchecked
Skew Width	0°
Lamination Sector	0

Table 27.4: Machine-Stator-Core setup.

- LMB on *Machine-Stator-Core-Slot* and select:

Parameter	Input
Auto Design	unchecked
Parallel Tooth Design	unchecked
$H_{s0}$	6 mm
$H_{s1}$	0 mm
$H_{s2}$	55 mm
$B_{s0}$	48 mm
$B_{s1}$	55 mm
$B_{s2}$	55 mm
$R_s$	2 mm

Table 27.5: Machine-Stator-Core-Slot setup.

- LMB on *Machine-Stator-Winding* and select:

Parameter	Input
Winding Layers	2
Winding Type	Whole-Coiled
Parallel Branches	4
Conductor per Slot	60
Coil pitch	1
Number of Strands	0
Wire Wrap	0 mm
Wire Size	0 mm
Conductor Type	Aluminium

Table 27.6: Machine-Stator-Winding setup.

Parameter	Input
Input Half-turn Length	unchecked
End Extension	0 mm
Correction Factor	1
Base Inner Radius	0 mm
Tip Inner Diameter	0 mm
End Clearance	0 mm
Slot Liner	0 mm
Wedge Thickness	0 mm
Layer Insulation	0 mm
Limited Fill Factor	0.75
Top Spare Space	0
Bottom Spare Space	0

Table 27.7: Machine-Stator-Winding (End-Insulation) setup.

At this step is already possible via RMB, on the right view of the motor section, select *Connect all coils* to see the coils connection.

- LMB on *Machine-Rotor* and select:

Parameter	Input
Number of Poles	8

Table 27.8: Machine-Rotor setup.

- LMB on *Machine-Rotor-Core* and select:

Parameter	Input
Outer Diameter	444 mm
Inner Diameter	310 mm
Length	160 mm
Stacking Factor	0.95
Steel Type	isovac 400 65A
Pole Type	4

Table 27.9: Machine-Rotor-Core setup.

- LMB on *Machine-Rotor-Core-Pole* and select:

Parameter	Input
$D_1$	438 mm
$O_1$	12 mm
$O_2$	24 mm
$B_1$	12 mm
$R_{ib}$	12 mm
$HR_{ib}$	4 mm
Layers	1
Layer Pitch	0 mm
Magnet Thickness Pitch	12 mm
Magnet Width Pitch	120 mm
Magnet Type	NdFe35

Table 27.10: Machine-Rotor-Core-Pole setup.

- LMB on *Machine-Shaft* and select:

Parameter	Input
Magnetic Shaft	checked
Frictional Loss	1200 W
Windage Loss or Power	0 W
Reference Speed	1500 min <sup>-1</sup> (rpm)

Table 27.11: Machine-Shaft setup.

### 27.3 Preparation for Maxwell-Analysis of the RMxprt design

- From **RMxprtDesign1-Analysis** → RMB → *Add Solution Setup*
- From *Add Solution Setup* select:
  - From *General*

Parameter	Input
Setup Name	Analysis_1
Operation Type	Motor
Load Type	Constant Speed
Rated Output Power	200 kW
Rated Voltage	400 V
Rated Speed	1500 min <sup>-1</sup> (rpm)
Operating Temperature	75 °C

Table 27.12: General - Solution setup.

- From *Generic Rotating Machine*

Parameter	Input
Rated Power Factor	0.8
Frequency	100 Hz

Table 27.13: Generic Rotating Machine - Solution setup.

- To create the solution:
  - RMB → **RMxprtDesign1-Analysis-Analysis\_1** → *Analyze*.
- When terminated check *Message Manager*.

## Chapter 28

# Maxwell Analysis

### 28.1 Maxwell 2D Design

- To create a Maxwell 2D design: RMB → *Analysis-Analysis\_1* → *Create Maxwell Design* and select
  - Type → Maxwell 2D Design
  - Solution Setup → Analysis\_1
  - Press OK

Once Maxwell 2D design is completed via RMB → *Maxwell2DDesign1* is possible to select the

- *Magnetic*
  - *Magnetostatic*
  - *Transient*

As default is selected the *Transient* analysis.

#### 28.1.1 Transient Analysis

Once the **Maxwell2DDesign1(Transient,XY)** is completed a validation procedure must be performed.

- From *Simulation* tab select *Validate*: results will show a exclamation mark over *Boundaries and Excitations*.

To fix the warning follows the steps:

- From drawing window select the stator iron (selected part will appear magenta) → RMB → *Assign Excitation - Set Eddy Effects* and select:
  - Use suggested values
- From drawing window select the rotor iron (selected part will appear magenta) → RMB → *Assign Excitation - Set Eddy Effects* and select:

- Use suggested values

Check *Simulation-Validate* again: the warning should be disappeared.

The PMSM is driven by a specific set of symmetric three phase current (amplitude and phase concur in the definition of the torque) which must be properly set in the excitation fields as follows

- LMB → **Maxwell2DDesign1(Transient)** → *Excitations* → *PhaseA*

Parameter	Input
Name	PhaseA
Type	Winding Group
Winding Type	Current
IsSolid	Stranded
Current	$-600*\sin(\text{position}*4-\pi/3)$
Number of Parallel Branches	4

Table 28.1: PhaseA Excitation setup.

- LMB → **Maxwell2DDesign1(Transient)** → *Excitations* → *PhaseB*

Parameter	Input
Name	PhaseB
Type	Winding Group
Winding Type	Current
IsSolid	Stranded
Current	$-600*\sin(\text{position}*4-\pi/3-2\pi/3)$
Number of Parallel Branches	4

Table 28.2: PhaseA Excitation setup.

- LMB → **Maxwell2DDesign1(Transient)** → *Excitations* → *PhaseC*

Parameter	Input
Name	PhaseC
Type	Winding Group
Winding Type	Current
IsSolid	Stranded
Current	$-600*\sin(\text{position}*4-\pi/3-4*\pi/3)$
Number of Parallel Branches	4

Table 28.3: PhaseA Excitation setup.

To run the simulation: *Simulation → Analyze All*

### 28.1.2 Magnetostatic Analysis

To perform a magnetostatic analysis:

- Create a new Maxwell 2D design: RMB → *Analysis-Analysis\_1* → *Create Maxwell Design* and select
  - Type → Maxwell 2D Design
  - Solution Setup → Analysis\_1
  - Press OK

When terminated RMB over **Maxwell2DDesign2(Transient, XY)** and select

- Magnetic: Magnetostatic
- Press OK

**Maxwell2DDesign2(Transient, XY) → Maxwell2DDesign2(Magnetostatic, XY)**

From **Maxwell2DDesign2(Magnetostatic, XY) - Analysis** RMB *Add Solution Setup*

Parameter	Input
Name	Magnetostatic_analysis_1

Table 28.4: Magnetostatic solution setup.

- Select via LMB select the rotor iron as well as the stator iron
- From *Field Overlays* select *field-B-Mag\_B*
- From *Create Field Plot* select *Mag\_B-Stator* and *Mag\_B-Rotor*

- uncheck *Full Model*
- Select via LMB select the rotor iron as well as the stator iron
- From *Field Overlays* select *field-A-Flux Lines*
- From *Create Field Plot* select *Flux Lines-Stator* and *Flux Lines-Rotor*
- uncheck *Full Model*
  
- Validate
- Analyze All

Simulation will results as shown in Figure

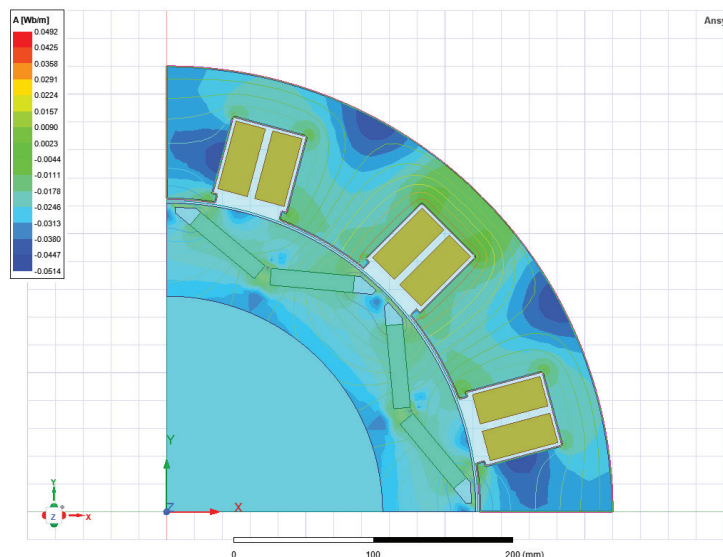


Figure 28.1: Magnetostatic analysis result.

## 28.2 Maxwell 3D Design

- To create a Maxwell 3D design: RMB → *Analysis-Analysis\_1* → *Create Maxwell Design* and select
  - Type → Maxwell 3D Design
  - Solution Setup → Analysis\_1
  - Press OK

When 3D model has been performed, the following steps shall be followed

- Check *Simulation-Validation*
  - From drawing window select the stator iron → RMB → *Assign Excitation - Set Eddy Effects* and select:

- Use suggested values
- From drawing window select the rotor iron → RMB → *Assign Excitation - Set Eddy Effects* and select:
  - Use suggested values
- Check *Simulation-Validation*

### 28.2.1 Transient Analysis

From 3D Maxwell design is possible to perform transient analysis, as follows

- LMB → **Maxwell3DDesign1(Transient)** → *Excitations* → *PhaseA*

Parameter	Input
Name	PhaseA
Type	Winding Group
Winding Type	Current
IsSolid	Stranded
Current	$-600*\sin(\text{position}*4-\pi/3)$
Number of Parallel Branches	4

Table 28.5: PhaseA Excitation setup.

- LMB → **Maxwell3DDesign1(Transient)** → *Excitations* → *PhaseB*

Parameter	Input
Name	PhaseB
Type	Winding Group
Winding Type	Current
IsSolid	Stranded
Current	$-600*\sin(\text{position}*4-\pi/3-2\pi/3)$
Number of Parallel Branches	4

Table 28.6: PhaseA Excitation setup.

- LMB → **Maxwell3DDesign1(Transient)** → *Excitations* → *PhaseC*

Parameter	Input
Name	PhaseC
Type	Winding Group
Winding Type	Current
IsSolid	Stranded
Current	$-600 * \sin(\text{position} * 4 - \pi / 3 - 4 * \pi / 3)$
Number of Parallel Branches	4

Table 28.7: PhaseA Excitation setup.

**START A TRANSIENT ANALYSIS** - to start a transient analysis, the following preliminary steps are required

- RMB → Maxwell3DDesign1(Transient) and select
  - *Validation Check* (all fields must be checked)
  - *Analyze All* (simulation will start)

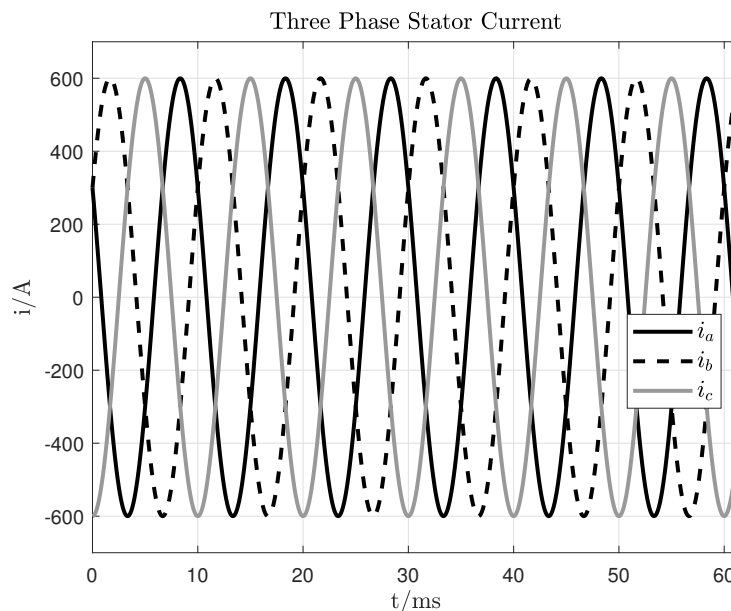


Figure 28.2: Simulation results: stator currents.

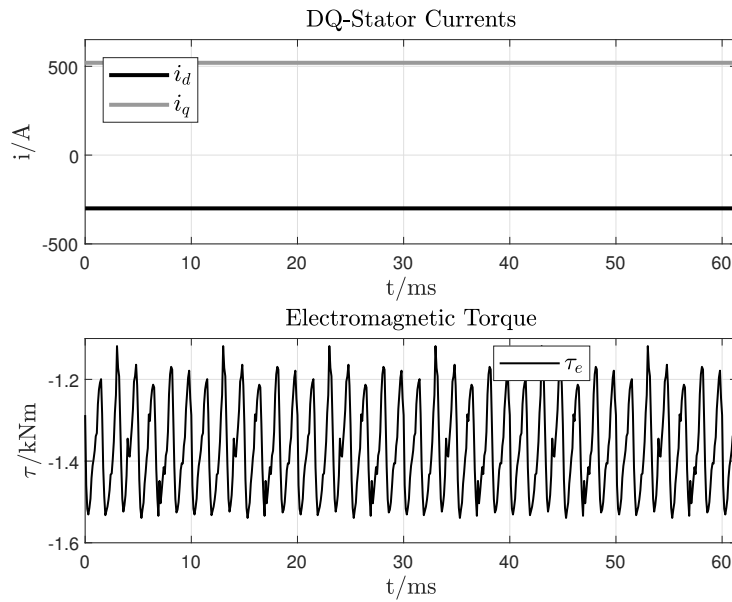


Figure 28.3: Simulation results: DQ-Stator currents and electromagnetic torque.

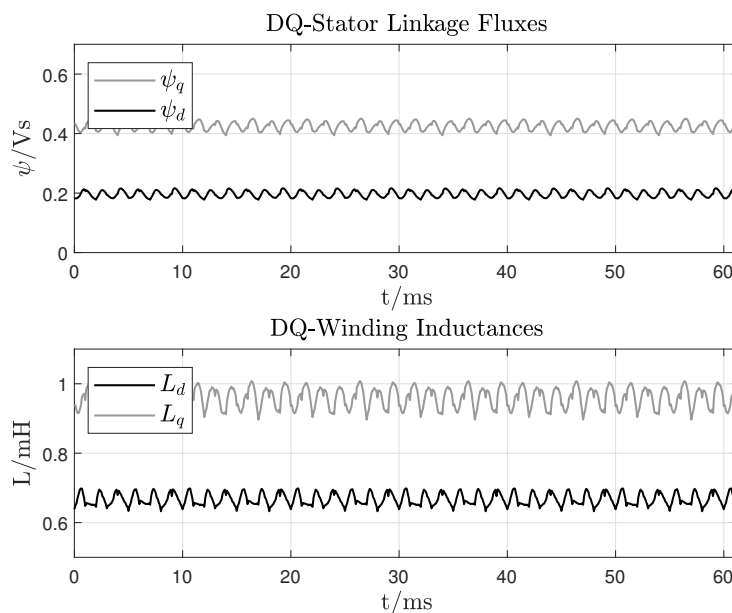


Figure 28.4: Simulation results: DQ-fluxes and DQ-inductances.

# Bibliography

- [H. Merritt, 1967] Herbert Merritt - *Hydraulic Control Systems*. Wiley 1967.
- [G.K. Costa, 2015] G. K. Costa, N. Sepehri - *Hydrostatic Transmission and Actuators*. Wiley 2015
- [N. Manring 2005] Noah D. Manring - *Hydraulic Control System*. Wiley 2005
- [P. Krause, 2013] P. Krause, O. Wasynczuk, S. Sudhoff, S. Pekarek - *Analysis of Electric Machinery and Drive Systems*. Wiley 2013.
- [D. Hanselman, 2012] D.D. Hanselman - *Brushless Motor. Magnetic Design, Performance and Control*. E.Man Press 2012.
- [J.R. Hendershot, 2010] J.R. Hendershot, T.J.E. Miller - *Design of Brushless Permanent-Magnet Machines*. Motor Design Books LLC 2010.
- [J. Pyrhönen, 2008] J. Pyrhönen, T. Jokinen, V. Hrabovcova, H. Niemelä - *Design of rotating electrical machines*. Wiley 2008.
- [S.Umans, 2003] S.D. Umans - *Fitzgerald and Kingsley's Electric Machinery*. McGraw-Hill 2003.
- [T. Lipo, 2017] Thomas Lipo - *Introduction to AC Machine Design*. Wiley 2017.
- [N. Bianchi, 2004] N. Bianchi, T. Jahns - *Design, analysis, and control of interior PM synchronous machines*. CLEUP 2004.
- [J. Rodriguez, 2012] J. Rodriguez, P. Cortes - *Predictive Control of Power Converters and Electrical Drives*. Wiley 2012.
- [T. Geyer, 2017] Tobias Geyer - *Model Predictive Control of High Power Converters and Industrial Drives*. Wiley 2017.
- [M. Nehrir, 2009] M. Nehrir, C. Wang - *Modeling and Control of Fuel Cells*. Wiley 2009.
- [A.L. Dicks, 2018] A.L. Dicks, D.A.J. Rand - *Fuel Cell Systems Explained*. Wiley 2018.
- [USDE, 2002] U.S. Department of Energy - *Fuel Cell Handbook*. U.S. Department of Energy 2009 - Seventh Edition.
- [G. Plett, 2015] Gregory L. Plett - *Battery Modeling. Volume I*. Artech House 2015.
- [G. Plett, 2015] Gregory L. Plett - *Battery Modeling. Volume II*. Artech House 2015.

- [**G. Plett, 2004]** Gregory L. Plett - *Extended Kalman filtering for battery management systems of LiPB-based HEV battery packs. Part 1. Background.* Journal of Power Sources 134 (2004).
- [**G. Plett, 2004]** Gregory L. Plett - *Extended Kalman filtering for battery management systems of LiPB-based HEV battery packs. Part 2. Modeling and identification.* Journal of Power Sources 134 (2004).
- [**G. Plett, 2004]** Gregory L. Plett - *Extended Kalman filtering for battery management systems of LiPB-based HEV battery packs. Part 3. State and parameter estimation.* Journal of Power Sources 134 (2004)
- [**M. Kazimierczuk, 2011]** M. Kazimierczuk, D. Czarkowski - *Resonant power converters.* Wiley 2011.
- [**E. Furlani, 2001]** Edward P. Furlani - *Permanent magnet and electromagnetical devices.* Academic Press 2001.
- [**H. Woodson, 1968]** H.H. Woodson, J.R. Melcher - *Electromechanical Dynamics, Part I: Discrete Systems.* John Wiley 1968.
- [**B. Gibbs, 2011]** B.P. Gibbs - *Advanced Kalman Filtering, Least-squares and Modeling.* John Wiley 2011.
- [**M. Verhaegen, 2007]** M. Verhaegen, V. Verdult - *Filtering and System Identification.* Cambridge University Press 2007.
- [**L. Ljung, 1999]** L. Ljung - *System Identification. Theory for the User.* Pearson 1999.
- [**W. Leonhard, 2001]** L. Ljung - *Control of Electrical Drives..* Springer 2001.
- [**H. K. Khalil 2002]** H. K. Khalil - *Nonlinear Systems.* Third edition, Prentice Hall 2002.
- [**J.J.E. Slotine 1991]** J.J.E. Slotine, W. Li - *Applied Nonlinear Control.* Prentice Hall 1991.
- [**G. Strang 2006]** G. Strang - *Linear Algebra.* Fourth Edition Brooks-Cole 2006.
- [**K. Ogata, 2009]** Katsuhiko Ogata - *Modern Control Engineering.* Pearson 2009.
- [**K. Ogata, 1987]** Katsuhiko Ogata - *Discrete-time Control Systems.* Prentice-Hall 1987.
- [**R. Isermann, 2011]** Rolf Isermann, Marco Munchhof - *Identification of Dynamic Systems: An Introduction With Applications.* Springer 2011.
- [**B. Gibb, 2011]** Bruce P. Gibb - *Advanced Kalman Filtering, Least-Squares and Modeling.* J. Wiley 2011.
- [**F. Lewis, 2012]** Frank Lewis - *Optimal Control.* J. Wiley 2012.
- [**N. Mohan, 1995]** N. Mohan, T.M. Undeland, W.P. Robbins - *Power Electronics.* Second edition J. Wiley 1995.
- [**R. Marino, 2010]** Riccardo Marino, Patrizio Tomei, Cristiano M. Verrelli - *Induction Motor Control Design.* Springer 2010.